Wavelength Selection and Wide-Temperature-Range Operation of Neodymium-Doped Lasers

Andrew Lee White

Thesis presented for the degree of
Engineering Doctorate in Photonics at Heriot-Watt University.

Heriot-Watt University School of Engineering and Physical Sciences
August 2014

Abstract

This thesis presents research results in two general areas of the solid-state laser technology commonly used in defence applications. The first area uses volume Bragg gratings (VBGs) as cavity mirrors, giving wavelength selection, linewidth reduction and improved frequency doubling efficiency. The second area is in extending the operating temperature range of diode-pumped Nd-doped pulsed lasers through the use of VBGs, external-cavity absorber-locked diode lasers and enhancements of pump chamber efficiency.

For a laser-diode end-pumped Nd:YVO_4 solid-state laser, a VBG laser cavity, with output powers of up to 6.2 W is demonstrated at 1064 nm. With a conversion efficiency of 0.4 and M^2 of $\leq$1.2, the laser linewidth is reduced by a factor of 16, to 72 pm, compared to a conventional dielectric mirror cavity. Intra-cavity losses due to the VBG are shown to be 2%. The 1064 nm VBG cavity is then Q-switched using an AO modulator to generate peak powers of 2.3 kW. The second harmonic generation in a MgO:PPSLT crystal produced a 20% increase in second harmonic power, compared to a cavity with a conventional dielectric mirror. The improvement is attributable to the reduced linewidth. A similar configuration, but using a VBG with 98% reflectivity at 1342 nm, generates up to 3.8 W of output power. The use of two VBG mirrors in a single cavity, further narrows the linewidth, allowing for output powers up to 2.3 W, in a single longitudinal mode. In-cavity heating of the VBG is found to give a reduction in reflectivity, a shift in the centre wavelength and increased linewidth. This is both modelled and experimentally demonstrated.

For enhanced pumping of high-energy Q-switched Nd:YAG zigzag-slab lasers, two techniques of externally locking the wavelength of the QCW laser diodes are demonstrated. A chirped 808 nm VBG locks the wavelength of a newly developed chirped quantum-well laser-diode array, without the need for fast-axis collimation. Locking over a temperature range of 50 °C is demonstrated, with a predicted locking range of 70 °C. As an alternative to VBG locking, a laser diode bar locked at 885 nm is also demonstrated by using a thin Nd:YVO_4 absorber. Filtered feedback locks the spectrum into peaks, which are in the Nd:YAG absorption bands over a 45 °C range. In a parallel effort, a pump laser array configuration that increases the overall absorption path length from 1 to 3 cm in a side-pumped zigzag slab is demonstrated. By optimising the bounce lengths of the pump light and the inclusion of multi-wavelength laser bars, operation up to 80 °C is demonstrated with an absorption efficiency of 80%. By adjusting the diode drive pulse duration, a Q-switched laser using this pump head operates from -40 to +60 °C with a constant energy of 60 mJ. The operational temperature range of this configuration is shown to be over 120 °C.

Acknowledgments

Firstly, I would like to thank Selex ES for giving me the opportunity to work within the advanced targeting group, allowing me to access cutting edge research opportunities and world class facilities. In particular, I would like to thank my academic supervisor Dr Gavin Hall for all his support and encouragement. I would also like to thank Professor Howard Baker for all his supervision and input into my thesis.

I also owe a huge amount of gratitude to my colleagues at Selex ES, without whom, I would not have been able to develop my knowledge and skills in the field of laser physics. In particular, Dr Ian Elder and David Legge for their support and input throughout my thesis. I would also like to thank Professor John Barr for his drive and direction during my time at Selex ES.

Special thanks must go to my parents Wendy and David, my sister Lisa and my partner Louise, without their support and love, I would not have made it to the end of my journey.

List of Publications, Conferences and Patents

1. A. White, G. Hall J. Barr, M. McElhinney P. Thiagarajan, " Thermally insensitive diode arrays for solid-state lasers ", *SPIE Defense, Security, and Sensing*, paper 7113-57, (2008), [Presentation only]

2. A. White, G. Hall, J. Barr, M. McElhinney, P. Thiagarajan, C. Cao " Thermally insensitive laser diode arrays ", *SPIE Defense, Security, and Sensing*, Laser Technology for Defense and Security V, 73250P pages 73250 - 6, (2009).

3. A. White, I. Elder, G. Hall. " Single longitudinal mode and dual wavelength CW VBG lasers at 1342 nm and 1064 nm ", *Proc. SPIE 8543*, Technologies for Optical Countermeasures IX, pages 85430A-85430A-8, (2012).

4. A. White, G. Hall, J. R.M. Barr, M. McElhinney, P. Thiagarajan, C. Cao " Thermally Insensitive Laser Diode Arrays for Solid State Laser Pumping " PhotonEx, High Power Diode Lasers and Systems Conference HPD, (2009).

5. J. Barr, A. White, and S. Moore. " Laser system and method of operation ", September 26 2013. US Patent App. 13/988,521

ACADEMIC REGISTRY
Research Thesis Submission

Name*:*	Andrew Lee White		
School/PGI:	EPS		
Version: *(i.e. First, Resubmission, Final)*	Final	Degree Sought (Award **and** Subject area)	Engineering Doctorate

Declaration

In accordance with the appropriate regulations I hereby submit my thesis and I declare that:

1) the thesis embodies the results of my own work and has been composed by myself
2) where appropriate, I have made acknowledgement of the work of others and have made reference to work carried out in collaboration with other persons
3) the thesis is the correct version of the thesis for submission and is the same version as any electronic versions submitted*.
4) my thesis for the award referred to, deposited in the Heriot-Watt University Library, should be made available for loan or photocopying and be available via the Institutional Repository, subject to such conditions as the Librarian may require
5) I understand that as a student of the University I am required to abide by the Regulations of the University and to conform to its discipline.

* *Please note that it is the responsibility of the candidate to ensure that the correct version of the thesis is submitted.*

Signature of Candidate*:*		Date:	

Submission

Submitted By *(name in capitals):*	
Signature of Individual Submitting:	
Date Submitted:	

For Completion in the Student Service Centre (SSC)

Received in the SSC by *(name in capitals):*			
Method of Submission *(Handed in to SSC; posted through internal/external mail):*			
E-thesis Submitted (***mandatory for final theses)***			
Signature:		Date:	

Please note this form should bound into the submitted thesis.

Updated February 2008, November 2008, February 2009, January 2011

Contents

Chapter 1

Introduction

Since the inception of the laser by Maiman in 1960 [1] and despite the claim that they were "solutions looking for a problem", militaries around world quickly recognised the potential of the laser for a wide variety of combat functions.

Whilst high-energy laser weapons were at the forefront of military aspirations, the initial role for the laser was to mark targets, guiding new sensor enabled bombs much more accurately than had previously been possible to achieve. For the last thirty years, targeting lasers have been fitted to a wide range of military devices, from fixed wing aircraft to ground-based vehicles. The deployment of hand-held targeting lasers has also increased over the past thirty years, and is now considered standard issue equipment for most special forces operators and joint forward air controllers.

The laser targeting market in Western countries was estimated to be in excess of £70 million [2]. As a result of technological advances improving size, weight, functionality and cost, the market is expected to grow by 50% over the next ten years [3].

A more recent requirement for military operators is the deployment of optical countermeasures. Increasingly, the use of stealth technology and optical sensors in military equipment has stimulated development in the optical countermeasures field. Roles, such as denying communications, disabling missile targeting systems and dazzling optical sensors, are now key capabilities for a modern military.

The first part of this thesis investigates the use of volume Bragg gratings to create multiple narrow-linewidth sources. The aim is to develop sources that, in the future, could be used to create a cost-effective multi-wavelength source for the countermeasure applications described previously.

The bulk of the predicted growth in the laser market is expected to occur in the hand-held segment, where older flashlamp-pumped systems are gradually being

replaced with diode-pumped technology. The focus of the second half of this thesis, chapters 7, 8 and 9, is the development of diode pumping technologies to satisfy the man-portable laser requirements. The main characteristic of the new pumping configuration is the ability to operate without any active thermal control. In current targeting lasers deployed in vehicles and aircraft, a significant portion of the power consumption, overall weight and cost are attributed to the thermal management. To allow for covert operation in the field, the laser must be lighter, more portable and more efficient and therefore must be able to operate without any thermal control.

1.1 Target Designator / Rangefinder Laser Requirements and Characteristics

The purpose of both the targeting laser and the laser dazzler is to direct energy onto a target. The incident energy on the target will either disable any optical sensor or the subsequent scatter from the target will allow for identification from sensors placed a large distance away. The first targeting lasers were based on the initial Ruby laser developed by Maiman, as well as the Q-switching techniques developed shortly after. The ability to increase the overall peak power onto a target by Q-switching, allowed for an increase in the range at which the signal could be detected [4] [5].

Fig. 1.1 shows the typical parameters that define the stand-off distance for a targeting laser, the diagram is based on that presented by Kruapech and Widjaja [6].

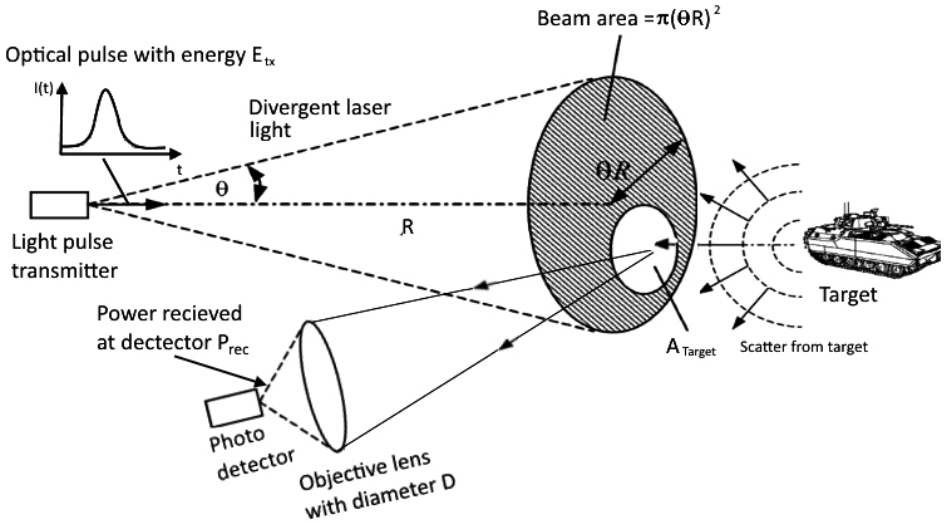

Figure 1.1 – Diagram of targeting system with key laser parameters.

The key parameters are also shown in equation (1.1) [6]. This equation determines the power received by a sensor placed at some distance away from a designated target.

$$P_{rec} = \frac{E_{tx} D^2 A_t}{8\pi R^4 \Theta^2 t} \times \tau_{atm} \tau_{sys} \tag{1.1}$$

where

E_{tx} = Output energy transmitted

P_{rec} = Power on target

R = Distance to target

D = Detector aperture size

Θ = Laser half angle divergence

A_t = Target area

τ_{atm} = Atmospheric transmission factor

τ_{sys} = System transmission factor

t = Laser pulse duration

λ = Wavelength

From equation (1.1), the laser performance can only affect a limited number of parameters. The first parameter is the transmitted energy. The simple linear relationship shows that by increasing the output energy from the laser, the level observed on the receiver can be increased. Likewise, by decreasing the pulse width, the peak power incident on the detector could be increased. For the adjustment of the pulse width however, we are limited by the performance of the sensor used to detect the scattered light. Older seekers typically operate with a bandwidth of 300 MHz, limiting the resolution to ≈ 3 ns. For the accurate detection of pulses at this operational bandwidth, the operating pulse width is typically above 11 ns.

The second parameter that is a function of the laser performance is the divergence. This will essentially control the size of the beam incident on the target. By increasing or decreasing the divergence, the amount of energy on a target can be varied . The optimum solution suggests that a narrow divergence will provide the optimum performance. In a real-life scenario however, it must be considered that the target reflectivity will not be uniform. By filling the target with the laser beam, a reflection from the whole target is received. Any variations in the reflectivity across the target will be averaged, ensuring low regions of reflectivity do not limit the scatter of the incident light. A certain level of divergence is therefore required to ensure that sufficient energy is distributed across the whole target. However, too large a divergence will significantly reduce the overall energy on the target, therefore limiting the range of the laser.

In the 1970s, experiments to determine the required energy on the target led to the development of the "Ground / Vehicular Laser Locator Designator" or G/VLLD,

which defined the required laser performance for land-based lasers. The performance outlined the required energy exiting from the laser to be in the region of 120 mJ. To achieve sufficient energy on target, the divergence of the laser was determined to be 200 μrads. The divergence produces a beam with a diameter of 2 m at a distance of 10 km. This is sufficient to achieve target coverage on an object such as a tank [7]. The requirement to operate the laser at certain repetition rates arose from the need to encode the designation signal. This allowed for the signal to be isolated from other optical sources and to prevent countermeasures from being deployed. The repetition rate of today's military targeting lasers is typically in the region of 10 - 20 Hz.

There are a number of other important characteristics of a targeting laser that must be considered. The first is the ability to maintain boresight of the laser to a given datum point. The boresight of the laser refers to the angular direction in which the laser fires. At all times, this must be referenced to a datum point such as a mechanical fixing or an optical viewing path. The potential for errors in the boresight of the laser will impact on the targeting accuracy of the system. At best, this would decrease the accuracy of the targeting systems, at worst it can lead to the marking of an incorrect target.

The final requirement of the targeting laser is the robustness and manufacturability of the design. The environments in which the laser is required to operate can be considered fairly extreme. The required operational temperature range varies depending on which vehicle the laser is deployed onto. For a laser deployed on an aircraft, the temperature range is over 100 °C. This range covers storage temperatures in a desert environment, which can lead to temperatures as high as 60 °C, and operation at high altitudes, where temperature can be as low as -40 °C. Hand-held lasers, deployed in Arctic operations, can also experience -40 °C temperatures. This wide temperature range, combined with the vibration and shock demands placed on the laser, affect how the laser is designed. As a result, the laser cavity and pump head configurations used in military lasers are typically bespoke when compared to other industries. In the next section we present the bespoke laser cavity and pump head designs used to meet both the operating conditions and performance characteristics discussed. Section 1.2 then develops the requirements and characteristics of an optical countermeasures configuration.

1.1.1 Laser Gain and Cavity Parameters

We first briefly describe the principles of operation for a laser. The description focuses on a 4-level diode-pumped laser, operating in both a continuous-wave (CW) and Q-switched regime. The absorption of optical emission in a material that possesses an

energy state identical to the energy of the incident photon, leads to the promotion of an atom to a higher energy level, this is shown in Fig. 1.2a. As a result of phonon interactions between the atom and the lattice, there is a rapid decay from this level into the upper lasing level. The ability of the atoms to remain in this upper level typically determines the storage capabilities of the material and its applicability for Q-switching. As a result of vibronic interactions, atoms can decay towards the ground state releasing energy as heat. Depending on the type of material, an atom can spontaneously emit a photon with energy E, decaying to the lower lasing level in the process. The average amount of time the atom will spend in the upper lasing level is a function of the materials kinetic constants. This average period is typically called the fluorescence lifetime. In the presence of a strong electromagnetic (EM) field with the same energy E however, the decay of the atom is stimulated, leading to optical gain for the incident EM field. The level of optical gain can be increased by promoting a large number of atoms to the upper lasing level, thereby generating a population inversion between levels 2 and 3.

The ability to store atoms in the upper lasing level determines the ability of the material to provide high gain for a pulsed or a CW EM source. For a CW source, the fluorescence lifetime is typically not as important, as incident intensity is always present, allowing for stimulated emission to occur. For a pulsed EM source, the lifetime will limit the build-up of the population inversion before the optical pulse arrives. The highest level of gain is therefore achievable from materials that possess a long fluorescence lifetime, allowing for a build-up of atoms in the upper lasing level prior to the pulse's arrival.

In a laser, the EM field builds up from spontaneous emission within a laser cavity. The cavity traps the EM radiation allowing for multiple passes of the laser crystal, thereby experiencing gain on each pass. A small amount of the EM radiation is coupled out, which provides the laser output. For the laser to be stable, the losses from the light coupled out, must be equal to the gain achieved by the EM radiation after a single round trip. The level of gain is a function of the population inversion and therefore the threshold level is denoted as N_{th} where N refers to the population density of the upper lasing level.

In a CW regime, the population inversion is clamped at threshold, and is therefore independent of the pumping rate. Pulsing the diode pump source would not significantly increase the overall gain. By introducing a large loss into the cavity, the effective population inversion threshold can be increased to a number of times above the initial threshold. By modulating this introduced loss, the threshold inversion can initially build-up during the high loss period. The limitation of increasing the population

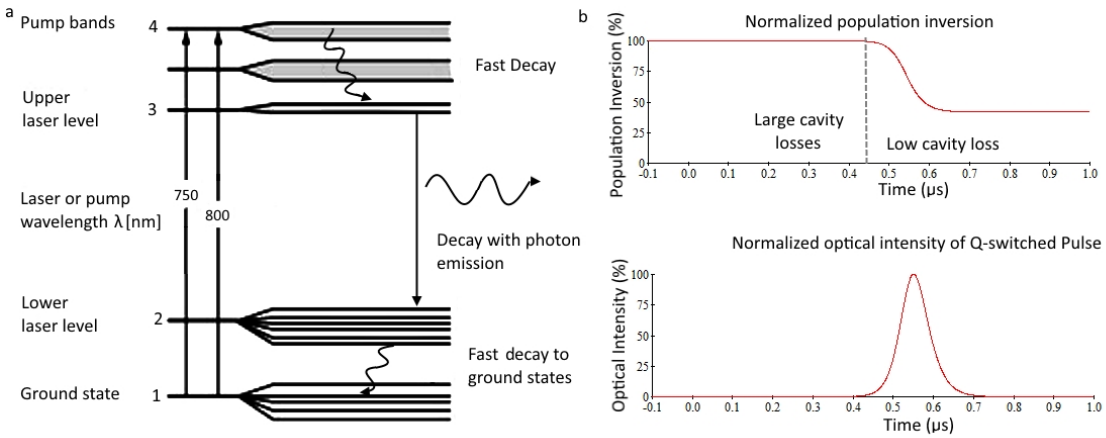

Figure 1.2 – a: Energy diagram of 4-level laser. b: Transient population inversion and optical intensity of a Q-switched pulse.

inversion is then the fluorescence lifetime of the atoms in the upper level. When an output pulse is required, the cavity losses are reduced. This allows for the build-up of a giant pulse which can extract the large inversion population. This Q-switching technique allows for significantly larger pulse energies to be generated for a given optical pump pulse. The population inversion and optical pulse build-up are shown in Fig. 1.2b.

Two different methods of Q-switching are presented in this thesis. The initial Q-switching technique uses a CW pump source, with an acousto-optic modulator (AOM) used to modulate the cavity losses. The inversion threshold builds up during the pumping period, with the AOM providing large cavity losses. The AOM is then opened for a short period allowing the optical pulse to build-up and decay in the cavity. The AOM is then closed to limit the build-up of a secondary pulse. This AOM is typically modulated at the fluorescence lifetime to maximise the gain build-up.

In the second method used in this thesis, the diodes are pulsed in a quasi-continuous-wave (QCW) manner, with pulse durations in the order of 230 μs. By pulsing the diodes and operating at a relatively low repetition rate, large pulse energies ($\geq$ 100 mJ) can be achieved with relatively low thermal loads within the gain medium, limiting the thermal lens. This is the typical method of operation for targeting lasers.

The first Ruby laser designs used for target designation were quickly replaced with Neodymium-doped glasses [5]. This was primarily due to the ease of manufacturing large Neodymium-doped glasses compared to that of the Ruby crystals. The glass host materials have poor thermal properties however, limiting scalability and increasing the size of the crystals used. The first demonstration of a Neodymium-doped yttrium aluminium doped garnet (Nd:YAG) laser in 1964 [8] quickly resulted in the material becoming the gain medium of choice for targeting lasers. The superior optical,

thermal and mechanical properties, as well as favourable laser properties, allowed for increased energies within much smaller gain mediums compared to that of Ruby and Neodymium-doped glass.

The doping of YAG with Nd^3+ ions leads to the most commonly used gain material Nd:YAG. Undoped YAG is an optically isotropic material with mechanical properties similar to that of sapphire. The relatively low thermal expansion coefficient and high thermal conductivity allow for reduced thermal gradients compared to glass materials. The cubic structure of the YAG host material results in a fairly narrow gain bandwidth, leading to a high emission cross-section at 1064 nm. Due to a size mismatch of the Nd ions, the doping level in single crystals is typically limited to 1.4% when grown by the Czochralski method [9], although higher doped material has been produced using the temperature gradient technique [10].

Increases in the doping density will also decrease the fluorescence lifetime due to increased energy transfer and phonon interactions [11]. The energy levels for Nd:YAG are shown later in Fig. 1.3. The main cause of concentration quenching is due to the interaction of a donor ion in the $F_{3/2}$ and an acceptor ion in the $I_{9/2}$ ground state. This interaction leads to two final ions in the $I_{15/2}$ state, which decay via multi-phonon emissions back to the ground state [12]. As the doping density is increased, the number of Nd ions present in the ground state also increases. This in turn increases the ion-to-ion interaction rate, thereby increasing the quenching effect [12] and decreasing the fluorescence lifetime. In the Q-switched configurations used in military designators, for longer optical pump periods, a decrease in the fluorescence lifetime will reduce the overall energy available. For a 1.1% doped Nd:YAG crystal the fluorescence lifetime is 230 μs compared with 119 μs for a 3% doped material [10]. Highly doped ceramic Nd:YAG has shown the ability to substitute up to 9% Nd^{3+} in YAG [13]. The fluorescence lifetime decreases to $\approx 40\,\mu$s [14] as a result.

Increasing the doping density does increase the effective absorption cross-section, allowing for an increased absorption efficiency. The absorption peak of a 1% doped Nd:YAG at 808 nm is 9 cm^{-1}. By increasing the doping density, the peaks in the absorption profile can be significantly increased [15]. The performance of an Nd:YAG system could be improved by highly doped Nd:YAG configurations when pumping away from the peaks in the absorption spectrum, or when limited absorption path length is available.

In a Q-switched configuration, a balance between the increased absorption and subsequent degradation of the fluorescence lifetime is required to optimize the perfor-

mance of the laser system. High conversion efficiencies in highly doped Nd:YAG have still been reported, with output energies of up to 8 mJ and conversion efficiencies of up to 28% demonstrated [16]. In the configurations used throughout this thesis the Nd:YAG doping density is limited to 1.1%. This allows for pump pulse widths of over 230 μs to be used, reducing the peak power requirements of the pump source.

More recently, other gain materials operating in the same wavelength region have been used to generate the required energy levels [17] [18]. Yb:YAG has similar mechanical properties, whilst optically pumping into the absorption band at 940 nm reduces the quantum defect. The reduced quantum defect, which is a result of the energy difference between the pump and emission wavelengths, increases the efficiency and also reduces the heat generation in the material. Conversion efficiencies of up to 81% in CW configurations have been demonstrated [19]. The long upper state lifetime of Yb:YAG also allows for the gain to be stored efficiently, however, the low emission cross-section limits the actual gain extraction. Operation at 1053 nm has been demonstrated at energies up to 220 mJ in a diffraction limited beam [20]. Another drawback is the fact that Yb:YAG is inherently a quasi 3-level system. As a result of increased ground state excitation at higher temperature, operation below 20 °C is required. As a result of the low emission cross-section and its temperature dependence, Yb:YAG is not typically used for military targeting lasers.

Whilst operation of the first laser-diode pumped Nd:YAG laser was published in 1973 [21], the use of flashlamp pumped targeting lasers is still prevalent in a large number of military targeting equipment used today. Whilst the dramatic increase in available power, efficiency and reduced cost over the last 10 years has seen the laser-diode-pumped solid-state laser become the most suitable choice for almost all modern designs. With military product life cycles of up to 30 years, it is no surprise to find flashlamp pumped systems still in use today.

As a result of the characteristics of flashlamp pumping, the design of most laser designators had a number of common features. The use of Nd:YAG rods or slabs within a reflective chamber was common in a number of military and commercial products as well as in scientific research. The advent of the laser-diode pumped Nd:YAG laser, however, has created a number of different configurations capable of achieving efficient pumping of the gain medium for high output energies [22] [23].

1.1.2 Thermal Lensing

In order to meet the requirements for output energy and divergence, the laser configuration must possess low induced thermal lensing and efficient absorption of the pump light.

Thermal lensing occurs as a result of spatial variations in the optical path length leading to an induced phase variation across the beam. The heat load arises due to non-radiative transitions that result from the absorption of the pump light. An energy diagram of the 4-level system in Nd:YAG is shown in Fig. 1.3. Nd:YAG has a wide absorption band in the 808 nm region allowing for atoms to be promoted from the ground level to the $F_{5/2}$ level. The strongest emission cross-section occurs at 1064 nm between the $F_{3/2}$ and $I_{3/2}$ level. The decay of promoted atoms from both the upper pump band to the upper lasing level and from the terminal laser level to the ground state generates heat through phonon interactions. Further heat is generated through various other non-radiative transitions that occur from higher-lying energy levels[24].

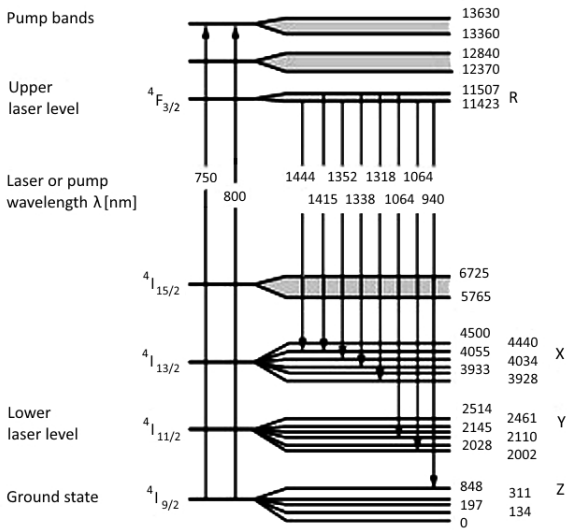

Figure 1.3 – Energy levels of Nd:YAG taken from Laser Physics and Applications, Landolt-Bornstein, Vol. 12, (2008)

The quantum defect created from pumping at 808 nm and lasing at 1064 nm leads a heat load fraction of 0.27 of the overall absorbed power. A number of different non-radiative transitions and cross-relaxations also occur, increasing the heat load to 0.39 [25]. One of the main sources of heat load arises from the quenching effect described previously. The ion-to-ion interaction rate has a dependence on the population inversion density. When stimulated emission occurs, the population inversion decreases, thereby decreasing the quenching effect. This effect reduces the heat load to 0.32. Excited-state absorption from ions promoted to the $F_{3/2}$ level, as well as ESA at pump wavelengths of around 820 nm [26], can also cause increased heat loads at high inversion densities

[24].

Zigzag Slab Gain Medium

The design of the pumping configuration should therefore look to create geometries that limit the overall induced thermal lens. A pumping geometry that reduces the thermal lensing strength has been demonstrated by using the zigzag slab laser gain medium [27]. A diagram of the zigzag slab laser is shown in Fig. 1.4.

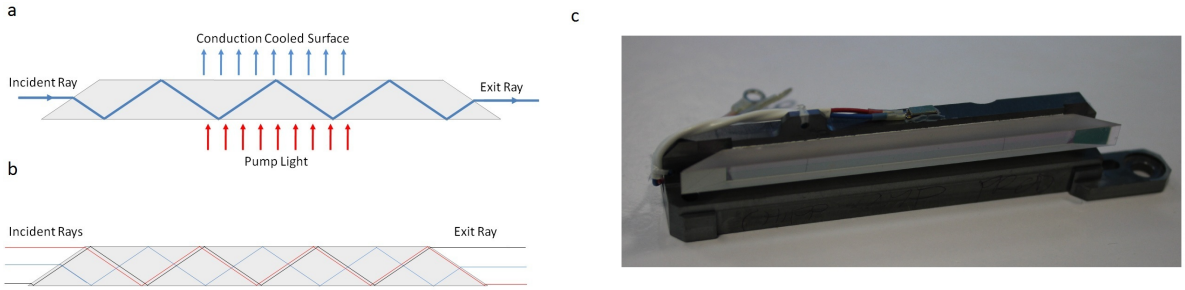

Figure 1.4 – a: Diagram of conduction-cooled, side-pumped zigzag slab. b: Zigzag path through slab. c: Image of Nd:YAG zigzag slab.

In its simplest form, the zigzag slab is pumped from one side and is conduction cooled from the opposite side. In an ideal case this pumping configuration produces a one dimensional heat flow in the slab, with the highest temperature at the pumping face. As a result of the thermo-optic effect in Nd:YAG, the temperature gradient will result in a refractive index change across the slab.

The zigzag path through the slab, shown in Fig. 1.4b, allows the beam to traverse back and forth between the higher temperature pump face and the low temperature heat sunk side. As a result, the optical path difference between rays starting from the pump side and heat sunk side are similar, reducing the strength of the thermal lens. Any optical birefringence in the slab will also be averaged across the beam as a result of the zigzag path. The use of zigzag slabs has shown to reduce the strength of the thermal lens by a factor of 4 when compared to a side pumped rod configuration [28].

In Q-switched configurations, energies of up to 0.5 J have been demonstrated at Selex using the conduction cooled thick Nd:YAG zigzag slab described here. The Nd:YAG zigzag slabs are also used in CW configurations to achieve high average powers. Powers as high as 100 W [29] have been demonstrated in these configurations. In order to scale to higher powers, the slab can be cooled from both sides either by conduction-cooling or water-cooled configurations. Water-cooling of both sides of the slab has allowed powers to be scaled to hundreds of watts [30] [31]. The complexity of the water-cooled configurations and the decrease in operational life as a result of a

sealed water system can limit their use in military products.

The slab faces and overall width are optimised to maximise the fill factor of the slab. A low fill factor will lead to areas of un-extracted gain, reducing efficiency. As presented by Chung *et al.* [32], for a slab with a square aperture of 5×5 mm, the required bounce angle to maximise the gain extraction is 59°. Rather fortuitously, this is also close to Brewster's angle, allowing for the possibility of un-coated slab ends. However, if slab aperture size was increased, the required bounce angle to maximise gain extraction will be different.

Thermal lensing, however, is still present in Nd:YAG zigzag slabs. The complete averaging of the induced phase errors across the beam is only true if an infinitely long slab is considered [33]. When taking into account the real life scenario of optically pumping a gain medium with laser-diode arrays (LDAs), changes in the deposition of gain and the one dimensional heat flow leads to an increase in phase errors [34].

The deposition of the gain into the material, and therefore the heat load, is dependent on the laser-diode pump configuration. A homogeneous pump profile in the slab will limit the induced phase errors. The relatively long length of the slab allows for LDAs (laser diode arrays) to be used in a side pumped configuration. LDA's can provide high peak powers in small overall emission areas, with arrays now providing up to 6 kW/cm^2 [35]. Fig. 1.5 shows the pump configuration used in Selex's current targeting lasers. The slab has a 5×5 mm optical face with a length of 67 mm.

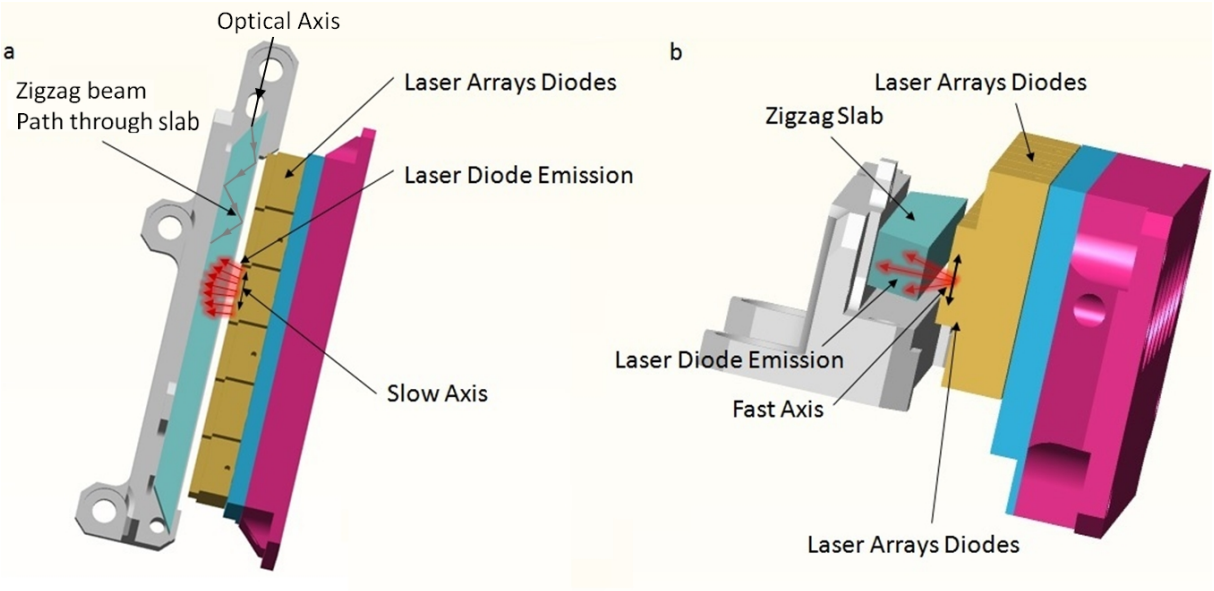

Figure 1.5 – a: Top view of diode-pumped zigzag slab configuration. b: Side view of diode-pumped zigzag slab configuration.

As shown in Fig. 1.5, the slow axis of the arrays is perpendicular to the optical axis of the slab. Each array contains 10 bars, stacked horizontally, with a 400 μm spacer between each one. As a result of the fast axis divergence, typically 36°, the intensity profile of each array is top-hat by the point it reaches the slab face. The arrays are placed side by side to create a continuous emission region.

The configuration does differ from the ideal case due to the finite length of the pump region. At the final LDA on either side, there will be a definitive edge to the gain profile. The diffusion of heat at this boundary point will result in the loss of the one dimensional temperature profile and will alter the optical path length across the beam. The variation in the optical path length will lead to an increase in the thermal lens strength.

Also, whilst the LDAs are placed as close together as possible, the low divergence of the slow axis, typically 16 °, limits the emission from adjacent arrays mixing together. The resultant pump profile across the slab face will have troughs in the regions between each array. The troughs in the pump profile will further alter the heat flow, varying the optical path length across the beam. As a result of the characteristics of the pump profile, the thermal lens strength will be increased from the ideal case [36] [37].

Deposition of the gain itself can also change the overall thermal profile in the gain medium. The strength of the absorption will determine how close to the surface the heat is deposited. In a 1.1% doped Nd:YAG slab, the absorption coefficient is as high as 9 cm^{-1}. If the emission of the LDA was fully locked into the peak wavelength, the overall power absorbed in the first 500 μm could be over 20 $\mathrm{kW/cm}^2$. The resultant heat load of 6.4 $\mathrm{kW/cm}^2$, calculated using the 0.32 factor introduced earlier, will lead to a large temperature rise close to the front surface of the slab. Large temperature gradients close to the surface can lead to surface bulging effects [8], introducing variations in the optical path length across the beam. By adjusting the centre wavelength of the emitters to avoid the strong absorption peak, the induced thermal lens can be reduced. In reality, the finite linewidth of the arrays typically limits the overall power at the peak absorption coefficient. To ensure the thermal lens strength is minimised, Selex operates the LDAs in the 806 nm region instead of the peak region at 808 nm [38]. Operating in this region also reduces the temperature sensitivity of the pump configuration slightly. The 808 nm peak is fairly narrow; even a small change in the temperature of the LDAs will lead to a shift in the emission wavelength, causing a large reduction in the absorbed power. The 806 nm region is much broader, reducing this temperature sensitivity.

Analysis of the thermal lens in zigzag slabs can be completed using a finite element

analysis (FEA) package, such as Comsol [8]. The analysis is often coupled with ray-tracing packages, such as Zemax or ASAP, allowing for the generation of accurate heat loads within diode-pumped configurations [36]. A combination of these packages has been developed at Selex and is further developed in this thesis. The use of the FEA package allows for the heat distribution in the slab to be determined by the use of accurate heat loads and boundary conditions. For a zigzag slab pumped with five LDAs, the typical focal power of the induced thermal lens is 20 m. The modelling of this is shown in more detail in chapter 8.

1.1.3 Laser Divergence

The previous section has shown that the use of a zigzag slab is ideally suited for high power applications where relatively low thermal lensing is required. The actual size of the gain medium will determine a number of different parameters. In the example shown in Fig. 1.5, a large gain medium would increase the overall pumping area, allowing for higher energies to be achieved. An increase in the cross section of the slab will, in the same cavity configuration, increase the required number of modes to efficiently extract the gain. As a result of the increased number of higher order modes, there will be a degradation in the beam quality of the laser [8]. The length of the slab can be increased however, without any degradation in the beam quality. Longer zigzag slabs can therefore achieve high output energies, whilst maintaining the divergence of a short slab. Practical issues involving the peak power density exceeding the material damage threshold inevitably limit the achievable power using this technique.

The divergence is related to the cross section of the gain medium by the Fresnel number N_{Fr}, where

$$N_{Fr} = \frac{a_{slab}^2}{L_{cavity}\,\lambda} \tag{1.2}$$

Where a_{slab} is the gain medium radius, L_{cavity} is the cavity length and λ is the wavelength. The Fresnel number describes the diffraction losses in a cavity. For Fresnel numbers close to 1, the cavity will exhibit large diffraction losses as a result of the aperture in the cavity. A low Fresnel number will typically favour lower order modes as a result of the strong diffraction losses. As the Fresnel number increases, the diffraction losses are reduced. These configurations will not attenuate the higher order modes as much, due to the reduced diffraction losses. As a result, the mode discrimination within the cavity is reduced compared to the previous case.

Selex lasers use plane-parallel, thermally-stabilised cavities, typically operating with Fresnel numbers of ≈ 6, with an aperture size of 5 mm. The 5 mm slab diameter allows for relatively easy handling and mounting of the gain material, without any

risk of damage to the slab. The cavity length is typically in the order of 1 m. The long cavity length not only allows for improved divergence from the resonator but also provides fairly long pulse durations for a resonator operating a number of times above threshold [39]. For a 1 m cavity length, the typical fundamental mode diameter, calculated using the resonator stability criterion with a thermal lens of 20 m, is 2.2 mm. To fully fill the 5 mm slab area and extract all of the gain, higher order modes are required. The mode diameter of the higher order Hermite Gaussian modes increases with the relationship [8]

$$\omega_m = \omega_o\sqrt{2m+1} \qquad \omega_n = \omega_o\sqrt{2n+1} \tag{1.3}$$

Where n and m are the mode numbers in the horizontal and vertical directions, ω_o is the size of the fundamental mode and ω_m/ω_n are the diameters of the higher order modes. To fill a mode volume of 5 mm, mode numbers of up to 2 are capable of propagating in the slab. Mode numbers higher than 2 would experience large losses per round trip as a result of clipping from the slab aperture. Lower order modes will experience lower losses and will be able to achieve threshold. Fig. 1.6 shows the mode radius as a fraction of power.

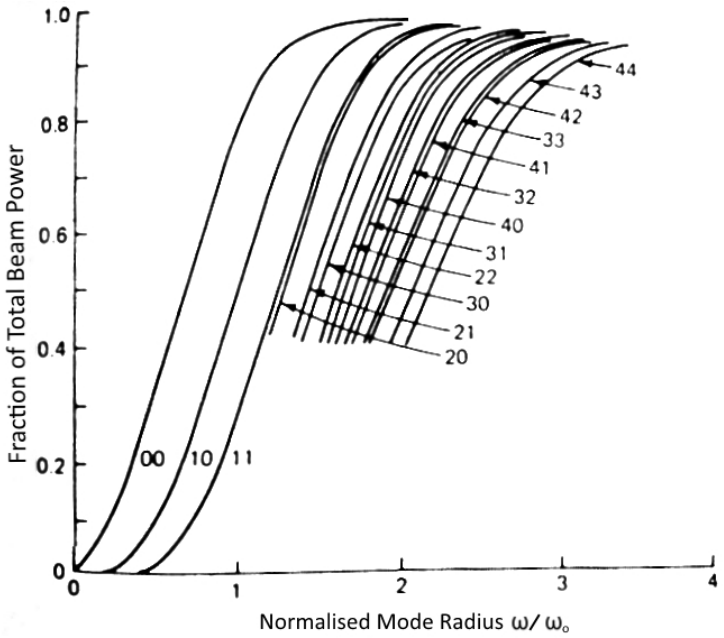

Figure 1.6 – Plot of fractional power in mode vs. encircled diameter for a series of higher order modes. Taken from Solid State Laser Engineering P 5th Ed. W. Koechner.

Fig. 1.6, at a mode volume of roughly 2.3 times that of the fundamental mode (= 5 mm aperture), confirms that modes as high as 2,0 are capable of fitting within the slab aperture without significant losses.

The divergence angle increases with the factor ω/ω_0, a mode with a $1/e^2$ diameter

of 4.4 mm will therefore increase the divergence by a factor of 2. The divergence of the fundamental mode Θ_d can be calculated using the equation

$$\Theta_d = \frac{2\lambda}{\pi\omega_0} \tag{1.4}$$

From this calculation, the divergence of the fundamental mode would be 614 μrads. A mode with a 90% diameter of 4.4 mm would increase the divergence to 1.25 mrads. Selex lasers typically operate with divergences of 1-1.3 mrads, in line with the calculation.

As the thermal lens strength increases, the fundamental mode size reduces, and the required number of modes to fill the aperture increases. An increase in the mode number will increase the divergence, for example, an increase in the thermal lens strength from 20 m to 5 m would reduce the fundamental mode size to 1.7 mm. Assuming a mode with a waist size of 4.4 mm can still operate within the cavity, the divergence would increase from 1.2 to 2.1 mrads. In order to meet the divergence requirements shown previously in equation (1.1), a low induced thermal lens strength is required to minimise the divergence.

The simple modal analysis completed here allows for divergence values to be calculated based on the size of the fundamental mode. This calculation, however, has only taken into account the Hermite Gaussian modes. When considering clipping from a square aperture, it would typically be expected to observe Hermite Gaussian modes over Laguerre Gaussian modes. We have assumed a thermal lens strength of 20 m for the mode size calculation. Modelling of the thermal lens strength has shown that the actual curvature of the phase is not a perfect parabolic function. The spatial variation in the thermal lens strength may allow for other higher order modes that have not been considered in this calculation. The result maybe a slightly larger or smaller divergence value than calculated here. To fully analyse the modal composition of the beam, a Fox-li analysis[40] of the resonator can be completed. This analysis allows for the total phase and intensity of the cavity mode to be calculated by propagating a beam through the cavity using the beam propagation method. Spatial phase variations, inhomogeneous gain profiles and diffraction from apertures can be factored in to produce a beam containing all the supported modes in the resonator. This analysis is planned for future work.

1.1.4 Laser Cavity Design

The cavity designs in military lasers typically differ from normal cavity designs due to the demands of the external environment. The requirement to maintain alignment over

a wide temperature range and the ability to operate under mechanical stress requires a resonator that is alignment-insensitive. As a result, resonator designs typically use refraction or prisms to steer the beam, rather than mirrors.

One of the most common resonator designs is the cross-Porro resonator [8]. The resonator is shown in Fig.1.7a. The alignment insensitivity arises from the coupling of two Porro prisms and a corner cube.

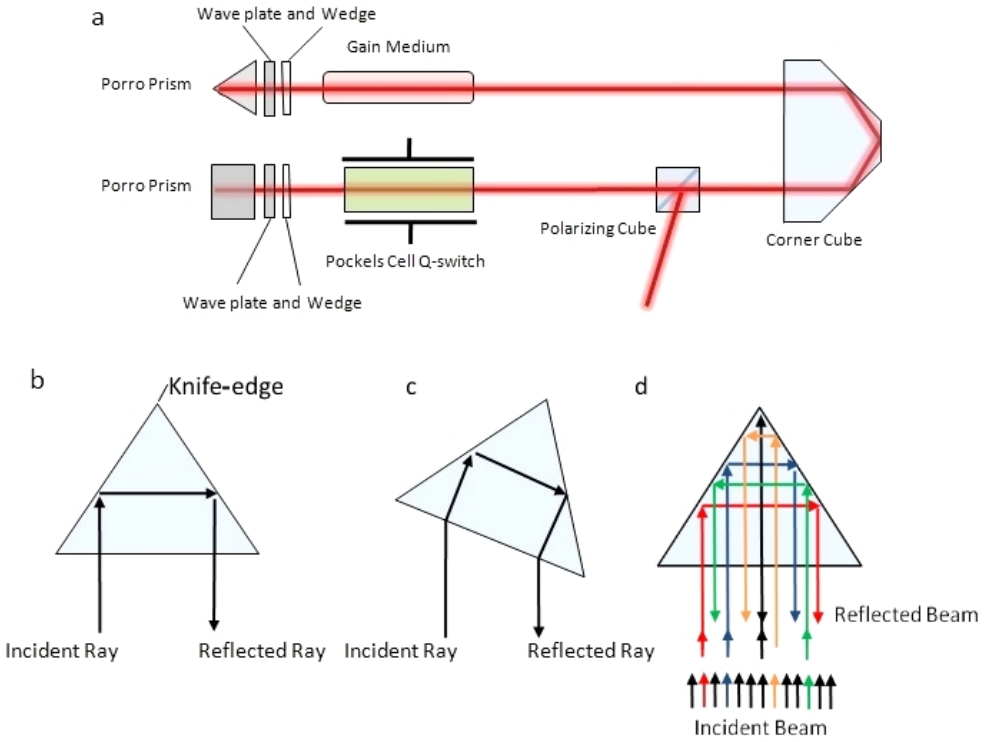

Figure 1.7 – a: Cross-Porro resonator configuration b: Single ray traced through Porro prism. c: Single ray traced through angled Porro prism. d: Full beam traced through Porro prism.

The Porro prisms provide angular insensitivity to any incident angle perpendicular to the knife edge of the prism [41]. This is shown in Fig. 1.7b and c for a single ray. The cavity beam actually fills the full aperture of the Porro prism, the resultant beam is rotated around the knife-edge of the Porro. This is shown in Fig. 1.7d. The incident beam undergoes a 180° image rotation upon reflection from the Porro. This is also shown in Fig. 1.7d, whereby a ray originating on the left side of the knife edge is reflected back on the right side of the knife-edge.

By coupling two Porro prisms together at 90° to each other, the resonator alignment becomes insensitive to the rotation of the Porros. The misalignment of either Porro will change the position and direction that the resonator modes pass through the gain medium, leading to a reduction in energy, but importantly, the resonator will still be

aligned.

The corner cube adds further stability due to its alignment insensitivity in both the horizontal and vertical directions. The inclusion of the corner cube also allows for the resonator to be folded, reducing the length of the overall laser chassis.

As stated earlier, the cross-Porro resonator is effectively a plane-parallel cavity, with the resultant thermal lens within the slab moving the resonator into the stable region of the cavity stability criterion. This resonator design typically uses polarisation to couple light out of the cavity. Adjustment of the resonator reflectivity is performed by the rotation of the wave plate in Fig. 1.7. The adjustment of the cavity Q-factor for Q-switching is typically achieved by using a Pockels cell. In the configuration shown in Fig. 1.7 the Q-switch is operated in a quarter-wave configuration, with a double pass of the Q-switch providing a full half-wave retardation.

As well as the inherent stability, the cross-Porro resonator design was often implemented in flashlamp-pumped cavities due to the averaging of the induced birefringence. The rotation of the beam within the Porros averaged any induced depolarisation as the beam double-passed the slab [8]. The image rotation, in which the near field beam is rotated on every round trip, can also reduce the effect of the thermal lens. As a result, the induced phase errors from a single pass of the gain medium are averaged across the beam as it propagates back with a 180° rotation [42]. The effect of thermal lensing has been shown to reduce, compared to a resonator without image rotation [43]. The image rotation per round trip can be varied simply by controlling the angle of the Porros [44]. As a result of the change in the relative Porro angles, the alignment sensitivity is increased.

1.1.5 Laser Performance

The laser cavity configuration and gain medium geometry discussed previously have been chosen to ensure that the beam quality and alignment sensitivity are capable of meeting the requirements of a military laser. Using the configuration outlined in section 1.1.4, we must now define the typical pump power required to meet the desired output energy. The pump power required will define the number of LDAs needed; this in turn will set the overall length of the slab needed to allow for coupling of the pump light.

The population inversion threshold for the cross-Porro resonator configuration discussed previously can be calculated by equating the round-trip losses of the resonator

to the level of gain within the slab. This is shown in equation (1.5), where the terms on the left-hand side represent the overall cavity gain and the terms on the right-hand side represent the cavity losses. Equations (1.5) - (1.8) use Svelto's notation and are taken from [45].

$$N_{th}\,\sigma\,l_{gain} = \frac{L_{cav}}{c\,\tau_{cav}} \tag{1.5}$$

where
τ_{cav} = Cavity lifetime
l_{gain} = Gain medium length
L_{cav} = Cavity length
σ = Emission cross-section

In a Q-switched configuration, however, the actual population inversion is a number of times above threshold. The actual population inversion N_2 can be calculated using the equation

$$N_2 = \frac{P_{pump}\,\eta_{fl}(t_p)\,t_p}{h\nu\,V_{pump}} \tag{1.6}$$

where
P_{pump} = Pump power
$\eta_{fl}(t_p)$ = Reduction in pump efficiency due to fluorescence lifetime
t_p = Diode pump pulse duration
V_{pump} = Pump volume

The factor N_2/N_{th} is therefore the number of times above threshold the Q-switched configuration is operating. The function $\eta_{fl}(t_p)$ is the reduction of the pump power due to spontaneous emission. The efficiency is a function of the diode pump pulse duration. As the diode pulse duration is increased towards the fluorescence lifetime, the overall efficiency is reduced. This is calculated using the equation shown below [46]

$$\eta_{fl} = \frac{1 - e^{\frac{-t_p}{t_{sp}}}}{t_p/t_{sp}} \tag{1.7}$$

The fluorescence lifetime t_{sp} for a 1.1% doped crystal is typically 230 μs, Fig. 1.8 shows the reduction in pump efficiency as the pump pulse duration is increased for a series of different fluorescence lifetimes. As discussed earlier, increases in the doping density will reduce the fluorescence lifetime. At a pump pulse duration of 230 μs the

overall pump efficiency is 0.66. As the fluorescence lifetime decreases, so does the efficiency at a fixed pump pulse width.

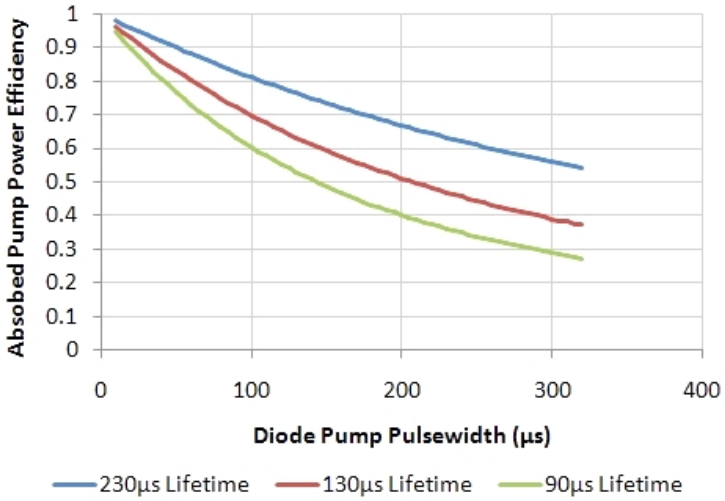

Figure 1.8 – Pump power efficiency as a function of fluorescence lifetime.

To achieve the same level of absorbed energy at the higher doping densities, the required peak power would be higher. This could be achieved either by increasing the number of diode bars or by increasing the peak power of the LDA. Both of these options will result in an increased cost. However, the result of increasing the peak power could also reduce the lifetime of the devices due to the higher operating current. As discussed earlier, the doping density of the crystals used in all of Selex's targeting lasers is 1.1%. This allows for efficient pumping of up to 230 μs.

The output energy is calculated using the equation [45]

$$E_{out} = \frac{\ln(R_{oc})}{2} \frac{N_2}{N_{th}} \frac{A_m}{\sigma} h\nu \, \eta_e \tag{1.8}$$

where
η_e = Extraction efficiency
A_m = Area of mode
R_{oc} = Cavity reflectivity

The extraction efficiency factor η_e is a function of the number of times above threshold the cavity is operating at [45]. For a laser operating at 7 times above threshold, this factor is ≈ 1. This drops to 0.9 for a laser operating only 3 times above threshold. Using equation (1.8), the output energy can be calculated as a function of the pump power. The calculation shown here uses typical values for the targeting lasers produced by Selex. Fig. 1.9 shows the slope efficiency as the pump power is varied from 3 - 5 kW with a pump pulse duration of 200 μs. The mode size was taken

to be 0.665 cm^2 and the cavity losses were set at 10% per round trip. The fluorescence lifetime t_{sp} for this calculation was 230 μs. In order to complete the calculation, the output coupling value is required. Fig. 1.9b shows the output energy versus reflectivity at 3 and 4 kW. The optimum reflectivity is slightly different for different pump powers. The optimum output coupling at 4 kW is 46%. In order to reduce the intra-cavity intensity however, the reflectivity is often reduced further. By reducing the reflectivity by 13%, the intra-cavity intensity reduces by 30%. This is also shown in Fig. 1.9b. By de-tuning the cavity in this manner, optical damage due to high intensities in the cavity can be reduced. For the calculation in Fig. 1.9a, the optimum reflectivity for each pump level was calculated, and a detuning factor of approximately 10% was applied.

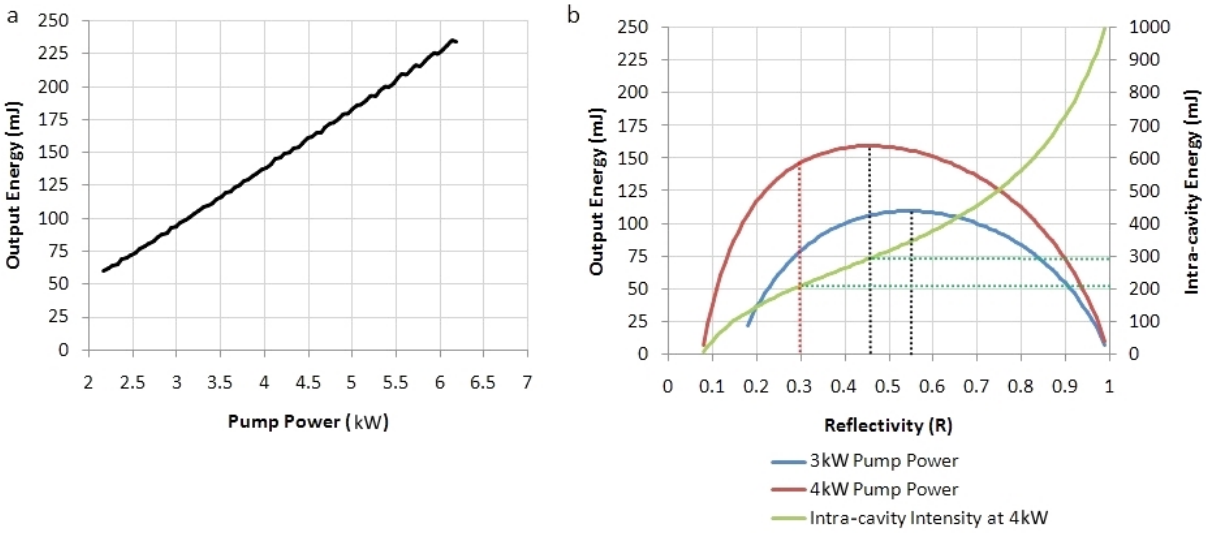

Figure 1.9 – a: Slope efficiency of Q-switched laser. b: Output energy and intra-cavity energy variation with output coupling.

From Fig. 1.9 we can see that for an output energy of 100 mJ, the required pump power is 3.1 kW. Selex's current airborne laser products typically look to generate in the region of 170 mJ from the oscillator section of the cavity. As a result, the pump power used for the current generation of airborne lasers is 5 kW. The technology developed throughout the second part of this thesis is aimed at generating similar pump powers to those discussed. Any change in the pump configuration should be capable of achieving these typical energies.

1.1.6 Laser Diode Configuration

The pump configuration of the LDAs has been discussed in section 1.1.2. The configuration is typically chosen to minimise the thermal lens by creating a homogeneous

pump profile. The overall power required will determine the emitter density, pump size and electrical characteristics. Currently, Selex legacy products use 1 cm diode bars capable of providing 100 W at 95 A. When the first laser-diode-pumped targeting lasers were produced by Selex, this represented the maximum output power available. To achieve the 5 kW required, up to 5 LDAs each providing 1 kW were aligned longitudinally as shown in Fig.1.5. Recently, pump powers of 300 W per bar [35] have been demonstrated using increased emitter density and high current operation.

1.1.7 Ring Resonator

More recently, military laser resonators have also been constructed using a ring geometry. The ring geometry differs from the cross-Porro resonator by operating with a unidirectional travelling wave, compared to the standing wave operation in the cross-Porro resonator. The ring geometry has a number of advantages over the cross-Porro resonator. One of the main advantages is the absence of Porro prisms in the resonator. Whilst Porro prisms provide insensitivity to angular rotation in one axis, the actual fabrication of the optic can lead to fairly low yields. The knife-edge region of the Porro is typically required to be less than 5 μm [8], which is difficult to manufacture reliably. Furthermore, any defect in the knife-edge region can also lead to a degradation in beam quality.

Fig. 1.10 shows a typical ring resonator configuration. The cavity consists of two folding devices. The first is simply a folding prism, the second is an image rotating prism used to provide 90° image rotation per round trip.

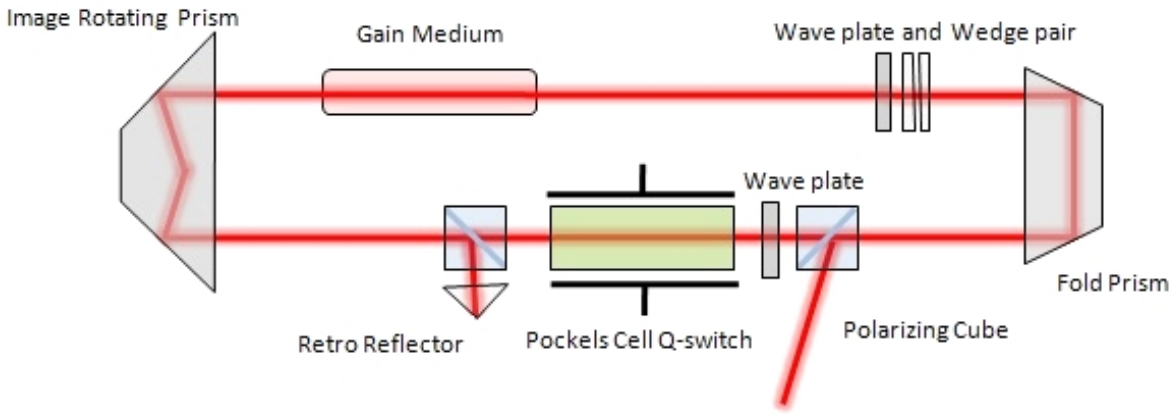

Figure 1.10 – Unidirectional ring resonator.

Without the inclusion of the retro reflector, the cavity operates in both directions. By reflecting one of the propagation directions back in the opposite direction, the threshold of one direction is smaller than the other. The direction with the lower

threshold then builds up faster, saturating the gain. As a result of the unidirectional operation, ring resonators are often used to achieve single longitudinal mode operation. The unidirectional nature ensures that travelling wave operation occurs, thereby reducing the spatial hole burning in the cavity. In the configuration used in Selex lasers however, the laser does not operate in a single longitudinal operation. The presence of higher transverse order modes and the limited extraction that occurs in the relatively low number of round trips within the Q-switch pulse allow for other modes to operate.

The characteristics of the ring resonator design also differ from the cross-Porro resonator. The ring resonator completes only a single pass of the gain per round trip. As a result, the threshold of the ring resonator, for a given set of cavity losses and reflectivity, is higher than that of the cross-Porro resonator. The optimum reflectivity in the ring cavity is much higher as a result.

Operation in a ring configuration also leads to the use of half-wave Q-switching instead of the quarter-wave configuration used in the cross-Porro resonator. This results in a higher Q-switch voltage to achieve the half-wave retardation. The contrast ratio of the half-wave configuration is higher than the quarter wave configuration shown in the cross-Porro resonator As the temperature varies, changes in wave plate thickness, coating performance, bulk optical stresses and polariser contrast ratio can lead to a significant reduction in the overall contrast ratio of a given setup. The cross-Porro resonator operates a double-pass of each component, increasing the risk of depolarisation, which can cause optical damage [47].

Ring resonators have been used to generate output energies of up to 250 mJ using a Nd:YAG zigzag slab gain medium at Selex. Similar beam qualities to those achieved with current targeting laser designs have been demonstrated[48] with output energies up to 130 mJ.

1.1.8 Thermal Control in Current Targeting Lasers

Until recently, forms of active thermal control have been present in most production military lasers. In flashlamp systems the pump source will dissipate up to 50% of the overall input power as heat. The walls can typically reach 1200 K at the end of the pump pulse. The main requirement for water-cooling is to prevent the overall temperature rise in the flashlamp, thereby increasing the lifetime. Water-cooling has been used in previous versions of hand-held markers from the 1970-2000 [49] [50] to remove heat from the flashlamp. Use of water-cooling significantly increases the size and weight of the device but also increases the risk of damage due to moving parts

and water-tight seals required around the cooling loop.

The broad emission bandwidth of the flashlamp does allow for pumping to be achieved over a wide temperature range, albeit inefficiently. Operating temperatures of flashlamp systems therefore do not require accurate temperature control, but rather the removal of excess heat. The bandwidth of a LDA is much narrower, typically 3 nm. The temperature dependence of the LDA, which is discussed in chapter 6, is much more sensitive and requires accurate control of the operating temperature. Most laser LDA pump heads use some form of active cooling to control the temperature. The most commonly used configuration is a thermo electric cooler (TEC) combined with some form of heat exchanger. The TEC is used to accurately control the LDA temperature, and the heat exchanger is used to remove heat from the system. Combined with a PID (proportional, integral and differential) feedback circuit, the TECs can accurately achieve stabilities of $\leq 1°C$.

The biggest disadvantage of this configuration is the power consumption of the TEC and thermal control. Fig. 1.11 shows a Selex pump head configuration with typical power consumption values of each function of the laser.

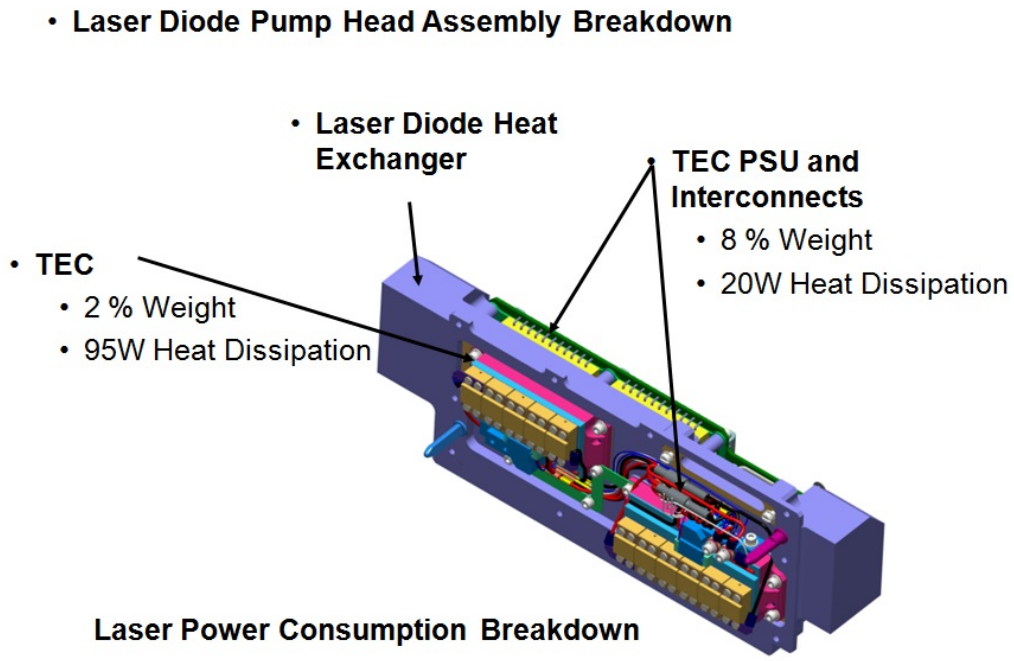

Electronics	39%
LDA's	21%
Cooling	40%

Figure 1.11 – Breakdown of thermal control characteristics.

In extreme conditions, such as operation at -40 °C, the TEC can account for some

40% of the overall power consumption of the laser. On most aircraft and vehicles the overall power consumption is not a key consideration. On hand-held lasers and lasers operating on UAVs, power consumption is the key factor.

The requirement to stabilise the temperature of the LDAs also introduces other performance limitations. The time taken for a laser operating at -40 °C to increase the LDA temperature to 60 °C will be in the order of 4 minutes. In a combat environment, the typical engagement time is less than 3 minutes. This method of operation would require the device to be switched on long before any engagement occurs. If the device was running off batteries, this would further reduce the operational time available. Another possible impact is the reliability of the devices. Whilst TECs do have a fairly long lifetime, any catastrophic failure of the cooling system could prevent the laser from operating. The removal of the cooling system could increase the reliability of the laser. The total weight and cost of the system can also be improved by removing the temperature control. The thermal control accounts for 10% of the total weight and 5% of the total cost of the laser. The removal of the thermal control would also improve these parameters.

1.2 CW Countermeasures

The other investigation completed in this thesis is the development of a laser source capable of generating a series of wavelengths for electro-optical countermeasures (EOCM). Electro-optical countermeasures have been used within military systems since the Second World War [51]. The use of dazzlers to visually impair both human operators and visual sensors have been in operation since 2009 [52], with frequency doubled Nd-based lasers operating at 532 nm [53] the most commonly used. More recently, dazzlers operating at similar wavelengths to the targeting laser wavelength have been used to dazzle missile seekers, preventing accurate targeting.

The most common form of counter-countermeasures used to limit the effect of the green dazzlers are narrow band filters that block out the desired wavelengths. Whilst filters can typically be used to block a specific emission region, a series of wavelengths, distributed throughout the total sensory band, is challenging to filter out without impairing the sensor performance. The investigation completed here is therefore focused on generating a minimum of three wavelengths, in both the low infra-red range and the visible range [54], preferably in CW operation. The different methods of achieving this requirement are discussed in chapter 3. The use of volume Bragg gratings is also presented in this chapter as the best solution to meet these requirements.

Chapter 3 first looks at the use of VBG's within a solid state laser configuration, operating at both 1064 nm and 1342 nm. Chapter 4 documents the thermal effects observed in VBGs under high thermal loads and the coupled nature of the VBG performance and the intra-cavity intensity. Section 5 then utilises the VBGs to achieve single longitudinal mode operation at 1342 nm. The final section looks to investigate the second harmonic generation of the 1064 nm emission to prove the possibility of generating a series of visible wavelengths and to demonstrate the improvements gained by using a VBG laser cavity. Further work completed outside of what is presented here includes the operation of a dual-wavelength laser operating at both the fundamental wavelengths described earlier [55]. The operation of a dual-wavelength laser combined with the second harmonic investigation completed in chapter 5 further develops the possibility of a single laser cavity providing all the required wavelengths for this application.

The aim of the overall programme for which this work was completed was to develop a number of different visible and IR sources for use within countermeasure applications. The actual operation of the countermeasure system is not within the scope of this thesis, however the overall requirements can be discussed. One mode of operation of an EOCM system could include the dazzling of a sensor array on a given target. As a result, the EOCM laser would be configured with a set of beam steering mirrors and guidance systems to allow for accurate targeting. The target itself may be a significant distance away therefore the same characteristics of defining the energy on a target discussed earlier are applicable.

The non-lethal optical countermeasures requirement was for CW operation, with a high beam quality. The ability to generate up to several watts in the red (630 nm), yellow (570 nm) and green (532 nm) regions would provide a capable countermeasures system. The following chapters therefore look to generate up to 8 W from both a CW and Q-switched source in the low IR region. This allows for second harmonic and sum frequency generation to be used to create a visible source. The investigation looks to use current off the shelf components to create a multi-band CW source. In the next section the characteristics of a CW laser are presented as well as the chosen gain material Nd:YVO_4.

1.2.1 CW Laser Characteristics

The gain material used in this investigation is Nd:YVO_4. The main requirements that drive the selection choice are both the favourable laser properties and the presence of multiple emission lines. The energy diagram of Nd:$YV0_4$ is shown in Fig. 1.12, the transition lines were taken from Sardar *et al.* [56]. The emission cross-section of Nd:$YV0_4$

is 10 times higher than that of Nd:YAG at the 1064 nm emission line. A second emission line in the 1340 nm region is also present with a cross-section of 6.5×10^{-19} cm^2 [57].

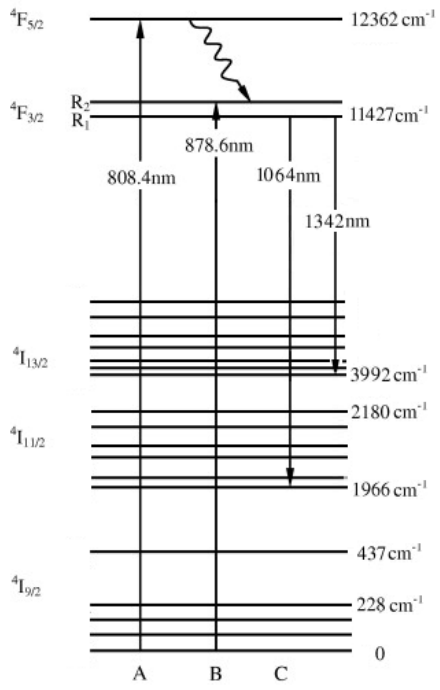

Figure 1.12 – Energy transitions of Nd:YVO_4.

The material also possesses strong absorption lines in the 809 nm region allowing for efficient pumping using GaAs laser diodes. The Nd:YVO_4 is uni-axial with the emission cross-section in the π polarisation much larger than that of the σ polarisation. As a result the laser emission is strongly polarised.

The biggest disadvantage of Nd:YVO_4 is its low thermal conductivity of 0.05 W/cm K [8]. As a consequence of the low thermal conductivity and a relatively low tensile strength, the fracture limit of Nd:YVO_4 is fairly low [58]. In end-pumped configurations, the fracture limit of 54 MPa is almost four times lower than that in Nd:YAG [59]. The use of undoped end-caps can reduce the thermal loading on the front face by reducing the overall temperature rise within the crystal [8]. Nd:YVO_4 crystals with undoped end-caps have been shown to decrease the thermal lens strength in the crystal by up to 50% [60]. Commercial sources of undoped end-caps are also now readily available.

Nd:YVO_4 has been used to generate up to 25 W in an end pumped configuration [61] with a pump wavelength of 808 nm despite the low thermal conductivity. In Q-switched configurations up to 4 mJ has been demonstrated [62].

1.2.2 CW Analysis

The analysis for the space-independent CW operation can be derived from the rate equations for a 4-level system developed by Statz and De Mars [63]. From equation (1.5) and the following equations, the output power in CW operation can be calculated [45]

$$R_{th} = \frac{N_{th}}{\tau_{sp}} \tag{1.9}$$

where
R_{th} = Pumping rate threshold
N_{th} = Inversion density threshold
τ_{sp} = Fluorescence lifetime

$$P_{out} = A_b\, I_s \left(\frac{\gamma}{2}\right) \left(\frac{R_p}{R_{th}} - 1\right) \tag{1.10}$$

Where A_b is the area of mode, I_s is the saturation intensity, R_p is the pumping rate above threshold and γ is the logarithmic loss due to the cavity output coupling. The pumping rate is dependent on both the power from the pump source and the incident spot size of the pump light. In the same manner as previously completed for the zigzag slab, the thermal loading should be limited to ensure thermal lensing does not limit operation on a single transverse mode. For CW configurations, a number of different pump regimes are available that can achieve this goal. In the previous section the zigzag slab configuration, which limited the thermal lens strength, was presented. The thick zigzag slab, however, does not allow for selection of the fundamental mode. To achieve improved beam quality, thin waveguide slabs [64] or grazing incidence bounce slabs [65] [22] are often used. Thin slab configurations allow for high pump powers to be focused into the crystal whilst limiting the overall induced thermal lens. The output beam quality is typically diffraction limited in the waveguided direction, but is often a number of times the diffraction limit in the other plane. The focusing of the pump light in these configurations is often complex due to the requirement for the pump light to totally internally reflect along the slab.

Grazing incidence bounce slabs have also shown operation at high powers whilst achieving operation on the fundamental mode. Using gain media with high absorption efficiencies, the pump light can be focused from an emitting bar into a narrow section of the gain medium. Selection of the fundamental mode can be achieved by limiting the absorption depth of the pump light, thereby only selecting the lowest order mode. The narrow bounce angle also allows for averaging of the thermally induced lensing.

Grazing incidence slabs have been shown to generate output powers of up to 40 W with an M^2 of 1.1 [66]. The absorption depth of the pump light must be well defined, and highly doped material is often used as a result in order to limit the absorption depth. The actual extraction of the pump light is also fundamentally limited by the grazing incidence of the cavity mode.

For near diffraction-limited performance, end-pumped lasers typically provide the highest efficiencies compared to the other configurations described here. The selection of the fundamental mode can be achieved by adjusting the pump spot size to match that of the cavity mode. In Nd:YVO_4 conversion efficiencies as high as 70% have been demonstrated with output powers up to 47 W [67] with pump powers of up to 200 W at 888 nm [68].

1.2.3 Thermal Lens and Cavity Mode Size Analysis

The selection of the fundamental mode is achieved by matching the size of the absorbed pump spot to that of the cavity mode. The two factors are interlinked however due to the induced thermal lensing within the laser crystal affecting the size of the cavity mode. In a plane-plane cavity configuration the thermal lens is the main determinant in the cavity mode size. The focal length of the thermal lens can be calculated from the temperature rise that results from the absorbed intensity.

For a basic calculation in an end pumped rod configuration, assuming a parabolic temperature profile and that all the heat is removed from the rod surface, the steady state radial temperature rise that results from the absorbed pump power is given by [8] where

$$\Delta T = \frac{P_h}{4\pi K_{th}\, l_{rod}} \tag{1.11}$$

Where K_{th} is the thermal conductivity, l_{rod} is the thickness of the rod and P_h is the thermal power. Ignoring photo-elastic contributions, the induced thermal lens strength can be calculated from temperature gradient of the rod, where the focal length is calculated using the following equation [8]

$$f_{th} = \frac{2\pi\omega_o K_{th}}{P_h \dfrac{dn}{dt}} \tag{1.12}$$

where dn/dt is the temperature dependence of the refractive index and ω_o is the

beam waist size. Fig. 1.13 shows the calculated focal power of the thermal lens as a function of the pump spot size for an incident pump power of 12 W. The two different plots in Fig. 1.13 are a result of the uniaxial nature of the Nd:YVO_4.

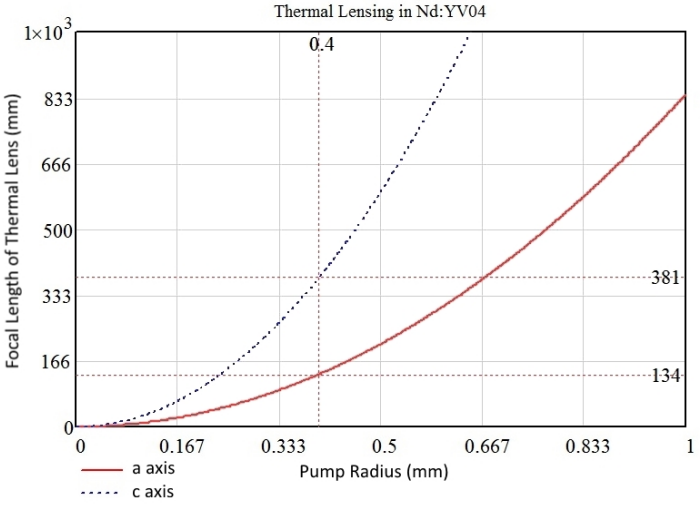

Figure 1.13 – Focal power of induced thermal lens in Nd:YVO_4 as a function of pump spot size.

To achieve a more realistic thermal lens calculation that takes into account the undoped endcaps, FEA can be completed in the same manner as that for the zigzag slab in the previous section. Fig.1.13 shows the thermal lens calculation for an Nd:YVO_4 rod with 4 mm undoped end-caps at either side. The modelled incident pump power was 12 W with a pump spot radius of 400 μm. Fig. 1.13a shows the temperature map of the crystal with 12 W of incident pump power. The resultant optical path length variation across the crystal is shown in Fig. 1.13b. For this calculation the diode spot size was constant through the rod and did not take into account the focused nature of the pump light. The variation in spot size through the rod will lead to a slightly different heat deposition than that modelled here.

From the temperature plot, the effective path length variation across the rod surface can be calculated. The calculated focal power of the thermal lens for 12 W of pump power is 200 mm. The FEA predicts a weaker thermal focal length than the calculation completed previously. The FEA model should provide a more accurate result as this takes into account the undoped end-caps in the crystal and the absorption profile of the pump light.

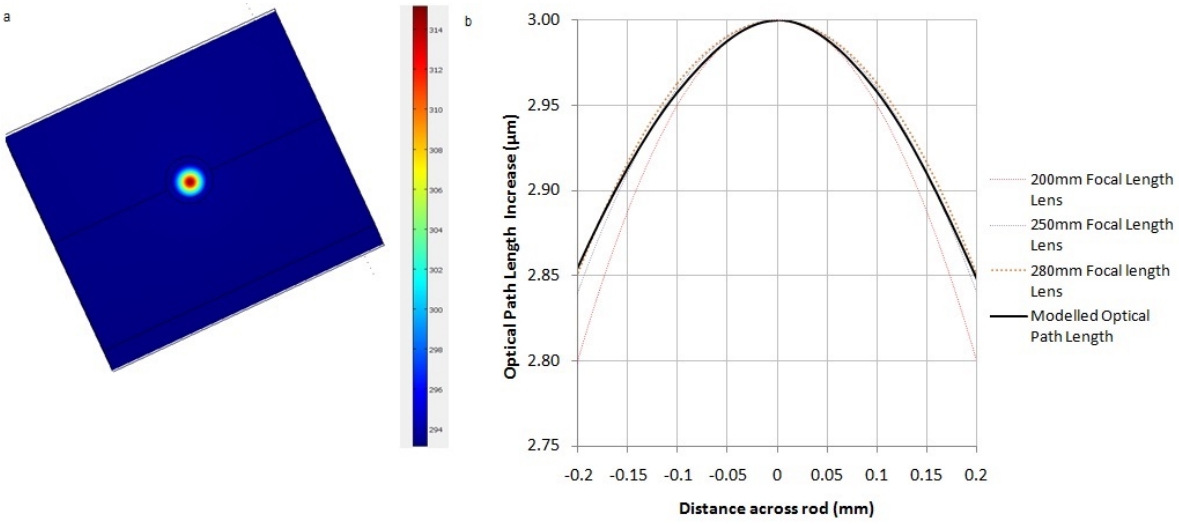

Figure 1.14 – a: Temperature profile of Nd:YVO_4 with 12 W of incident power. b: Modelled optical path difference across mode.

1.2.4 Cavity Mode Analysis

To calculate the effect the thermal lens strength has on the fundamental mode size, ray matrix propagation calculations can be performed. The ray matrix calculations are shown below starting with the complex beam parameter q.

$$\frac{1}{q(z)} = \frac{1}{R(z)} + i\frac{\lambda}{\pi n {\omega_z}^2} \tag{1.13}$$

The complex beam parameter describes a Gaussian beam at a given location z. The real parameter refers to the curvature of the wavefront R_z and the imaginary part refers to the waist ω_z, where n is the refractive index at point z. The ray transfer matrix method is then used to describe how the beam propagates through the cavity. The standard transfer matrices are shown below.

$$\text{Curved Mirror} = \begin{pmatrix} 1 & 0 \\ \frac{-2}{R} & 1 \end{pmatrix} \tag{1.14}$$

$$\text{Free Space Propagation} = \begin{pmatrix} 1 & L \\ 0 & 1 \end{pmatrix} \tag{1.15}$$

$$\text{Lens Duct} = \begin{pmatrix} cos(\gamma_{th} z) & (n\gamma_{th}^{-1}) sin(\gamma_{th} z) \\ -(n\gamma_{th}) sin(\gamma_{th} z) & cos(\gamma_{th} z) \end{pmatrix} [46] \tag{1.16}$$

where $\gamma_{th} = \sqrt{n_2/n_0}$, n_0 is the bulk crystal refractive index and n_2 is the radial refractive index variation. Using the basic matrix transfers, the size of the fundamental waist, as well as the stability of the cavity can be determined.

The new complex beam parameter for a beam that has traversed the optical system

represented by the transfer matrix M is

$$q_2 = \frac{M_{1,1}q_1 + M_{1,2}}{M_{2,1}q_1 + M_{2,2}} \tag{1.17}$$

The cavity is stable when periodic focusing occurs, whereby $q_1 = q_2$ and is defined by the relationship

$$-1 \ \leq \ \frac{M_{1,1} + M_{2,2}}{2} \ \leq 1 \tag{1.18}$$

The embedded waist at the first mirror in the matrix calculation is then calculated using the equation

$$\omega_2^2 = \frac{|M_{1,2}|\,\lambda}{\pi}\sqrt{\frac{1}{1-(0.5(M_{1,1}+M_{2,2}))^2}} \tag{1.19}$$

The spot size at any point in the cavity can then be calculated by equation (1.17) using the waist calculated at q_1 to determine q_2. By equating the real and imaginary parts of the q1 to the complex beam parameter, the waist in the crystal can be calculated.

The cavity mode size and stability can be calculated using commercial software, such as Lascad or GLAD. The cavity analysis for this thesis was calculated using the freely available software package LASCAV from the university of St. Andrews.

In the next four chapters, an investigation of VBGs operating as high reflective mirrors is completed. The calculations described here are used to calculate the optimum spot size within the cavity, the induced thermal lens and the required cavity length to match the pump spot to that of the fundamental mode of the cavity. The performance characteristics of the laser are also considered using equations (1.10) and (1.9).

1.3 Conclusion

This chapter has introduced both the requirements of military resonators and the subsequent design developments used to meet these requirements. The characteristics of the laser resonators, in terms of pump power, output coupling reflectivity and efficiency have also been presented for both Q-switched and CW operation.

1.4 Thesis Layout

The main consideration in the first section is the development of a diode pumped Nd:YVO_4 laser using VBGs as high reflectivity (HR) mirrors. In chapter 2 an in-

troduction to VBG theory is completed and modelling of the VBG performance is presented. In chapter 3 the configuration of VBG lasers operating at 1064 nm and 1342 nm is presented, with the effects on the laser efficiency, mode parameters and spectral line width investigated. In Chapter 4, the thermal effects within VBGs are discussed and the coupled nature of the cavity intensity to the VBG performance is proposed. Chapter 5 shows the construction of a double VBG laser operating at 134 2nm. The ability to achieve SLM operation up to an output power of 2.3 W is shown and predictions of the optimum configuration for the laser are discussed. Finally, a Q-switched VBG laser is constructed and the effects of the spectral performance of the VBG on the efficiency of the second harmonic generation is investigated.

The main consideration in the second section of this thesis is the development of the military lasers discussed in section 1.1, that can operate without thermal control. An investigation into locking the laser-diode wavelength is completed in chapter 7. In chapter 8, the use of a long absorption length configuration to achieve athermal performance is investigated. Chapter 9 looks at selectively locking the LDA over temperature to improve the performance compared to that in chapter 7.

Chapter 2

Volume Bragg Grating Theory

In this chapter, the theory and operation of Volume Bragg Gratings, or VBGs as they are commonly known, is described. VBGs have been used in a number of different configurations from line narrowing of laser cavities [69], locking of laser diodes [70], to transverse mode selection within end-pump resonators [71]. The mathematical solution of Bragg scattering is outlined in this chapter and applied to VBG's. The chapter provides a basic outline of the key VBG parameters that determine the spectral performance. The chapter then highlights the effects of a change in these parameters as a result of thermal aberrations. The main output of this chapter is the demonstration of two models that can calculate the performance of a VBG, with and without thermal loading. The results of this chapter therefore have an input into future chapters, where the thermal effects can degrade the laser performance. The actual manufacturing of VBGs is also discussed and the performance limitations outlined.

2.1 Basic Bragg Theory

VBG's can be used as an optical element in both transmissive and reflective modes. Fig. 2.1 shows both these modes of operation. The angle θ is the angle of the incident array from normal and ϕ is the slant angle.

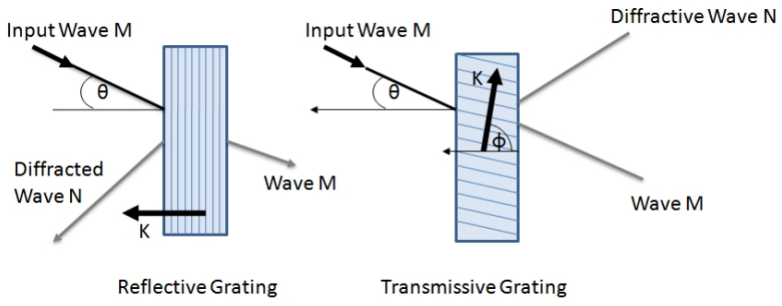

Figure 2.1 – Reflecting and transmitting VBGs.

The theory for VBG transmission and reflectivity was first developed by Kogelnik

et al. in 1969 [72]. Kogelnik's derivation of the solutions for a volume grating is briefly outlined here, allowing for a model of the performance of a grating to be constructed. Starting with the scalar wave equation

$$\nabla^2 E + k_c^2 E = 0 \tag{2.1}$$

where k_c is the propagation constant in the grating. The value k_c is defined as

$$k_c^2 = \omega_a^2 c^2 \epsilon - j\omega_a \mu\sigma \tag{2.2}$$

where ω_a is the angular frequency. The actual spatial modulation in the grating in terms of both ϵ and μ is defined as

$$\epsilon = \epsilon_o + \epsilon_1 cos(K \cdot x) \tag{2.3}$$

$$\sigma = \sigma_o + \sigma_1 cos(K \cdot x) \tag{2.4}$$

where ϵ_o and σ_o refer to the average dielectric constant and conductivity and K is the grating vector. The factors ϵ_1 and σ_1 refer to the dielectric and conductivity variations arising from the index modulation in the grating. By combining these equations and defining two new constants, equation (2.5) can then be defined as

$$k_c^2 = \beta^2 - 2j\alpha\beta + 2\kappa\beta(e^{iK.x} + e^{-iK.x}) \tag{2.5}$$

The two constants are defined as the propagation constant $\beta = \frac{2\pi n}{\lambda}$, where n is the refractive index, and the absorption coefficient $\alpha_1 = \frac{\mu c \sigma_0}{2n}$. A coupling constant κ is also defined as

$$\kappa = \pi\Delta n/\lambda - j\alpha_1/2 \tag{2.6}$$

where α_1 is the absorption coefficient in the grating and Δn is the refractive index modulation. The coupling constant refers to the interaction between the input wave and the reflected wave. The coefficient contains two elements in a similar manner to the complex refractive index. The real parameter represents the coupling of the waves as a result of the index modulation variation. The imaginary part represents the absorption within the grating. As highlighted by Kogelnik, in the absence of absorption, the coupling constant is dependent on the amplitude of the refractive index modulation only. If the modulation decreases to zero, the coupling coefficient also reduces to zero.

The solution to the scalar wave equation describes two waves [73]. Firstly, an incoming forward propagating wave, denoted here as M, and a second backwards

travelling wave denoted as N. Considering the two propagating waves in the VBG, the total electric field intensity is

$$E = M(z)e^{i\delta.x} + N(z)e^{-i\rho.x} \tag{2.7}$$

The propagation constants of the forward travelling wave and the backwards travelling wave are δ and ρ. The propagation constants of the backwards travelling wave ρ are determined by the propagation constant of the grating itself. The incoming beam will possess its own propagation constant, dependent on both the grating parameters and the properties of the beam itself. In order for sufficient coupling to occur, momentum must be conserved and therefore

$$\delta = \rho - K \tag{2.8}$$

Equation (2.8) shows the requirements for the matching of the input wave characteristics to that of the reflected wave. As a result of moving away from these conditions, a phase mismatch will result and momentum would not be conserved. The effect of this would be to decrease the coupling efficiency, as the forward and backward propagating wave move out of phase with one another. The parameters that affect the propagation constant of the incoming wave are the wavelength of the input beam and the incident angle relative to the Bragg angle. The term $\Delta\lambda$ describes the difference in wavelength from the input wave to that of the grating vector. The angle $\Delta\theta$ of the input wave will also result in dephasing and a reduction in the diffraction efficiency. A dephasing parameter ν_{vbg}, that describes these effects is shown in equation (2.9).

$$\nu_{vbg} = \Delta\theta K sin(\phi - \theta) - \Delta\lambda * K^2/4\pi n \tag{2.9}$$

The wave equations can be derived by inserting the combined electric fields into the scalar wave equation. By comparing the similar exponential terms that result from this and by using a few assumptions, equations (2.10) and (2.11) are derived. The first assumption is that we can ignore the higher order M'' and N'' terms as we assume a slowly varying field envelope. That is to say we assume the energy exchange between the two waves is slow. We also assume no absorption within the grating eliminating the α_1 terms. The term ν_{vbg} has been included to represent the change in phase of the incident beam as a result of the factors described previously.

$$c_t M' = j\kappa N \tag{2.10}$$

$$c_r N' = -j\kappa M + j\nu_{vbg} N \tag{2.11}$$

Two new constants c_t and c_r have been defined. These constants refer to the propagation vectors of each wave. The solution to the wave equation for the transmitted

and reflected wave can be calculated as

$$M(z) = m_1 e^{(\gamma_1 z)} m_2 e^{(\gamma_2 z)} \tag{2.12}$$

$$N(z) = n_1 e^{(\gamma_1 z)} n_2 e^{(\gamma_2 z)} \tag{2.13}$$

The boundary conditions from the VBG configuration can then be applied. The boundary conditions are different for transmitting and reflective gratings. Here we only consider a reflective grating. For this configuration there are two conditions, at the point $z = 0$ the solution $M(0) = M_{input}$. For the second known boundary condition, at the end point of the grating, the reflective wave $N(d) = 0$.

The boundary conditions are therefore

$$at\ Z = 0\ M_1 + M_2 = 1 \tag{2.14}$$

$$at\ Z = d\ N_1 + N_1 = 0 \tag{2.15}$$

By inserting the solutions for M and N into the coupled wave equations in to (2.10) and (2.11) and applying the boundary conditions, the magnitude and phase of the reflected wave can be calculated. In the following sections, two separate methods of calculating the performance of the VBGs are described. The first is for an exact solution to the equations introduced here. This solution can be used when the parameters of the grating are constant and no thermal or mechanical distortions are present. The second method uses a Runge Kutta solver to iterate towards an intensity distribution within the grating that satisfies both the boundary conditions and the solution described in equations (2.12) and (2.13).

2.2 Exact Solution to VBG Coupled Wave Theory

The derivation of the analytical solution is shown previously [74]. The solution to the grating reflectivity R_{vbg} is shown below

$$R_{vbg} = (1 + \frac{1 - \xi^2/\Phi^2}{sinh^2\sqrt{\Phi^2 - \xi^2}})^{-1} \tag{2.16}$$

Two new parameters have been defined in equation (2.16). The first is a new dephasing term ξ. This term is related to the previous phasing parameter by the following equation

$$\xi = \frac{\nu_{vbg} d}{2c_r} \tag{2.17}$$

where c_r is the angular variation of the input and reflected waves defined by $c_r =$

$cos\theta - \frac{K}{\beta}cos\phi$ and d is the thickness. The second new defined parameter is Φ, which is shown in equation (2.18). This describes the reduction in the coupling coefficient of the grating, as a result of the phase mismatch of both the input and output wave vectors, to that of the grating vector.

$$\Phi = \frac{\pi n d}{\lambda (c_r c_s)^{\frac{1}{2}}} \tag{2.18}$$

2.2.1 VBG Performance

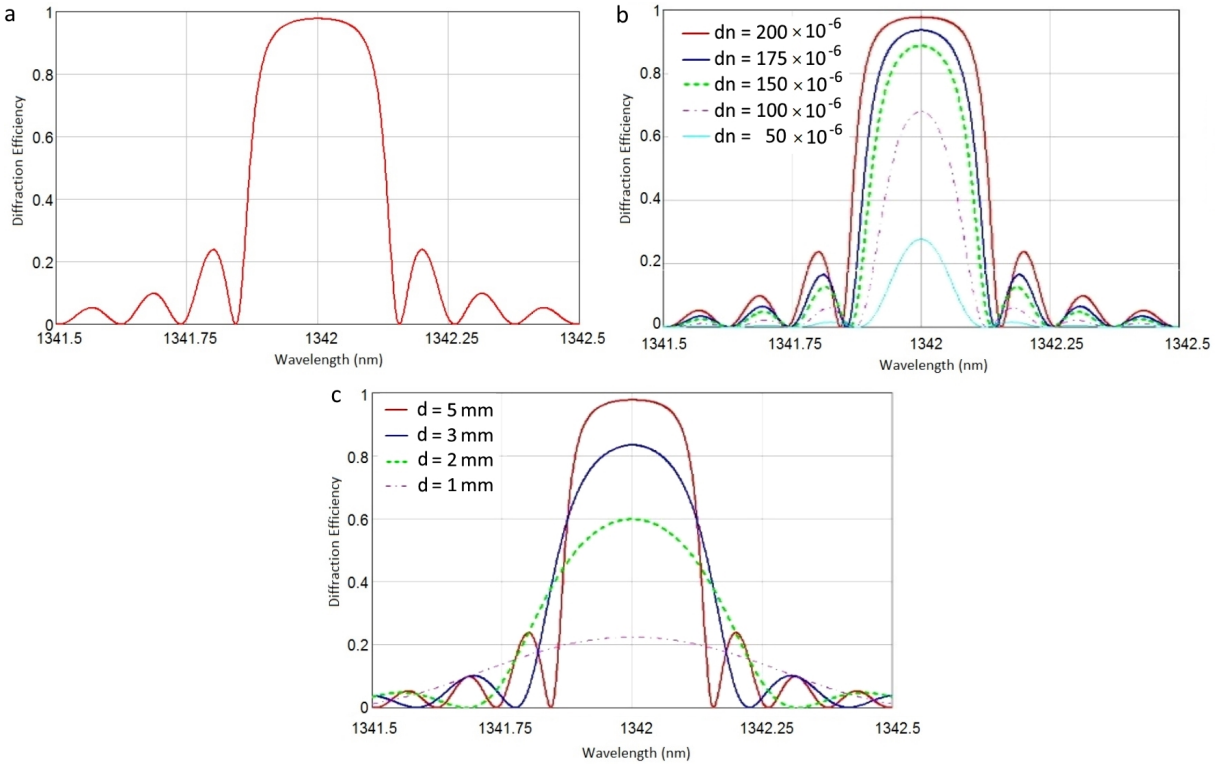

Figure 2.2 – a: Spectral response of 1342 nm high reflectivity grating. b: Spectral response of VBG for a series of refractive index modulations dn. b) Spectral response of a VBG at various lengths.

Using equation (2.16), the spectral performance of a high reflecting VBG can now be calculated. Fig. 2.2a shows the reflectivity of a 1342 nm VBG. The grating parameters are as follows: the refractive index variation $\Delta n = 220 \times 10^{-6}$, the average refractive index, n, is 1.488 and the grating spacing was 450 nm. These values were provided by the grating manufacturer Ondax.

Fig. 2.2a shows how both high reflectivity and a narrow spectral response can be achieved in the grating. The effect of varying the parameters of the grating on the spectral response can also be explored. By analysing the equations that define the reflectivity, it can be observed how decreasing parameters such as the grating modulation affects the performance. From equations (2.6) and (2.18) it can be seen

how a reduction in the refractive index modulation will reduce both the coupling coefficient and Φ. A reduction in Φ will also result in a reduction in the reflectivity R_{vbg}. Fig. 2.2b shows how the spectral response of a VBG varies for a selection of different refractive index modulations.

The effect of varying the length of the grating can also be explored. The grating length d is present in both the coupling coefficient factor and also in the dephasing parameter. An increase in the grating length would see the dephasing parameter increase. This change would see the gratings spectral response narrow as the grating length increases. The grating is therefore more sensitive to changes in wavelength. However, the grating length will also increase the effective reflectivity at each spectral point. The overall effect of changing the length of the VBG is shown in Fig. 2.2c.

2.3 Runge Kutta Method For Imperfect Gratings

A method to allow for the spectral response of a VBG grating that possesses parameters such as spatial frequency, refractive index and index modulation whose values vary through the grating is also required. A method for modelling spectral response of VBGs with thermal distortions has been presented previously by Shu *et al.* [75]. This solution uses the Runge Kutta method to iteratively solve the intensity distribution using the coupled equations described previously. The transfer matrix technique has also been used to solve the intensity distribution within the VBG [76]. The transfer matrix can often be computed quicker. However, programs such as Matlab already have in-built functions for the Runge Kutta method and are therefore easier to program.

The coupled equations from the scalar wave equation are again shown in equations 2.19 and 2.20.

$$c_t M' = j\kappa N \tag{2.19}$$

$$c_r N' = -j\kappa M + j\nu_{vbg} N \tag{2.20}$$

The parameters ν_{vbg} and κ have previously been defined to take account of the dephasing and the coupling respectively. There are now two coupled equations and boundary conditions from section 2.1. The Runge Kutta method allows for the calculation of the intensity distribution of the transmitted and reflected waves as they propagate through the grating.

The two equations are coupled and therefore to calculate one wave, the intensity of the other at any given point must be known. A solution to the coupled equations can

still be iterated towards. By starting with estimated values for the transmitted wave intensity distribution, an intensity distribution of the reflected wave can be generated. The calculated values for the reflected wave can then be used to re-calculate the transmitted wave intensity distribution. This process of updating the intensity profile of each wave is repeated until the values for each wave have stabilised.

The model becomes more complex when high reflectivity gratings are used. For reflectivities higher than 50%, it is found that the solution does not converge. A method for calculating the intensity distribution of the higher reflectivity gratings has been reported by Shu [77]. In order to allow the solution to converge, the grating must be split into four parts. Each section is iterated in the same method described previously. This time, however, the boundary conditions for each split section are now taken from the calculated values of transmitted and reflected waves for the previous section of the VBG. Initially, the values are guessed, and by repeating the steps a number of times, at each point using the most recently calculated values for the boundary conditions, a solution is reached. Fig. 2.3 shows the spectral performance of a high reflectivity grating, calculated using both the exact solution described in section 2.2 and the adapted Runge Kutta method.

The Runge Kutta model gives good agreement with the exact equation method using the same input parameters. A small difference was observed between the reduction in the transmitted wave, and the value of the reflected wave by around about 2%. It is believed that this error arises from the adaptive step size method used in MatLab to perform the fourth order Runge Kutta iteration. This adaptive step size significantly improves speed, but leads to different step sizes being taken for the transmitted and reflected waves. As a result, when attempting to use the previously stored intensity distribution for the opposite wave, there are discrete points that do not coincide with the values required to calculate the wave. Currently, a nearest neighbour routine is employed, which will lead to a slight error. Interpolation techniques could improve the accuracy of the code, although they would also increase the calculation time.

There is now a method to calculate the reflectivity of an unmodified grating, using an exact method and an iterative method. The iterative method can also allow for the calculation of thermally distorted gratings by using spatially dependent values for the refractive index and grating vector. If, for example, the spatial variation in the grating vector is known, for each iteration performed, a different value for the grating vector can be used. This is the method of operation described by Waritanant *et al.* [78].

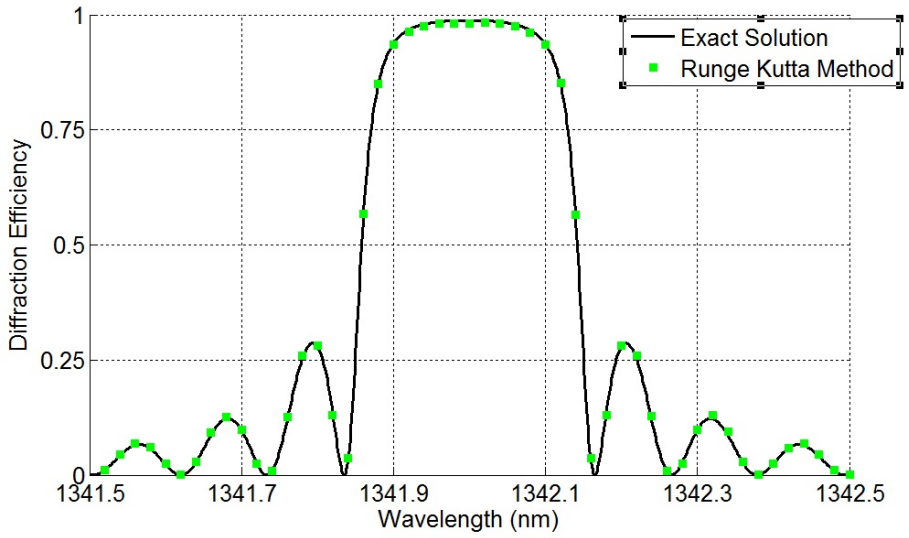

Figure 2.3 – Comparison of exact and Runge Kutta model for high reflectivity VBG.

2.4 VBG Construction

Two different methods of calculating the reflectivity of VBG's have been demonstrated. It has been shown from equations (2.16) to (2.18) that in order to achieve a high reflectivity, narrow bandwidth VBG, both the smallest refractive index modulation possible and a long grating length are required. These parameters will also depend on the actual processing of the VBG itself, such as the parameters of the glass and the limitations of the index writing process.

VBGs are constructed from Photo-Thermo-Refractive glass (PTR). PTR glass is a silicate based glass with composition (mol.%) 70 SiO2, 15 Na2O, 5 ZnO, 5 NaF, 4 Al2O3, 1KBr, 0.01 Ag2O [79]. The glass blanks are processed to achieve thermal insensitivity and allow for the production of high diffraction efficiency gratings. The actual fabrication of the grating is completed in a two stage process. First, the device is selectively exposed to high intensity UV radiation. The band gap energy for the PTR glass is centred at 305 nm but is highly transmissive above 400 nm. UV radiation in the 300 nm region is therefore strongly absorbed. Typically, He:Cd lasers operating at 325 nm [80] are used for irradiation, although other laser such as N_2 or Ar lasers can also be used. The pulse energy of the exposure depends on the required refractive index change, ranging from 0.1-10 J/cm^2 [81]. To write the actual refractive index modulation, two coherent UV sources are used to produce an interference pattern on the glass plate. The exposure to the intense UV produces ionization of the cerium ion. The ionization releases an electron which is trapped by a silver ion, allowing the silver ion to become a neutral atom.

The second process is the baking of the glass, at a temperature of around 450-500 °C

[82]. The baking process contains two phases. Initially, the glass is heated up to 400 °C, allowing for diffusion of the silver atoms. The silver atoms then group to form tiny silver crystals. These crystals then act as the nucleation site for formation of NaF crystals. The formation of the NaF crystals leads to a refractive index change within the glass. The baking process typically lasts around two hours although the duration can be varied to adjust the refractive index variation. The refractive index changes as a function of dosage, with changes as small as 125×10^{-6} [74] achievable.

The formation of the NaF crystal that results in the change in refractive index is a permanent feature within the glass. As result, the damage threshold of the VBG's are in the order of 10 J/cm^2 [81]. The characteristics of the damage threshold are typically due to the intrinsic quality of the glass sample itself. The damage threshold has been found to vary from 20 J/cm^2 for an inclusion free glass down to 3 J/cm^2 for a glass that contained inclusion. The grating strength and angle of incident beam relevant to the grating axis were found not to affect the damage threshold [81].

Whilst the UV irradiation process allows for narrow band filters to be accurately fabricated, the material proprieties of the glass itself also contributes to performance of the grating. The low thermal expansion [83] and small thermo-optic coefficient, dn/dt, also make the grating stable over temperature. The low absorption from 400 nm up to 2500 nm [84] also allows for gratings to be used over a wide range of wavelengths. Residual absorption can play a role in altering the performance of the VBGs, as is shown later. Whilst absorption within region of 800-1500 nm is small, thermally induced aberrations have been shown to be present within VBGs [85]. The thermal abberations can cause a number of different behaviours in the VBG. The spectral performance of the VBG can vary, leading to chirping of the VBG or shift in the actual centre wavelength of the device.

2.4.1 VBG Thermal Modelling

The thermal effects within VBGs have been documented previously [85] [78]. The PTR glass that the VBG is constructed from still has a small amount of absorption above the bang gap of 365 nm. Published data suggests an absorption coefficient in the region of 10^{-3}cm^{-1} [86] [87] in the near IR region. Whilst this value is small, when used in high power configurations we can observe the effects of this absorption. In order for VBGs to be used within future systems, an understanding of the causes of these effects and ideally, a model that will predict these effects is required. Using the Runge Kutta model, coupled with Finite Element Analysis (FEA) of the thermal induced aberrations, the behaviour of the VBGs can be analysed. This method of

VBG modelling has been presented by Waritanant *et al.* [78].

Starting with the coupled equations that describe the performance of a VBG, to first order, the equation has two parameters that will be affected by thermal heating, both to differing degrees. The main contribution to the thermal behaviour arises from the dephasing term ζ. It can been seen that n_{av}, which is the average refractive index taking into account the grating modulation, and K (where $K = \frac{2\pi}{\Lambda}$), will have a temperature dependence. This temperature dependence arises from both the thermal expansion coefficient varying K and the thermo-optic coefficient which will affect n_{av}. The overall temperature dependence is a combination of these two factors, as shown below [87]

$$\frac{d\lambda_B}{dT} = 2\frac{dn_{av}}{dT}\Lambda + 2\frac{d\Lambda}{dT}n_{av} = \lambda_B(\frac{1}{n}\frac{dn}{dT} + \alpha_p) \tag{2.21}$$

Where α_p is the effective absorption in parts per million. The refractive index coefficient dn/dt is $0.05 \times 10^{-6}\,^{\circ}\mathrm{C}^{-1}$. This will cause the refractive index to change slowly as a function of temperature. The thermal expansion coefficient dL/dt is $8.4 \times 10^{-6}\mathrm{m}\,^{\circ}\mathrm{C}^{-1}$. The combined temperature effect is therefore dominated by the thermal expansion, which is much larger than the dn/dt coefficient. Equation (2.21) shows a Bragg wavelength temperature coefficient will therefore be equal to the thermal expansion coefficient 8.4 pm/°C [87].

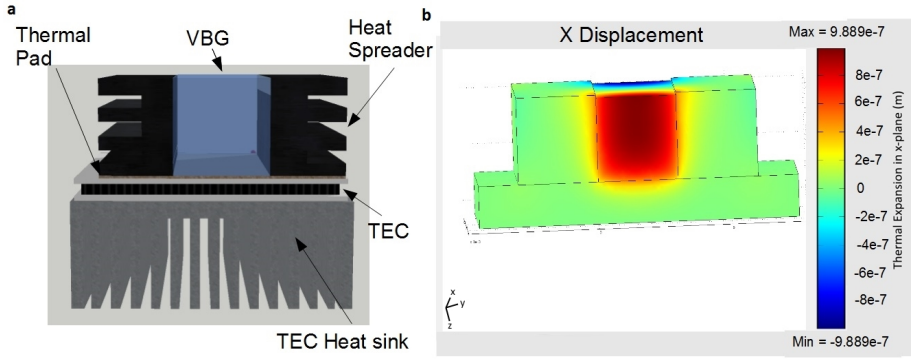

Figure 2.4 – a) Modelled setup. b) Thermal modelling of VBG.

The analysis shows that the bulk temperature tuning is simply a function of the absorption coefficient. However, when considering the spatial distortion of the grating, more complex modelling will be required.

A model was constructed in Comsol to generate a temperature profile within the grating. Firstly, the bulk temperature tuning of the VBG is checked, to ensure it is

consistent with the simple analysis completed above. Fig. 2.4 shows the VBG setup and the corresponding thermal expansions in the plane of the grating.

Fig. 2.4b shows the cumulative thermal expansion of the grating for a temperature increase of 50 °C. A total of 1.95 μm expansion across the grating is observed. This corresponds to a shift in the Bragg wavelength of 0.42 nm. From equation (2.21) a shift of 0.41 nm would be expected. The small difference may arise from the modelling method. The model does not actually increase the ambient temperature but instead simulates a temperature rise in the TEC. This represents a real life scenario, rather than the simple calculation presented previously.

The thermal effects that will arise from an incident laser beam can now be investigated. Initially a 200 μm 1342 nm beam incident on a 99% reflectivity grating was modelled. There are two main parameters that affect the thermal gradients. The first parameter is the absorption coefficient. As discussed earlier, this is typically in the region of 0.01 cm^{-1}. The second parameter is the power distribution of the incident beam within the grating. The intensity profile will affect the grating by expanding it in a nonlinear fashion, modifying its parameters in all three dimensions. An initial Runge Kutta model, completed for an unperturbed grating, allows for the calculation of the intensity distribution through the VBG. The model assumes that a small change in VBG reflectivity will not significantly affect the intensity distribution. If the VBG reflectivity reduces significantly, the intensity profile within the grating will change, thereby changing the overall heat load. For the incident beam, we simply consider a monochromatic source at the Bragg wavelength. It would be possible however, to model a broad linewidth source by simply interrogating the spatial intensity profiles across the spectrum of the source. Fig. 2.5 shows the overall intensity profile modelled in Matlab and the actual converged solution of the spectral intensity distribution.

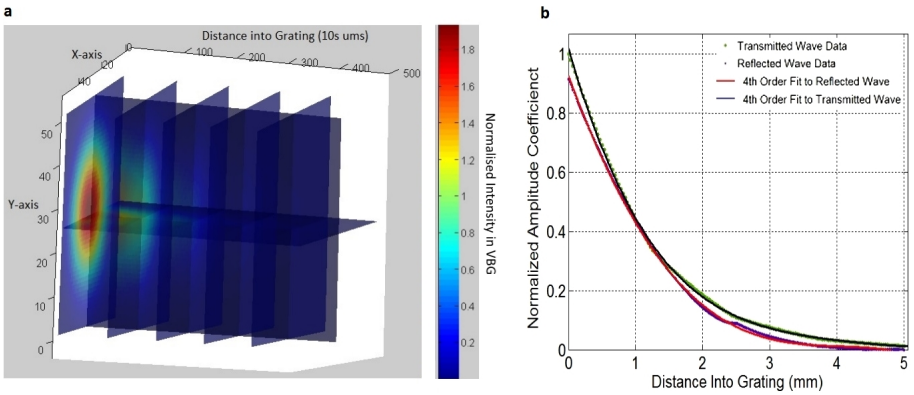

Figure 2.5 – a: Modelled intensity distribution in VBG. b: Intensity distribution of transmitted and reflected beam for incident intensity profile.

An exponential curve was fitted to both the reflected and transmitted wave to allow for simple integration into Comsol, this is shown in Fig. 2.5b. By including the absorption coefficient, the thermal load within the grating can then be modelled. Fig. 2.6 shows the resultant temperature rise in the grating.

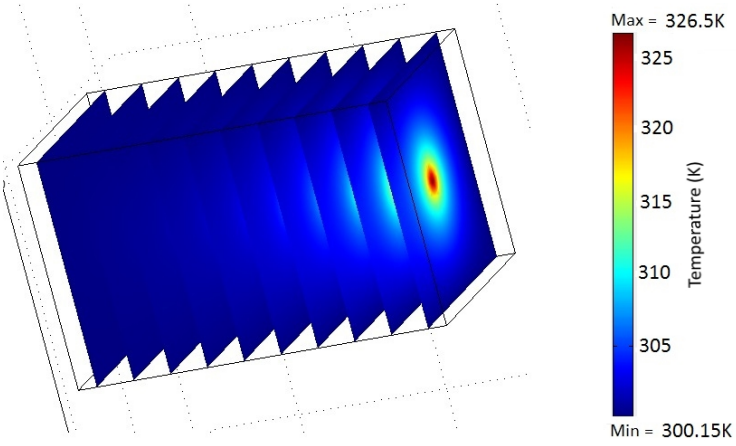

Figure 2.6 – Modelled temperature map in a VBG.

A temperature rise of 20 °C in the VBG was modelled for an incident of power of 150 W. The localised thermal expansion data is then extracted from the Comsol model for the Runge Kutta VBG reflectivity calculation. The reflectivity is now adapted to include a spatial dependence on the modulation spacing. Fig. 2.7 shows the spectral response of the thermally modified grating compared to the unmodified grating. We can observe a significantly different response to the unmodified grating. The first parameter that has changed is the peak reflectivity, which has reduced from 99% to 97%. We also observe a significant broadening effect which arises as a result of two secondary peaks that are now represent a portion of the VBG's spectral response.

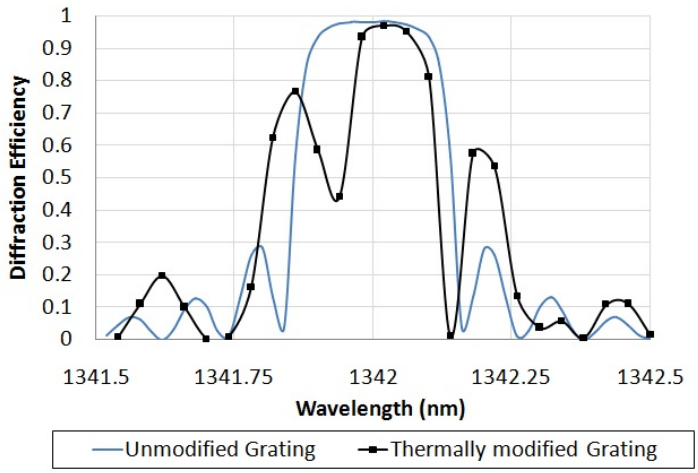

Figure 2.7 – Modelled spectral diffraction efficiency of thermally distorted VBG.

We can now see how the thermal distortions of the grating will ultimately limit the ability of the VBG to achieve a narrow linewidth. The presence of the secondary spectral peaks may also allow for a larger linewidth than that of the unmodified grating.

2.5 Conclusion

This chapter has introduced the basic concept of the VBG grating. The methods used in this thesis to calculate the performance of a grating, in both an unmodified configuration and a thermally distorted configuration have been outlined. The parameters that define the VBG's spectral performance have been been discussed and the actual variation in performance these parameters produce is presented. The concept of using FEA, combined with a Matlab code using the Runge Kutta solver method has been shown to predict the spectral performance of a thermally distorted VBG. The thermal effects within VBGs are further investigated in chapter 4, where the performance of a VBG under high thermal loads is actually measured.

Chapter 3

Single VBG Lasers

3.1 Introduction

In this chapter the development of an initial solution that could meet the requirements outlined in chapter 1 section 1.2 is considered. The demand for a broadband visible source is to provide dazzling capabilities to defeat optical sensors [54]. Whilst the requirements for a multi-wavelength visible source can be met by a number of different laser technologies, a true broadband visible laser in this power region can only be met by a limited number. Sources such as supercontinuum generation within a fibre can readily achieve this and, at the time of writing, is the most efficient method of generating a broad spectrum within the visible region [88]. The threshold for the χ^3 nonlinearity is very high however [89], leading to the use of pump sources with ultra-short pulses. As a result, this method cannot be used to generate a CW source. If the use within a ruggedized military platform is also considered, ultrafast lasers are typically not suited to this environment due to their size and weight as well as their susceptibility to external factors such as temperature or misalignment.

This complex spectral requirement could also be met by a series of discrete wavelengths. By using more readily available mature technology, a source with a series of discrete wavelengths could replicate the dazzling performance observed from a true broadband source. To create a quasi-broadband source at least three discrete wavelengths would be required [54]. In this chapter, the development of a source that, in the future, could generate three different wavelengths within the visible spectrum is investigated. The use of VBGs as a replacement for HR mirrors is detailed in this chapter, to demonstrate their ability to operate in a laser cavity that could be used for this purpose, whilst also providing wavelength selection and narrow linewidth. As discussed later, complex coating requirements for dielectric mirrors that would allow for wavelength selection are difficult to manufacture. A high power VBG cavity could therefore provide improved performance, in-terms of narrow linewidth and increased conversion efficiency, compared to traditional dielectric mirrors.

One of the simplest ways the wavelength range could be spanned is through use of a series of optically pumped semiconductor lasers (OPSL). By the adjustment of the active layer material type and concentration, OPSLs can be fabricated to operate on a number of different wavelengths. OPSLs in the red and green region have already generated up to 15 W of pump power [90]. More recently, OPSLs operating in the yellow/orange region (560-600 nm), generating up to 5 W CW have been demonstrated [91]. By beam combining a series of these OPSLs, a broadband visible source could be created.

Whilst this method may provide the simplest route to a turn-key solution, the limited commercial availability of both the lasers, and the inability to procure stand alone active gain regions, may limit their use within a number of systems. This typically occurs when manufacturers look to add maximum value and minimize cost through their supply chain.

CW Raman lasers operating in these regions have also been demonstrated by intra-cavity frequency doubling the first-stokes Raman line. In this configuration watt level powers have been generated in the 580 nm region [92]. However, high incident intensities are required to achieve efficient conversion.

Lasers using different emission lines in Neodymium host materials could also provide a simple, cost effective route to achieve the requirements. Materials such as Nd:YAG and Nd:YVO_4, pumped with 808 nm diodes, could act as the pump source for second harmonic generation (SHG) and sum frequency generation (SFG), generating a series of visible wavelengths. The various emission lines in these materials have been discussed in chapter 1 section 1.2.1. The ability to generate both a 1 and 1.3 μm source could allow for generation of 532, 590 and 670 nm emission, therefore achieving the minimum requirements for a visible source.

CW and Q-switched SHG and SFG at these wavelengths have been demonstrated previously in a number of different configurations [8] [93]. In future work, presented in [55], the possibility of using a single laser to generate the fundamental wavelengths simultaneously is discussed. Dual wavelength setups have been described previously [94] to generate 590 nm emission. By power scaling such configurations, and using the residual 1064 nm and 1342 nm lines to produce the other visible emission wavelengths, a quasi-white-light source could be created. This setup could achieve the outlined requirements using only a single laser. The laser would also produce three visible beams that are co-linear to one another, removing the need for beam combining.

One of the challenges in these configurations, and in particular the SFG and dual wavelength setups mentioned above, is the complex coating requirements. The coating requirement for the SFG, for example, would require three different reflectivity specifications: two at the fundamental wavelengths and one at the sum frequency wavelength. A dual wavelength laser could require up to five different features within the spectral response, leading to a complex coating requirement.

To address this issue, VBGs could be used instead of normal dielectric mirrors. VBGs can provide high reflectivity in a narrow wavelength range, whilst providing negligible losses at all other wavelengths. Combined with a broadband anti-reflection (AR) coating, VBGs could operate as the wavelength selective element in a solid state laser cavity.

VBGs can also be used to suppress the stronger emission lines in a cavity. The main 1064 nm transition line in both Nd:YAG and Nd:YVO_4 typically builds up within the laser cavity, preventing oscillation at any other wavelength. By providing high reflectivity at a weaker emission line and limited feedback at the stronger emission line, the operating wavelength can be controlled. VBGs could also be used to provide high reflectivity at the stronger emission line and couple this out of the cavity, preventing a high Q-factor cavity being formed at this wavelength.

At the time of writing, VBGs have been used in solid state laser cavities in a number of different configurations. The first demonstration of a VBG solid state laser was by Chung *et al.* [69] in which a high diffraction efficiency VBG was used to narrow the linewidth of a Ti:Sapphire laser. A number of papers have shown the ability of VBGs to create narrow linewidth configurations without the need for other intra-cavity components such as etalons. Up to 1.9 W have been generated in these configurations [95] [94].

The use of VBGs to force operation on weaker emission lines has also been demonstrated [94]. VBGs have also been used within high average power slab waveguide lasers to control the emission wavelength. Lasers generating up to 80$\dot{W}$ in a Tm:YLF slab [96] with an M^2 of 2.5 in the waveguided plane have been demonstrated. Scaling of these configurations is achievable due to the relatively large spot sizes incident on the VBG, limiting the thermal aberrations.

End-pumped rod and thin disk VBG cavities operating with low M^2 have also been demonstrated, with powers up to 4.7 W [97] and 2 W [98] respectively.

A multi-spectral VBG cavity would therefore be an efficient method of generating the requirements, based on mature solid-state technology. VBGs are now commercially available in customizable specifications. This chapter firstly explores the viability of using VBGs as a replacement for dielectric high reflectivity (HR) mirrors within an end-pump rod laser cavity, at higher powers than have previously been demonstrated. To achieve this, a dielectric mirror laser cavity running at 1064 nm, is compared to that of a VBG / dielectric mirror laser cavity running at the same wavelength.

Initially the various parameters of the laser configuration are investigated. The aim is to optimize the setup for 1064 nm operation in terms of cavity mode size, pump spot size and cavity output coupling. Two differing configurations are then constructed, a 1064 nm cavity based on dielectric mirrors and a dielectric / VBG cavity. Comparing the performance of the two cavities allows us to compare the performance of a VBG to that of a standard dielectric mirror. Finally, a second VBG cavity is configured to allow the laser to run on the weaker emission line at 1342 nm, thereby demonstrating the VBGs ability to suppress the stronger emission line, whilst operating at relatively high powers.

3.2 1064 nm Dielectric and VBG Laser Configuration

The laser used in this configuration was a diode-pumped, three mirror Nd:YVO_4 laser cavity, constructed for this investigation. This is shown in Fig. 3.1. A 0.5 % doped Nd:YVO_4 rod based crystal, with a length of 28 mm, including 4 mm undoped end-caps at either side, was mounted into a copper heat sink and air-cooled. The pump source was a 40 W 808 nm diode, fibre coupled into a 800 μm core fibre. Two focusing lenses were used to focus the diode light into the crystal through a dual coated mirror. The mirror provided high transmission at 808 nm and high reflectivity at 1064 nm. By adjusting the position of the two lenses, the focussed spot size can be varied.

3.2.1 Optimum 1064 nm Nd:YVO_4 Laser Parameters

In this section the expected performance of the laser resonator introduced previously is briefly described. This allows the optimum setup in terms of spot size, coupling and beam quality to be achieved. Using the equations described in section 1.2.2 in chapter 1, the cavity characteristics were modelled.

The cavity was operated in a plane-plane configuration to limit the need for curved optics. The thermal lens strength would therefore provide the cavity stability. The magnitude of the thermal lens was calculated from the equations in chapter 1 section 1.2.3. The pump spot must be matched to the size of the fundamental mode, but the

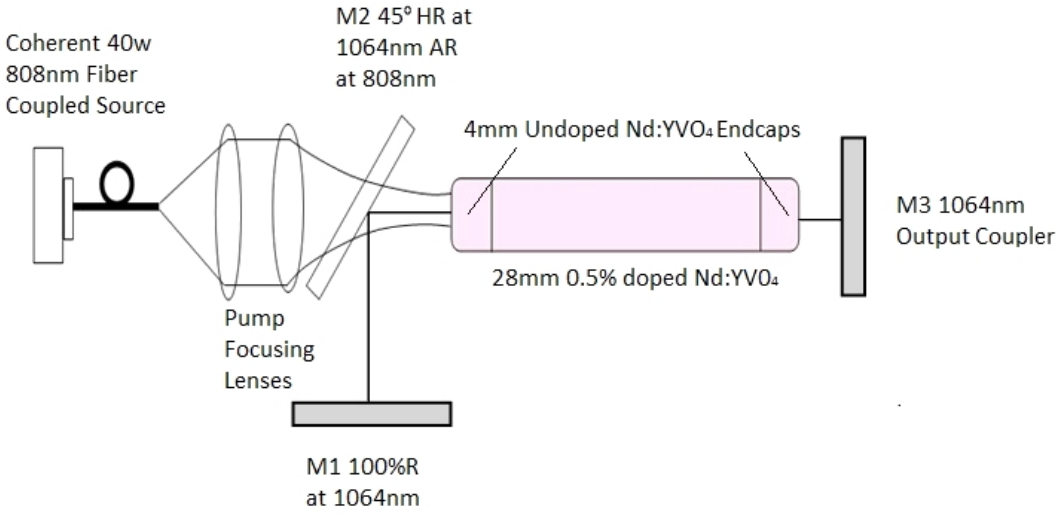

Figure 3.1 – 1064 nm three mirror cavity diagram.

defined pump spot size will also impact on the thermal lens strength. By calculating the thermal lens focal length and the resultant cavity length required to match the pump spot size, the best configuration for the plane-plane cavity was ascertained. This configuration allowed for 16 W of pump power in a 400 μm spot, with a cavity length of 364 mm. The cavity configuration produces a fundamental mode size of $\approx 400\,\mu$m in both the x and y axis. The thermal lens strength was calculated to be 134 mm in the vertical axis and 381 mm in the horizontal axis. The optimum output coupling for this configuration was calculated to be 78%.

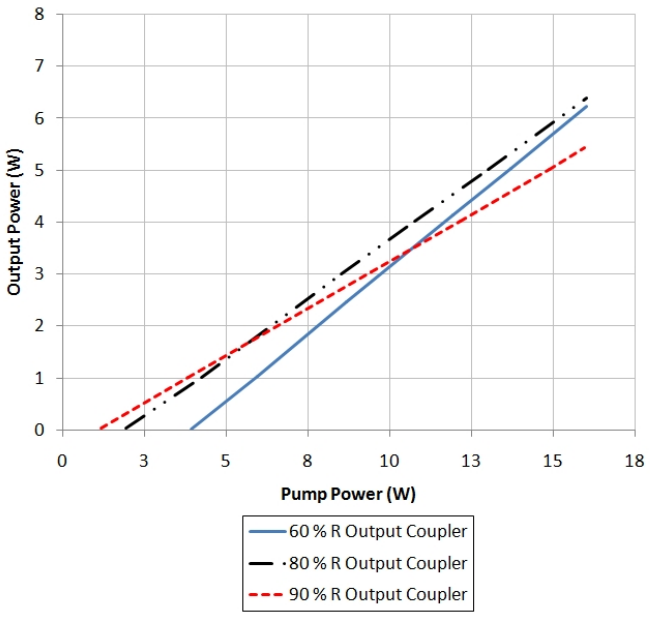

Figure 3.2 – Modelled laser output power with various output couplers.

The slope efficiency of the laser was then calculated for the various output couplers available. The reflectivity of the output couplers was 60%, 80% and 90%R. The model

uses a constant cavity mode size, therefore any variation in the focal length of the thermal lens is not included in this model. The result is a linear relationship between pump power and output power. The calculated output power for each coupler is shown in Fig. 3.2. For the model, losses of 3% were estimated. This was calculated from the coating scans of the mirrors and AR surfaces. The 80% coupler provided the optimum performance in the calculation, with a slope efficiency of 0.48 and a maximum output power of 6.4 W.

3.2.2 1064 nm Mirror Cavity Results

The cavity shown in Fig. 3.1 was then constructed. The spot size of the pump was adjusted by displacement of the two lens focusing setup to achieve a 400 μm waist within the crystal. A waist size of 385 μm was measured using a CCD camera. The performance of the cavity was then investigated under lasing conditions to ensure agreement with the calculated values shown previously.

The performance of the cavity with output couplers ranging from 60-90 % reflectivity was then characterised. The results of this are shown in Fig. 3.3.

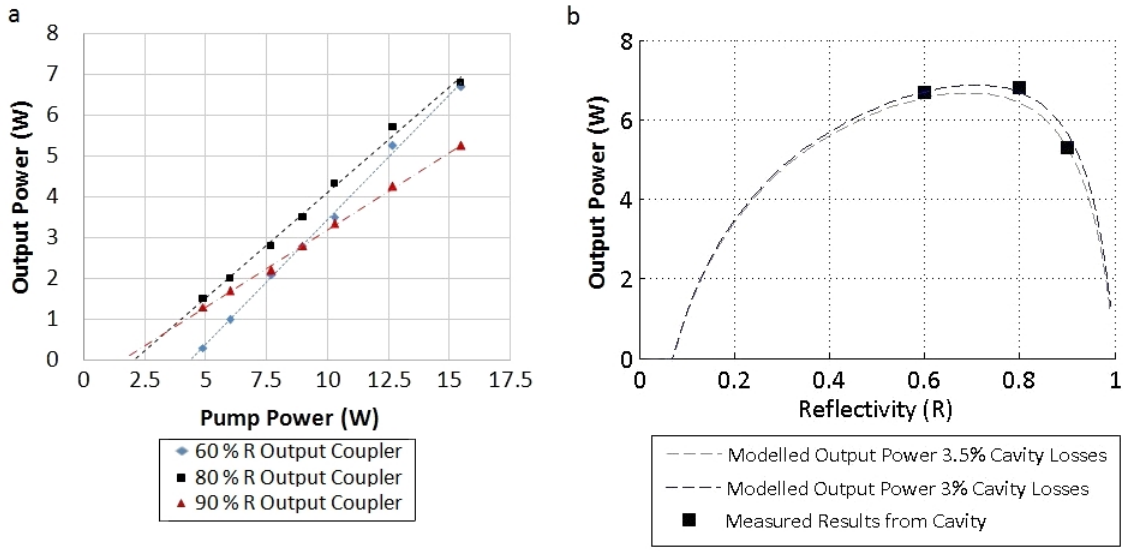

Figure 3.3 – a: 1064 nm dielectric mirror slope efficiency measurement. b: Modelled and measured power vs. reflectivity.

A maximum power of 6.8 W was generated using the 80% R coupler. The slope efficiency of the 80% and 60% output couplers was calculated to be 0.51 and 0.61 respectively. This is in good agreement with the calculations completed in the previous section, validating the calculations. The output power also shows a linear relationship with the pump power suggesting the variation in the thermal lens focal power does not vary the pump / cavity mode overlap.

In the next section, where VBGs are used instead of a standard dielectric mirror, one of the main factors that may differ will be the losses introduced into the cavity. A comparison of the output power and reflectivity values are compared in Fig. 3.3b for the measured and modelled results. The modelled results show cavity losses of around 3-3.5% provides reasonable agreement with the measured results. A second analysis of the cavity loss was completed by performing a Findlay-Clay analysis (FCA) [99] from the different output couplers. This is shown in Fig. 3.4

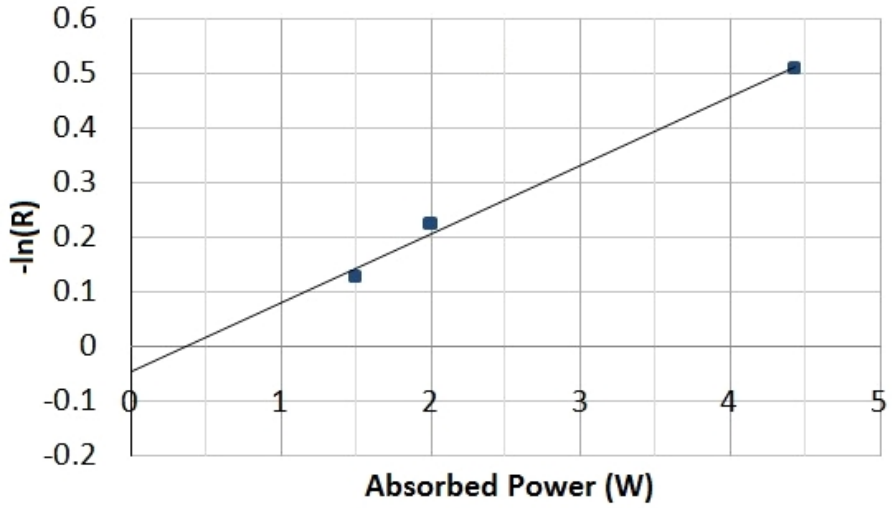

Figure 3.4 – Findlay-Clay analysis of 1064 nm cavity using dielectric mirror.

From the FCA, the cavity losses were measured to be 4.5 %. This is compared to 3.5 % from the previous results. The FCA values represent actual measured values from the cavity, compared to the modelled results in the output coupling analysis. Whilst there is a small difference, the model does appear to provide reasonable agreement with the measured results. A number of different factors could affect both the parameters in the model and assumptions made to calculate the threshold in the FCA. For example, whilst each output coupler was aligned for optimum performance, small variations in the alignment for each output coupler may have occurred. Due to the limited data points taken for the FCA analysis, any small change in the threshold values will represent a larger change in the calculated cavity losses.

The beam quality of the laser was then measured using the 80% output coupler. This is shown in Fig. 3.5

The M^2 was measured to be 1.12 and 1.08 in the vertical and horizontal planes respectively. The M^2 measurement of the mirror cavity will allow for a comparison to the VBG cavity, and any phase errors introduced by the VBG will be highlighted.

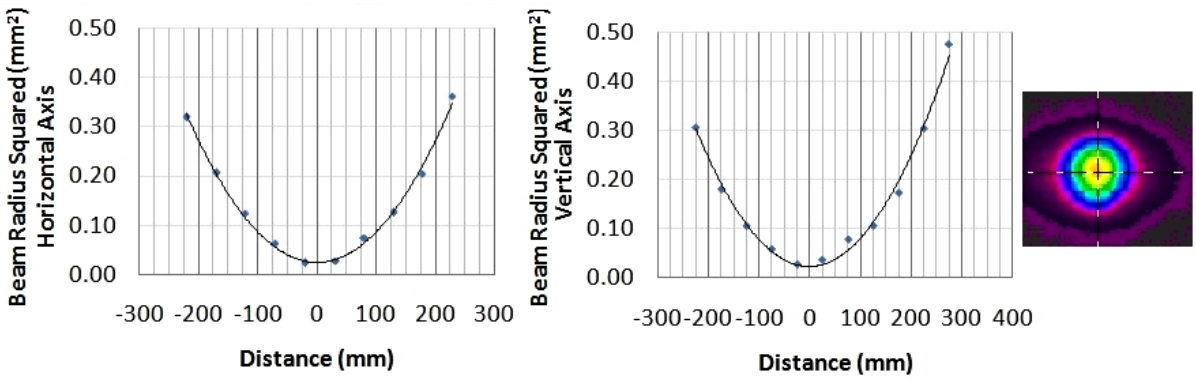

Figure 3.5 – M^2 measurement of 1064 nm mirror cavity in the horizontal and vertical axis. Far field beam inset.

A degradation of the beam quality or change in the divergence would show that the introduction of the VBG has introduced such errors upon the reflected beam. The error can arise from a number of different sources, the biggest error, as discussed in chapter two, could be thermal lensing in the VBG. The VBG may also exhibit degraded beam quality as a result of variations in the polished surface, or even the grating itself.

The final factor to be measured is the linewidth of the cavity. The narrow spectral response of the VBG should significantly narrow the spectrum compared to the mirror cavity. The linewidth was measured using a Jarrel-Ash Grating based spectrometer, with a resolution of 0.25 nm. The spectrum is shown in Fig. 3.6

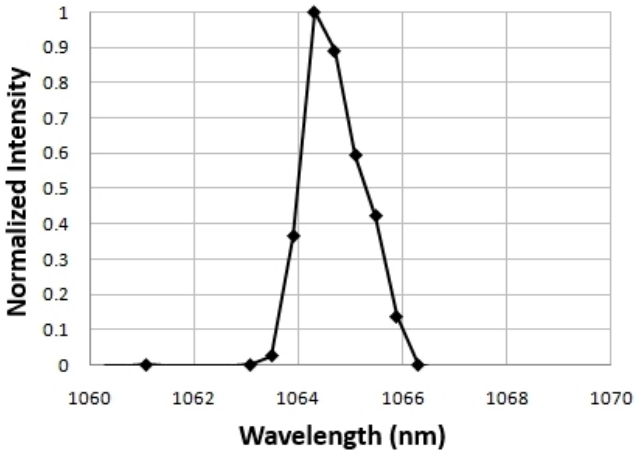

Figure 3.6 – 1064 nm dielectric mirror linewidth.

The FWHM spectrum was measured to be 1.25 nm and is centred at 1064.3 nm ± 0.25 nm . The spectrum in Fig. 3.6 is fairly broad, and possesses a slight kink at 1065 nm. The fluorescence spectrum of Nd:YVO_4 peaks at 1064.4 nm [100]. The output spectrum of the laser therefore follows that of the emission cross-section, as

expected.

Overall, the cavity performed as expected when compared to the modelling and theory. The output power and threshold values were similar to those calculated in section 3.2. A small difference of 1% was present between the modelled losses and the measured results, a number of different factors that could cause this discrepancy have been considered. The beam quality measurement suggests the mode matching between the pump and cavity mode is sufficient to select operation on the fundamental mode. The output spectrum also follows the emission cross-section spectral characteristics.

3.2.3 VBG Cavity

To analyse the performance of the VBG, an identical cavity was configured and the HR mirror M1 replaced with a VBG. This is shown in Fig. 3.7a. Fig. 3.7b shows a photo of the setup. The cavity length and pump spot size were identical to those in section 3.2.2.

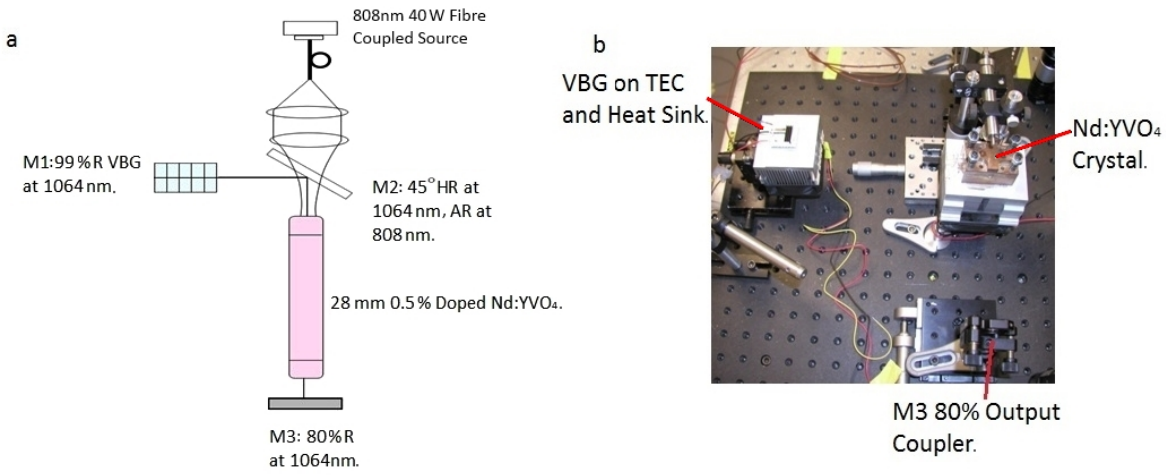

Figure 3.7 – a: VBG cavity diagram. b: Photo of configuration.

The VBG was ordered from Ondax with a specification reflectivity of 99% at 1064 nm and spectral bandwidth of 0.3 nm. The VBG grating parameters needed to achieve the required performance were provided by Ondax. The index modulation in the grating was 180×10^{-6} with a grating spacing of 357 nm. Using these parameters the VBG reflectivity and spectral response can be calculated. This is shown in Fig. 3.8. The VBG linewidth was modelled to be 180 pm, in agreement with the performance data supplied by Ondax.

The VBG was mounted within an aluminium mount and placed onto a TEC as shown previously in Fig. 2.4. As discussed in chapter 2 section 2.4.1, the VBG spectral

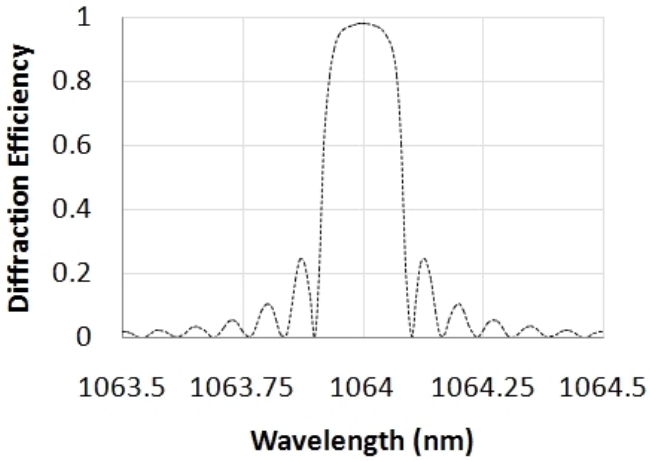

Figure 3.8 – Calculated spectral response of 1064 nm VBG.

performance and centre wavelength is temperature dependent. The VBG temperature was controlled by TEC driven by a Marlow SE5000 TEC controller with a temperature accuracy of ±0.25 °C. The centre wavelength was measured at room temperature to be 1063.25 ±0.5 nm using a Perkin Elmer spectrometer, this compares to the quoted value of 1063.8 nm measured by the manufacturer. For both measurements, the VBG centre wavelength was lower than the specified value. As result, in order to operate the VBG at the peak emission cross-section in Nd:YVO_4, the VBG will require high temperature operation. Tuning the VBG centre wavelength from 1063.8 nm to 1064.4 nm would require a temperature increase of 60 °C from ambient.

The same measurements as those taken in the mirror characterisation were then repeated for the VBG cavity to allow for a comparison between the two.

3.2.4 VBG Cavity Characterisation

The laser was configured as shown in Fig. 3.7a, using the 80% output coupler at position M3. To maximise the output power, the VBG must be tuned to the optimum operating temperature. By temperature tuning the VBG, the centre wavelength of the VBG can be tuned across the emission cross-section of Nd:YVO_4. Initially the temperature tuning effect of the VBG was characterised whilst the cavity was lasing. The absorbed pump power for this measurement was 16 W. The centre wavelength was measured using a High Finesse WS6 high precision wavelength meter with an accuracy of 1 pm. The tuning of the VBG with centre wavelength is shown in Fig. 3.9.

The overall linear slope in Fig. 3.9 shows the VBG tunes with a temperature coefficient of 10 pm/°C, in agreement with the literature. However, the tuning is not completely continuous and distinct shifts in the discreet measurement points are present. The measurement taken here is the actual centre wavelength of the cavity

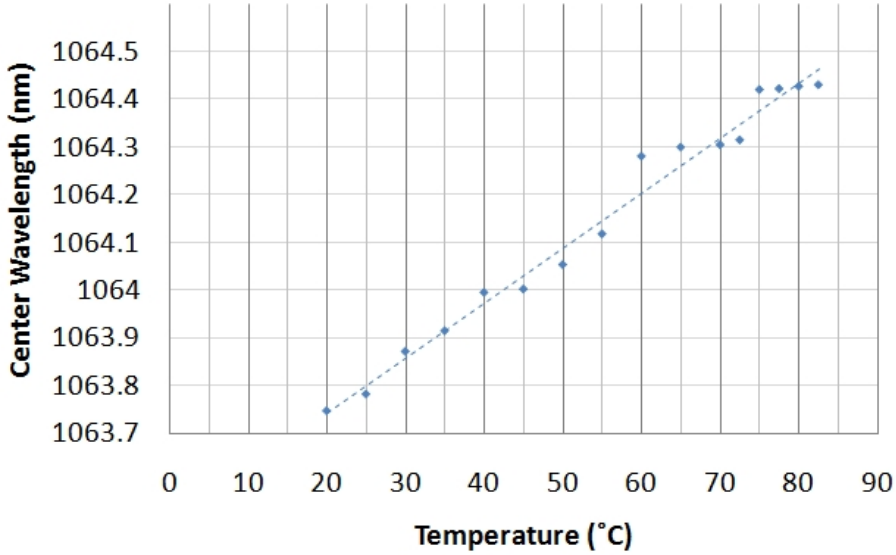

Figure 3.9 – 1064nm VBG temperature tuning performance.

emission, not the VBG centre wavelength. The VBG should tune linearly as shown previously [97] [101]. Whilst the grating centre wavelength is tuned linearly as a function of temperature, the cavity will still lase on the mode with the lowest threshold. Where troughs in the emission cross-section exist, the threshold of the modes either side of the trough will be much smaller. The wavelength is then locked into a given operating wavelength until the emission cross-section or round-trip net gain increases. As a result, the VBG centre wavelength appears to be remaining constant despite the increasing VBG temperature. This locking effect can be observed strongly at the peak emission wavelength of 1064.455 nm, whereby an increase of 8°C does not appear to change the wavelength significantly.

The optimum performance of the cavity should be achieved at the peak emission cross-section. The temperature tuning of the laser and the output power vs. wavelength is shown in Fig. 3.10.

The graph shows significant variation in output power as a function of wavelength. We observe distinct shifts in centre wavelength, with peaks at 1064.045 nm and 1064.45 nm. These regions represent peaks in the emission cross-section of Nd:YVO_4 [100]. From Fig. 3.9 these peaks also represent the locations where the VBG tuning rate was not linear.

The limitation of this behaviour is that continuous tuning range across the emission cross-section of Nd:YVO_4 cannot be achieved. From figs 3.9 and 3.10, a large jump in the wavelength region from 1064.10 - 1064.24 nm is observed. It was not possible to operate the laser in this wavelength range suggesting a trough in the emission

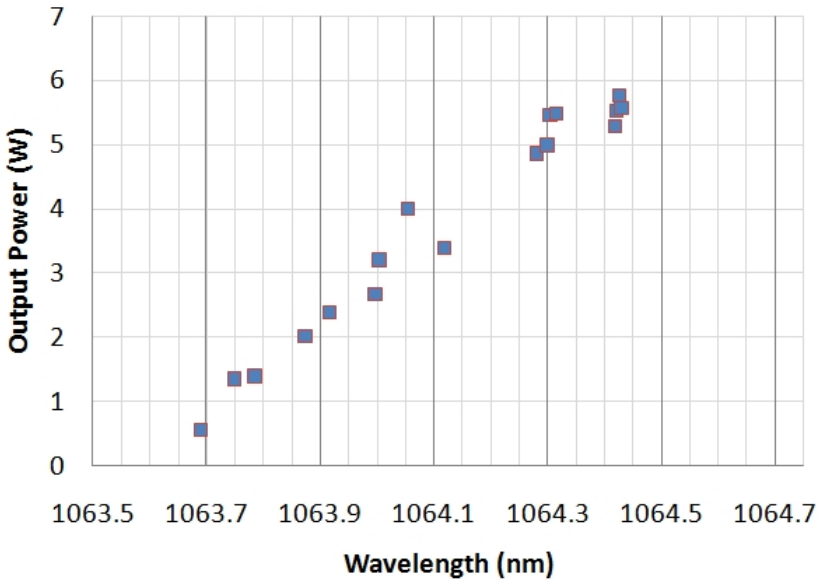

Figure 3.10 – 1064 nm VBG cavity wavelength tuning.

cross-section is present. Fundamentally the emission region relates to the $4\,F_{3/2}$ to $4\,I_{11/2}$ transition in the Nd^3 material. The emission from 1062-1064.5 nm is due to two transitions. The peak emission wavelength at 1064.45 nm is consistent with those reported elsewhere [102], this occurs from the R_1-Y_1 transition line. The weaker emission, at 1064.055 nm, is due to the R_2-Y_1 emission. It can be inferred from Fig. 3.10 that the emission cross-section of the R_1 line is much stronger than that of the R_2 line, which agrees with previous results [100]. The shift in wavelength is therefore a result of a change from one transition to the other.

The cavity was then characterised with a series of output couplers with differing reflectivities, as was completed in the previous section. The same three output couplers were used, however, using the 90%R coupler induced thermal lensing within the VBG, degrading the grating reflectivity. The performance and investigation of this effect is discussed in chapter 4. A comparison between the remaining output couplers was completed for the conventional mirror and VBG cavities. These are shown in Fig. 3.11.

Fig. 3.11a and b shows a comparison of the VBG and mirror cavities for the 60%R and 80%R output couplers respectively. Fig. 3.11a shows that with the 60% coupler we observe comparable performance, albeit with the VBG slightly worse than that of the mirror cavity. Fig. 3.11b shows slightly different behaviour, the output power of the VBG cavity is now lower when compared to that of the mirror cavity. It was observed that a small amount of power still leaked from the rear surface of the VBG in each configuration. The levels of light in each case suggested the reflectivity of the VBG was $\geq 99.3\%$.

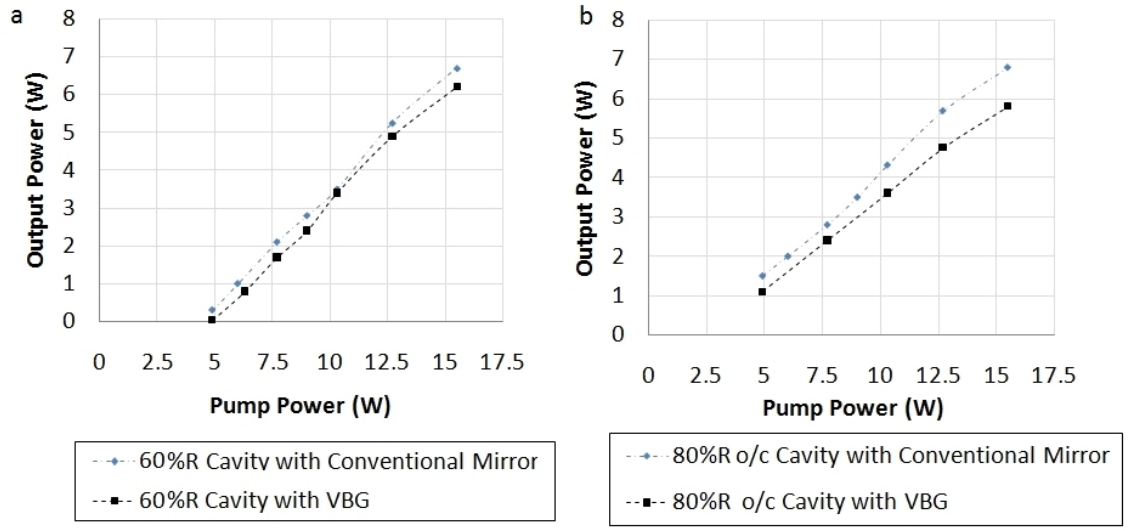

Figure 3.11 – a: Performance of 1064 nm laser cavity with: a: 60%R output coupler. b: 80%R output coupler.

It was also observed that for each output coupler, the VBG had a different optimum operating temperature. The optimum for the 60% R was 61 °C compared with 71 °C for the 80%R coupler. A slight difference in the centre wavelength between the two couplers of around 10 pm was also measured. These effects can be explained by heating within the VBG as a result of minute absorption of the cavity light, this is further discussed in chapter 4.

A FCA was then performed. In this analysis the threshold values from the 90% coupler were also used. The performance of the cavity at threshold, and low output powers should not be affected by thermal gradients within the VBG due to the low intra-cavity power. The analysis is shown in Fig. 3.12.

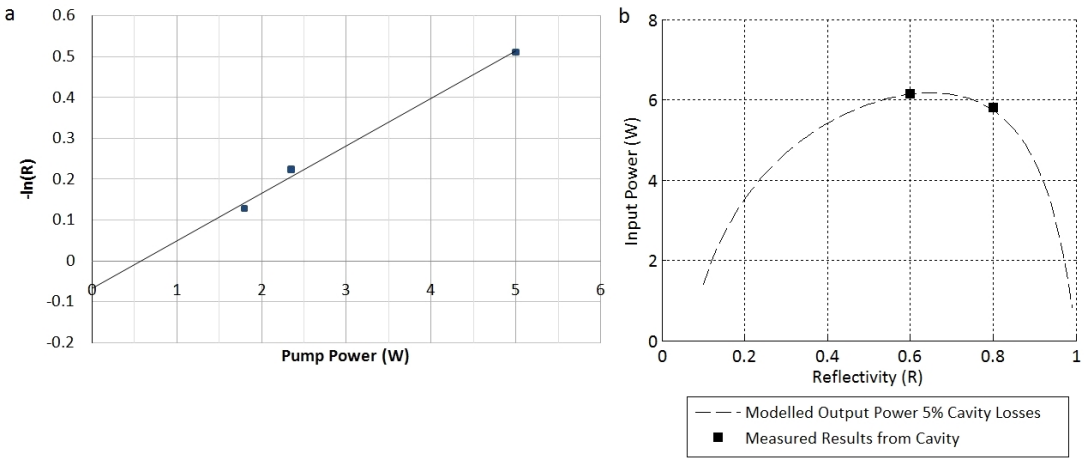

Figure 3.12 – a: 1064 nm VBG laser Findlay-Clay analysis. b: Output coupling analysis.

The FCA analysis shows that the intra-cavity losses have increased to 6% compared to 4% measured for the mirror cavity. In the output coupling loss analysis the losses were calculated to be 5%, compared to 3.5% measured for the mirror cavity. The offset of the two measurement techniques is consistent with that measured for the mirror cavity. The possible causes for this have been highlighted previously.

The different measurement methods allow for an analysis of losses from both the slope efficiency threshold measurement and the maximum pump power operating point. Due to thermal effects in the VBG, it is possible the losses of the cavity could increase with the intra-cavity intensity. The measurement of the threshold point for the FCA analysis may not give an indication of these losses. The output coupling analysis would highlight this effect as only the peak pump power values are used. Both analyses show an increase of 1.5% compared to that of the mirror cavity. This suggests that whilst the VBG exhibits higher losses than the mirror cavity, these losses are constant with varying pump power.

The higher losses clearly affect the VBG performance. This is shown in Fig. 3.11b where the VBG performance differs from the mirror cavity. This effect is not observed strongly in Fig. 3.11a due to the lower reflectivity. The output coupling dominates the cavity losses in the 60% R case, where the cavity lifetime, and therefore the number of round trips, will be less. The result is that the losses are not as significant for the higher output coupled configuration, reducing the effect of the VBG losses.

To further investigate the source of the losses, a simple transmission test using a 1060 nm laser diode was completed. The wavelength is sufficiently different so as to ensure no coupling with the grating occurs. If the losses were due to absorption this would be measured in this test. The literature suggests the losses should be in the order of $10^{-2}\,\mathrm{cm}^{-1}$, which for a 5 mm grating, would not be easily measured. The losses were measured to be $\leq 1\%$ which is within the measurement error. This suggests the losses are not due to any intrinsic absorption or any defects in the coating on the VBG.

As a result of these measurements, there may also exist a secondary loss mechanism which is not a function of linear absorption. The losses may also be a property of the reflected beam. The coupling of the forward wave into the backwards travelling wave introduced in chapter 2 may induce further losses. If we move away from the assumption of the perfect grating parameters, scattering of the transmitted beam as we move close to the Bragg wavelength / angle could lead to poor coupling into the reflected beam. The loss would be characterised as a variation in the grating

vector. The symptom of this would be the scattering of the reflected wave, causing an intra-cavity loss.

The M^2 of the VBG cavity was measured. Any induced phase errors or grating vector errors could degrade the beam quality of the laser compared to that of the mirror cavity. The results are shown in Fig. 3.13.

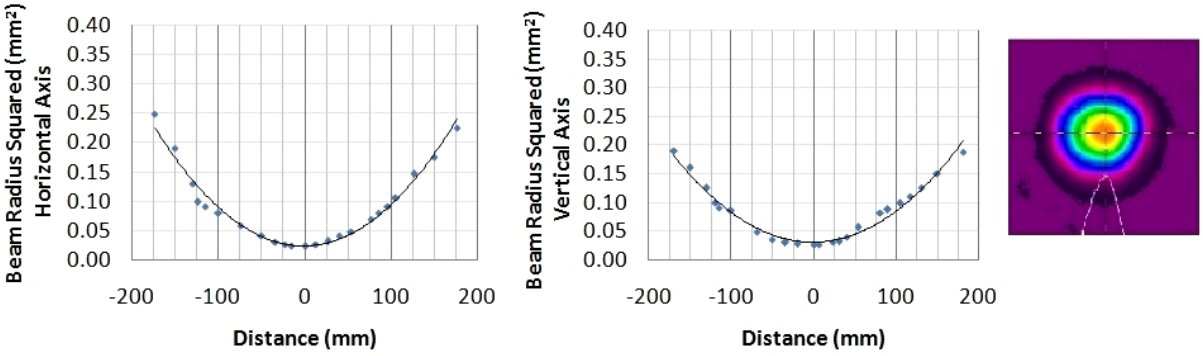

Figure 3.13 – 1064 nm VBG M^2 measurement.

The M^2 of the VBG laser was measured to be 1.18 and 1.14 in the vertical and horizontal axis respectively. The analysis shows the VBG does not particularly improve or degrade the beam quality of the laser for this setup. A comparison of the far field profiles was also completed. From Figs 3.5 and 3.13 the variation in the far field divergence was analysed. The divergence of the dielectric mirror cavity was measured to be 2.41 mrads and 2.15 mrads in the vertical and horizontal axis respectively. For the VBG cavity the divergence was measured as 2.36 mrads and 2.29 mrads in the vertical and horizontal axis. From Fig. 3.13, the beam profile is more circular than that in Fig. 3.5, which has an elliptical profile. The elliptical profile arises due to the biaxial nature of the Nd:YVO_4, producing different thermally induced focal lengths in the vertical and horizontal planes. The increase in divergence of the VBG cavity beam suggests a small amount of additional focusing is occurring in the horizontal axis. However, the strong modal selection of the pump beam ensures that beam quality does not degrade. A small phase error may be present a result of the VBGs introduction. If the magnitude of the phase error was larger however, a degradation in the M^2 would be expected, as a change in mode size would give rise to higher order modes. Errors in the grating vector are also not strongly observed. A variation in this parameter would also allow for higher order modes to oscillate within the cavity, thereby increasing the M^2 values.

Finally, the linewidth of the laser was measured. An interferogram linewidth measurement, described in the Appendix I, was used to provide an accurate measurement of the laser linewidth. A linewidth of 72 pm was measured, an order of magnitude

reduction compared to the 1.25 nm measured for the mirror cavity. Fig. 3.14 shows the Fabry Perot rings captured to measure the linewidth.

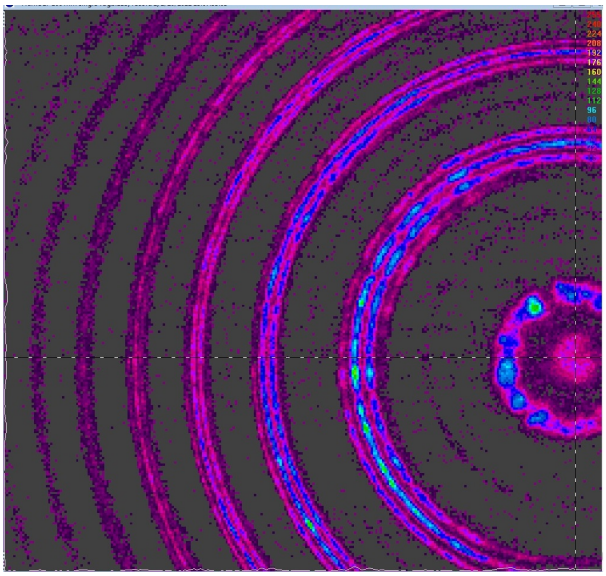

Figure 3.14 – Fabry Perot rings for VBG cavity.

The FWHM spectrum of the laser is narrower than the actual spectral response of the VBG. The presence of spatial hole burning will force operation on a number of modes, beyond this, gain saturation will further broaden the spectrum. However, within a free-running laser, the full spectrum will observe the same reflectivity. In the VBG configuration, as soon the wavelength moves away from the VBG centre wavelength, the reflectivity reduces. From the VBG spectral performance modelled earlier, 72 pm corresponds to a reduction in reflectivity of 3% from the centre point. In current cavity configuration, this represents a large increase in the overall cavity losses. The result shows that the effects of line broadening can be countered by a small reduction in the reflection coefficient.

3.2.5 Discussion

A single VBG laser operating at 1064 nm up to 6.8 W has been demonstrated. The comparison of the dielectric mirror cavity to that of the VBG shows how VBGs can be used as a replacement for HR mirrors within laser cavities. The VBG did exhibit increased losses when compared to that of the mirror cavity. This could limit their use within low gain configurations. The increased cavity losses were investigated within this chapter. Transmission losses, measured at a wavelength out with the acceptance bandwidth of the grating, accounted for only a small amount of the measured losses.

As described in chapter 2 section 2.1, further losses may arise from poor coupling of the transmitted beam into the reflected beam. This is essentially a decrease in

the reflectivity of the grating. The reduced reflectivity does not account for total increase in cavity losses. A small amount of the increased loss must be a result of scattering from the VBG grating. This effect would be characterised by incident light being reflected from the VBG, but not actually coupled into the cavity mode. The scattering is a result of small variations in the grating vector. The magnitude of the vector errors would have to be small otherwise the diffraction efficiency of the grating would decrease. The fact that a small increase in the divergence occurred for the VBG cavity shows that some form of phase error is present. The strong modal selection of the cavity will limit any change in the beam parameters. In another cavity, where the mode selection is not as strong, a large change in the beam quality or divergence may occur.

3.3 1342 nm Single VBG Laser

The use of VBGs as a replacement for HR mirrors has been demonstrated in the previous section. The initial configuration operated on the 1064 nm emission line, which possesses the highest emission cross-section. As a result, attenuation of any the other wavelengths is not required. In this section a VBG is used to achieve operation at the weaker 1342 nm emission line. In order to force oscillation at 1342 nm, the 1064 nm emission line must be sufficiently attenuated. Dielectric mirrors can be coated to provide strong attenuation at 1064 nm and high reflectivity at the weaker 1342 nm line. If the role of a visible source with an intra-cavity SHG element is considered, a further HR or AR coating at the second harmonic wavelength may also be required. A coating that possesses a number of features in its spectral performance is therefore required. Furthermore, if the operation on an even weaker line such as that of 1123 nm (in Nd:YAG) in considered, a coating with four different wavelength performance specifications would be required. As discussed earlier, this complex requirement could be met with a high diffraction efficiency VBG, combined with a broad-band AR coating.

The energy diagram of the 1342 nm transition was shown in Fig. 1.12 in chapter 1. Pumping at 808 nm and operation on the 1342 nm emission line leads to a large quantum defect. The quantum efficiency is therefore $\eta = 0.6$. Despite the large quantum defect, which will inevitably limit efficiency, Nd:YVO_4 represents the ideal laser crystal at this wavelength due to the high emission cross-section.

This section investigates the use of VBGs as a HR mirror in a 1342 nm laser. Following the same process as the previous section, the cavity is modelled to determine the optimum configuration. The cavity is then setup in this configuration and the performance investigated.

3.3.1 Modelling of 1342 nm Nd:YVO_4 Laser

The performance of the laser at various pump spot sizes was initially modelled. Due to the reduced emission cross-section at 1342 nm, the optimum focusing of the diode pump spot will be reduced, as higher intensities are now required to extract the gain. Fig. 3.15 shows the output power at various spot sizes. The total cavity losses were estimated to be 6%, including VBG losses of 2% from section 3.2.4. In Fig. 3.15a, for each calculation the cavity mode was assumed to be matched to the pump spot size.

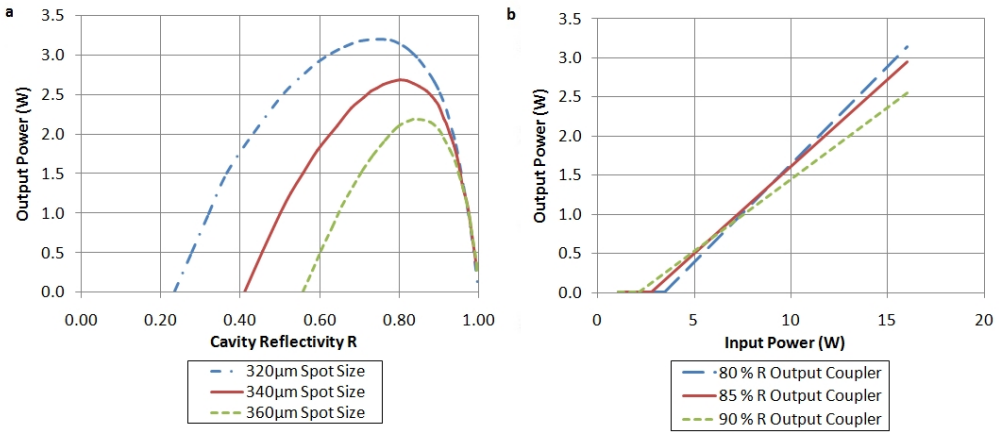

Figure 3.15 – Modelling of 1342 nm cavity. a: Power vs. cavity reflectivity at various pump powers. b: Laser characteristics with a 320 μm spot size.

Using the thermal lens model described in chapter 1 section 1.2.3, the thermal lens strength was calculated. In the 320 μm spot configuration, the thermal lens focal length was calculated to be 90 mm and 185 mm in the vertical and horizontal axes respectively. The cavity length required to match the fundamental cavity mode to pump spot was 233 mm. The limitation of reducing the pump spot size further is the increased thermal lens strength. This causes an astigmatic cavity mode within the laser crystal, which cannot operate on the fundamental mode in both axis.

1342 nm Volume Bragg Grating

A second VBG with a centre wavelength of 1342 nm was also ordered from Ondax with a reflectivity of 99% and a bandwidth of 0.3 nm. The grating parameters required to achieve this were provided by Ondax. The grating modulation size was 220×10^{-6} with grating spacing of 376.9 nm and a length of 5 mm. The calculated performance is shown in Fig. 3.16. The bandwidth of the VBG was calculated to be 250 pm and the diffraction efficiency 98%.

The same cavity configuration described in the previous section and shown in Fig. 3.7 was used. However, the cavity length was decreased to 233 mm. The VBG was again mounted on a TEC to provide temperature control, with the TEC mounted

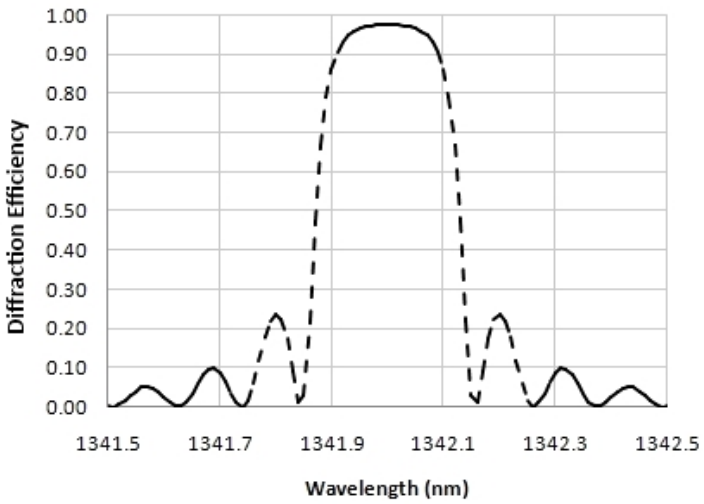

Figure 3.16 – Diffraction efficiency as a function of wavelength for 1342 nm VBG.

onto a heat sink. The pump spot size was adjusted by changing the separation of the focusing lenses and the displacement from the crystal.

3.3.2 1342 nm VBG Cavity

In the same manner as the 1064 nm VBG, the temperature performance of the laser was investigated to obtain the optimum operating point. The temperature of the VBG was varied from 50 °C up to 80 °C using the 80% output coupler at position M1. Fig. 3.17a and b shows the output power as a function of wavelength and the operating wavelength as a function of VBG temperature.

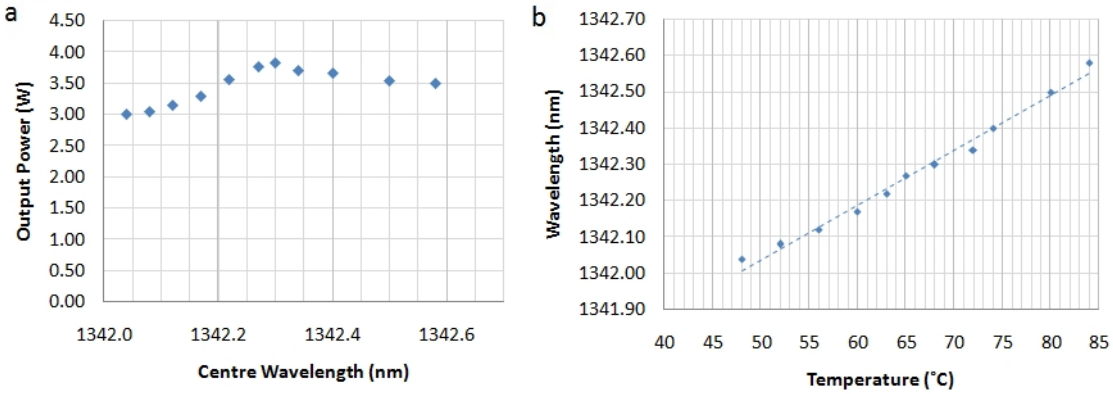

Figure 3.17 – a: Variation in output power with wavelength for 1342 nm VBG cavity. b: Tuning of cavity centre wavelength with temperature.

The optimum temperature was measured to be 64 °C, operating at a centre wavelength of 1342.3 nm. At this operating point the VBG cavity output power was 3.8 W for 16 W of pump power, giving an optical conversion efficiency of 23%. The thermal tuning rate, shown in Fig. 3.17, shows the ability to tune across the full wavelength

range without any significant jump in wavelength.

The wavelength coefficient was measured to be 15 pm/°C compared to 10 pm/°C measured for the previous 1064 nm VBG. The values shown in the literature are typically 11 pm/°C at 1342 nm [94].

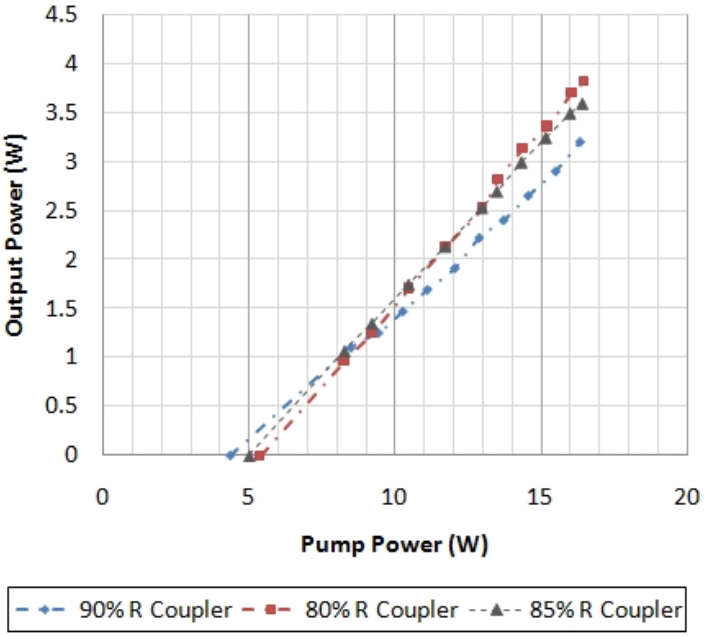

Figure 3.18 – Slope efficiency measurement for various reflectivity output couplers.

A series of output couplers were fitted in position M3 and the slope efficiency measured. The best performing output coupler was determined to be the 80 % reflectivity coupler, in good agreement with the modelled results from earlier. Fig. 3.18 shows the performance. The slope efficiency of the 80%R output coupler was measured to be 0.35.

A Findlay-Clay analysis was then performed to calculate the cavity losses to compare to the 1064 nm configuration. This is shown in Fig. 3.19

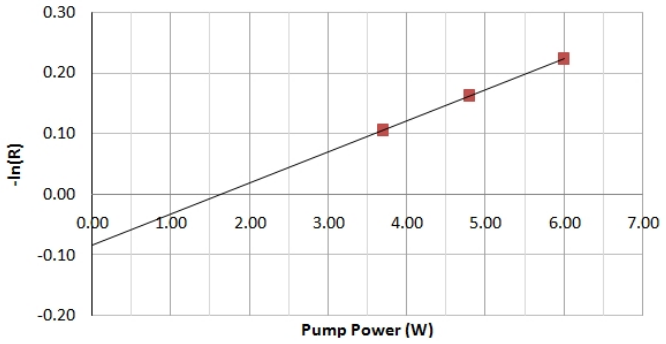

Figure 3.19 – Findlay-Clay analysis of 1342 nm cavity.

The FCA shows the losses of the cavity were measured to be 8%, slightly higher than the 6.5% measured for the 1064 nm VBG cavity. Cavity losses other than those attributed to the VBG will also contribute to this value. Losses from AR coatings and optical surfaces may be larger for the 1342 nm case than for the 1064 nm cavity. As a result, it cannot be determined that the VBG losses are larger in this case. It is clear from all the measurements of the cavity losses that the inclusion of a VBG as a cavity mirror does induce higher cavity losses.

The M^2 of the laser was then measured using the 80%R coupler. The far field profile of the laser is also shown in Fig. 3.20b.

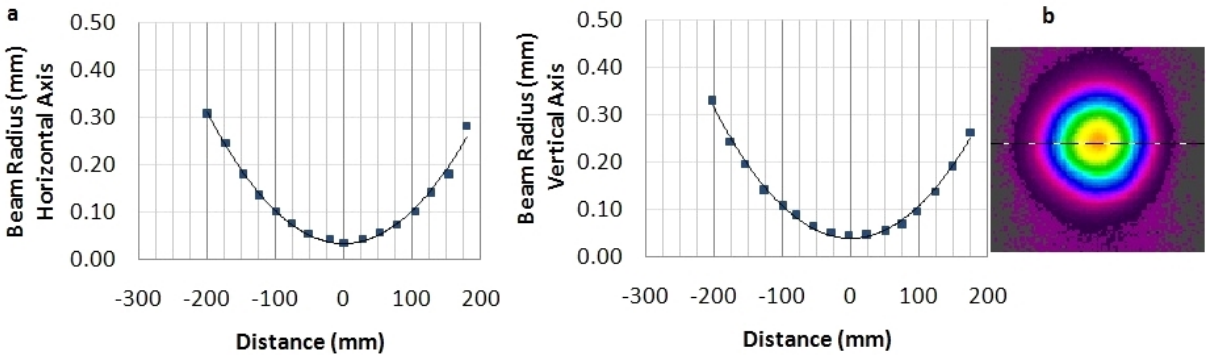

Figure 3.20 – a: M^2 of laser. b: Far field image.

The M^2 of the 1342 nm laser was measured to be 1.13 in the horizontal and 1.21 in the vertical. In a similar manner to the 1064 nm cavity, the 1342 nm VBG cavity is capable of providing a near diffraction limited beam.

The linewidth of the laser was measured using the interferogram technique described previously. The finesse of the etalon at 1342 nm is only 6, reducing the minimum measurable bandwidth to 8 pm. Fig. 3.21a shows the interferogram result for 3.8 W of output power using the 80% coupler. Fig. 3.21b shows a comparison of the bandwidth of the laser for each output coupler.

At the highest output power of 3.8 W, a linewidth of 46.5 pm was measured. Very limited difference in the measured linewidth was observed for different values of output coupling reflectivity. This suggests that the linewidth is strongly controlled by the grating's spectral response rather than any other broadening effects.

3.3.3 Discussion

In the first part of this chapter the performance of a VBG cavity was compared to that of a standard mirror cavity to show the ability to operate at higher average

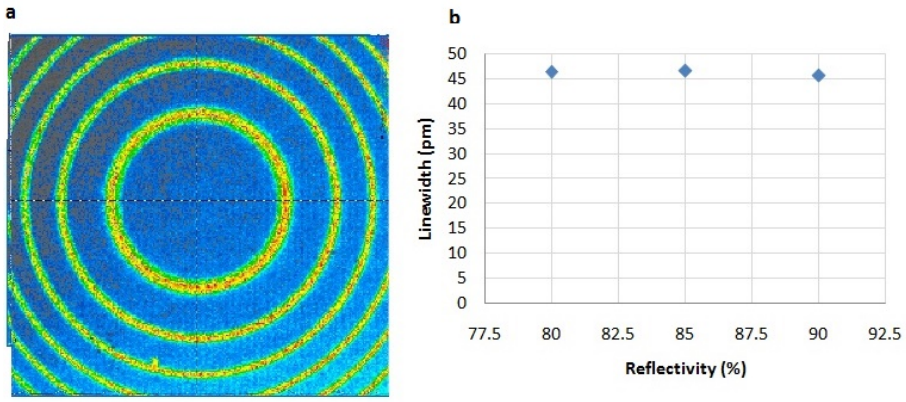

Figure 3.21 – a: Interferogram for 1342 nm laser at 3.8 W output power. b: Measured linewidth at various output coupler reflectivities.

powers than previously demonstrated. The VBG cavity demonstrated up to 6.8 W of output power without any degradation in other parameters such as beam quality. This represents the highest power achieved at this wavelength within a VBG solid state laser configuration, operating with an M^2 of 1.1. It has been shown through experimental results, that VBGs can provide an alternative to standard dichroic mirrors. The ability of the VBG to dramatically reduce the linewidth of the laser without any impact on the overall performance has also been demonstrated. The linewidth was reduced from 1.25 nm to 73 pm as a result of the VBG. The narrow linewidth, whilst not single longitudinal mode operation, can improve other processes such as second harmonic generation, this is investigated in chapter 6. In chapter 5, the ability of a VBG cavity to achieve single longitudinal mode by further narrowing the cavities spectral response is also investigated.

The ability to allow lasers to operate efficiently on a weaker emission line has also been demonstrated. The section highlights the ability of the VBG to scale to higher power than has previously been demonstrated in an end-pumped solid-state laser configuration at 1342 nm. The laser in this configuration was able to generate 3.8 W with an M^2 of 1.2 and a linewidth of 47 pm.

In both configurations, a linewidth that is narrower than the actual VBGs spectral response is observed. As discussed previously, the VBG reflectivity reduces as the wavelength moves away from the VBG centre wavelength. Whilst the grating bandwidth in the case of the 1342 nm VBG is 250 pm, this bandwidth represents the FWHM spectral response. It is unlikely that a longitudinal mode at the half maximum point, where the VBG reflectivity is 50%, would be able to achieve threshold. As the wavelength moves closer to the centre point, the likelihood of a laser mode achieving threshold increases. The limitation of operating on only a single mode will be spatial

hole burning, once enough modes can experience gain to sufficiently extract from all the node points in the crystal, a small change in reflectivity will be sufficient to prevent the lasing of modes. For the 1064 nm VBG, a 3% reduction in the reflectivity appears to be sufficient to prevent any subsequent modes from achieving oscillation. For the 1342 nm VBG only a 0.5% drop in reflectivity is sufficient to attenuate other modes. The variation in the different levels of cavity losses required to narrow the bandwidth is expected due to the different emission cross-sections of each emission line. The smaller emission cross-section is more sensitive to losses due to the reduced extraction of gain.

3.3.4 Conclusion

The ability to operate an Nd:YVO_4 laser in a cavity containing a VBG instead of an all mirror cavity has been investigated in this chapter. The results have shown the VBGs provide similar performance in terms of efficiency to that of a mirror cavity. The output powers were scaled to 6.8 W at 1064 nm highlighting the ability of the VBGs to operate with relatively high intra-cavity powers. The cavity losses were found to increase by 2% when changing from the mirror cavity to the VBG cavity. However, the inclusion of the VBG was found to have no effect on the beam quality. The VBGs have also been used to operate a Nd:YVO_4 laser on the weaker 1342 nm emission line. Output powers as high as 3.8 W were achieved. At both emission wavelengths, narrow linewidths of 73 pm and 47 pm for the 1064 nm and 1342 nm emission lines respectively were achieved.

Chapter 4

Thermal Effects of VBGs Operating in Laser Cavities

4.1 Introduction

In this chapter the model from chapter 2 section 2.3 is used to predict how VBGs behave when high peak powers are incident. The VBG cavity performance is also experimentally characterized under high thermal loads. The modelling and experimental results allow for the determination of the maximum intensity a VBG can withstand, whilst maintaining its spectral performance. Any degradation in the spectral parameters will lead to a reduction in the resonator performance. The goal of this chapter is therefore to determine the maximum power density a VBG can withstand in an end-pumped configuration similar to that introduced in chapter 3. In the next chapter single longitudinal mode operation is investigated. For SLM operation an unperturbed grating is required to operate on a narrow linewidth. To achieve the effect the absorption of the cavity radiation in the VBG has on the grating properties must be understood.

As highlighted in chapter 2, thermal effects within VBGs have been characterised in a number of different setups [78] [85] [87]. The different testing configurations have shown the changes in the reflectivity, linewidth and wavefront error that arise as a result of thermal distortions. These configurations have characterised the VBG with an external source. More recently the thermal effects from VBGs within a laser cavity generating up to 2 W at 1029 nm have been analysed [86]. In this chapter we investigate the effects of the VBG when used as a cavity mirror at output powers up to 6 W at both 1064 nm and 1342 nm. The thermal behaviour of the VBG is now coupled to the cavity dynamics and will directly impact on the intensity incident on the VBG. The impact on the beam profile as well as the cavity linewidth is presented.

The performance of the VBG is first investigated using the model developed in

chapter 2 section 2.3. By modelling the typical parameters used in previous chapter, the point at which thermal effects occur can be determined. Two different configurations are then investigated. The initial configuration investigates the effects of the heat build-up within the VBG by purposely inducing thermal effects. A second configuration investigates the practicalities of the VBG configuration in a setup identical to that in chapter 3 Fig. 3.1. This allows us to determine the maximum operating conditions for a given VBG setup.

4.2 Thermal Modelling of VBG with Incident Laser Intensity

Using the Runge Kutta VBG model, the performance of the VBG in terms of reflectivity, centre wavelength and linewidth can be calculated. The spectral performance of the VBG under various loads is first investigated. The absorption coefficient of the incident light in the VBG has been reported to be in the region of $0.01\,\mathrm{cm}^{-1}$ [78] at 1064 nm. The effect of changes in incident power on a 1064 nm VBG with the same specification as that shown in chapter 3 section 3.2.3 is modelled in this section. Fig. 4.1 shows the spectral performance of the VBG under varying incident powers. The incident power levels represent those typically expected from a configuration identical to that in chapter 3 section 3.2 with varying levels of cavity reflectivity and an incident spot diameter of 300 μm. The incident power refers to one way incident intensity on the VBG.

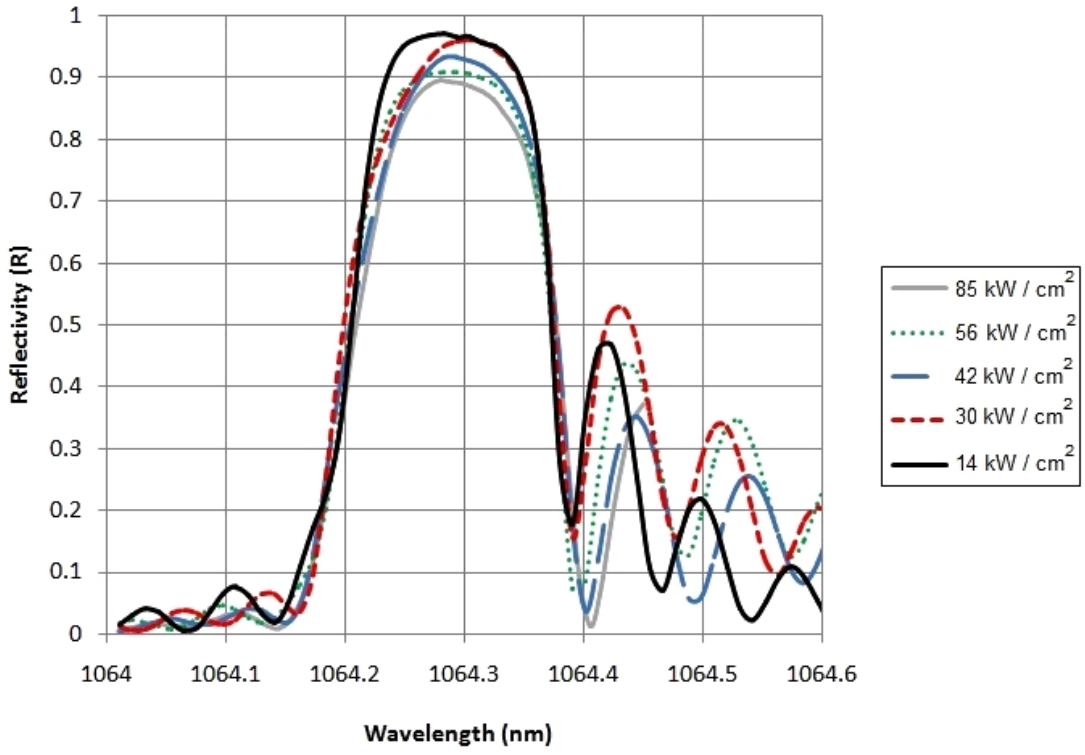

Figure 4.1 – Modelled VBG spectral reflectivity at various incident intensities.

Fig. 4.1 shows the expected performance of the VBG at various incident powers. From this, the main peak of VBGs spectral performance can be seen to narrow and the peak reflectivity reduce, as the incident intensity increases. The reflectivity of the side lobes also increase at higher intensities. A change in all three of the parameters discussed previously is observed. Each parameter is briefly investigated to quantify the effect on the VBG performance.

In Fig. 4.1 the peak reflectivity is reduced as the incident power is increased. With an incident optical power of 85 kW/cm^2, the VBG reflectivity has decreased to 89%. This compares to the 14 kW/cm^2 case in which only a 1.5% reduction is observed. Fig. 4.2a shows a plot the peak reflectivity of the VBG as a function of the incident intensity on the grating. The actual grating reflectivity reduces as soon as a thermal load is incident on the VBG.

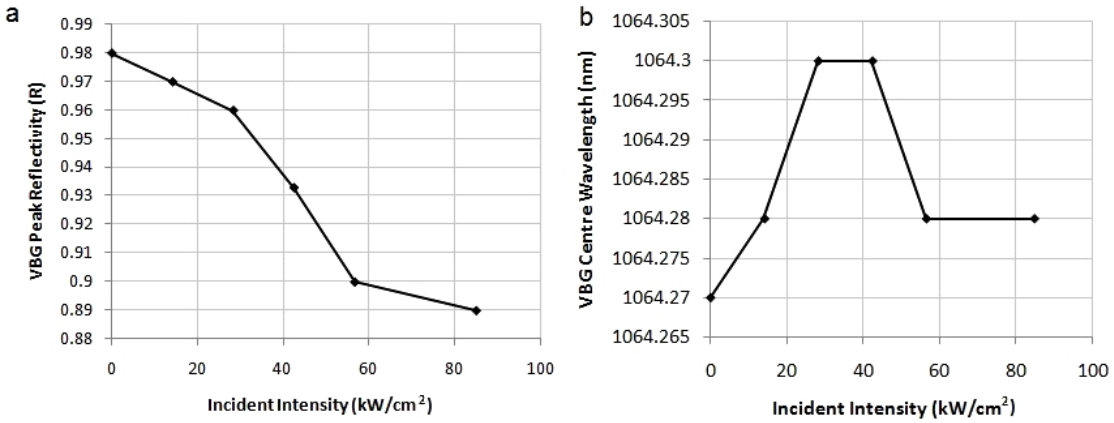

Figure 4.2 – a: Modelled VBG reflectivity at various incident intensities. b: Modelled centre wavelength at various incident intensities.

When considering only the smallest load modelled, the 14 kW/cm^2 case, a reduction in the VBG reflectivity is still observed. From the modelled results, the use of a VBG in high intra-cavity intensity applications would be difficult to implement. The actual load represents only a 10 W source in a 300 μm spot diameter, which for an intra-cavity power, is fairly small. To limit the overall reduction in reflectivity to less than 1%, the intra-cavity intensity should be reduced to less than 10 kW/cm^2. The thermal performance will therefore have implications on low emission cross-section setups where high intra-cavity intensities are required to extract the gain. However, a setup that operates with an increased spot size on the VBGs could allow for this.

The variation in the centre wavelength, taken in this case to be the peak of the reflectivity curve, was also investigated. Fig. 4.1 also shows a red shift in the centre wavelength of the VBG as the thermal load increases. The increase in operating wavelength could limit the thermal tuning capability of the VBG. The red shift in

centre wavelength could be counteracted simply by temperature tuning. This may add cost and complexity however. Fig. 4.2b shows the centre wavelength variation with increasing intensity.

The tuning rate also varies as the incident power is increased. Initially, a linear tuning rate is observed, with the VBG centre wavelength increasing by 0.03 nm from the unloaded case to the 28 kW/cm^2 case. Beyond this, the centre wavelength actually decreases slightly. This behaviour can also be seen in Fig. 4.1. The actual tuning of the centre wavelength stops as the secondary peaks in the spectral response begin to rise. The secondary peaks also exhibit a centre wavelength shift as the thermal load is increased.

The final parameter modelled is the change in the linewidth. In chapter 5 single longitudinal mode operation is investigated, for which the VBG linewidth is a clearly a key parameter. In chapter 6 the performance gains from second harmonic generation as a result of a line-narrowed configuration is demonstrated, which again relies on the VBG linewidth. Any increase in the linewidth would have an adverse affect on these configurations. As a result, the operating parameters should be optimized to limit any variation in the VBGs spectral response. Fig. 4.3 shows the FWHM spectral linewidth as the incident pump power is increased.

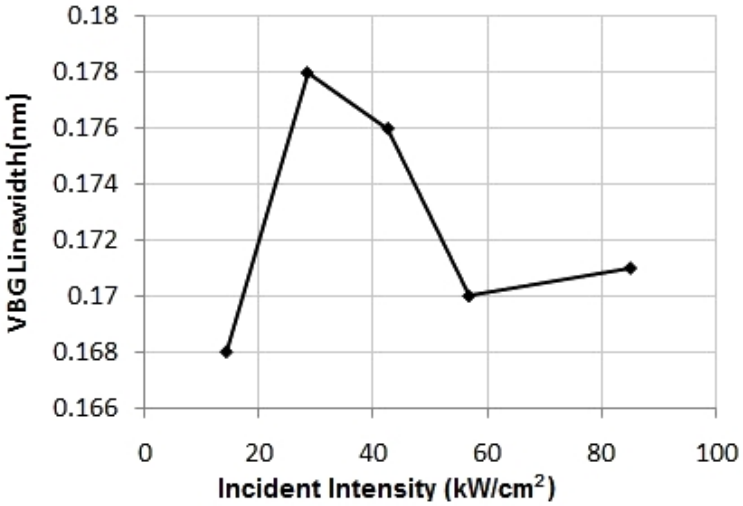

Figure 4.3 – Modelled spectral linewidth of VBG at various intensities.

The linewidth shows similar behaviour to the temperature tuning effect. An initial increase in the VBG linewidth is observed from 14-28 kW/cm^2. As intensity increases further, the linewidth actually decreases. The effect of the shift towards the secondary peak appears to narrow the linewidth of the main peak. This result is interesting as it suggests the linewidth will decrease with larger intensities, possibly aiding narrow

linewidth operation of the laser. Narrow linewidth operation may be more difficult to achieve however due to the rise of the secondary peaks within the VBG. As the pump power is further increased, the secondary reflectivity peak may rise to the point where it becomes possible for a mode to operate on this emission line.

The modelling has shown how the performance of the VBG degrades under higher thermal loads. At the maximum incident power, the reflectivity of the VBG was found to reduce to 87% whilst the centre wavelength increases by 0.03 nm over the modelled range. The linewidth of the VBG also increased by 10% over the modelled range.

Up until this point only the axial performance of the VBG at the centre of the grating has been considered. The model predicts the resultant performance of the VBG from a heat source that is distributed into the grating, in the same direction as the beam. The actual diffusion of the heat into the edges of the grating, and the Gaussian nature of the heat load, will create a 3 dimensional heat profile, as shown in chapter 2 section 2.4.1. The resultant heat load will create a variation in the reflectivity and centre wavelength over the surface of the VBG. Fig. 4.4 shows a 2D plot of the reflectivity of the VBG for an incident intensity of 87 kW/cm^2. The spatial profile of the VBG reflectivity is constructed by propagating a series of discrete plane waves in a grid.

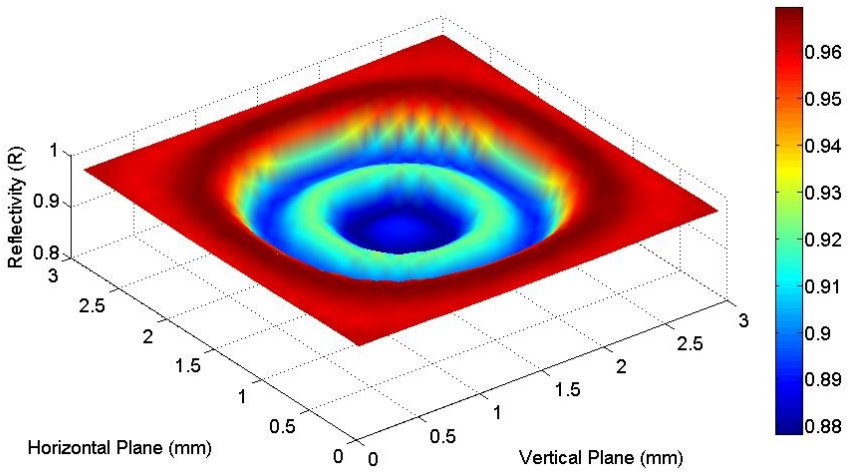

Figure 4.4 – Spatial reflectivity of VBG.

It can be seen from Fig. 4.4, at a fixed centre wavelength significant change in the reflectivity of the VBG is observed. Whilst the reflectivity reduces to 87% at the centre of the VBG, the outer edges have a reflectivity of 99%. The spatial reflectivity performance of the VBG could lead to the excitation of higher-order modes by providing a higher reflection coefficient to modes incident on the edges of the VBG. By limiting the incident power, the variation in the reflectivity over the surface of the

VBG could be limited.

The limitation of this modelling method is the assumption of a plane wave through VBG. Whilst the cavity is in the stable region of the stability criterion, the plane wave assumption is valid as the wavefront must be flat at the VBG surface. If however, due to the nature of the variable VBG reflectivity, the cavity becomes unstable, the plane wave assumption may not be valid. To accurately model the reflection of a wave with varying intensity and phase distributions, the plane wave assumption can still be used. However, the decomposition of the incident beam into a series of plane waves with varying angular components must be performed. The reflectivity of finite intensity distributions has been presented previously in this manner by Hellstrom *et al.* [73].

4.3 Experimental Thermally Induced VBG Behaviour

In the previous section the expected behaviour of the VBG under high incident intensities has been modelled. It has been shown that the residual absorption of the intra-cavity intensity should significantly degrade the performance of the VBG. Initially, a cavity that should suffer from these effects is configured to experimentally confirm the behaviour of the modelled VBG. When using the VBG as a cavity mirror, the intra-cavity intensity is much higher than the actual output power of the laser. The level of incident power is therefore much higher than previous investigations, which used an external probe source [78]. The performance of the grating within a laser cavity, with high intensities incident on the VBG, is therefore investigated.

To achieve the high incident intensities, the 3 mirror thermal lens stabilised 1064 nm cavity introduced in chapter 3 was used. The cavity length was increased to 58 cm to reduce the spot size on the VBG to a 200 μm diameter. The increased cavity length should still ensure the pump beam is matched to the fundamental cavity mode. The pump radius was 400 μm, the same as the 1064 nm configuration in chapter 3 section 3.2. Initially, a 1064 nm high reflectivity mirror was used in combination with the VBG. By operating the cavity without an output coupler, the intra-cavity intensity will be significantly higher. To further increase the thermal effects in the VBG, the heat sinking shown in chapter 2 Fig. 2.4a was removed and the VBG mounted on a thermally isolated mount. The motivation for doing this was to allow for the external temperature to be measured using a thermal imaging camera and to observe the thermal effects within the grating. A thermal image of the VBG was taken whilst lasing to illustrate the temperature rise in the VBG. Fig. 4.5 shows the thermal image with a side view of the VBG glued onto an optical mount. The thermal image has some artefacts in the VBG that are a function of the thermal camera rather than the

temperature distribution in the VBG.

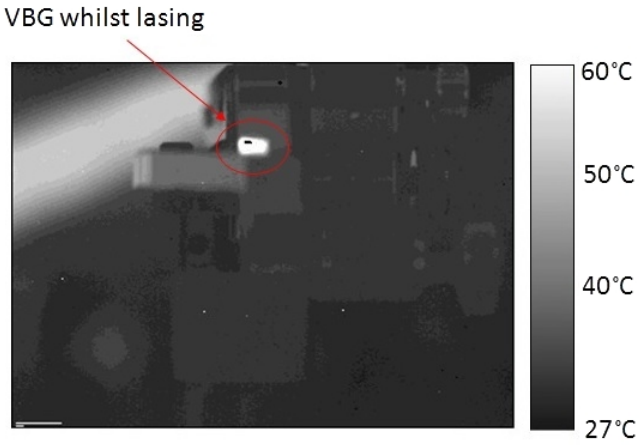

Figure 4.5 – Thermal image of VBG whilst lasing.

Fig. 4.5 shows how the edges of the VBG reach a maximum of 60 °C, with an ambient of 27 °C. Due to the limited resolution of the camera, the actual peak temperature of the VBG cannot be determined, only the temperature at the edges. It is expected that the temperature rise at the centre will be much larger. It is clear from this image that residual absorption causes an increase in the overall temperature of the device.

The performance of the VBG with the limited thermal extraction and no output coupler was then compared to an identical cavity with an 80% reflectivity output coupler fitted instead of the VBG. When operating the VBG cavity with no output coupler, the emission was found to leak solely out of the VBG suggesting the reflectivity had decreased. A comparison of the slope efficiencies are shown in Fig. 4.6 where the output power from the VBG cavity was measured solely from that exiting from the grating.

The mirror cavity performance was similar to that detailed in chapter 3. When comparing the VBG cavity to the mirror cavity, at pump powers above 12.5 W a similar slope efficiency is observed. The performance suggests the reflectivity of the VBG is close to 80% at this operating point. From the previous chapter, the optimum coupling for the cavity is 80%, the VBG has therefore tuned close to the optimum coupling for the cavity. At lower powers however, the slope efficiency appears to vary. A variation in the slope efficiency would be expected if the reflectivity of the VBG was changing as the pump power is increased.

The characteristics of the beam were also investigated. Fig. 4.7 shows a comparison of the beams exiting the output coupler in the mirror cavity and VBG cavity. The camera was placed 15 cm away from the cavity output coupler.

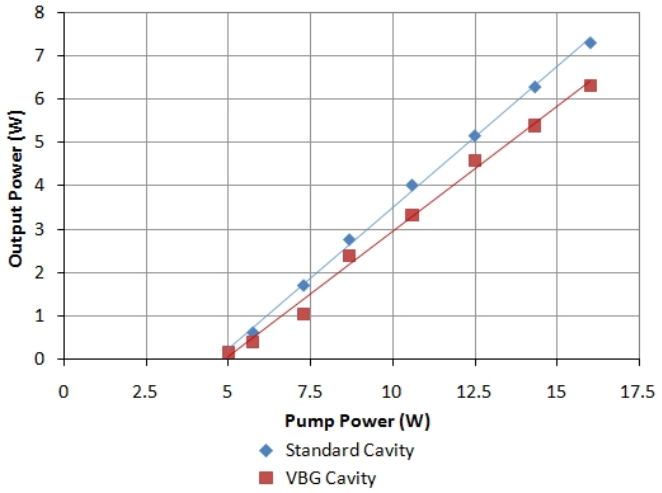

Figure 4.6 – Comparison of slope efficiency measurement of mirror cavity and VBG cavity.

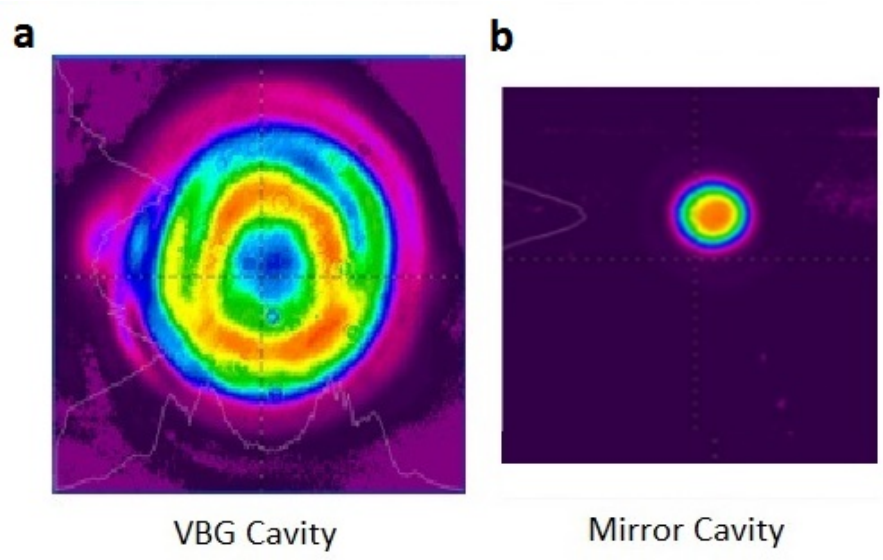

Figure 4.7 – a. VBG cavity beam profile. b. Mirror cavity beam profile.

Fig. 4.7a shows the degradation in the beam profile as a result of a worst case thermal load within the VBG cavity. The doughnut mode, which appeared within the first 10 seconds of operation of the VBG cavity, is significantly different to the mirror cavity profile shown in Fig. 4.7b. Both beam profiles are shown on the same scale with the size of the VBG beam significantly larger than for the mirror cavity. The mirror cavity mode size was measured as 0.9 mm compared with 3 mm for the VBG cavity.

In the previous chapter, no degradation in the beam parameters were observed for the VBG cavity when compared to that of the mirror cavity. In an end-pumped plane-plane mirror cavity, strong modal selection occurs as a result of mode matching the focused spot of the pump beam to that of the cavity mode. Small variations in

the curvature of the end mirror will not strongly affect the cavity mode. In this configuration, however, the mode matching is clearly not sufficient to maintain operation on the lowest order mode.

This behaviour may be a result of either the varying spatial reflectivity of the VBG, as shown in the section 4.2, or a thermal lens within the grating affecting the mode size. We can probe the VBG under these lasing conditions using a probe beam to observe any optical power within the VBG. Fig. 4.8a shows the experimental setup. A helium-neon laser operating at 633 nm was used to probe the grating. After passing through the VBG, the probe beam was focused using a 1 m mirror. The beam profiler was placed at the focal plane of the 1 m mirror. Any changes in the focal power of the VBG will lead to a large change in the spot size observed on the beam profiler. For example, only a 1 m thermal lens focal length would see the probe beam diameter expand by a factor of 4. The probe beam will only measure the induced refractive index variation across the VBG. It will not be affected by any changes in the VBG grating vector.

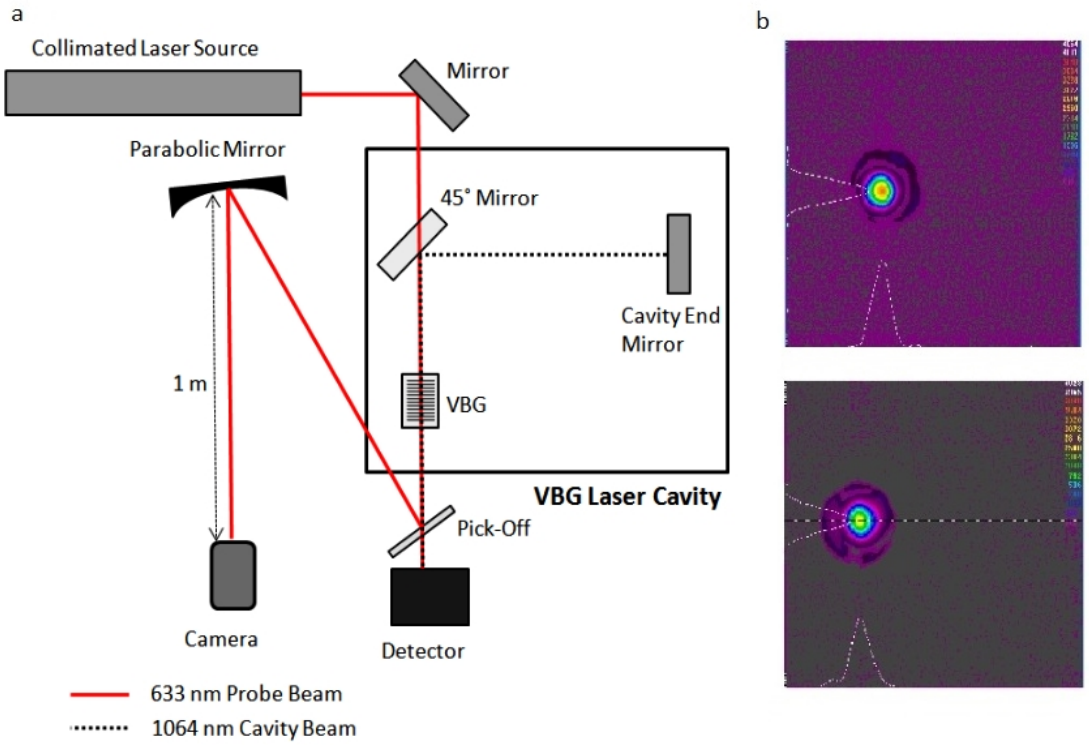

Figure 4.8 – a: External probe beam measurement configuration. b: Probe beam under non-lasing conditions. c: Probe beam under lasing conditions.

Figs 4.8b and c show the probe beam under non-lasing and lasing conditions. There are two noticeable effects. The first is the change in the location of the beam under lasing conditions. This suggests an angular component is present when the cavity intensity is incident on the VBG. The wedging of the probe beam will be caused by

the heat flow within the VBG. The VBG is mounted and therefore cooled from one surface. Whilst the mounting surface was thermally isolating, some heat extraction will still occur, the subsequent thermal gradient will cause a wedging effect in the probe beam. The second effect observed is a change in the probe beam diameter. In the non-lasing condition the beam diameter is 1 mm giving a divergence of 1 mrad. In the lasing case, the probe beam is smaller with a diameter of 950 μm. The behaviour suggest a small change in the focal power of the VBG under the lasing conditions. The magnitude of the thermal lens strength however would not cause the degradation observed in the VBG profile. The cause of this is therefore due to spatial changes in the grating periodicity.

The variation in the reflectivity and centre wavelength will change the overall mode profile within the laser. In Fig. 4.7a the diameter of the centre hole is 1mm, similar to the actual mode size of the mirror cavity beam. The decrease in the reflectivity at the centre of the VBG may allow for modes towards the outer diameter to extract gain better than the those at the centre. The modelling has shown previously that each point in the VBG will have a different spectral response and centre wavelength. The resultant beam profile may be a result of both a variable reflectivity for a given mode and spectral selection of higher order modes. Qualitatively there is good agreement between the modelled spatial reflectivity of the VBG in Fig. 4.4 and the actual beam profile from the cavity shown in Fig. 4.7a. In order to confirm that the beam profile is caused by this effect, a full Fox-Li [40] analysis would be required allowing for the calculation of the mode profile within the cavity.

The worst case thermal loading experiment has shown both a change in the reflectivity of the VBG and a significant variation in the beam profile. These results are different to those presented in chapter 3. The results also show that the expected behaviour predicted in section 4.2 does occur in a worst case scenario. The setup is not representative of most laser systems however due to the omission of an output coupler and the lack of any thermal extraction from the VBG. In the next section the behaviour of a VBG with both an output coupler and thermal extraction is investigated as well as the coupled nature of the heat source and VBG performance. The intra-cavity intensities are still similar to those modelled in the first section.

4.4 1342 nm VBG Resonator Testing

The aim of this section is to highlight the coupled nature of the VBG reflectivity and intra-cavity intensity, and determine the thermal effects present within a VBG that is sufficiently cooled. The coupled nature of the cavity intensity and VBG reflectivity

should lead to a reduction in the intra-cavity intensity, potentially limiting future setups. The thermal response of the VBG configuration, including the heat flow out of the VBG, is now a factor in its spectral response. This section therefore looks to determine the maximum intra-cavity intensity allowed before thermal effects degrade the VBG performance in terms of cavity linewidth and VBG reflectivity. The following investigation was completed at an operating wavelength of 1342 nm. This differs from the previous setup which operated at 1064 nm. The motivation for operating at this wavelength was to allow for the VBG effects to be characterised, in preparation for the SLM operation detailed in the next chapter. The effects shown in section 4.2 will still be observed at 1342 nm as the effective heat loads, and therefore grating expansion, will be similar. The residual absorption in the VBG is similar from 1064 nm up to 1575 nm [103]. The aim of this section is to determine where the effects predicted in section 4.2 will occur in the 1342 nm cavity, not to numerically validate the results.

The 3 mirror cavity described in chapter 3, operating on the 1342 nm emission line, was used for this investigation. The smaller cavity length and mode size compared to the 1064 nm cavity in chapter 3 section 3.2 also allows for better variation of the incident intensities. The cavity length was 17 cm and the cavity mode diameter at the VBG surface was 350 μm. The VBG was cooled in the manner shown in chapter 2 Fig. 2.4a and unlike the previous setup, output couplers were used in this cavity. To introduce the thermal effects predicted, 3 different output couplers with reflectivity's of 90, 95 and 97% were used. The modelled intra-cavity intensity at a fixed pump level of 16 W is shown in Fig. 4.9. Fig. 4.9 shows the modelled intra-cavity power as a function of cavity reflectivity. The expected operating point for each output coupler is marked in black on the graph. For the range of output couplers used, the intra-cavity intensity is in the region 37 - 65 kW/cm^2. The modelling completed previously shows the predicted thermal load on the VBG should lead to a degradation in the VBGs performance.

Using the 3 mirror 1342 nm cavity from chapter 3 section 3.3.2 with the output couplers stated, the output power was measured from both the VBG and the output coupler. In each case the measurement was taken after 3 minutes of operation to ensure a steady state scenario. Fig. 4.10a shows the total output power for the 90%, 95% and 97% reflectivity couplers. The cavities will be referred as 90%R, 95%R and 97%R from this point on. Fig. 4.10b shows the output power exiting from the VBG only.

From Fig. 4.10a, the slope efficiency of all the cavities at pump powers above 15 W are similar, despite the variation in cavity reflectivity. The slope efficiency of the 97%R cavity is 0.197 compared with 0.247 for the 90%R cavity. It would be expected that the slope efficiency of the 97%R cavity would be significantly reduced compared to the

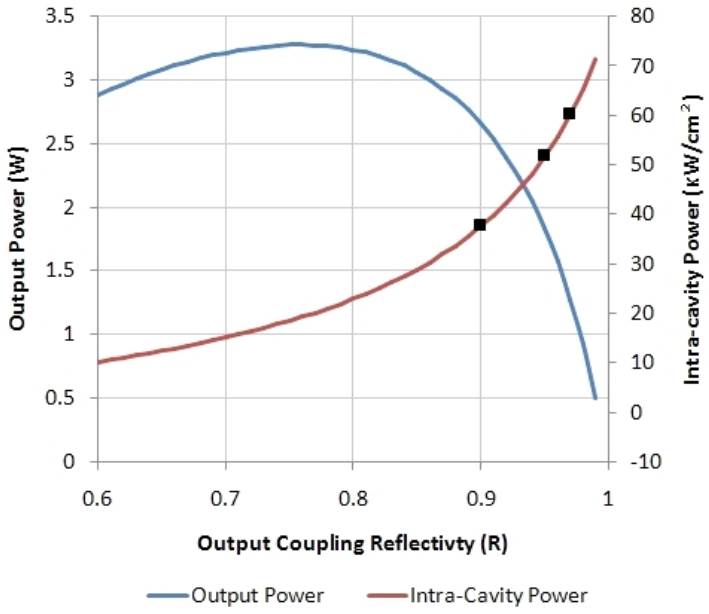

Figure 4.9 – Modelled output power and intra-cavity power vs. output coupling for 1342 nm VBG laser, different output couplers used in investigation are shown in black.

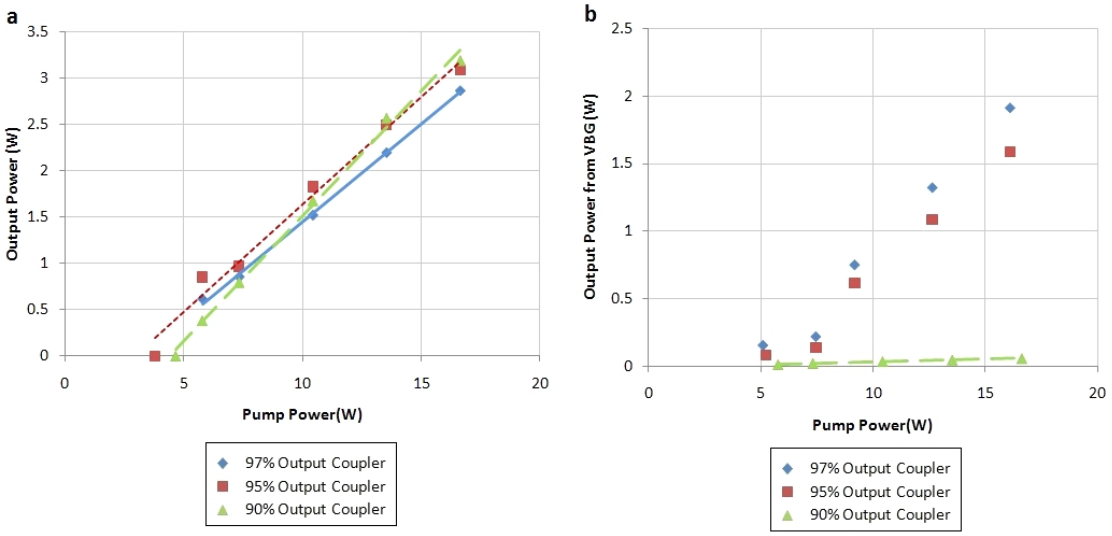

Figure 4.10 – a: Slope efficiency measurement of VBG cavities. b: Output power from VBG.

90%R cavity. Fig. 4.10b shows the amount of power leaking from the VBG. As the reflectivity of the output coupler increases, an increase in the amount of light exiting the VBG is observed. This suggests the VBG reflectivity changes with the intra-cavity intensity.

Fig. 4.11a and b shows the calculated reduction in the VBG reflectivity as a function of the intra-cavity power and the total coupling of the cavity. The effective VBG reflectivity was calculated from the output power exiting from the output coupler. This approximation assumes a mean intensity field within the resonator [8].

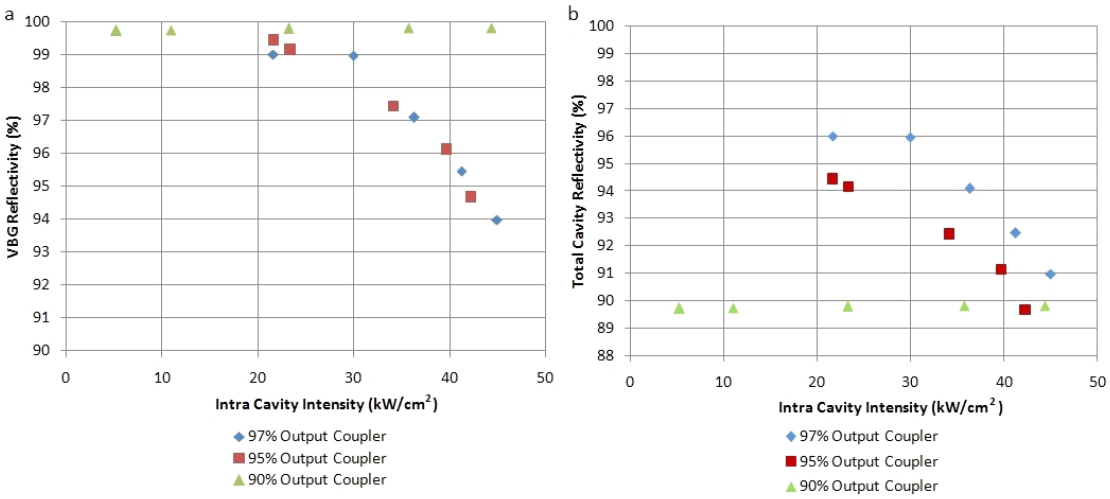

Figure 4.11 – a: VBG reflectivity as a function of intra-cavity intensity. b: Total cavity reflectivity as a function on intra-cavity intensity.

In the 95%R and 97%R cases in Fig. 4.11a a similar trend is observed for the reduction in reflectivity as the intra-cavity intensity is increased. In the worst case the reflectivity of the VBG reduces to 94%. The behaviour of the 97%R and 95%R cavities is very similar to that predicted in Fig. 4.2, although the actual modelled centre wavelengths are different for this setup. The VBG reflectivity in the 90% coupled cavity does not change at all however. In Fig. 4.11b, at the peak intra-cavity intensity, similar cavity reflectivities are observed for all the configurations, despite each configuration having a different reflectivity output coupler.

For the two different couplers which induce the thermal loads, each VBG has reduced by a different amount to achieve a similar intra-cavity intensity. This is in contrast to the 90%R coupled case in which the VBG reflectivity has not decreased at all.

The modelling has shown previously a change in the reflectivity is caused by an increase in the intra-cavity intensity. In this scenario we now have 3 different VBG reflectivities for a given intra-cavity intensity. This behaviour suggests the reflectivity of the VBG is being clamped by the cavity. This is due to the coupled nature of the VBG reflectivity and the intra-cavity intensity. Fig. 4.12 shows the change in one-way intra-cavity intensity as a function of pump power. In the 90%R coupled case there is a linear relationship with intra-cavity intensity, as expected. Both the 95 and 97% coupled cases exhibit a nonlinear relationship, with the intra-cavity intensity rolling off at higher intensities.

The external temperature rise of VBG was also measured to determine if the

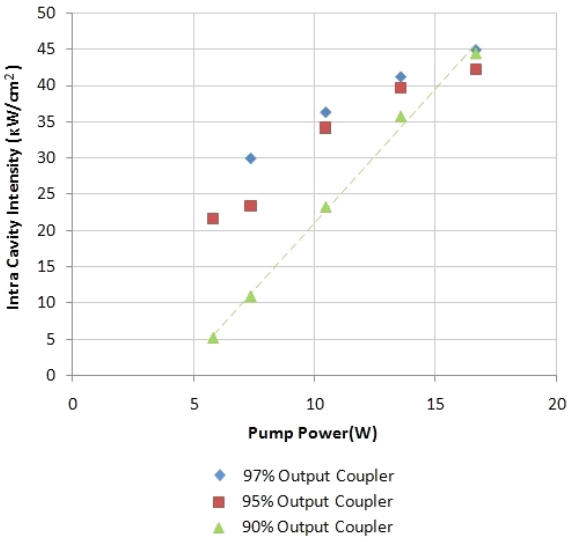

Figure 4.12 – One-way intra-cavity intensity as a function of pump power for various output couplers.

deformed VBGs also exhibit a larger temperature increase. The VBG temperature was measured at the base of heat sink placed on top of the VBG. For the VBGs reflectivity to vary, a change in the heat diffused from the grating should be present. The external temperature rise is shown in Fig. 4.13a.

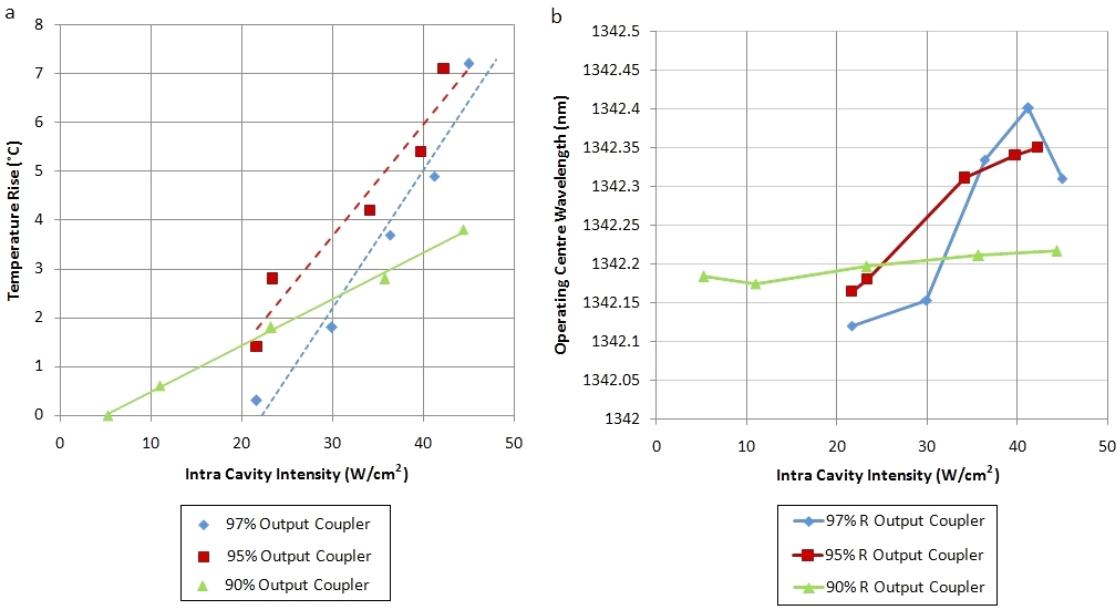

Figure 4.13 – a: VBG temperature rise as a function of intra-cavity intensity. b: Operational centre wavelength of cavity

From Fig. 4.13 the higher coupled cavities have a much steeper temperature rise rate than the lower coupled cavity.

Fig. 4.2 has previously shown how the centre wavelength increases as we increase

the thermal effects of the grating. It would therefore be expected that the centre wavelength of the higher coupled cavities to operate at higher wavelength. Fig. 4.13b shows the centre wavelength of the cavity when the VBG was operated at a constant heat sink temperature of 55 °C.

The thermally distorted grating shows an increase in the centre wavelength of 0.25-0.35 nm as the intra-cavity intensity is increased. At intra-cavity intensities above 35 kW/cm^2 there is a change in the rate at which the grating wavelength tunes. The modelling in Fig. 4.1 has previously shown the effect of a thermally distorted grating, where the tuning rate decreases at the higher intensities due the rise of a secondary peak. The results are therefore consistent with this although, the magnitudes are different. Secondary effects such as angle tuning may also be present as wedge effects in the grating may occur as the VBG heats up. The wedging would also affect the cavity centre wavelength.

The final measurement was that of the linewidth of each cavity. The modelling has shown an initial increase in the linewidth should occur when operating the VBG under high thermal loads.

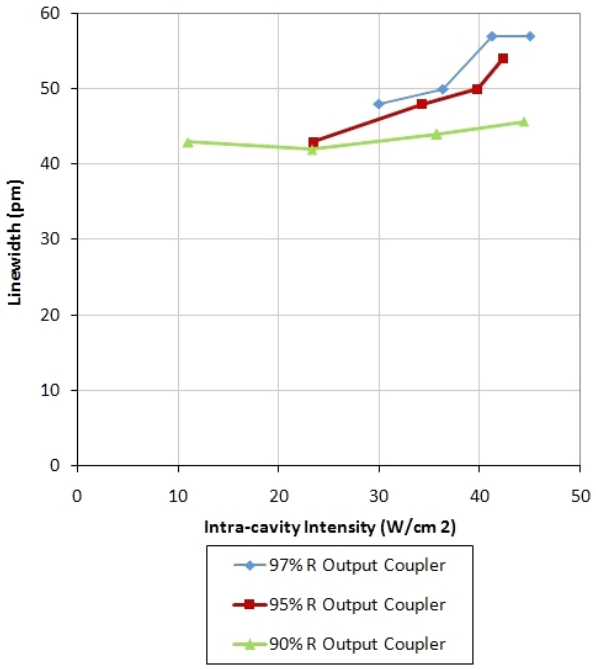

Figure 4.14 – Cavity linewidth at increasing intra-cavity intensity.

Fig. 4.14 shows the linewidth variation as the intra-cavity intensity is increased. For the higher coupled cavities an increase in the linewidth of the VBG is observed, for the 90% coupled cavity there is a limited increase. The performance is similar to that modelled previously in Fig. 4.3. The roll-off predicted at the higher intensities is

also consistent with the measured results.

4.5 Discussion

The measured results shown in section 4.4 are consistent with expected effects predicted in 4.2. Future analysis will allow for more accurate modelling of the 1342 nm grating parameters to exactly correlate the performance. The overall effects will be comparable as thermal load from the intensity profile within the VBGs will be similar.

One of the parameters of the performance that was not discussed in the previous section was the differing reflectivities of the VBGs in the 95%R and 97%R cavities compared to the 90% R cavity, despite the presence of similar thermal loads. In the 95%R and 97%R cases, with the steady state intra-cavity intensity at 40 kW/cm^2, the reflectivity of each VBG has reduced under the presence of a thermal load. The reflectivity of each VBG is $\approx 94\%$; for the same intra-cavity intensity the 90%R cavity VBG is undistorted and the VBG reflectivity is 99%.

This behaviour is due to both the thermal impedance of the VBG and the coupled nature of the intra-cavity intensity to the VBG reflectivity. The two are coupled as the intra-cavity intensity is a function of the VBG reflectivity. The VBG reflectivity is also a function of the thermal load in the grating, which is a result of the intra-cavity intensity. The intensity will reduce as the VBG distorts. The VBG reflectivity will subsequently reduce, until the two reach a steady state condition.

To explain the varying reflectivity behaviour, the heat sources are analysed. Despite similar intra-cavity intensities at steady state, the cumulative heat source in the 95%R and 97%R coupled cases will be larger than the 90%R case. At the initial starting condition, where the VBG is undistorted, the intra-cavity intensity for the 95%R and 97%R cavities will be larger. This will cause the VBG to deform. The thermal impedance of the VBG will therefore lead to a larger temperature rise in the 95%R and 97%R cavities compared to the 90%R case, reducing the grating reflectivity. Depending on the magnitude of the thermal impedance, the level of cumulative heat stored in the VBG will vary.

The definition of steady state operation suggest that at 40 kW/cm^2 of intra-cavity intensity, the rate at which the VBG diffuses heat is equal to the heat source. This trend can be seen in Fig. 4.12 where the intra-cavity intensities start to level off for the 97%R and 95%R cavities, despite the increase in pump power. If the intra-

cavity intensity was increased further and the diffusion of heat is fixed, the VBG temperature would rise, its reflectivity would then reduce, reducing the intra-cavity intensity and steady state would be maintained. The steady state operation of the other couplers suggest that the heat load is starting to reach equilibrium close to 40 kW/cm^2, with similar cavity reflectivities observed for all cases. At intensities slightly above 40 kW/cm^2, it would be expected that the 90%R cavity VBG would deform.

As a result of its thermal impedance, the VBG is therefore an optical limiter within the cavity, adjusting its reflectivity when higher intra-cavity intensities are present to maintain a lower overall intra-cavity steady state level. If the thermal impedance could be adjusted, the level of intra-cavity intensity could be controlled.

Further modelling could be completed to determine the thermal response of the VBG to the intra-cavity intensity. One of the challenges is the absorption co-efficient of the VBG, which varies by an order of magnitude in the literature [86] [103]. Furthermore, the practicalities of accurately modelling the heat sinking of the VBG is often difficult due the variable nature of the thermal interfaces.

To fully model the performance, a fully integrated simulation using all the models presented in the previous chapters, coupled together, would be required. This would also allow for the transient behaviour of the VBG to be analysed. Using this analysis, the steady state operation of the VBG could be found and should predict the intra-cavity behaviour observed here. The model would start with the initial output coupling of the cavity and calculate the intra-cavity intensity. The deformed grating reflectivity could be calculated from the FEA completed in chapter 2. The model would then update the corresponding reflectivity, calculate the heat load from the intra-cavity intensity and re-update the VBG reflectivity from the thermal model again. A series of iterations would be required to achieve the steady state condition. A similar model has been proposed by Tjornhammar *et al.* [86].

As a result of the characterization of the thermal effects in the 1342 nm VBG, the maximum intra-cavity intensity can be estimated. The modelling completed in section 4.2 suggests that thermal effects should occur from 14 kW/cm^2. From Fig. 4.12, it has been shown that above 40 kW/cm^2, the VBG reflectivity will reduce and the linewidth will increase, degrading the cavity performance. Future cavity designs should therefore look to reduce the intra-cavity intensity incident on the VBG.

4.6 Conclusion

The thermal effects in VBGs have been investigated in this chapter. The initial modelling shows changes in VBG reflectivity, centre wavelength and linewidth will all occur, as a result of high intra-cavity intensities. The effects on the spatial degradation of the VBG have also been shown, with the possibility of a doughnut like reflectivity profile occurring. Two separate test cavities were constructed to investigate these effects. A 1064 nm VBG cavity was constructed with no output coupling. The VBG reflectivity was found to reduce to 80%, whilst the profile of the near field was degraded. A second cavity, operating at 1342 nm was constructed and the thermal effects on the VBG cavity parameters were measured. The reflectivity was found to reduce by up to 4%, with an increase of 0.3 nm in the centre wavelength of the cavity. A 28% increase in the linewidth was also observed.

Chapter 5

Double VBG Laser

5.1 Introduction

Chapter 3 has shown the ability to achieve a narrow linewidth using a single VBG cavity. In order to generate visible light, intra-cavity SHG or SFG will be required. To produce a stable intra-cavity CW second harmonic output, the cavity must operate on either a single mode, or on a large number of modes [104]. This is due to the "green problem", which leads large temporal fluctuations in the second harmonic intensity. The linewidth of the VBG is not sufficient to achieve single longitudinal mode operation in this configuration. To do this, a much narrower spectrum or shorter cavity length is required. This chapter investigates the modelling and characterisation of a double VBG configuration for SLM operation at 1342 nm. The use of a double VBG cavity allows for a large gain medium to be used in a linear cavity, that can operate on a SLM. Typically, SLM cavities are limited to using small active crystals to limit the mode spacing, limiting scalability. The ability to use a large gain medium, and also tune the cavity linewidth by adjustment of the VBG temperature, could allow for much higher powers to be achieved in SLM operation compared to other techniques currently used.

The most straight forward route to operate on a SLM is to use a ring configuration. The increased longitudinal mode spacing and the absence of spatial hole burning allows for SLM to be more readily achieved [105]. A ring configuration does require an increased number of optics and accurate alignment of the retro-reflector to achieve this.

Non-planar rings [8] are a popular route to generate SLM operation, without the requirement for a separate retro-reflector. The non-planar ring cavities are often used for SLM operation due to the short cavity lengths and the ability to force unidirectional operation. Non-planar ring resonators have been demonstrated up to 3.5 W at 1064 nm [106], but scalability of these devices is often limited by thermal aberrations and the physical size of the gain medium.

The simplest form of SLM cavity is the microchip configuration. Short cavities, using only two optics, can readily achieve SLM due to the large spacing between each longitudinal mode. An SLM microchip VBG laser cavity generating 0.85 W has been demonstrated previously [107]. Short, single VBG cavities have also demonstrated up to 1.4 W in a SLM [108]. To scale the output power, larger gain mediums are required, decreasing the longitudinal mode spacing making it difficult to operate on a SLM in this configuration.

A configuration that allows for a large gain medium, utilising a limited number of optics which can easily achieve SLM, could have a number of uses as a pump source for industrial and metrology products. This chapter presents the configuration of a double VBG laser operating at 1342 nm on a single longitudinal mode, at much higher output powers than has previously been demonstrated.

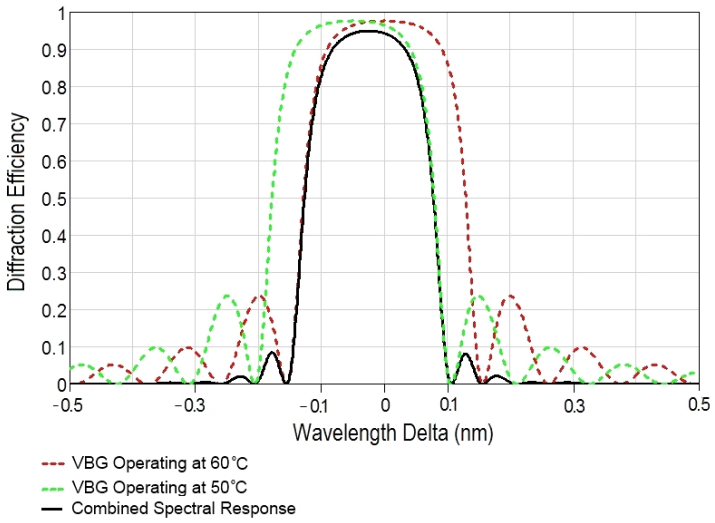

Figure 5.1 – Combined spectral response of double VBG setup.

5.2 Double VBG Setup

Equation (2.16) in chapter 2 shows how the response of a reflective VBG is determined by the smallest refractive index change(Δn) achievable. Currently, the narrowest response of a reflective VBG is limited to 80 pm. The spectral response of a single grating will therefore limit SLM operation to microchip cavities, where the mode spacing is very large. Another technique for spectral narrowing has been described by Hemmer *et al.* [95], where two VBGs are used within a single cavity to narrow the spectral response. This configuration has been shown to reduce the operating linewidth of a double VBG Ti-sapphire laser cavity that operated with a linewidth of

8 pm, although SLM was not achieved. By using two VBGs in the same cavity, the spectral response now becomes the product of the two. A diagram of the double VBG is shown in Fig. 5.2. By tuning the centre wavelength of one VBG with respect to the other, either by temperature or angle tuning, we can reduce the effective bandwidth of the cavity. Fig. 5.1 shows the spectral diffraction efficiency of the 1342 nm VBG taken from chapter 3, where one VBG is operating at a temperature of 60 °C. A second VBG, operating at a temperature of 50 °C is also shown. The combined spectral product of the two VBGs is shown in black in Fig. 5.1.

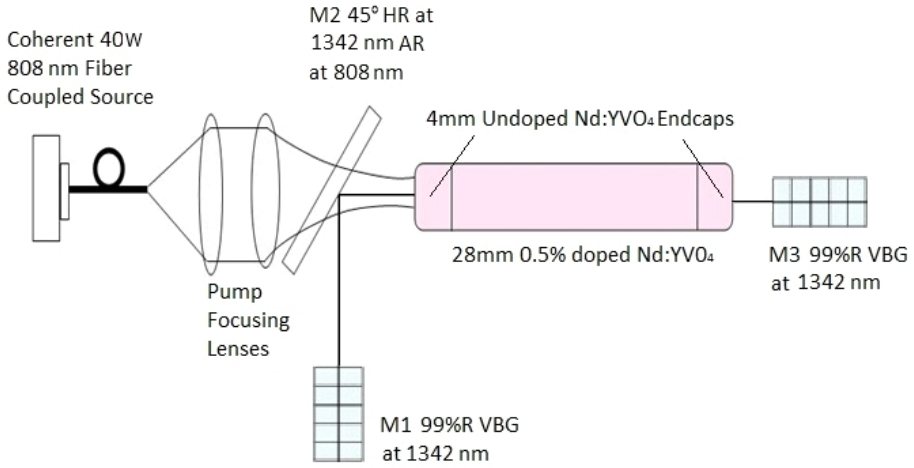

Figure 5.2 – Double VBG cavity.

The tuning rate of the VBGs will determine how the spectral response changes as the temperature of one VBG is varied relative to the other. The linewidth of the double VBG configuration can be modelled using the tuning rate of 14 pm/°C, as measured in chapter 3 section 3.3.2. This is shown in Fig. 5.3 as a function of the temperature difference between the two gratings. In this configuration narrow linewidths of up to 10 pm have been achieved [95]. However, single longitudinal mode operation has not been achieved in a double reflective VBG configuration, utilising a large gain medium.

Fig. 5.3 shows the reduction in overall bandwidth as the temperature between the two VBGs is increased. The effective reflectivity of the cavity is also calculated as the temperature difference between the two gratings is increased. As shown in Fig. 5.1, the combined spectrum of the VBGs leads to an overall reduction in peak reflectivity of the cavity. As the VBG configuration moves towards a 50 pm bandwidth, the effective reflectivity of the setup decreases beyond the optimum coupling value of 80 % measured in chapter 3 section 3.3.1.

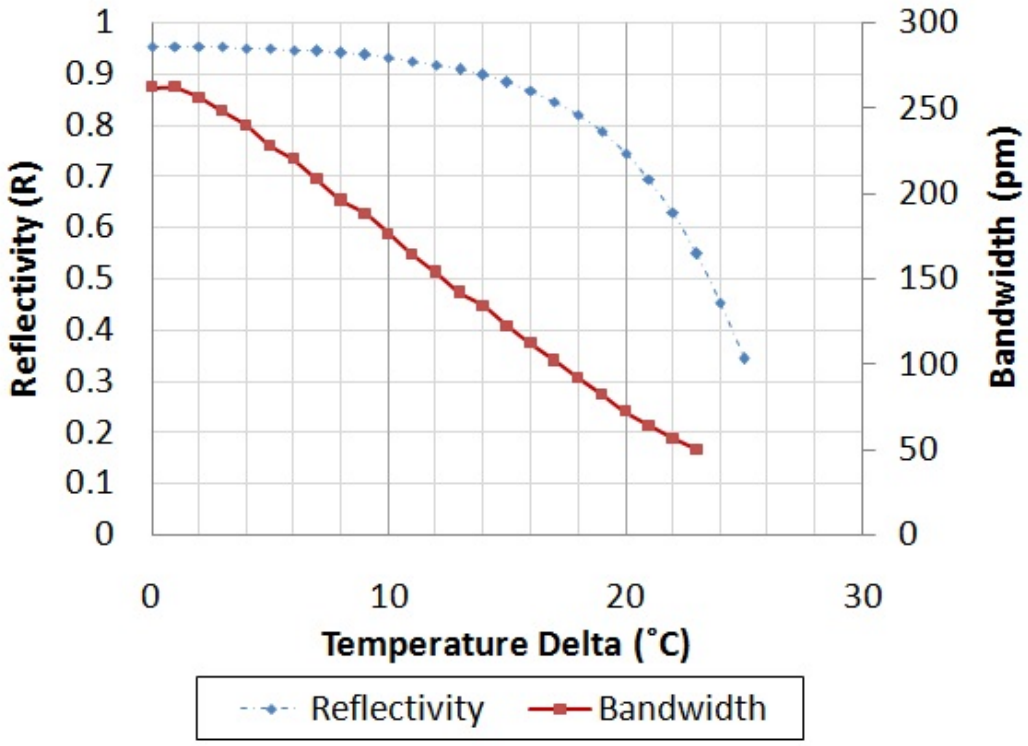

Figure 5.3 – Bandwidth and effective reflectivity of double VBG configuration.

5.3 Single Longitudinal Mode Operation

The temperature dependent spectral response of the VBG setup will allow for the spectral response of the cavity to be tuned, narrowing the cavity linewidth. If the required narrowing of the cavity spectral response is too narrow however, the output coupling effect described previously, could lead to a less than optimal coupling. To determine this, the spectral response required to achieve SLM must be calculated. The method for calculating the required attenuation of adjacent modes has been described previously by Zayhowski [109]. The derivation here follows that of Zayhowski's. The spectral response of the VBG is now applied to this derivation. This method of calculating the required mode attenuation has previously been used for a single VBG analysis [107]. In this chapter it is applied to the double VBG configuration.

From chapter 1 it can be seen how different cavity configurations can affect the ability to achieve SLM. The plane-plane mirror cavity used in this configuration will lead to the formation of standing waves in the resonator. The presence of these standing waves will lead to the intra-cavity intensity for any given mode to look like Fig. 5.4a. The actual extraction of the population inversion with this intensity pattern will lead to a spatially dependent population inversion defined by the equation

$$N(z) = \frac{N_o}{1 + I_m/I_{sat}} \tag{5.1}$$

Where $N(z)$ is the spatially dependent population inversion, I_m is the intensity of a given mode in the cavity, I_{sat} is the saturation intensity and z is the distance into the gain medium. N_o is the inversion in the absence of spatial hole burning, which for this calculation, has been assumed to have a weak dependence on z. Depending on how high above threshold the cavity is operating, which is equivalent to I_m/I_{sat}, the population inversion will now look like that in Fig. 5.4b.

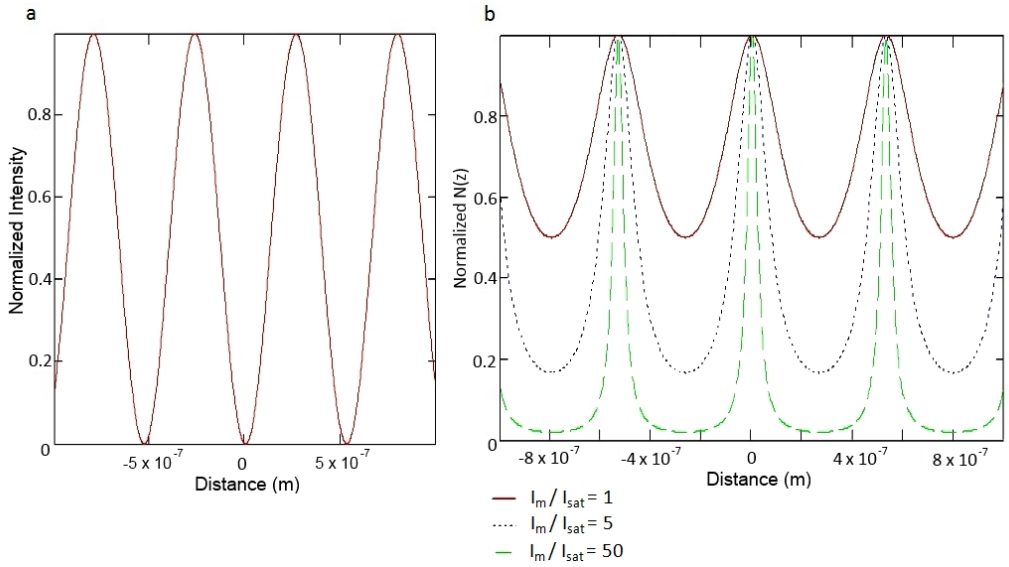

Figure 5.4 – a: Intensity profile of standing wave as a function of distance within the cavity. b: Spatially varying population inversion for I_m/I_{sat} = 1,5 and 50 normalised to N_{th}.

Fig. 5.4 also shows how the intra-cavity intensity I_m affects the extraction of the population inversion. If we simplistically describe the small signal gain of each mode as

$$g_o = \int \sigma N(z) dz \tag{5.2}$$

each mode therefore will observe a different level of gain, depending on the presence and extraction of other modes, as well as the circulating intensities of these modes. The spatial hole burning effect described here can lead to a larger bandwidth when compared to lasers that do not suffer from this effect. The increased bandwidth arises due to gain saturation of the lasing modes where the anti-nodes occur, and limited extraction of the population inversion at the node points. As a result, non-lasing modes can experience gain at these points, sufficient to achieve lasing threshold. In order to achieve SLM operation, we must ensure that the single-pass gain of any adjacent mode is smaller than the single-pass loss for that mode. The formation of spatial hole burning will increase the gain for unwanted modes, increasing the required level of attenuation.

To determine the threshold, the level of gain available to a particular mode, compared to a given central mode, must be determined. A phase correlation factor between the central mode m_1 and a second mode m_2 is therefore defined. This factor takes into account how the phase difference between a set of modes will affect the gain that each mode will compete for. The phase correlation factor is described as the spatially weighted average cosine of the phase difference between the two modes. The factor also includes a normalized z dependence. The phase correlation factor for an end-pumped laser is shown below

$$\psi(2,1) = \frac{\int_0^z (1 - e^{-\alpha_p z}) cos(2\Delta k_m z)}{\int_0^l (1 - e^{-\alpha_p z})} \tag{5.3}$$

$$\text{where } \Delta k_m = \frac{2\pi}{\lambda_1} - \frac{2\pi}{\lambda_2}$$

The factor α_p is the average pump absorption coefficient, z is the distance into the laser crystal and $\lambda_{1/2}$ are the wavelengths of each mode. Secondly, a discrimination factor is introduced as the ratio of round trip loss between two adjacent modes.

$$\beta(2,1) = \frac{\sigma_1 \gamma_2}{\sigma_2 \gamma_1} \tag{5.4}$$

For modes close together, the emission cross-sections $\sigma_{1,2}$ are assumed to be similar. We are left with $\gamma_{1,2}$, which is the effective loss ratio between each mode. The total attenuation of the modes adjacent to the central mode will be a function of the combined spectral response of the VBGs. By creating a narrow spectral response, we increase the losses of the adjacent modes, thereby increasing the effective threshold of that mode. To achieve SLM, a spectrum that will sufficiently attenuate the modes to ensure they cannot achieve threshold is required.

From these two equations, the threshold inversion density ratio of any given mode compared to that of the central mode can be calculated. This is denoted as $\zeta(1,2)$ where $\zeta(1,2)$ is equal to $\frac{N_{m=2}}{N_0}$ and defined as

$$\zeta(1,2) \equiv \left(\frac{\beta(2,1) - 1}{1 - \langle\psi(2,1)\rangle + 1)} \cdot \left(\frac{(2\beta(2,1) - 1)}{1 - \langle\psi(2,1)\rangle} + 1\right)\right. \tag{5.5}$$

Finally, the longitudinal mode spacing of any given cavity is taken into account, which limits the allowed modes to

$$\lambda = \frac{\Delta m {\lambda_0}^2}{2nL_n} \tag{5.6}$$

where λ_0 is the centre wavelength which obeys the equation $L = q\frac{\lambda_0}{2}$, in which q is an integer, n is the refractive index and L_n is the cavity length.

In order to calculate at which point a given laser will move from SLM operation to multi-mode operation, the relative thresholds of all modes, compared to the central mode must then be calculated. We start by assuming that the central mode will typically occur at the centre of the gain curve. Secondly, we assume that the emission cross-sections for all the modes are equal. We must then calculate the comparative threshold of each subsequent mode. Fig. 5.5 shows how the threshold of the Δm = 1-4 modes vary as the cavity length is increased. The combined linewidth of the VBGs was taken to be 60 pm, this compares to the 180 pm linewidth of a single VBG.

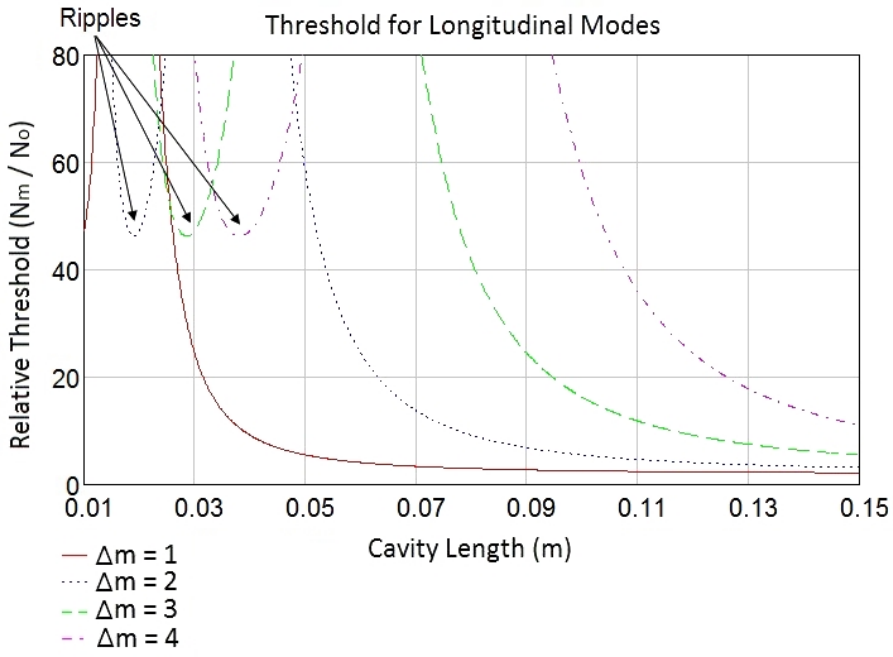

Figure 5.5 – Inversion threshold of modes N_m relative to N_0 as a function of cavity length.

Fig. 5.5 shows how the relative thresholds decrease as the cavity length is increased, with a fixed VBG temperature difference of 20 °C. The main effect observed here is the decrease in spacing of the modes, allowing each mode to move closer to the peak of the VBG. Some new behaviour can also be observed at $\approx$ 45 times above threshold, where a small region of decreased threshold can be seen for each mode. The decreased threshold of the modes in this region is due to the centre wavelength of that mode aligning with the secondary peaks of the VBG spectra. The modes operating in this region would be unlikely to oscillate due to the high threshold levels.

The bandwidth required for SLM operation can now be modelled by analysing the threshold of every adjacent mode and comparing it to the threshold of the actual cavity. In practice, however, only low Δm numbers must be considered, due to the spectral response of the grating. From this, the threshold of the lowest secondary mode, for any given bandwidth, can be determined. For this calculation the cavity length was taken to be 7 cm, this is the smallest cavity length possible with the optics used in chapter 3.

The red line in Fig. 5.6 shows how the threshold for the lowest mode varies as a function of the VBG bandwidth. The variation in the VBG bandwidth is achieved by varying the temperature of one VBG relative to the other. The blue line in Fig. 5.6 shows how high above threshold the actual laser operates for a given bandwidth, and therefore output coupling, assuming a pump power of 16 W. For the cavity calculation the same analysis as that completed in chapter 3 section 3.3.1 is used, with a pump spot of 320 μm and intra-cavity losses of 10 %. The point at which the laser will operate in SLM can be calculated by analyzing the points where the two lines cross. Below 60 pm, the threshold for the secondary modes is larger than 3.5 times the central mode threshold. With 16 W of pump power, the actual cavity is operating below this level. Therefore, SLM operation should be achievable beyond this operating point. The model predicts that with a cavity length of 7 cm, a spectral FHWM bandwidth of 62 pm is required to achieve SLM. Above this bandwidth, the secondary modes should be able to achieve threshold. Referring back to Fig. 5.3, a temperature difference of 21 °C between the two gratings would be required to achieve a spectral bandwidth of 60 pm.

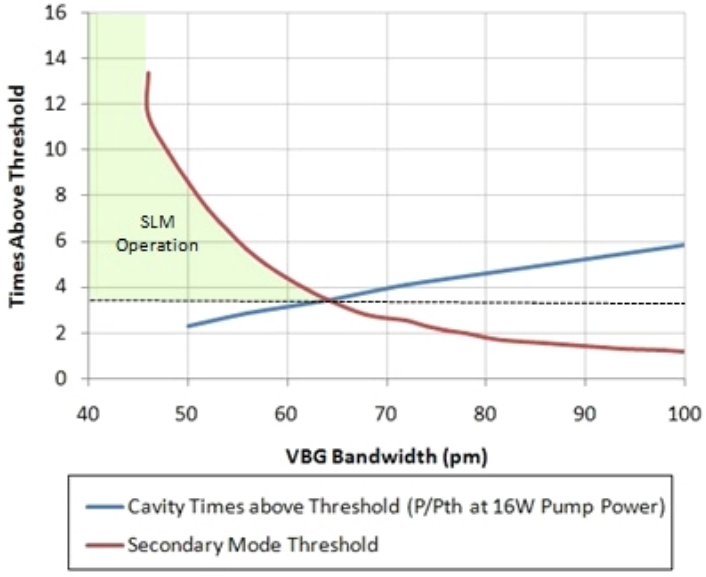

Figure 5.6 – Threshold for secondary modes and cavity threshold.

5.4 1342 nm Double VBG Configuration

Initially, a double VBG cavity was constructed as shown in Fig. 5.2. The optical cavity length was 7.2 cm. The longitudinal mode spacing was 12.5 pm. For SLM operation, a temperature difference of 21 °C would be required. Fig. 5.7 shows the performance of the double VBG cavity. The red line shows the combined output from both VBGs. The blue line shows the cavity linewidth.

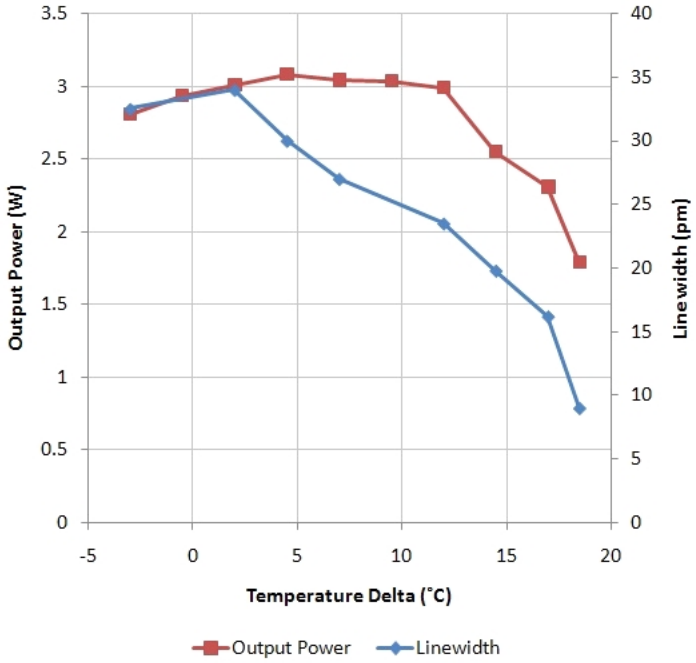

Figure 5.7 – Double VBG performance showing the combined output power from the VBGs and cavity linewidth.

In this configuration single longitudinal mode operation was achieved up to 2.3 W. At this operating point mode hopping was present and the laser would occasionally jump into two modes. Beyond 2.3 W, two modes were present and at 3 W three modes were present. The VBG temperature difference required to achieve SLM was 17 °C. This is slightly different to the modelled value of 21 °C. Fig. 5.8 shows a series of the Fabry-Perot rings as the VBG is tuned.

Here the increase in cavity bandwidth can be observed, as well as each mode jumping in as the temperature difference between the VBGs is varied. The maximum linewidth for single mode operation was measured to be 16 pm.

5.4.1 1342 nm VBG Output Coupling Analysis

In the previous section the calculated temperature difference required to achieve SLM was higher than the actual values measured. With a temperature difference of 17 °C, the bandwidth of the VBG configuration should be 90 pm. The mode spacing in the

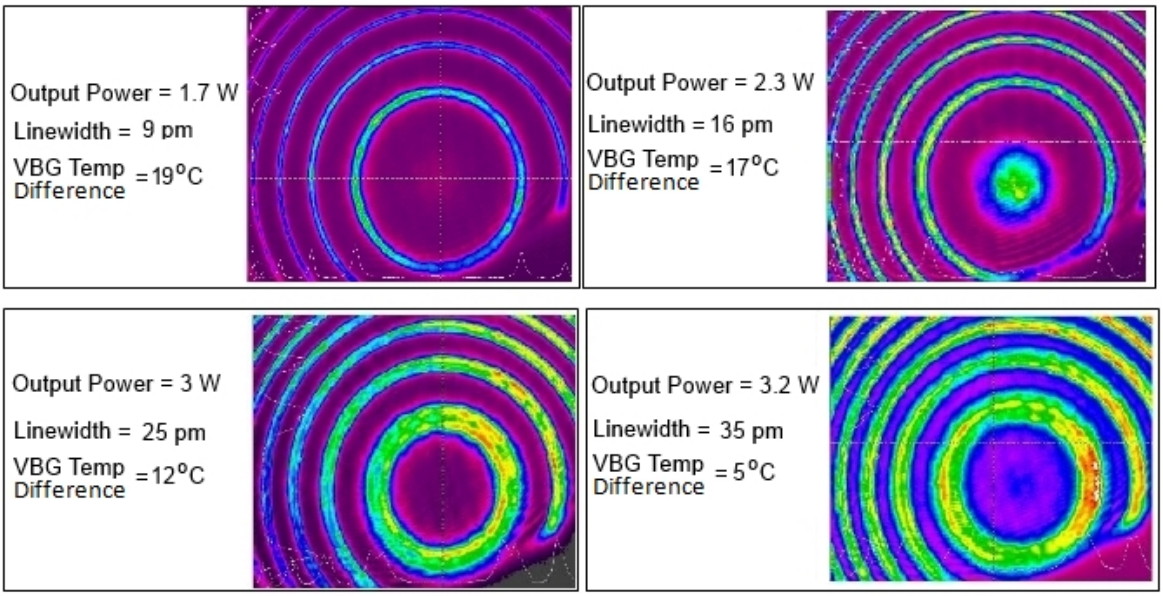

Figure 5.8 – Series of images from Fabry-Perot imaging setup at various temperatures.

cavity is 12.5 pm, the attenuation of the adjacent modes should therefore be insufficient to achieve SLM. The actual value of output coupling in the cavity was then measured to determine the double VBG reflectivity. By measuring the VBG reflectivity, its spectral response can be determined.

In order to investigate the output coupling in the cavity, another data point was added using a fixed coupling value. This was achieved by replacing the steering mirror at M2 with a 5 %T output coupler, providing 10 % output per round trip. This setup is shown in Fig. 5.9a.

This configuration allows for the actual reflectivity of the second VBG to be measured. Using the two detectors, the effective reflectivity of the VBG is measured as the temperature of the VBG is tuned. From Fig. 5.9b, the reflectivity is calculated using the coupled equations

$$R_{vbg} = 1 - \frac{P_{out}}{P_1 R_{mirror}} \tag{5.7}$$

$$R_{vbg} = \frac{P_{2out}}{P_1 R_{mirror}(1 - R_{mirror})} \tag{5.8}$$

Where R_{vbg} is the VBG reflectivity, P_{out} is the power leaking from the VBG and

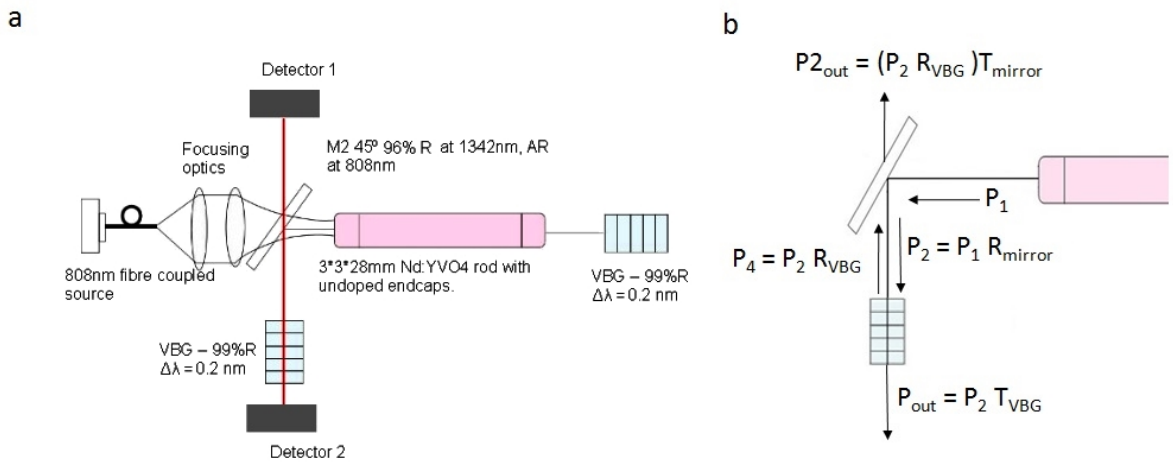

Figure 5.9 – a: Output coupling measurement of double VBG. b: Intra-cavity power calculation.

P_{2out} is the power leaking from the coupler at M2. P_1 is the calculated intra-cavity power at the position shown in Fig. 5.9b. Fig. 5.10 shows how the measured reflectivity of the VBG varied as a function of the temperature difference between the two VBGs.

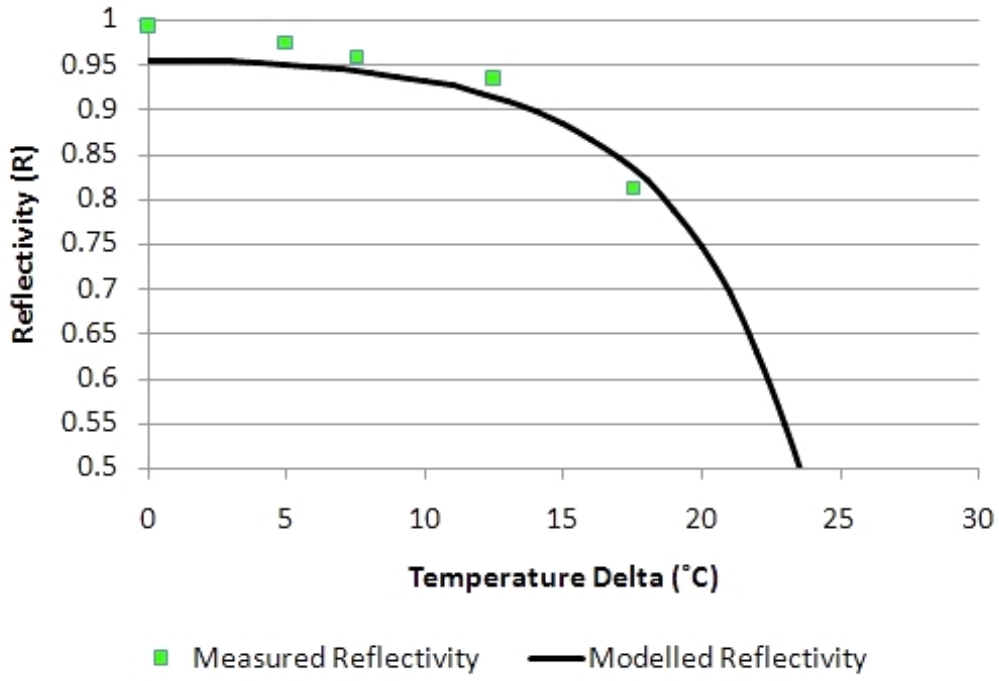

Figure 5.10 – Output coupling of double VBG cavity.

The measured reflectivity values show good agreement with the expected reflectivity values from the VBG temperature tuning. At a temperature difference of 17 °C, a VBG reflectivity of 81 % is measured, compared with an expected value of 83 %. The VBG spectral response is therefore 83 pm.

The spectral response of the double VBG spectrum required to achieve SLM is different from that calculated in the previous section. The calculation predicted a spectral response of 65 pm compared with an actual value of 83 pm. However, there are a number of sources of error in this calculation. It was assumed that the spectral response of the VBGs is identical to that modelled in chapter 3 Fig. 3.16. This may not be the case as the spectrum may be slightly different to the modelled data. Whilst the actual output coupling was also measured in the configuration in Fig. 5.9, the cavity was re-aligned to allow for insertion of the additional output coupler. As a result, the relative angles of the VBGs may be different in each configuration. This would lead to a different spectral response and output coupling level than for the case of the double VBG cavity.

Using an output coupling reflectivity of 81%, the expected VBG spectral response can be calculated, this is shown in Fig. 5.11.

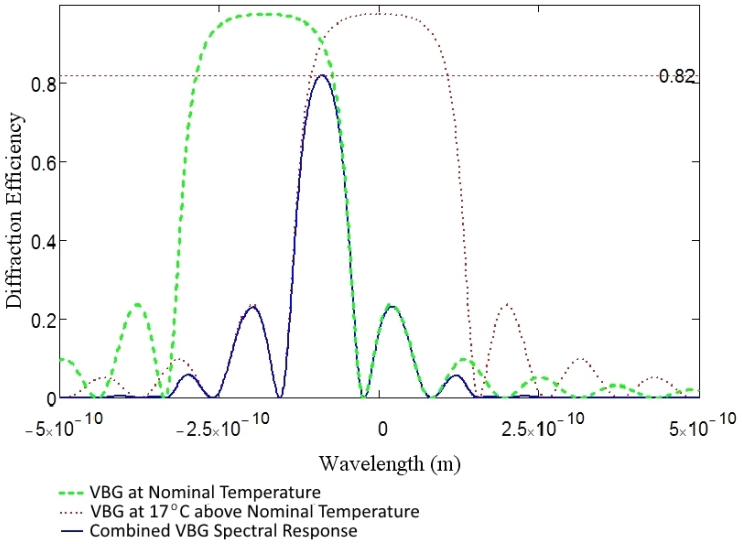

Figure 5.11 – Combined spectral performance of cavity with 81 % reflectivity.

Fig. 5.11 shows the spectral response at 83 pm FWHM. The centre wavelength of the second VBG is shifted by 180 pm from the nominal position. Using the tuning rate of 14 pm/°C, a temperature delta 17 °C would be required to achieve SLM.

5.4.2 Discussion

The double VBG setup has allowed for single longitudinal mode operation to be achieved up to an output power of 2.3 W; much higher than previous setups reported in the literature [95]. However, this configuration does have drawbacks, such as the nature of the output coupling, which produces output in both directions. In the worst case, half the power would be lost if the setup does not allow for the beam to be

combined further downstream. It must also be considered how the source would be suited for use within ICSHG setups, where the output coupling is achieved through harmonic conversion rather than reduced reflectivity of the cavity mirrors. In this case, all the coupling from the VBGs must be viewed as a cavity loss, rather than useful output coupling. The required spectral bandwidth of VBGs leads to a reflectivity in the order of 80%, which would represent a large loss in the cavity. If however, the spectral response could be narrowed without the associated decrease in reflectivity, the cavity then would be able to use the useful output coupling for ICSHG. In order to achieve this, the VBGs must exhibit a much more top-hat spectral response than those shown in Fig. 5.1. The narrower spectral response would allow for tuning of the gratings and narrowing of the combined spectra, without the associated output coupling effect.

In the absence of narrow spectrum gratings, changes to the setup could improve the overall useful output coupling. The reduction in useful output coupling could be counteracted by an increase in gain. The simplest method to achieve this is to decrease the spot size of the cavity mode. As the gain is increased, the optimum output coupling will decrease. The output coupling will then become dominated by useful output coupling rather than that required for spectral narrowing. The smaller spot size and subsequent reduced cavity mode size will increase the peak power density on the VBG. A balance must therefore be found in achieving the narrow linewidth, and subsequent chirping of the grating. A Z-fold astigmatically-compensated cavity would allow for a tightly focused mode within the crystal and for large spot sizes on the VBG to limit thermally induced chirping.

5.5 Conclusion

In this chapter we have demonstrated for the first time a double VBG configuration capable of operating on a single longitudinal mode. The double VBG technique was able to generate up to 2.3 W whilst operating on a single longitudinal mode with a linewidth of 16 pm.

Chapter 6

Q-switched VBG Laser and Second Harmonic Generation

6.1 Introduction

In chapter 1, the need for a visible source, spanning a wide wavelength range was introduced. In this chapter the focus is on the development of a 1064 nm laser to generate the 532 nm second harmonic in the visible region. The aim of this chapter is also to demonstrate the performance enhancements in second harmonic generation that can be gained by using a pump source narrowed from a VBG. The laser source is operated in a Q-switched configuration to generate the high peak powers required to achieve efficient SHG. Future work will investigate the ICSHG configuration discussed in chapter 5. The motives for operating at 1064 nm rather than the 1342 nm emission line previously investigated is simply due to the availability of optics and nonlinear crystals at this wavelength. Future work is also planned for the generation of the 1342 nm second harmonic.

The results documented in this chapter were completed by the author with help from M.Sc student A. Barron. The experimental work was completed by the author, or by A. Barron, under supervision. The modelling and calculations completed, as well as the analysis, are all the work of the author in their entirety.

The material used in this chapter to generate the second harmonic is MgO doped periodically poled stoichiometric Lithium Tantalate (MgO:PPSLT). PPSLT has a number of advantages compared to the more commonly used periodically poled Lithium Niobate (PPLN). Whilst the effective nonlinearity of PPSLT is lower than that of PPLN, 13 pm/V [110] compared with 25 pm/V [111], the near stoichiometric Lithium Tantalate material does not suffer as severely from the photo-refractive effect as Lithium Niobate [112]. The result is an increased damage threshold and the ability to operate at lower temperatures. PPSLT is now commercially available in a number of

different orientations and poling periods from manufacturers such as HC photonics.

When using PPSLT to frequency double a 1064 nm source, output powers of up to 18 W have been demonstrated [113]. In OPO configurations, PPSLT has been used to generate wavelengths from 400 nm [114] up to 3.5 μm [115]. The transparency of PPSLT is similar to that of PPLN, with transmission of up to 5 μm, allowing for a wide variety of wavelengths to be generated.

The first part of this chapter investigates the setup of a Q-switched laser operating at 1064 nm. The peak power of the short pulses allows for efficient SHG. A Q-switched laser operating at 1064 nm in both a plane-plane mirror configuration and a single VBG configuration is demonstrated, in a similar manner to chapter 3. The use of VBGs in Q-switched configurations has been demonstrated previously [116]. In this chapter, the ability of the VBG to operate in a Q-switched configuration at similar average powers to those shown in chapter 3 section 3.2.4 is investigated. The changes in the pulse characteristics, beam profile and output power are presented. The sources are then used to pump a nonlinear crystal, and the improvements in the conversion efficiency are reported. It is important to note that, in the Q-switched configuration, we do not intend to achieve single longitudinal mode (SLM) operation. This is simply due to the inability to achieve SLM using the setup described. The inclusion of an active Q-switch, either acousto-optic (AO) or electro-optic (EO), will significantly increase the length of the resonator. As a result, the longitudinal mode spacing will decrease, making it difficult to achieve SLM.

6.2 1064 nm Q-switched Laser

The laser was initially built with the same operating characteristics as those described in chapter 3 section 3.2. However, due to the unavailability of the Nd:YVO_4 crystal, a crystal without end-caps was used. The result was a degradation in the M^2 of the laser at pump powers above 13 W. To maintain the beam quality of the laser for this investigation, the pump power was limited to 13 W.

6.2.1 Q-Switched Performance

The AO Q-switch was fitted to the cavity in the position shown in Fig. 6.1. (Please note that this diagram is not to scale). The 32 mm long AO Q-switch with a diameter of 1.8 mm, was purchased from Gooch and Housego with an RF modulation of 40 MHz. The RF power required for a 90% diffraction efficiency is 20 W. For the output coupler reflectivity used in the Q-switched setup, the need to limit the intra-cavity intensity is

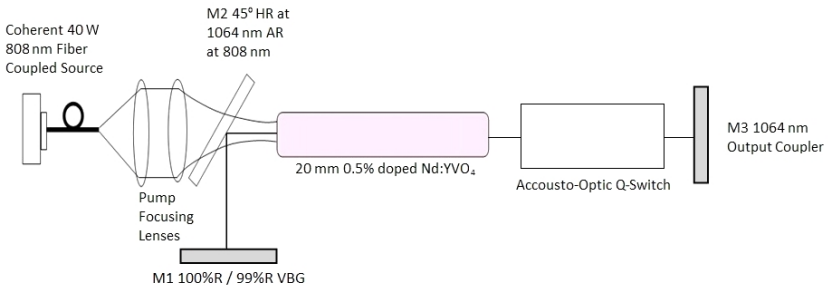

Figure 6.1 – Q-switched laser cavity diagram.

also considered. This is to ensure that damage to the Q-switch does not occur and that thermal effects in the VBG are minimised. By decreasing the reflectivity of the cavity, the overall peak power incident on the optical components is reduced. In the current configuration, the 80% reflectivity coupler was chosen to limit the intra-cavity intensity and to limit the thermal load on the VBG.

The cavity was then characterised in the Q-switched regime. The pump diode was run in a CW manner, with the AOM diffraction lowering the Q of the cavity, allowing for the population inversion build-up. The length of the RF pulse, which allows for the Q-switched operation, is referred to as the inversion build-up period. The inversion build-up period was varied from 10-60 μs. This period is limited by the fluorescence lifetime of the Nd:YVO_4 which, for a 0.5% doped crystal, is typically 90 μs [117]. The cavity was held in a high-Q state for less than 10 μs. This allowed for the initial pulse to build up, whilst limiting that of a second pulse.

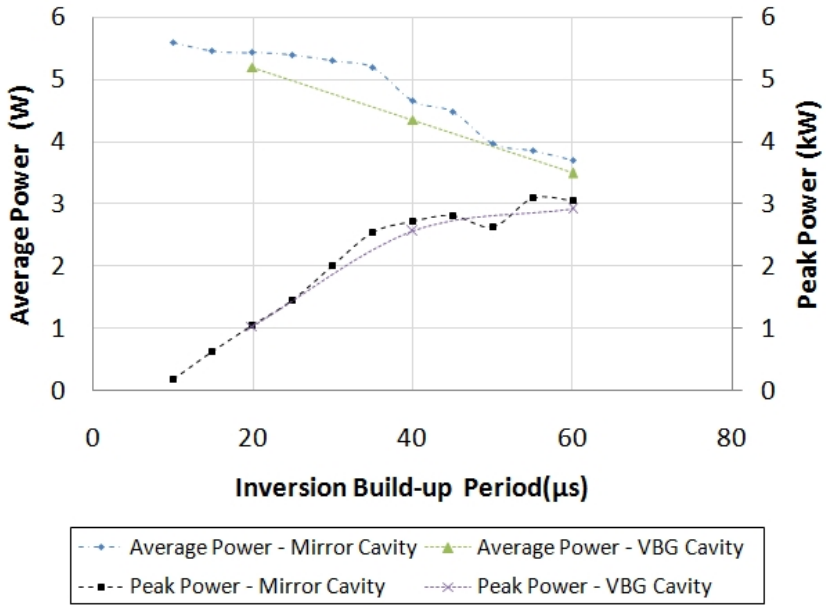

Figure 6.2 – Comparison of Q-switched performance of VBG and mirror cavity.

Fig. 6.2 shows both the average and peak power from the Q-switched laser. The

minimum peak power occurs for the shortest inversion build-up period. Conversely, the highest average power is achieved at this operating point. This behaviour is consistent with that described in [105]. A slight difference between the mirror and VBG cavity is also observed. Similar to the CW results in chapter 3 section 3.2.4, the VBG cavity average power is less than that of the mirror cavity. The peak power is also lower for the VBG.

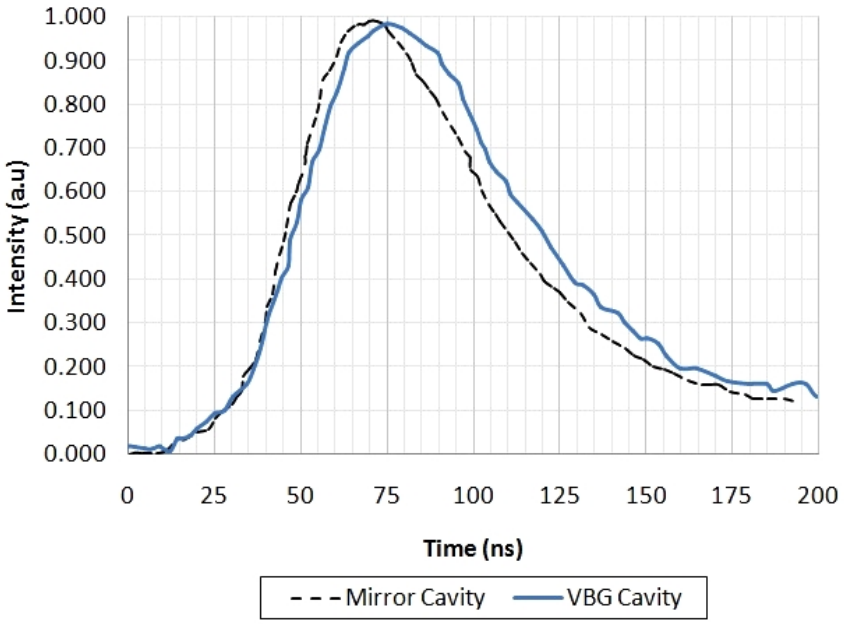

Figure 6.3 – Comparison of Q-switched pulse for VBG and mirror cavity.

The Q-switched pulse duration of the two configurations was then compared. The pulse shapes with a 40 μs inversion build-up period are shown in Fig. 6.3. The VBG has a FWHM pulse duration of 72 ns compared to 64 ns for the mirror cavity. By analysing the shape of the optical pulse for both cavities, the characteristics that cause the reduction in performance of the VBG cavity can be determined. Using Siegman's approximation for the pulse width [105], denoted as τ_p and shown in equation (6.1), it can be seen that the pulse width is a function of the number of times above threshold r, (where $\eta(r)$ is an extraction factor dependent on the number of times above threshold [118]) and the cavity lifetime τ_c. The pulse can be split into a rising component, which is a function of the number of times above threshold, and the pulse decay, which is typically dominated by the cavity lifetime.

$$\tau_p = \frac{r\eta(r)}{r - 1 - ln(r)}\tau_c \tag{6.1}$$

The 20-90% rise time for the laser pulse is 30 and 36 ns for the mirror and VBG cavities respectively. The 90-20% decay times are 69 and 67 ns for the mirror and VBG cavities respectively. The mirror cavity rises faster than the VBG cavity, but

decays slightly slower. In chapter 3 section 3.2.4, the inclusion of the VBG was shown to increase the intra-cavity losses. The pulse width behaviour is consistent with this result. The slightly shorter decay time of the VBG cavity is a result of the increased losses and therefore shorter cavity lifetime compared to the mirror cavity. The faster rise time of the mirror cavity is due to the increased number of times above threshold operation, due to the lower cavity losses, when compared to the VBG cavity.

The build-up duration of the two cavities at 40 μs was also measured to further investigate losses of the VBG. The build-up time is also a function of both the number of times above threshold and the cavity losses [105]. The duration of the build-up is measured from the point where the Q-switch opens to the point where the pulse reaches 10% of its peak value. In a similar manner to the comparison completed in the pulse duration measurement, the build-up times allow us to compare the losses between the two cavities. The build-up time for the VBG cavity was 660 ns compared to 637 ns for the mirror cavity. This behaviour confirms that the VBG cavity possesses a higher threshold than the mirror cavity.

The M^2 of the laser was then measured in each configuration. The M^2 was measured to be 1.04 in the horizontal plane and 1.1 in the vertical plane for the mirror cavity. The VBG cavity M^2 was 1.25 in the horizontal plane and 1.2 in the vertical. The plots from this are shown in Fig. 6.4, along with beam profiles taken in the far field.

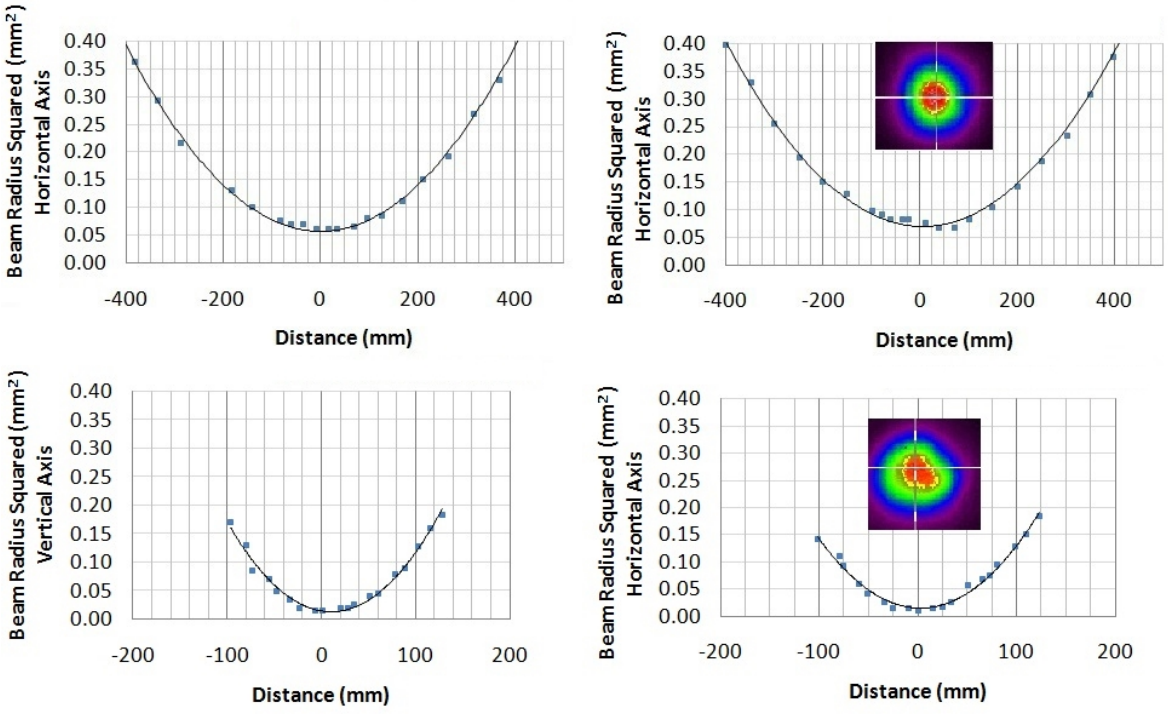

Figure 6.4 – M^2 of laser. Top: Mirror cavity M^2 measurement, beam profile inset. Bottom: VBG cavity M^2, beam profile inset

In this configuration a small degradation in the M^2 is observed for the VBG laser. This behaviour is different from that shown in the chapter 3 section 3.2.4 where the M^2 was found to be similar for both the VBG and mirror cavity. In this configuration increased thermal lensing is present due to the absence of undoped end-caps on the crystal. The stronger lensing does produce a smaller spot onto the VBG than the previous configuration. This may degrade the M^2 when compared to the mirror configuration. Slight adjustment of the cavity length was made, but this did not improve the beam quality.

The final parameter measured was the linewidth of the two different cavities. Different techniques were used to measure the linewidth of each cavity. A grating-based spectrometer was used to measure the spectrum of the mirror cavity due to the broad linewidth. This is shown in Fig. 6.5a. The VBG cavity was measured using the interferogram technique described in appendix A. The interferogram beam profile for the Q-switched laser is shown in Fig. 6.5b.

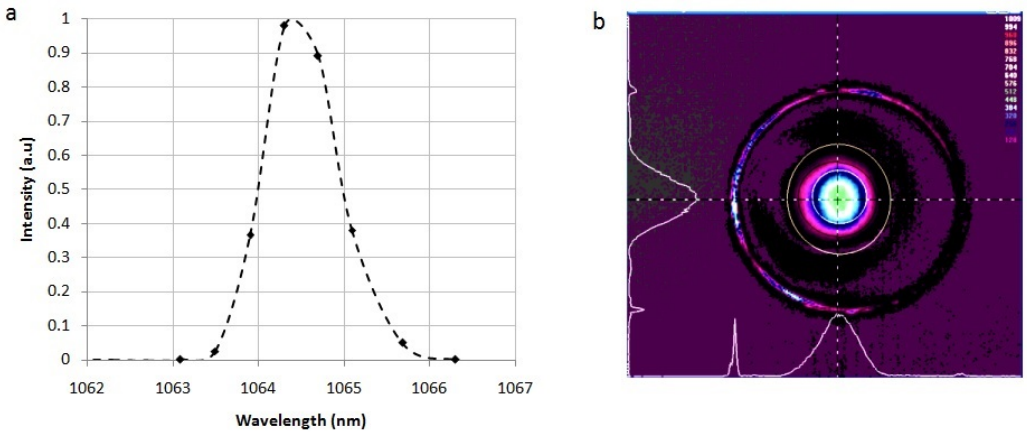

Figure 6.5 – a: Mirror cavity spectrum. b: Interferogram measurement for VBG linewidth.

The linewidth of the mirror cavity was measured to be 0.97 nm. The linewidth of the VBG cavity was measured to be 0.19 nm. This behaviour differs from the CW results, in particular, the VBG linewidth is slightly larger than that measured for the CW configuration in chapter 3 section 3.2.4. From the results shown in Fig. 6.5b, the cavity linewidth is now filling the full spectrum of the VBG. Typically, it would be expected that the linewidth in the Q-switched configuration would narrow due to the modal selection during the build-up phase, as presented by Sooy [119]. The presence of spatial hole burning during the build-up of the pulse can, however, lead to a reduction in the overall pulse energy [120], leaving gain un-extracted. Furthermore, the effect of the spatial hole burning will typically lead to gain being available to those modes further out of phase with the centre wavelength.

The longitudinal mode spacing for the 475 mm cavity is 0.5 pm, therefore a number of modes are present during the build-up phase, all of which will compete for gain. Modes further out of phase with the central wavelength of the VBG may observe higher gain due to the poorer extraction at the anti-node points. As the actual Q-switch pulse begins to grow and gain saturation starts to occur, the level of gain observed by the off-centre modes may be significantly higher. Further work is required to investigate this effect. By using an etalon with a higher finesse, the actual spectral features of the cavity linewidth could be determined.

The mirror cavity does experience the expected line narrowing from Sooys analysis. The CW linewidth in chapter 3 section 3.2.2 was 1.25 nm compared to the Q-switched linewidth of 0.97 nm. Here the narrowing occurs due to the shape of the gain curve. The gain curve is fairly flat, therefore only a limited amount of spectral narrowing occurs.

6.2.2 Q-Switching Conclusion

The ability of a VBG to operate in a Q-switched laser without a significant degradation in performance has been shown. The VBG laser was slightly less efficient when compared to an identical mirror cavity, and a small degradation in the beam quality was observed. The linewidth of the laser was narrowed to 0.19 nm compared to a free running linewidth of 0.97 nm. This linewidth reduction should improve the second harmonic conversion efficiency. The laser was then used as a pump source for SHG to generate the visible wavelengths required to meet the programme objectives. The investigation also allows for the effect that the cavity linewidth has on the conversion efficiency to be demonstrated.

6.3 523 nm Second Harmonic Generation

In order to meet the requirements for a visible countermeasure source, the IR wavelengths must be converted to the visible region of the spectrum. Second harmonic generation of the Q-switched VBG and mirror cavities is therefore investigated. As a result of the narrow linewidth, the VBG cavity should demonstrate improved SHG, compared to the mirror cavity. The improved efficiency will allow for cost or performance improvements over a traditional mirror cavity. The future investigation into dual-wavelength operation will also require a SHG stage. This investigation will therefore highlight the VBG-cavity's potential as a second harmonic pump source.

6.3.1 532 nm Second Harmonic Generation Modelling

The possible performance improvements gained from using the VBG-cavity as a pump source was then modelled. The different linewidths of the mirror and VBG cavities will change the phase mismatch in the crystal, changing the second harmonic conversion efficiency. Fig. 6.6 shows an illustration of the modelled linewidth of the two sources, which have been assumed to be Gaussian. By calculating the phase mismatch as a function of wavelength, it can be seen how the acceptance bandwidth of the nonlinear conversion compares to the linewidth of both sources. The efficiency due to the phase mismatch is calculated using the following equation,

$$\eta = \frac{1}{L_{nc}} \int exp^{-i\Delta K L_{nc}} dL \tag{6.2}$$

where

$$\Delta K = 2K_{\omega} - K_{2\omega} - \frac{2\pi}{\Lambda} \tag{6.3}$$

The term Λ in equation (6.2) is the poling period of the PPSLT. The term $K_{\omega/2\omega}$ refers to the propagation constant of both the fundamental and harmonic wavelengths and L_{nc} is the length of the nonlinear crystal. In Fig. 6.6, a large portion of the mirror cavities spectrum can be seen to be outwith the acceptance bandwidth of the MgO:PPSLT. It would expected that the overall conversion efficiency of the mirror cavity would be much lower, when compared to that of the VBG cavity. The acceptance bandwidth of the crystal can be increased by reducing the overall length L_{nc}. However, a reduction in the nonlinear crystal length will lead to a reduced overall interaction length, therefore limiting the conversion efficiency.

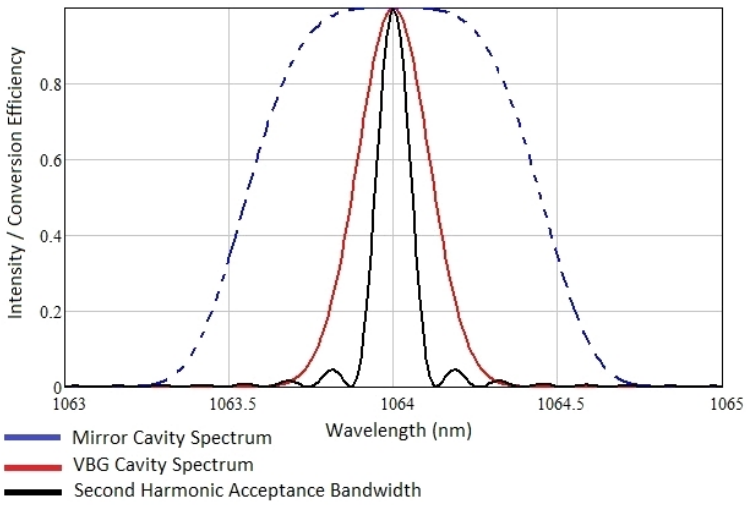

Figure 6.6 – Comparison of Q-switched spectrums for both the mirror and VBG cavities to that of the acceptance bandwidth for a 20 mm PPSLT crystal.

In order to calculate the efficiency, the overall phase mismatch that exists as a

result of the linewidth must be calculated. The calculation has been previously shown by Helmfrid *et al.* [121] and we use his notation going forward. The normalised contribution to the second harmonic conversion is calculated using the following equation

$$P^{(2\omega)}(\Omega) = 2\int P_{\omega}(\Omega - \Omega')P_{\omega'}(\Omega)d\Omega' F(d\delta) \tag{6.4}$$

where

$$F(d\delta) = \left|\frac{2\pi}{L}\int exp^{-i(\Delta kL)}dL\right|^2 \tag{6.5}$$

Ω = Central angular frequency deviation from Ω_0
Ω'= Angular frequency of input spectrum
$P^{(2\omega)}(\Omega)$ = Power at second harmonic wavelength
$P_{\omega}(\Omega)$ = Power at the fundamental wavelength

The overall contribution to the nonlinear drive can therefore be calculated by integrating with respect to Ω. For the VBG cavity, the reduction in the nonlinear drive was calculated to be 0.6, compared to 0.18 for the mirror cavity. These results are consistent with those presented by Kontur *et al.*[122]. The limitation of this method is that the bandwidth of each source is only considered as a reduction in the overall intensity contribution. The analysis does not consider that the broad bandwidth may drive back-conversion or even sum frequency mixing. To calculate the actual SHG power generated, the following equations are used [123]

$$\eta_0 = C^2 L_{nc}^2 h(\xi) I_w \int P^{(2\omega)}d\Omega \tag{6.6}$$

where

$$C = \frac{8\pi^2 d_{eff}^2}{\epsilon_0 c \lambda_0^2 n_0^3} \tag{6.7}$$

The function $h(\xi)$ refers to the Boyd-Kleinman focusing parameter [124], d_{eff} is the effective nonlinearity of the crystal used, n_0 and λ_0 are the refractive index of the material and the centre wavelength at the fundamental wavelength, I_{ω} is the incident intensity at the fundamental wavelength. In order to correctly model the conversion efficiency, depletion of the pump wavelength due to the SHG process must also be considered. To do this, the following equation [125] is used

$$\eta_{shg} = tanh(\sqrt{\eta_0}) \tag{6.8}$$

Note that this equation does not take into account the dephasing effects and subsequent back-conversion that would be expected from the actual crystal characteristics, as well

as other secondary effects. These are considered in a later section.

From these equations the optimum pump conditions and the effects of the various parameters on conversion efficiency can be determined. These are shown in Figs 6.7.

For these calculations, a constant Boyd-Kleinman focusing parameter of 0.7 was assumed. The configuration is limited to a focal waist size of 70 μm to ensure that the 2 J/cm^2 damage threshold of the PPSLT coating is not exceeded. The maximum PPSLT length is also limited to 20 mm. This is primarily due to cost and availability of off-the-shelf components with the required coating. Fig. 6.7a shows the modelled variation in SHG efficiency as the pump spot size is varied. Using a focused spot of 70 μm, Fig. 6.7b shows the modelled conversion efficiency as the pump power is increased for both the VBG and plane-mirror setups. Both these calculations were completed for a 20 mm crystal.

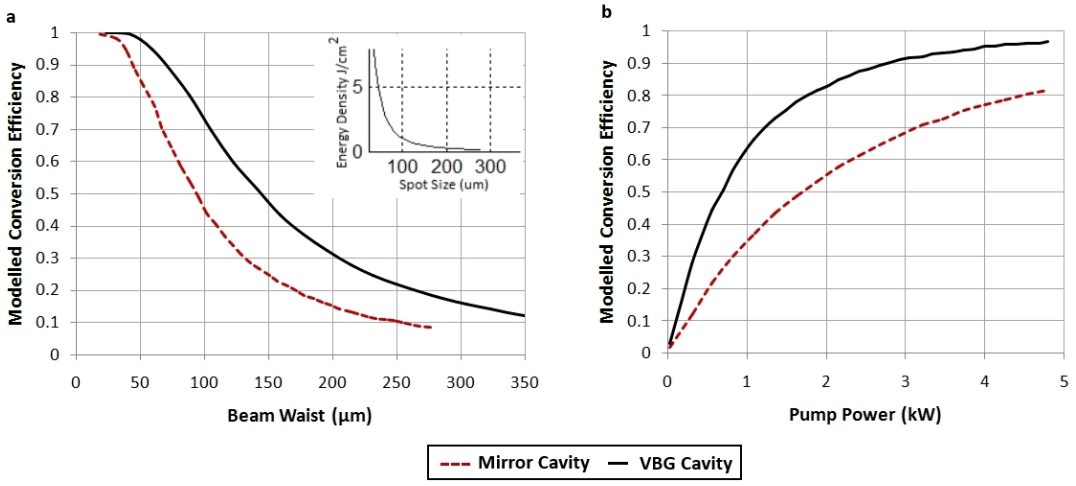

Figure 6.7 – a: Modelled conversion efficiency with spot size, inset: Energy density plotted with spot size. b: Modelled SHG conversion efficiency vs. peak pump power.

At a peak input power of 2.6 kW an increase of 24% in the conversion efficiency, from the mirror cavity to the VBG cavity, is predicted.

6.3.2 532 nm Second Harmonic Generation Results

The cavity was then configured from the parameters modelled previously. Using a 170 mm lens placed 100 mm from the output aperture of the laser, the cavity beam was focused to a modelled spot radius of 70 μm for the mirror cavity and 83 μm for the VBG cavity. This is slightly larger than the minimum spot size achievable for each configuration which is 43 μm and 48 μm for the mirror and VBG cavity respectively. The variation in spot size for each cavity is due to the differences in the measured M^2 values. The crystal was a 20 mm long, 5% MgO doped PPSLT, with a poling length of 8 μm purchased from HC Photonics. The crystal was cut to a 2×1 mm aperture

size. Initially, the losses were measured through the crystal. This was measured in a low-power CW regime, to ensure that second harmonic conversion would not occur. The single-pass loss was measured to be 3%. Fig. 6.8 shows the SHG configuration.

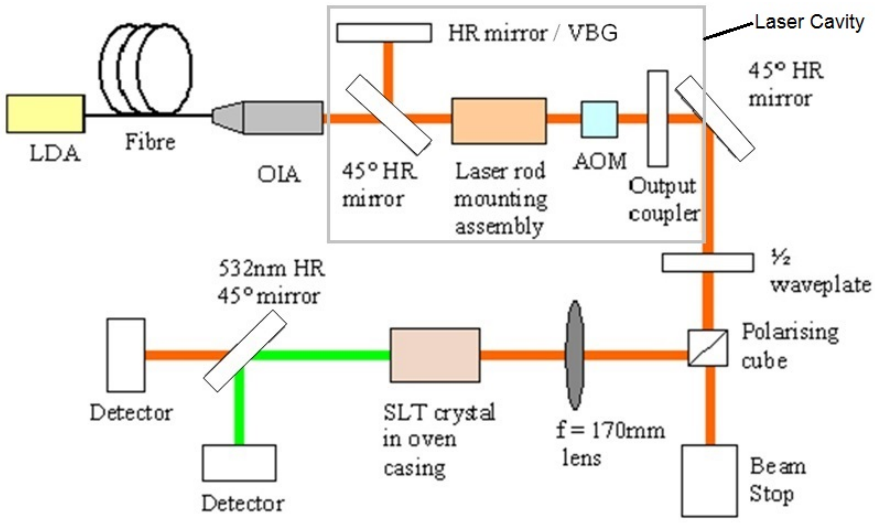

Figure 6.8 – Second harmonic configuration.

The crystal was mounted in an oven to allow for accurate temperature control. The polarizing cube and waveplate allowed for adjustment of the input power without affecting the cavity characteristics.

The crystal temperature was tuned to obtain the optimum performance. Temperature tuning the crystal will change the poling period, allowing for the phase mismatch to be minimised. Fig. 6.9 shows the normalised output power as the temperature of the crystal is tuned for both laser cavities.

From Fig. 6.9 the temperature bandwidth of both the VBG and mirror cavity can be calculated. Using the mirror cavity, the temperature bandwidth was 1.75 °C, this compared to only 0.6 °C for the VBG cavity.

By comparison, the VBG cavity exhibits a much sharper tuning curve. The narrow linewidth of the VBG limits the overlap with the acceptance bandwidth of the crystal as it is tuned. The pump linewidth clearly affects the overall temperature performance of the laser. As the linewidth is increased, the temperature sensitivity is reduced. However, the conversion efficiency will also be reduced as a result of the increased phase mismatch.

The conversion efficiency and SHG power as a function of pump power was also

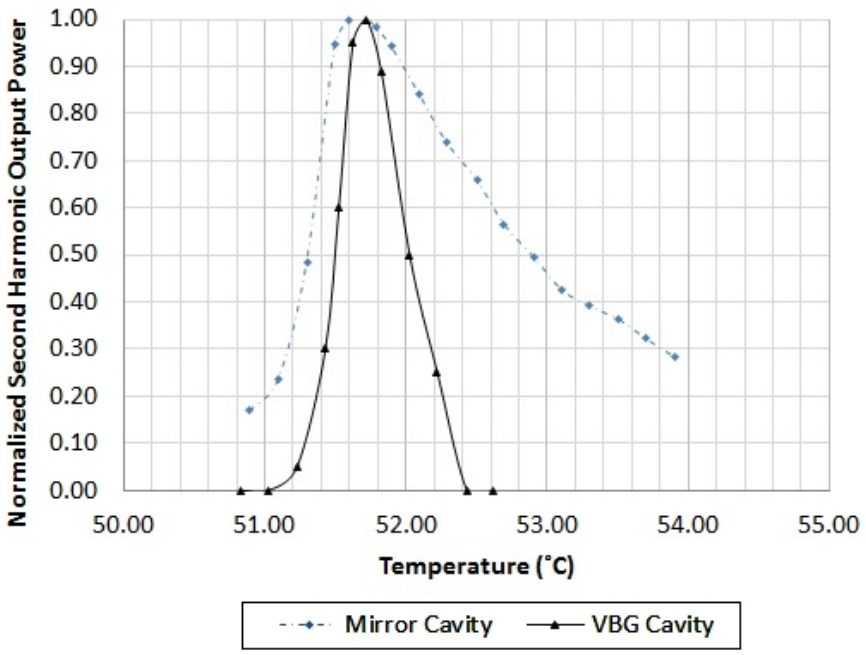

Figure 6.9 – Effect of temperature tuning MgO:PPSLT on the second harmonic power.

measured for the two configurations. This is shown in Fig. 6.10.

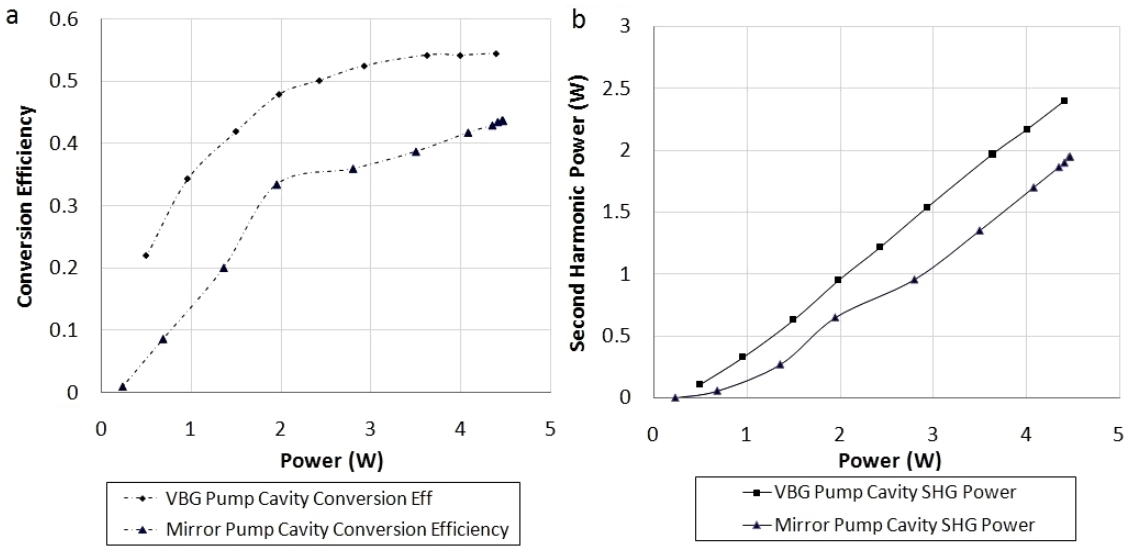

Figure 6.10 – a: Conversion efficiency of the two pump sources. b: Second harmonic output power for two pump sources.

The maximum generated power for the VBG cavity was 2.4 W compared to 1.9 W for the mirror cavity. The use of the VBG cavity improved the output power by 25%. The overall conversion efficiency increased from 44% to 56%.

The results of the mirror and VBG cavities show different behaviour in terms of conversion efficiency. In the VBG cavity, as the pump power is increased towards its maximum, the conversion efficiency appears to have reach its peak. Beyond this operating point, no further improvement in SHG conversion efficiency would be gained.

This contrasts with the conversion efficiency of the mirror cavity which still appears to be rising.

When investigating the conversion efficiency it was found that the optimum temperature of the PPSLT crystal for a given input power was different. This characteristic suggests that absorption within the crystal is leading to an increased operational temperature. As the pump is depleted through the crystal, through absorption and conversion, a temperature gradient will be created. This gradient will lead to an expansion of the poling period at the front of the crystal compared to that at the end of the crystal. The absorption of the 1064 nm fundamental pump source due to the MgO doping has previously been reported [126]. The MgO doping does increase the damage threshold but also increases the residual absorption. A second cause of the thermal effects could be green induced infra-red absorption (GIIRA) [127]. GIIRA has previously been reported in a number of different nonlinear crystals.

The performance of the SHG also differed from the modelled values shown in Fig. 6.7. The model predicted that the conversion efficiency would rise to 77%, but experimentally, it is clamped at a maximum of 56%. The cause of this is due to the simplicity of the model and the absence of dephasing through the nonlinear crystal. The dephasing parameter was first introduced by Armstrong *et al.* [125] to account for these effects. The dephasing parameter δ describes the difference in phase between the second harmonic waves originating at the input and exit faces of the crystal. There are a number of contributors to the dephasing of the second harmonic beam. These include variations in the beam divergence due to optical irregularities, the thermal gradients within the crystal described earlier, random errors in the poling period of the crystal and thermal stress-induced dephasing. The model is adapted to include a dephasing parameter using the following equation [8]

$$\eta = \eta_m sn^2[\sqrt{\eta_0/\eta_m}, \eta_m^2] \tag{6.9}$$

where

$$\eta_m = 1 + (\delta^2/2\eta_0) - \sqrt{[1 + (\delta^2/2\eta_0)]^2 - 1} \tag{6.10}$$

where the sn(x,y) function is the Jacobian elliptic with the arguments (x,y), shown in the brackets. The dephasing value can be estimated by analyzing the temperature gradient within the crystal [128]. A reduction in second harmonic power due to dephasing within PPSLT has been reported previously at pump powers above 3 W [129]. For efficient conversion, the dephasing parameter should be kept below $\pi/10$ [123].

From the behaviour measured previously, whereby the crystal temperature required adjusting for different input powers, it is clear that thermal aberrations in the crystal are present. The dephasing at input powers of around 40 W has been measured as high as $\pi/10$ [113].

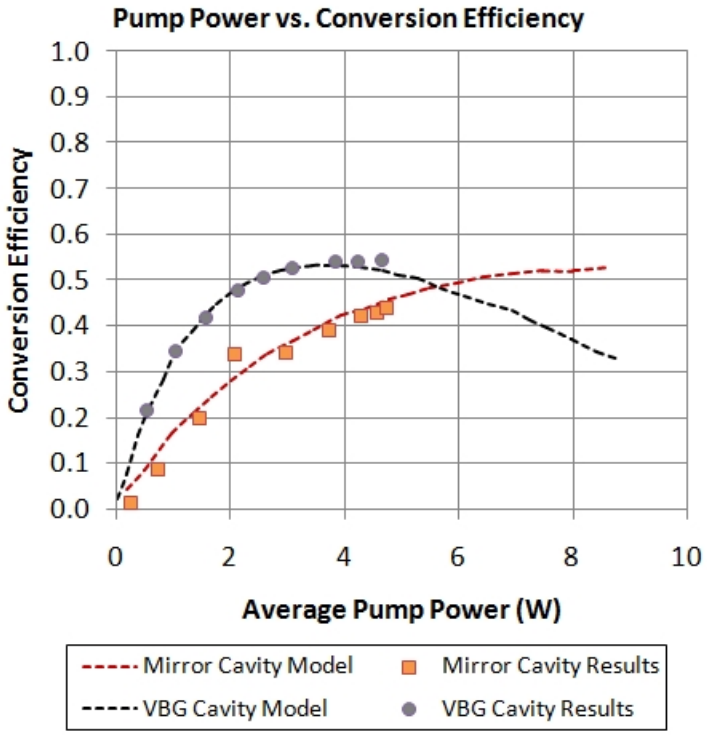

Figure 6.11 – Comparison of modelled and measured results for conversion efficiency.

In Fig. 6.11, the dephasing parameter δ is adjusted and fitted to the measured data points for both the mirror cavity and VBG cavity, allowing for agreement between the measured and modelled values. The dephasing parameter is therefore not directly measured. For the modelled calculations, the contribution of the linewidth of the pump source, depletion of the pump source through the crystal and the depahsing from the crystal is now included. The dephasing parameter modelled for both cavities is 0.088 or $0.0044\,\mathrm{mm}^{-1}$ for a 20 mm crystal, within the values quoted within the literature.

In the case of the VBG cavity, the graph shows that the configuration is operating at the optimum point for conversion efficiency. It would be expected that as the pump power is increased further, a drop in second harmonic output power would occur. In the case of the mirror cavity, limited improvement in the output power would be expected as the pump power increases further. The modelling shows good agreement with the measured values with the fitted dephasing parameter. To improve

the conversion efficiency further, future investigations could look at the parameters that affect the dephasing within the crystal to limit these effects.

The M^2 of the SHG was then measured for both configurations. For the mirror pump source an M^2 of 1.33 in the horizontal and 1.11 in the vertical was measured. For the VBG cavity pump source, the M^2 was 1.45 in the horizontal and 1.3 in the vertical direction. The M^2 measurement shows a reduction in the beam quality as the fundamental beam is converted. The degradation in the beam quality could be due to a number of parameters. Thermal lensing within the crystal as a result of absorption of the pump light can degrade the M^2 of the beam, variations and dislocations in the poling period can also degrade the 532 nm beam. The higher M^2 measured for the VBG-cavity-pumped SHG would be expected, as the VBG cavity itself has a larger M^2 compared to the mirror cavity.

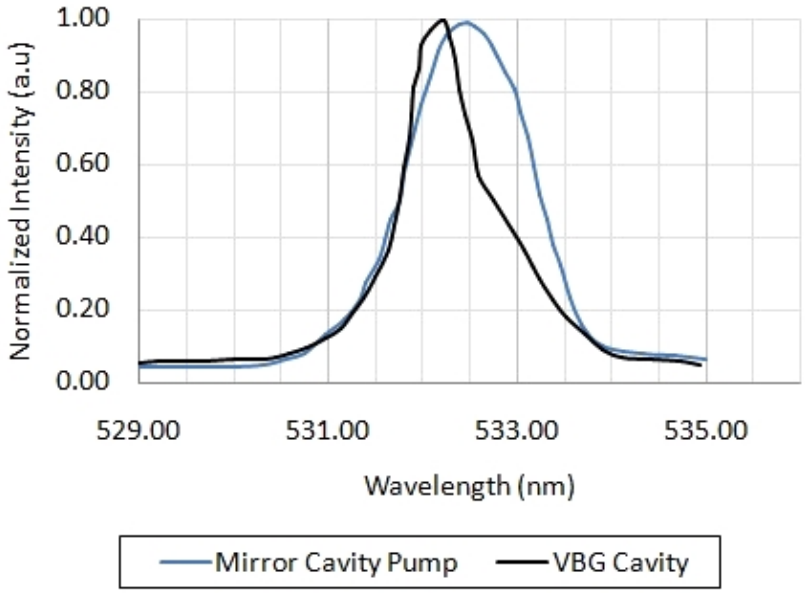

Figure 6.12 – Second harmonic spectrum from both pump sources.

The linewidth of the second harmonic was also measured for both configurations. This is shown in Fig. 6.12. The figure shows the second harmonic bandwidth is narrower when pumped with the VBG cavity source. The narrow spectrum does possess broad wings away from the centre wavelength at 532 nm. This broadening may be a characteristic of the crystal, rather than a result of the pump spectrum. Any variation in the poling period or other induced phase errors discussed earlier when defining the dephasing parameter, would also lead to a broadening of the second harmonic spectrum.

Finally the pulse width of the two configurations was also compared. The pulse widths were measured at 43 ns and 50 ns for the mirror and VBG cavities respectively.

Both configurations produced pulse widths of around $\sqrt{2}$ of the pump pulse widths, in agreement with the theory [105].

6.4 Discussion

The aim of this chapter is to demonstrate Q-switching of the VBG cavity introduced in chapter 3 and to investigate the efficiency of second harmonic generation, from the line-narrowed source.

In a Q-switched configuration, the VBG cavity generated average output powers of up to 4.6 W at a rep rate of 20 kHz with pulse durations of 72 ns. A comparison of the performance between the standard mirror cavity and the VBG cavity for Q-switched operation was also completed, highlighting the comparable performance of the two cavities.

The configuration did, however, lead to slightly different behaviour from that shown in chapter 3 section 3.2.2; most notably a degradation in the M^2. This behaviour was present in both fixed Q and Q-switched configurations, and is therefore not a characteristic of the Q-switched operation itself, but of the cavity configuration. By switching to a crystal with undoped end-caps, the beam quality may have improved as a result of weaker thermal lensing and an increased spot size on the VBG.

The linewidth of the Q-switched cavity was also wider than the linewidth for the CW operation shown in chapter 3 section 3.2.2. It would be expected that the resultant linewidth of the Q-switched cavity would be narrower than that measured for CW operation. The cause of the increased linewidth is thought to be due to spatial hole burning and gain saturation in the build-up phase, as well as the VBGs spectral response. The resultant linewidth of the Q-switched cavity was 0.19 nm compared to 0.97 nm for the CW cavity.

When using the Q-switched VBG cavity, high conversion efficiency SHG was also demonstrated. As a result of the narrow linewidth, a 12% improvement in the conversion efficiency, compared to the traditional mirror cavity was achieved, leading to an increase of 25% in the second harmonic output power. The investigation has highlighted that cavities similar to the configuration shown here could provide a genuine alternative to standard solid-state laser cavities and improve the efficiency of a number of different industrial laser systems.

6.5 Conclusion

This chapter has demonstrated the improvements in second harmonic conversion efficiency through the use of a VBG-narrowed source and highlighted the suitability of a VBG cavity for efficient SHG. Initially a Q-switched laser is demonstrated in both a plane-plane mirror cavity and a line-narrowed VBG cavity. In these setups 2.6 kW of peak power is generated, with pulse widths of 66-72 ns. In the VBG cavity configuration, the setup generated a linewidth of 0.19 nm. This compared with a linewidth of 0.97 nm for the mirror cavity. The M^2 was found to be 1.1 for the mirror cavity and 1.25 for the VBG cavity. The two pump sources were then used to pump a MgO:PPSLT nonlinear crystal. An improvement of 12% in overall conversion efficiency was observed, giving an increase of 25% in the second harmonic power.

Chapter 7

VBG-Locked Laser-Diode Arrays

7.1 Introduction

In this chapter the use of VBG-locked laser-diode arrays are investigated with the aim of improving the environmental operating range of current diode-pumped solid-state laser configurations. The operational temperature range for lasers operating on military aircraft is typically -40 - 60 °C. The implications of the thermal control were discussed in section 1.1.8. This chapter focuses on LDAs that can pump a solid-state gain medium over this temperature range by locking their emission wavelength using VBGs. If successful, this will allow for the removal of TEC based coolers, therefore reducing cost, weight and power consumption. The work completed in this chapter was presented in a SPIE publication [130].

First, an analysis of the performance of current laser-diode array designs used within military products is completed, highlighting the requirement for temperature control. A brief analysis of laser diode technology is provided, as well as calculations to determine the requirements for locking the wavelength of the LDA. Within this analysis, the locking of a LDA capable of being a drop-in replacement to lasers currently in service is investigated. As a result of this constraint, the locked LDA investigated here differs from others in terms of the LDA growth design, feedback and line width. The work was completed as part of a joint programme with laser diode manufacturer Lasertel. A custom-made quantum well gain structure was designed specifically for locking of the LDA over a broad temperature range within the constraints of the design requirements. This work was completed by M McElhinney *et al.* . The investigation and optimisation of each of these parameters is presented in this chapter. The performance of the VBG-locked devices over temperature is then analysed and compared to that of the temperature controlled LDAs.

The VBG-locked devices used in this chapter were supplied by Lasertel. These devices were designed and constructed by Lasertel. The subsequent modelling of the

temperature range, impact on laser resonator performance and testing was completed by the author.

7.2 Conventional Temperature Controlled LDAs

As highlighted in chapter 1 section 1.1.1, the most common military laser configuration is a diode-pumped Nd:YAG slab in a cross-Porro resonator cavity. The investigation is primarily based on this configuration. The characteristics of this cavity are discussed in chapter 1 section 1.1.4.

The pump geometry uses a 1.1 % doped Nd:YAG zigzag slab with a 5 x 5 mm aperture, 67 mm in length. The slab is side-pumped by LDAs operating in the 800 nm region.

Whilst the zigzag slab gain medium reduces the thermal lens strength, the geometry limits the absorption depth that is achievable. The slab sizes are scalable, however, any increase in the dimensions will typically increase the Fresnel number of the resonator, therefore degrading the divergence of the laser system. As a result, the investigation is limited to the use of 5 mm slabs.

The overall absorption efficiency in the slab will be dependent on the operating wavelength of the pump diodes and the absorption coefficient profile of the active gain medium used. Fig. 7.1a shows the absorption coefficient of 1.1 % Nd:YAG, from results provided by crystal manufacturer Northrop Grumman SYNOPTICS, as well as the effective absorption efficiency as a function of wavelength for a 10 mm absorption depth. This represents a double pass of a 5 mm thick zigzag slab.

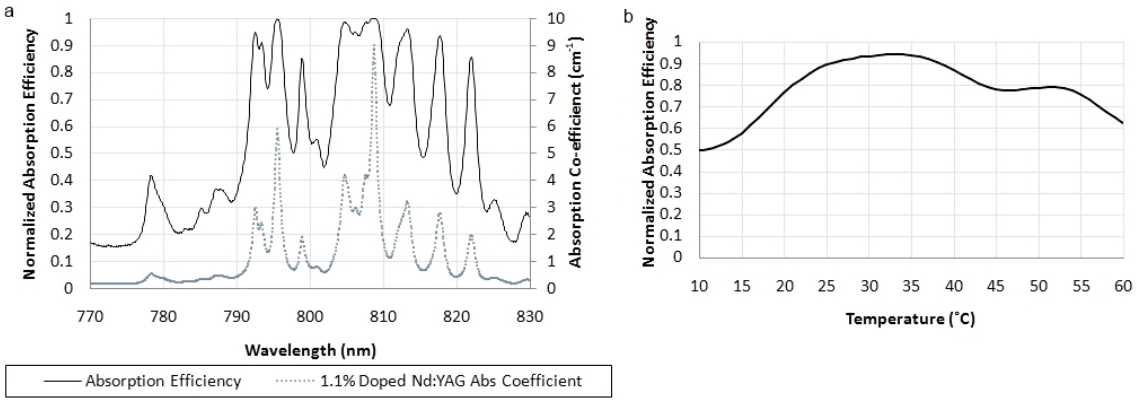

Figure 7.1 – a: Absorption coefficient of 1.1% Nd:YAG and absorption efficiency of zigzag slab versus wavelength. b: Absorption efficiency over temperature of 5 nm FHWM LDA.

As expected, Fig. 7.1a shows how the absorption efficiency at the peak coefficient values is close to 100 %, assuming no coupling losses. As the centre wavelength moves away from the peaks in the absorption profile, a reduction in the absorption efficiency is observed. The reduction in the absorbed power will lead to a reduction in the output energy of the laser.

The emission wavelength of the laser-diode is temperature-dependent. This temperature dependency arises primarily as a result of the changes in the band gap energy. The temperature dependence of the density of states in both the conduction and valence bands leads to a change in the quasi-Fermi levels within the junction. As the junction of the diode is heated, the density of states increases, reducing the separation of the quasi-Fermi levels and thereby decreasing the band gap energy. Contributions from the changes in refractive index that occur when current is applied, can also increase the emission wavelength. In the quasi-CW operation, discussed in section 1.1, two different temperature effects occur. The transient chirp of the wavelength and linewidth occurs during the pulse [131] due to thermal heating of the gain region and the refractive index variations. Bulk wavelength shifts due to the external temperature, and the overall thermal time constant of the laser diode package will also occur. It is the bulk temperature tuning effect that is considered in this analysis. The bulk temperature coefficient of the emission wavelength of a GaAs based laser diode is typically 0.27 nm/°C [8] at 808 nm.

The performance shown in Fig. 7.1a can therefore also be considered a function of temperature. The operating range, over which the diode achieves 80 % absorption efficiency, is only 7 nm. This corresponds to a temperature range of only 26 °C. Fig. 7.1b shows the absorption efficiency of a laser diode centred at 808 nm at 35 °C with a 5 nm linewidth and 10 mm absorption depth over temperature. With an operating temperature range of over 100 °C, it is clear from this basic analysis, that temperature control would be required to operate the laser in this pump configuration.

If the temperature dependence of the laser diodes could be removed, the devices would no longer require thermal control, allowing for un-cooled devices to be used in targeting lasers. One method of achieving this is by locking the laser diode centre wavelength.

7.3 Wavelength-Locking of Laser Diodes

Simplistically, locking of the laser diode wavelength is achieved by preferentially seeding a specific section of the gain spectrum within the laser diode material. The ability

to lock over a wide wavelength range can be achieved due to the fairly broad gain bandwidth present in laser diode structures. Fig. 7.2 shows the shape of a typical gain spectrum of a GaAs singe-quantum-well (SQW) heterostructure emitter. This data was provided by M. McElhinney at Lasertel [132].

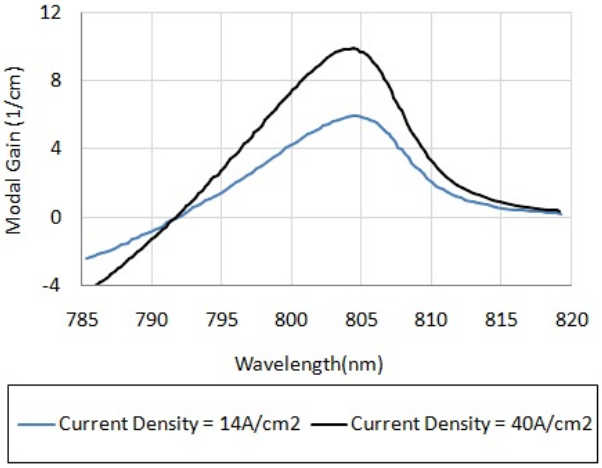

Figure 7.2 – Modelled modal gain spectra of single-quantum-well laser-diode from [132].

The gain curve shape is consistent with those reported elsewhere [133]. The typical bandwidth of a single quantum well is 10 nm. The peak gain is given by [131]

$$g(N) = a(N - N_{tr}) \tag{7.1}$$

where N_{tr} is the carrier density at transparency, N is the injected carrier density and a is the gain parameter. The typical values of N_{tr} and a in GaAs are 1-2$\times 10^{18}$cm^{-3} and 3-5$\times 10^{-16}$cm^2 respectively [131].

The emitter will lase on the longitudinal modes closest to the peak of the gain curve, assuming that cavity losses are similar across the curve. The longitudinal modes of the diode cavity are given by the equation

$$\lambda = 2n_{sc}L_{sc}q \tag{7.2}$$

where n_{sc} is the semiconductor refractive index, L_{sc} is the semiconductor cavity length and q is the mode number. Under normal conditions, where no attempt has been made to narrow the linewidth, the emitter will lase on a number of longitudinal modes. The resultant finite linewidth is typically caused by both gain clamping of the modes within the laser cavity and changes in the refractive index due to carrier injection [134]. The increased linewidth as a result of these effects is referred to as the linewidth enhancement factor LEF [135].

The carrier-induced refractive index change will cause a number of different effects. The complex part of the refractive index, which accounts for the gain or losses within the medium, will change as current is applied. This typically causes a transient variation in the gain curve, leading to a red shift in the emission as the device is switched on. The resultant linewidth of an SQW emitter is often $\geq 1\,\text{nm}$ when operating at a number of times above threshold.

The threshold condition for each mode is [131]

$$\Gamma g(\lambda) = \alpha_i + \alpha_m \tag{7.3}$$

where Γ is the confinement factor in the laser diode, typically 0.25 in weakly-guided double heterostructures and 0.03 in single quantum-well structures [136]. α_i and α_m refer to the internal loss and the losses through the end-mirror facets respectively. $g(\lambda)$ refers the gain as a function of wavelength.

In the configuration described in chapter 1 section 1.1.6, the QCW arrays will have a much broader linewidth than that of a single emitter. A single bar containing up to 60 emitters will have a linewidth of around 3 nm as a result of thermal, structural and molecular growth variations. These variations lead to chirping of the various emitters across the bar, widening the linewidth.

The threshold current I_{th} for a broad area multi-mode emitter can be calculated from the following equations, using the notation from Buus et al. [131].

$$N_{th} = N_{tr} + \frac{\alpha_{tot}}{a\Gamma} \tag{7.4}$$

$$R(N_{th}) = \frac{N_{th}}{\tau_s} + BN_{th}^2 + CN_{th}^3 \tag{7.5}$$

$$I_{th} = eV_aR(N_{th}) \tag{7.6}$$

Where τ_s is the cavity lifetime, the parameter $\frac{N_{th}}{\tau_s}$ refers to the non-radiative recombination leakage, and α_{tot} is the total losses from α_i and α_m. The parameter R is the spontaneous recombination rate, B refers to the radiative band-to-band rate and C is the non-radiative auger recombination rate. N_{th} is the threshold carrier density, V_a refers to the volume of the cavity and e is the charge of an electron. From these equations, the threshold of a given configuration can be calculated. The calculation, completed as a function of wavelength, is shown in section 7.4.

7.3.1 Methods of Locking

Whilst the lasing emission of the emitters typically occurs in the central region of the gain, a number of different designs for controlling central emission wavelength and limiting the temperature tuning rate are available. Configurations such as distributed feedback (DFB) lasers, distributed Bragg reflector DBR lasers, external locking with gratings and injection-locking all have the ability to define an operational central wavelength that differs to the peak in the gain spectrum. The most commonly used design in telecommunications is the distributed feedback (DFB) Laser. In this design a grating is written into the actual active region of the semiconductor. The overall round-trip gain is higher for the modes that are resonant with the grating, resulting in the emission occurring at the grating centre wavelength. As the gain curve centre wavelength drifts over temperature, the grating centre wavelength drifts with a much smaller temperature coefficient, resulting in a reduced temperature sensitivity [137].

The DBR laser has a Bragg reflector at one or both ends of the laser cavity. The grating is fabricated outside of the active region but still constructed from the semiconductor material. The Bragg reflector acts as an end mirror which favours operation at the Bragg wavelength due to the increased round-trip gain compared to wavelengths out with the Bragg resonance.

The techniques described here for controlling the emission wavelength of an emitter all typically achieve locking by decreasing the overall round-trip losses of the resonant wavelength, thereby reducing the threshold compared to those not at the Bragg wavelength. The threshold is reduced by increasing the mirror reflectivity, α_m at the desired emission wavelength.

For these resonant devices, the threshold condition for a given mode is now calculated using the equation

$$\Gamma g(\lambda) = \alpha_i + \alpha_m(\lambda) \tag{7.7}$$

The wavelength dependence is now included in the mirror losses $\alpha_m(\lambda)$. A narrow spectral reflectivity response, centred at the desired wavelength, will decrease the threshold at this wavelength, whilst increasing the threshold for all other wavelengths. If the periodic grating has a smaller temperature coefficient than the gain curve, the temperature response of the operating wavelength will be reduced. As a result, the typical spectral temperature dependence of a DFB laser is 0.1 nm/ °C [137]. When considering this temperature coefficient for pumping the central absorption peak from 803-809 nm in Fig. 7.1, this performance could provide temperature-insensitive opera-

tion over a 60 °C range.

Whilst this does not cover the full temperature range required, it provides a reasonable percentage of the 100 °C range. Other methods of operation could be considered to allow for operation at lower temperature. Heating the diodes using simmer currents or even multiple emitters with different wavelengths could be used. The main issue with the use of DFB/DBR lasers is the ability to fabricate DBF structures into an emitting bar. The complex and involved growth requirements of the grating typically limit the devices to single emitter configurations, although DBR bars are now available [138].

7.3.2 VBG-Locked LDA Characteristics

In order to circumvent the more complex growth issues, locking of the wavelength using a grating external to the semiconductor material is often used. The use of an external grating allows for a series of emitters in a single bar to be locked by the same element. The grating can also be fabricated from a material other than the semiconductor, thereby reducing the overall temperature sensitivity of the feedback.

In order to provide stable temperature operation, VBGs written into thermo-refractive-glass are often used. As shown in chapter 2, the temperature coefficient of the grating is 9 pm/°C, providing a stable feedback over a broad temperature range. VBG-locked laser diodes were first demonstrated by P. Mills *et al.* [139] in 1985, using a LiNbO3 volume holographic grating to stabilise a 1.55 μm laser diode. The use of a PTR glass VBG-locked laser diode was demonstrated by B. L. Volodin *et al.* [140]. The ability to lock the wavelength of laser diodes has allowed for better control over the centre wavelength [141]. It has also allowed for efficient pumping of solid-state gain media that possess narrow absorption bands [142].

The configurations for a typical VBG-locked laser diode are shown in Figs. 7.3a and b.

To lock the wavelengths of the bars, feedback from the emitting intensity is required to seed the desired wavelength. The angular emission from the diode array is typically very broad, with a half angle divergence of 5 and 16° in the slow and fast axis respectively.

In order to achieve sufficient feedback from the VBGs, lensing of the fast axis is commonly used. The fast-axis collimation (FAC) improves the locking mechanism by

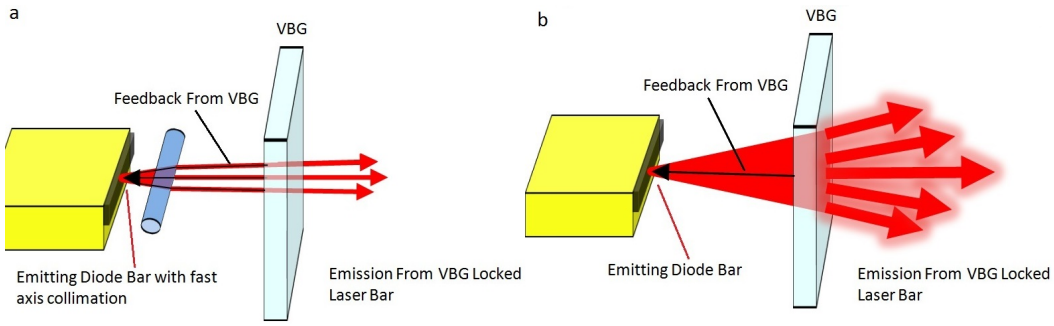

Figure 7.3 – a: Laser bar with fast-axis collimation, locked by VBG. b: Laser bar without fast-axis collimation, locked with VBG

both increasing the reflectivity from the VBG and increasing the coupling of light into the emitter due to improved spatial overlap of the reflected beam. This is shown in Fig. 7.3a. As a result of the increased coupling into the facet, the locking range can be improved [141]. Losses are still present in this configuration due to the divergence in the slow axis.

Lensing does have a number of disadvantages. The increased complexity and reliability of the design has an impact on the life of the device when considered within a military environment. The main disadvantage, however, is the increased cost of a collimated laser-diode. The use of lenses within laser-diode arrays can, at the time of writing, double the cost of the LDAs. In a typical laser, the LDAs can form a large percentage of the total cost. As a result, any cost saving gained from the removal of the thermal control would be greatly outweighed by the lensing costs.

For use within the configuration shown in Fig. 7.4, which is the conventional LDA design first shown in chapter 1 section 1.1.6, the divergence of the LDAs also acts to homogenise the gain profile within the slab. In a lensed LDA configuration, however, the absorption in the profile is no longer homogeneous [143], leading to a reduction in the beam quality.

The simplest and cheapest locking method is the use of an un-lensed array, as shown in Fig. 7.3b. The feedback from an un-lensed emitter is significantly reduced due to the emission angle. The two factors that reduce the coupling of the VBG in this configuration are the large divergence angle of the LDA compared to the acceptance angle of the grating and the spatial mismatch of the reflected light. The coupling of an un-lensed array is shown in Fig. 7.5. As a result of the reduced feedback, previously reported configurations have estimated the coupling efficiency of the VBG to the emitter to be in the region of 2-10% [141].

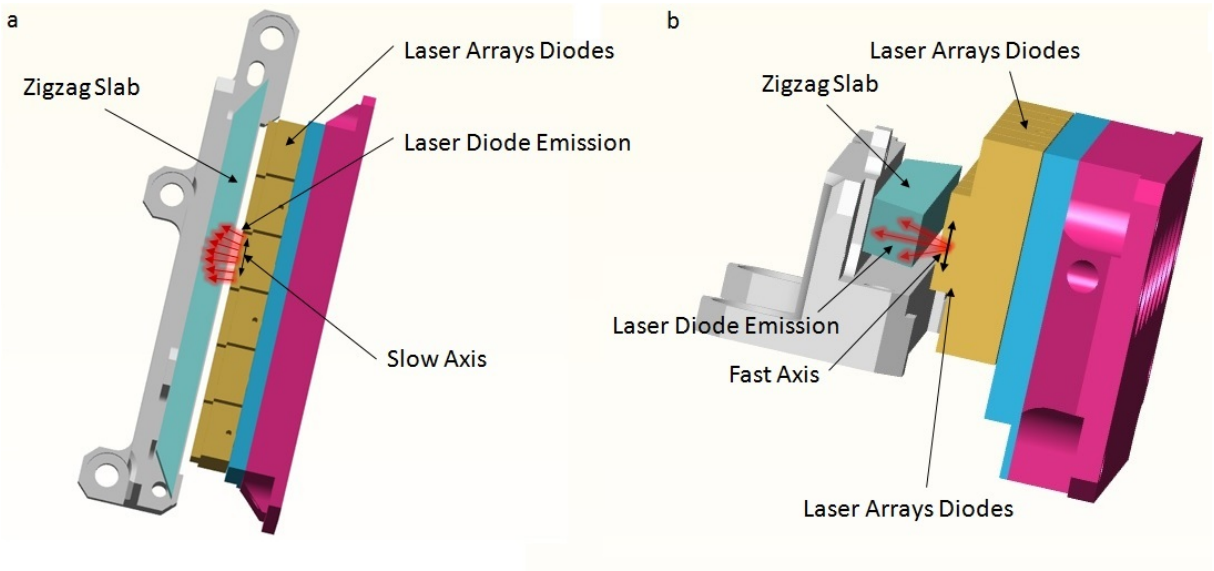

Figure 7.4 – a: Top view of conventional diode-pumped zigzag slab configuration. b: Side view of conventional diode-pumped zigzag slab configuration.

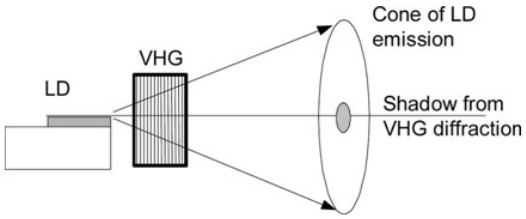

Figure 7.5 – Diagram of VBG coupling (taken from Steckman *et al.*, IEEE J. Sel. Topics Quantum Electron. Vol:13 No:3).

7.3.3 VBG Spectral Linewidth Effect on Pumping of Zigzag Slab

The use of VBG-locked LDAs allow for both new lasers to be designed without any thermal control as well as retro-fitting into existing programmes. In order to do so, the new LDAs must meet the same specification as those they displace. From a power and centre wavelength consideration, the aim would be to match the specification of the current design outlined in chapter 1 section 1.1.5. The spectral bandwidth specification of the current design is $\Delta\lambda = 2 \leq \lambda \leq 6$nm at a centre wavelength of 805 nm. The wide bandwidth of the arrays is due to the spectral features in the Nd:YAG absorption spectrum, shown previously in Fig. 7.1. The bandwidth ensures that the absorption profile within the slab is uniform by distributing the absorbed power within the broad absorption feature from 803-808 nm. This limits the overall power within the large peak at 808.6 nm and therefore the power density within the slab. The 2 nm minimum bandwidth specification is too wide compared to the narrow response of the grating, typically ≤ 0.5 nm. The narrow bandwidth is a function of the refractive index change in the VBG, which is limited to 10^{-3}.

A comparison of the absorbed power density in a 5 mm slab with a double pass for a number of different linewidths and centre wavelengths is shown in Fig. 7.6a. To ensure that the one dimensional heat flow is preserved, matching the absorbed power density from a narrow band source to that of the broad emission from a conventional device was investigated. By changing the centre wavelength of the VBG to 806 nm, the exponential profile can be reduced. The resultant profile is still not as uniform as the profile created by the 4 nm free-running spectrum. The impact of this could be to modify the thermal lens characteristics of the gain medium, thereby changing the beam quality of the laser. For lasers currently in production, any change in components that would result in a change in performance would require full re-qualification, the cost of which would outweigh any advantages gained from the new configuration.

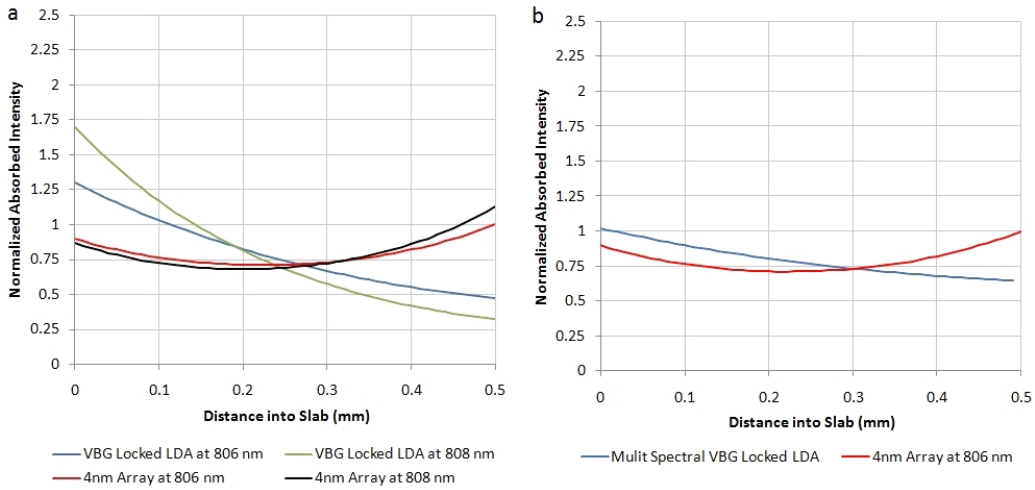

Figure 7.6 – a: Double-pass normalised absorbed intensity of single VBG within a zigzag slab compared to two examples of a 4 nm bandwidth unlocked array. b: Normalised absorbed intensity of chirped VBG within a zigzag slab.

By creating a spectrum with three discrete wavelengths, each with a 0.5 nm bandwidth, a broader spectrum can be achieved whilst maintaining the same absorption profile. This is shown in Fig. 7.6b. The multi-spectral VBG profile contains three 0.5 nm FWHM peaks centred at 803,804 and 806 nm. The three peaked spectrum provides a much closer match to the free-running emitter intensity profile than the single wavelength VBG.

The simplest solution to creating a VBG with multiple peaks is to apply a chirp to the grating wavelength as a function of depth[144]. In these configurations the VBG grating vector is expanded throughout the grating, thereby allowing for a wider bandwidth, or even multiple peaks in the VBG reflectivity spectrum. The challenge in this incorporation is that the reflected beam must travel much further into the

grating than it would for a single wavelength grating. The result of this would be a reduction in the coupling of the reflected light into the emitter in the same manner as that discussed in section 7.3.2. Another solution is to apply chirp across the grating, rather than into the grating. This is shown in Fig. 7.7.

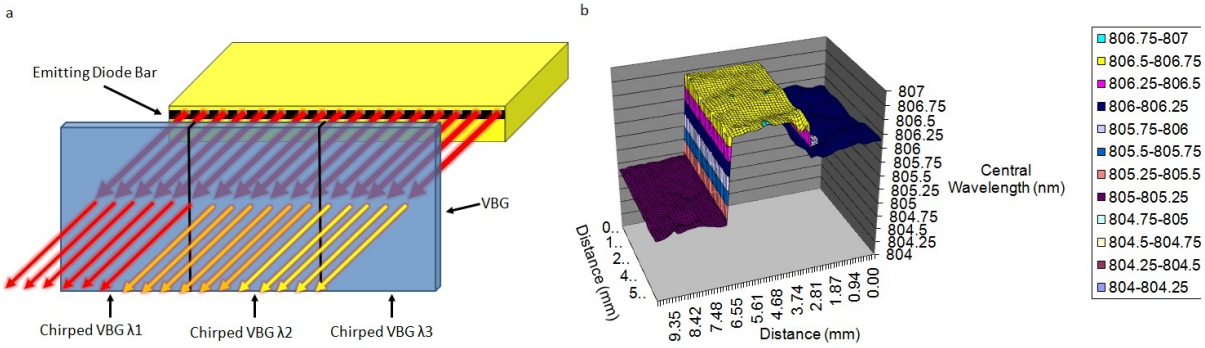

Figure 7.7 – a: Diagram of emitting bar with chirped VBG. b: Three Dimensional VBG centre wavelength profile (supplied by grating manufacturer Ondax).

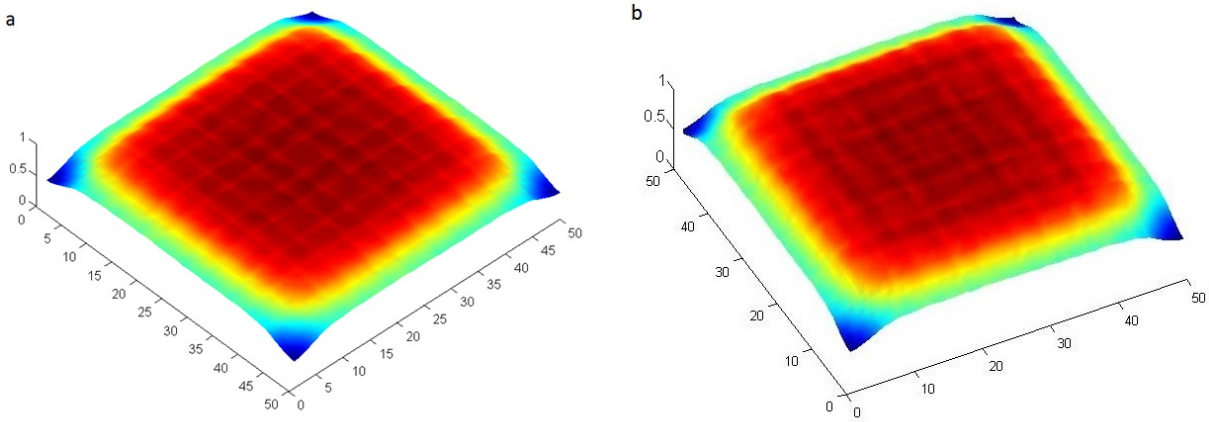

Figure 7.8 – a: Normalised small signal gain profile conventional LDA. b: Normalised small signal gain profile for chirped VBG-locked LDA.

The configuration shown in Fig. 7.7a could result in a spatially varying power density, and therefore small signal gain, across the slab. The divergence of the slow axis will ensure that mixing between the discrete wavelengths occurs to a certain extent, therefore homogenising the profile. The intensity profile was modelled in the ray tracing program ASAP [145] and compared to the conventional free-running scenario. A more detailed analysis of this model is outlined in chapter 8 section 8.2.2. The variation in small signal gain along the zigzag path as a result of this is shown in Fig. 7.8 compared to that of the conventional array. The gain profile of the chirped VBG is not significantly different to that of the conventional array. Limited variation in the actual mode profile would therefore be expected as a result of the chirped VBG profile, whilst the wider overall linewidth is compatible with the current specification.

7.4 Temperature Threshold Analysis of Locked LDA

In this section, the temperature range of the VBG locking is calculated. Using the laser diode equations described previously in equations (7.4)-(7.6), the effect of the grating feedback on the threshold of an emitter, and therefore the round-trip gain, can be calculated. Using the modal gain spectrum from Fig. 7.2, the threshold of an emitter can be calculated as a function of the wavelength. This is shown in black in Fig. 7.9. This represents the free-running emitter threshold. The current threshold is calculated from the carrier density threshold N_{th}. For this calculation, the cavity length was 500 μm with an emitter area of 100×1 μm. The transparency level N_{tr} was $1\times10^{18}\,\mathrm{cm}^{-3}$ and the gain parameter a was $6\times10^{-16}\,\mathrm{cm}^{2}$.

The threshold of a device that has a narrow spectrally dependent feedback is also calculated. To ensure a wide locking range, the round-trip losses at all wavelengths other than those within the spectrally locked region should be increased. This is typically achieved by decreasing the facet reflectivity, so that the cavity is dominated by the VBG feedback. Decreasing facet feedback is commonly used for high-power QCW LDAs to reduce the intra-cavity intensity. An AR coating is applied to the passive layer on the output facet, with reflectivities typically ranging from 5-15%. For the VBG threshold calculations, the facet feedback was reduced to 2%. A narrow reflectivity over the central wavelength region was also applied representing the VBG feedback. The total VBG coupling reflectivity was 1.9%. This includes a VBG reflectivity of 95% and a 2% coupling efficiency factor described in section 7.3.2. For this calculation we have taken the lowest coupling efficiency value quoted. The VBG-locked device threshold is also shown in Fig. 7.9 in blue, with the VBG spectral response shown in green.

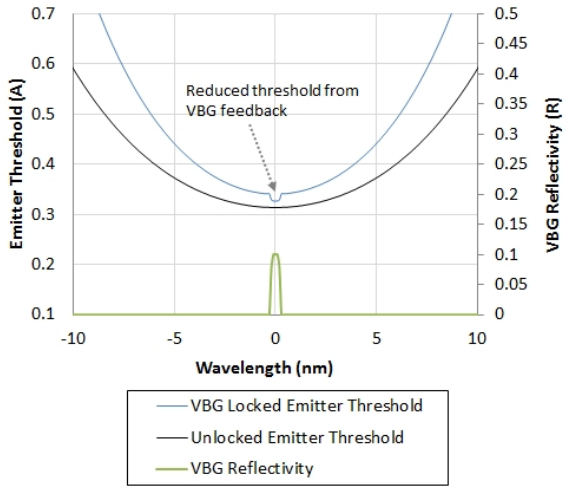

Figure 7.9 – Threshold of free-running and VBG-locked laser diode.

The threshold curve of the VBG-locked device shows a small trough where the VBG reflectivity peaks. The result is a lower threshold current in the VBG feedback region. Fig. 7.9 also shows that the threshold is higher for the VBG-locked devices in all other regions, including those within the VBGs spectral response. The shape of the gain curve is also steeper. This is due to the reduction in the combined feedback from the facet and VBG, which is 4% compared to 10% for the free-running case.

For the VBG-locked device, the emission should be locked to the spectral response of the VBG. The assumption for this basic analysis is that the laser will typically lase at the lowest threshold point. This assumption has been used in previous analyses [146] [147]. The condition for locking the spectral emission is therefore

$$I_{th\,VBG} \leq I_{th} \tag{7.8}$$

where I_{th} is the threshold current outside the VBG-locked region. For this calculation the carrier density is assumed to be clamped at the threshold level [148]. A number of different parameters that affect the gain within the cavity can cause locking of the LDA to be lost. One of the effects that must be considered is the longitudinal mode spacing of the semiconductor cavity. The wide mode spacing will limit the number of modes present within the VBG spectral response, forcing oscillation outside this range. The longitudinal spacing of a 500 μm cavity is 0.18 nm, allowing only two modes to operate within the VBG bandwidth. However, in a broad area emitter, a number of higher order transverse or lateral modes ($\geq$100) are present [133], each possessing a slightly different centre wavelength frequency. In this configuration, these modes can fill the full spectrum of the VBG, allowing for efficient extraction of gain. In single mode lasers, larger attenuation of the areas outside the VBG response is required due to both the longitudinal mode spacing and spatial hole burning, which allows for side modes in the unwanted spectrum to occur [131].

Fig. 7.9 shows how the device characteristics change when the VBG spectral peak is placed at the centre of the gain curve. At this operating point, the actual VBG feedback will not shift the spectral output of the LDA, as the peak in the gain curve is within the VBGs spectral response. If the gain curve centre wavelength changes, the VBG feedback will no longer be at the peak.

The locking range of the VBG can be determined by increasing the temperature of the emitter. This will cause the gain curve to red shift at the rate of 0.27 nm/°C, the VBGs spectral response will only shift at 0.009 nm/°C. Fig. 7.10a shows the gain curve shifted by 8 °C. The shape and magnitude of the gain curve has been assumed to be

constant over temperature. The section within the VBG feedback is clearly visible, and the threshold within the locked section is slightly lower than the centre of the gain curve. At this operating point locking should occur and the laser will emit at the VBG wavelength. It should also be noted, however, that the threshold has increased further compared to that of the free-running spectrum. This would manifest itself as a reduction in output power of the bar.

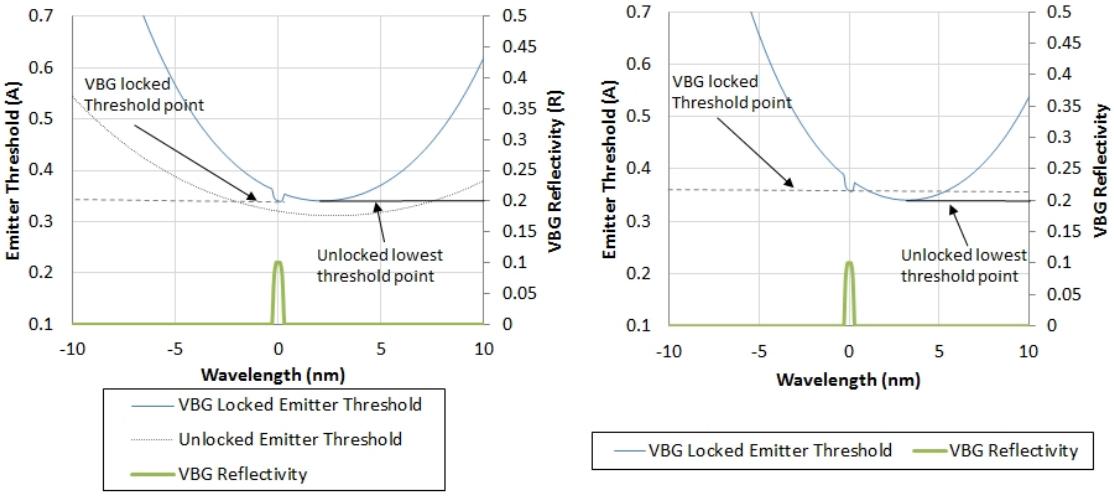

Figure 7.10 – a: Modal threshold of free-running and VBG-locked emitter running at +8 °C from ambient. b: VBG-locked emitter running at +12 °C from ambient.

As the VBG centre wavelength occurs further to the left or right of the central peak in the gain, the threshold will increase as a result of the Lorentzian line shape of the gain function. This will continue to occur until the point at which the threshold level of the centre gain point is lower than the actual VBG-locked section of the gain. At this operating point, the laser diode will un-couple from the feedback of the grating and power will start to leak from other regions in the gain curve. This is shown in Fig. 7.10b for an operating temperature of 12 °C above ambient.

From the previous calculation, the point at which locking is lost from the grating can be predicted. Fig. 7.11 shows the effective threshold of the VBG-narrowed spectrum and the lowest threshold for modes outside the VBG-locked section over temperature. The temperature range in which locking should occur is highlighted. When the threshold of the VBG-locked region rises above the free-running threshold, locking is lost. This is also highlighted in Fig. 7.11.

This calculation predicts a locking region of 16 °C, when both the operation above and below the ambient temperature is included. This result is similar to other reported results [141]. Note that the model does not predict an increase in the threshold of the

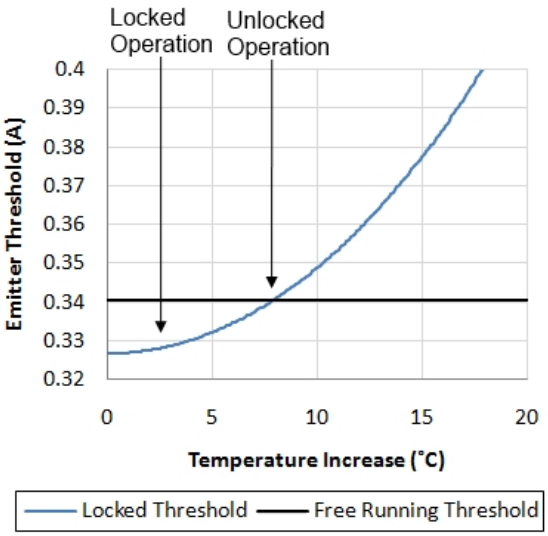

Figure 7.11 – Lowest mode threshold of free-running and VBG-locked region.

free-running spectrum. In reality, the threshold would be expected to increase with temperature due to changes in the overall gain level and a rise in non-radiative effects within the diode junction [133].

It is clear from this simple analysis that the VBG-locked device would not be suitable for operation over the full temperature range. The limitation of the locking range is a function of both the strength of the feedback from the VBG and the shape and width of the gain curve. By modifying either of these parameters the locking range can be improved.

The feedback of the grating is limited to 2%, provided a 99%R grating is used. The limited feedback is due to the method of operation, as described in section 7.3.2. In order to improve the operating temperature range of the device, a broader gain curve is required. This would ensure that the threshold of the locked section does not degrade as quickly, when the temperature increases. A chirped multi-quantum-well (MWQ) structure with a broader gain spectrum was subsequently investigated. The gain spectrum was designed by McElhinney *et al.* at Lasertel. The gain structure was specifically designed for wide temperature operation. The modelled gain spectrum of a MQW device is shown in Fig. 7.12.

The MQW structure expands the gain region from 12 nm to 25 nm by chirping the quantum-wells in a single emitter. The result is three quantum wells with a chirp of 7 nm between each quantum well layer. The expansion of the gain region allows for locking to be achieved over a wider temperature range. The same calculation as completed for the single quantum well structure is completed for the MQW structure. For this calculation, the VBG reflectivity was also increased from 95% to 99% to

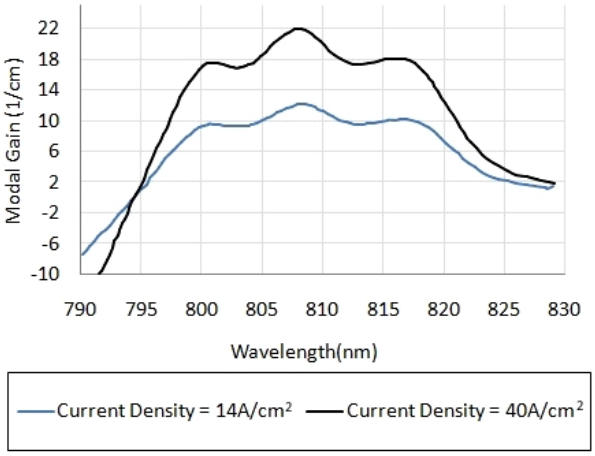

Figure 7.12 – Modelled modal gain of multi-quantum-well (from McElhinney *et al.*).

further improve the locking range. The threshold analysis is shown in Fig. 7.13a and b.

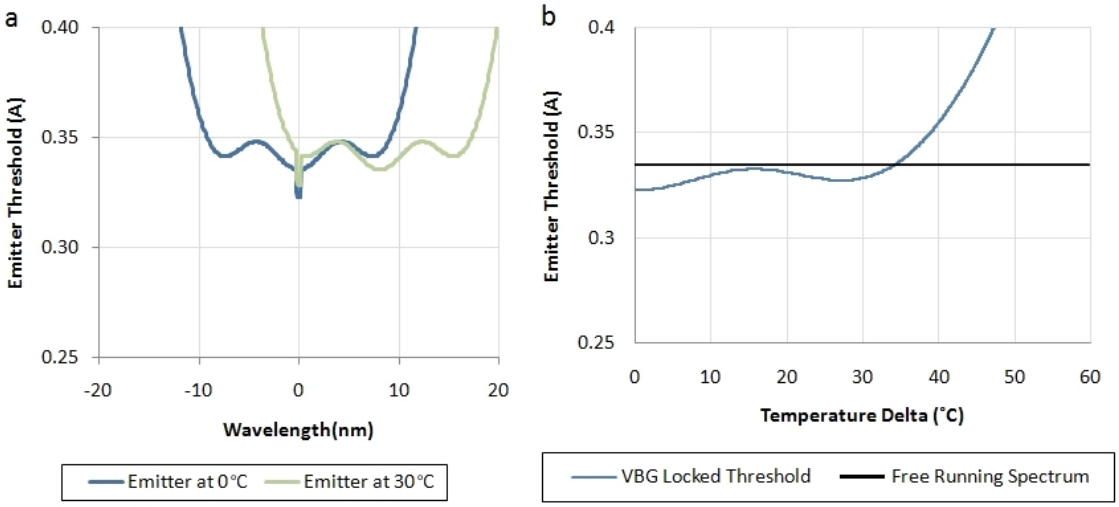

Figure 7.13 – a: Modal threshold of emitter at ambient and +30 °C. b: Threshold of free-running and VBG-locked spectrum.

Fig. 7.13b shows the VBG-locked threshold drops below the lowest mode threshold at 35 °C. The MQW structure can therefore achieve a locking range of 70 °C. VBG-locked devices could therefore achieve locking across a large percentage of the required temperature range. Although the current predicted range does not cover the required military temperature range, in an un-lensed VBG-locked configuration, the locking range is much wider than has previously been reported. To operate across the full temperature range, a number of different methods of operation could be considered. Simmer currents similar to those used in flashlamp-pumped systems [149] could be implemented to increase the operating temperature before firing commences. The simmer current would heat the diode when operating at lower temperatures, thereby reducing the observed temperature range. Increased duty cycle operation at the colder

temperatures could also be used to increase or maintain the temperature of the devices within the locked range.

The limitation of these devices is also considered. Previously it was highlighted that the two main factors that could improve locking are the feedback reflectivity and the width of the gain curve. In this method of operation, the VBG reflectivity cannot be increased any further. The gain curve has also been broadened by the inclusion of the MQW structure. The limitation to further broadening of the gain spectrum is both the semiconductor growth complexity and the associated costs. A further expanded gain curve would require significantly more production effort, therefore increasing the complexity, yield and cost of the devices. As such, the construction of the devices was completed with the current chirped MQW structure investigated here.

The other aspect of the LDA performance to consider is the increase in threshold as the VBG tries to lock further away from the centre of the gain curve. In Fig. 7.13, an increase of 5% in the threshold value is observed, as the temperature is increased from the centre gain region to the point where the emitter becomes unlocked. As a result, the gain will also reduce, leading to a reduction in the output power at any given operating current. In the single quantum well structure shown in Fig. 7.11, a similar reduction in threshold was observed from only a 7 °C increase in temperature. The larger increase is due to the narrower gain profile. A smaller temperature rise will therefore move the locking position further up the gain curve. Depending on the actual quantum well shape, a larger increase in threshold may be observed, and therefore a larger reduction in power in the chirped MQW device.

In this section, the performance of the VBG-locked LDA with a chirped multi-quantum well structure has been predicted, with an estimated locking range of 70 °C. A 5% increase in the threshold of the laser was also calculated, which may impact on the performance of the LDA. In the next section, VBG-locked LDAs using a chirped MQW gain structure are characterised in both a stand-alone configuration and pumping an Nd:YAG zigzag slab. This basic analysis has shown that the locking range of the VBGs is smaller than the 100 °C range required. As a result, it is unlikely that VBG-locked devices, in this configuration at least, could meet the requirements for drop-in replacement in current targeting lasers that would allow for the complete removal of thermal control. Future developments could see improvements in the feedback from the VBG or an increased spectral bandwidth from the chirped MQW structure. Characterisation of the LDAs is still being completed to examine the locking range and the performance of a resonator pumped with VBG-locked LDAs.

7.5 Experimental VBG-Locked LDA Characterisation

The LDAs described in the previous section were constructed by Lasertel. The VBG's were bonded onto the arrays at the front as shown in Fig. 7.14.

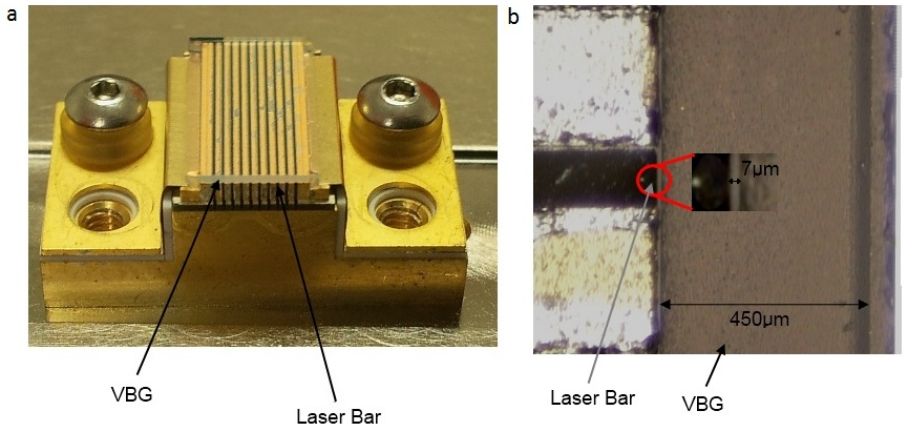

Figure 7.14 – a: Picture of VBG-locked LDA. b: Magnification of emitter VBG interface.

The devices were specified to provide a peak power of 1 kW per LDA in a 230 μs pulse duration with a 20 Hz repetition frequency. Five LDAs would be used to pump the zigzag slab as shown previously in Fig. 7.4. The spectral specification defined a centre wavelength of 805 nm, with a FWHM of 2-6 nm. The locking range was based on a best effort basis, however, the aim was to provide locking over the full 100 °C range, from -40 to +60 °C. The devices were compared to the conventional unlocked arrays with the same power and centre wavelength specification. These devices require a fixed operating temperature of 45 °C and are also supplied by Lasertel. The LDAs were mounted onto a water-cooled heat exchanger to provide temperature control. The water-cooling only provides coarse temperature control. As the LDAs begin to fire, they still exhibit an initial warm-up period before a steady state temperature is reached. This temperature increase was measured by monitoring the emission wavelength of the free running LDAs as they fired. The temperature rise was measured to be 5 °C.

One of the key performance characteristics is the output power from the arrays. It has been shown in the previous section how an increase in the threshold of the arrays may be present as a result of the VBG locking. The output power performance of the VBG-locked LDAs over temperature was compared to the conventional LDAs, which were held at a fixed temperature of 45 °C for all of the subsequent testing. This is shown in Fig. 7.15a. The output power was measured using a Scientech power meter and laser calorimeter. The operating temperature of the VBG-locked devices was adjusted by changing the water temperature.

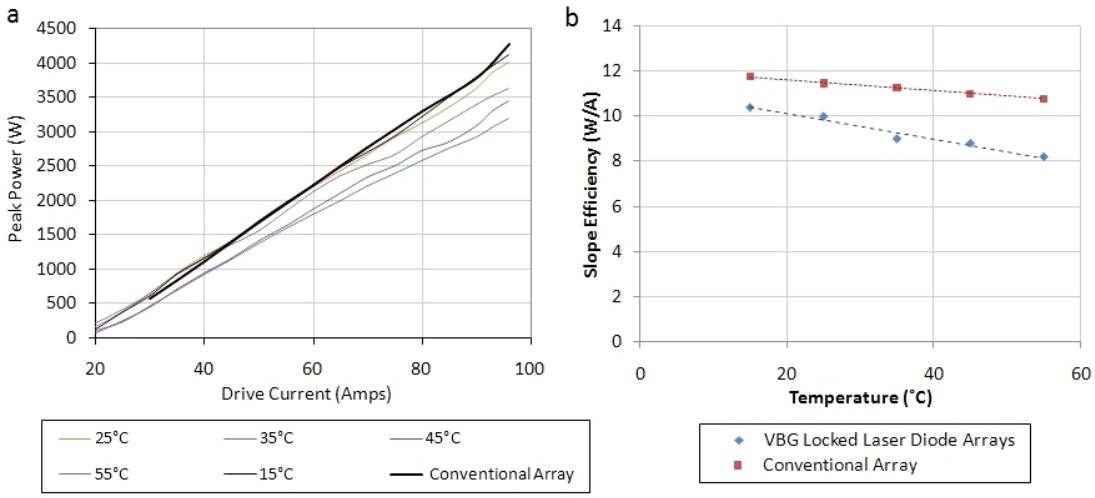

Figure 7.15 – a: LI curve of VBG-locked and conventional pump head configuration. b: Slope efficiency of VBG-locked and conventional LDA over temperature.

The comparison shows that at 15 °C the output power of the VBG-locked arrays is similar to that of the free-running conventional devices. As the temperature of the locked arrays is increased, a significant reduction in the output power is observed. At 55 °C the output power has dropped by 23 % compared to the 15 °C performance.

A comparison of the slope efficiency for both a conventional free-running array and the VBG-locked array is shown in 7.15b. For both arrays, as the temperature is increased, a reduction in the slope efficiencies will be observed due to changes in the Fermi levels, an increase in the transparency level and increased non-radiative transitions. A larger drop is observed in the VBG-locked case when compared to the conventional free running LDA. The main cause of this was discussed in the threshold analysis in section 7.4. The analysis showed the increased threshold is the result of the reduced gain due to locking. The reduction in gain will lead to a reduction in the slope efficiency. The increase in threshold from the locking is therefore compounded by the temperature related threshold increase discussed earlier.

The spectral performance of the VBG-locked LDA was then analysed. Both a static and a transient analysis were performed on the LDAs. Fig. 7.16 shows the spectral output of the device measured after 120 s of operation from 15 - 65 °C. The spectral traces were recorded using a USB 2000 Ocean-Optics fibre coupled spectrometer, the resolution was 0.15 nm.

Fig. 7.16a shows the spectrum remains static as the temperature is increased, highlighting the locking of the VBG. The chirped nature of the VBG spectrum can also be observed, with three defined peaks at 803,804 and 807 nm. At higher temperatures, a broader peak occurring outside the locking range of the VBG can be observed. This

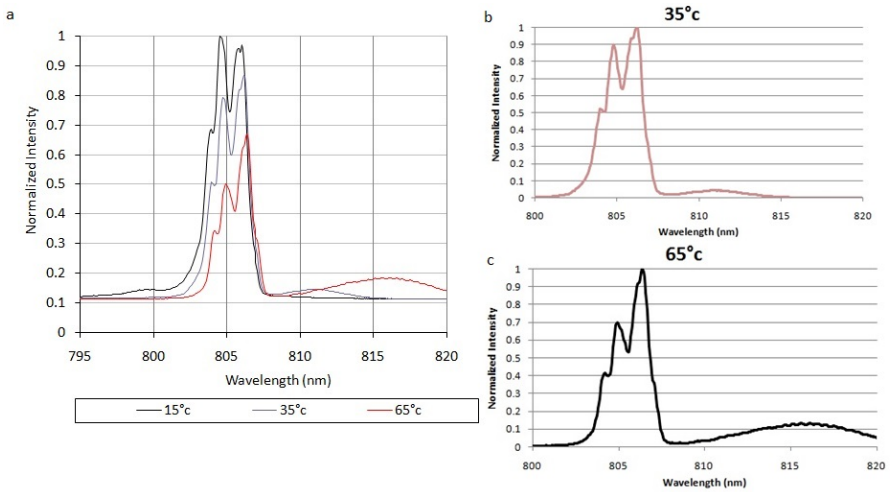

Figure 7.16 – a: VBG-locked spectrum at various diode temperatures. b: VBG-locked spectrum at 35 °C. c: VBG-locked spectrum at 65 °C.

is power from the LDA beginning to unlock from the VBG reflectivity. The operating performance at 35 and 65 °C is investigated in further detail to observe the effect of the unlocked power. These are shown in Fig. 7.16b and c.

From Fig. 7.16c, a broad emitting peak outside of the VBG reflectivity ($\geq$808 nm) can be observed. The wavelength of this emission is clearly temperature dependant. From Fig. 7.16 the smaller unlocked peak was measured to be shifting at a rate of 0.2 nm/°C. This rate is similar to the rate expected of an unlocked emitter. The amplitude and total power within the broad peak also increases as a function of temperature. Fig. 7.17 shows the percentage of power within the locked spectral region. The figure does not include the actual reduction in output power from the LDAs, only the spectral variation.

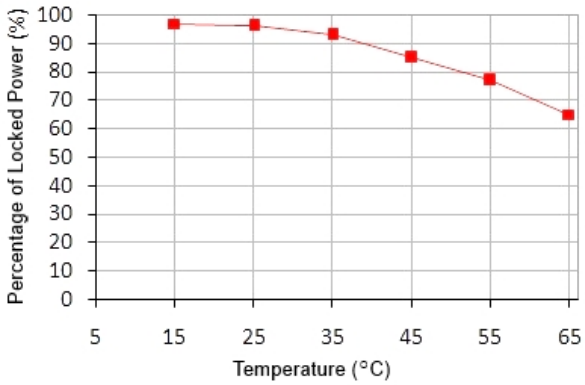

Figure 7.17 – Percentage of power contained within locked region.

The overall percentage of locked power reduces linearly beyond 35 °C, where over 95% of the power is contained in the locked spectrum, to 65 °C where only 65% of the power is locked. The implications of this performance are discussed later in section

7.5.1.

The transient effects of running the devices were also analysed, and the changes in the spectrum and output powers were recorded. This method of operation better represents the typical operating environment of the LDAs. Fig. 7.18 shows the transient performance at 45 °C.

The same overall spectral characteristics can be observed. The power can be seen starting from within the locked region and leaking into the unlocked section of the spectrum as the device heats up. The normalised integrated output power from the spectral trace is shown inset in Fig, 7.18. This output power reduces by 7% over a 40 s period once the LDA commences firing.

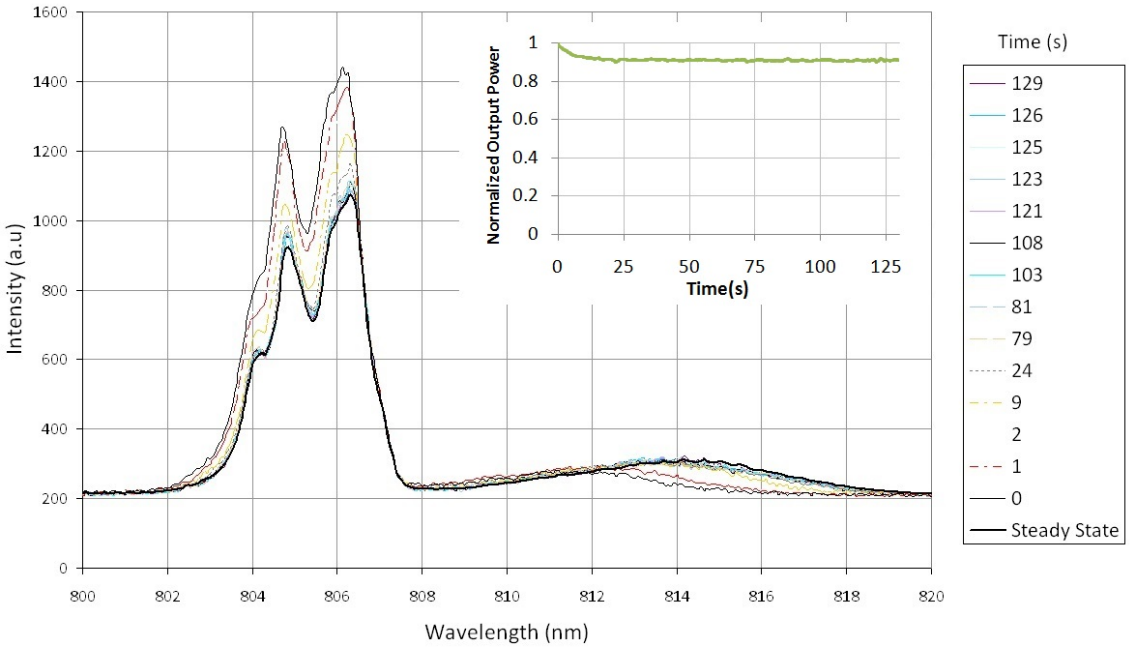

Figure 7.18 – Transient analysis of VBGs spectral response. Inset: Normalised output power with time.

7.5.1 VBG-Locked LDA Discussion

The performance of the LDAs shows that locking of the centre wavelength can be achieved over a wide temperature range. The devices can operate up to 40 °C with over 90% of the total power contained within the locked spectrum. If we assume, from Fig. 7.17, that locking will follow a similar pattern as the LDA temperature is reduced to below 5 °C, an estimated total locking range of 70 °C should be achievable. However, this range may vary as the laser diode gain parameters will increase as the temperature is reduced, possibly lowering the locking range.

Whilst the spectral analysis shows that locking is achieved over a wide range, at 45 °C, the output power from the LDA is still only 87% of the peak power at 15 °C. The overall useful power, when taking into account only the power within the locked region, is therefore 75%. This still represents a significant performance level, if improvements in the feedback strength could be achieved, both the locking range and the temperature dependant output power could be improved.

As the temperature is increased beyond 45 °C, the amount of power contained within the locked region continues to reduce. The emission of the unlocked power is spectrally broad, similar to an LED rather than that of a laser diode. The spectrum of the unlocked section suggests that the feedback provided by the facet reflectivity, which has been reduced to 2%, is insufficient to achieve lasing action. The behaviour observed is more similar to amplified spontaneous emission rather than stimulated emission. This effect could be caused by band-filling of the MQW structure [150] [133]. This can cause gain to be trapped by current injection into regions that are below threshold, causing an increase in the spontaneous emission rate.

With the VBG centred on the gain spectrum at 20 °C, the modelled locking range in section 7.4 was 35 °C. The point at which the threshold of the unlocked region should rise above that of the locked region is therefore 55 °C. The temperature at which the locked power decreases below 85% is 45 °C, with the amount of locked power decreasing linearly from 35 °C, rather than a single shift from a locked to an unlocked regime. The two processes are slightly different. The modelling completed previously only looks at the threshold of the lasing modes. In the experimental behaviour, the lasing outside the locked region may be a result of emission from modes that are below threshold.

The decreasing power and the increase in fluorescence could also occur due to the inability of the locked section to provide sufficient feedback for efficient extraction. This effect would be stronger for the chirped quantum well structure. The two quantum wells that are not within the peak resonance of the VBG are essentially being locked a large distance away from their peak gain values. As a result, poor extraction and increased fluorescence will occur. The result would be spectrally broad emission from the unlocked spectrum. As the temperature is increased further, the unlocked power increases as the peak gain of the quantum-wells move further away from the VBG.

To improve the locking range further, a reduction in the gain and a subsequent increase in the VBG reflectivity would lead to a larger separation between locked and unlocked sections of the spectrum. The reduced gain would also reduce the spontaneous emission from the unlocked section of the gain curve. A reduced gain structure was

postulated by Lasertel after analysing of the results and modelling presented here and from their own investigations. Further investigation of these devices have presented elsewhere [130]. The reduction in gain did show an improved locking range with the absence of the unwanted spontaneous emission up to 65 °C. As a result of the reduced gain, these devices showed a reduction in output power.

7.6 Laser Cavity Characterisation

The VBG-locked LDAs were then used to pump a zigzag slab within a cross-Porro resonator design. The configuration is shown in Fig. 7.19

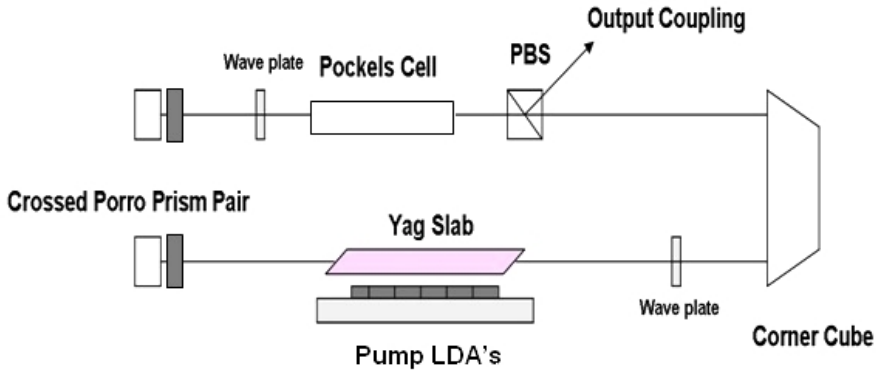

Figure 7.19 – Experimental configuration of cross-Porro resonator.

The characteristics of the cross-Porro resonator have been discussed in chapter 1 section 1.1.4. In this chapter we use the resonator configuration to investigate the performance of the VBG-locked LDAs compared to the conventional LDAs. The LDAs were configured into a pump head with five arrays, as shown in Fig. 7.4. The diodes were operated at a constant current of 96 A, and a voltage of 100 V.

This analysis will determine the effects of the VBG-locked LDAs on the output energy, beam profile and beam quality of the Nd:YAG laser compared to conventional LDAs. The output energy is of key consideration, this parameter determines the amount of energy on the target. The near and far field profiles are also analysed. The near field parameter is analysed to determine the extraction of gain and also the peak power density within the resonator. The far field profile will also determine the energy on target. Any degradation in the beam quality will manifest itself as a reduction of these parameters.

The laser is operated in the Q-switched regime, using a $LiNbO_3$ Pockels cell to

provide a half-wave retardation, changing the Q of the cavity. The actual single pass retardation is only quarter-wave, with the full half-wave occurring after a double-pass. The reflectivity of the cavity is de-tuned from the optimum of 50%R to 30%R to limit the peak power within the cavity, as discussed in chapter 1 section 1.1.5. Fig. 7.20 shows both the energy performance of the laser over temperature and the transient energy variation.

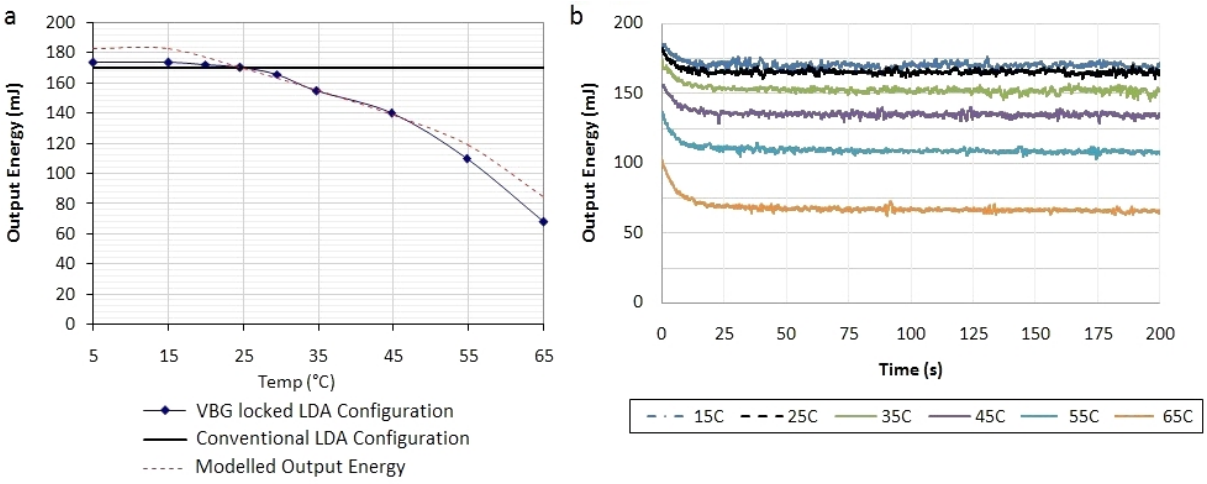

Figure 7.20 – a: Output energy over temperature. b: Transient energy performance.

Fig. 7.20a shows the energy reduction over temperature of the VBG-locked devices, compared to the conventional LDA performance, which was measured at a fixed temperature. The laser performance shows the same characteristics as the diode output power. The modelled output energy utilises the output power results measured previously, as well as the calculated absorption efficiency from the measured output spectrum. The agreement between the modelled and measured values show that the reduction in energy is caused by the diode output power and spectrum variation. The transient output energy is shown in Fig. 7.20b. This shows the reduction in output energy as a function of time. In Fig. 7.18 the transient behaviour of the LDAs was investigated and the output power as a function of time was characterised. The output energy of the laser is consistent with this behaviour.

The laser performance shows a reduction of 40% in the output energy at 65 °C when compared to the conventional LDAs. This reduction in energy will ultimatley lead to a reduction in the overall performance of the targeting system.

The beam characteristics were also analysed. Fig. 7.21 shows the near and far field beam profiles over temperature. In this figure the trend of decreasing near and far field diameters as a function of temperature can be observed. The cause of this is the reduced pump power available at higher temperatures. This was confirmed by

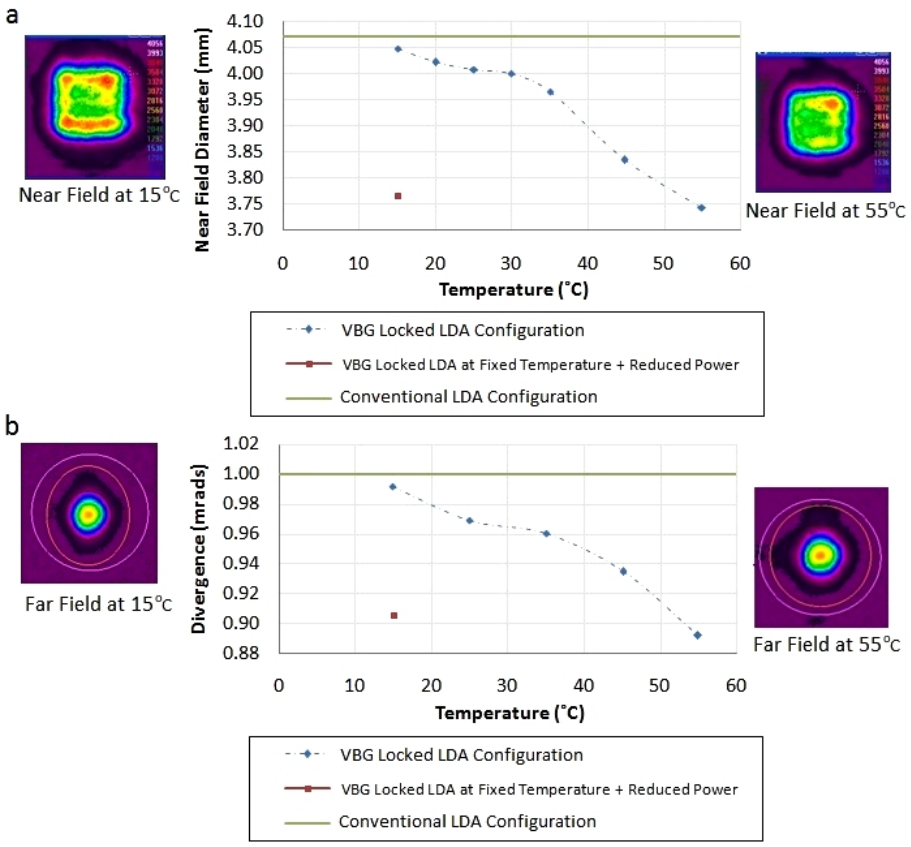

Figure 7.21 – a: Comparison of near field values for VBG-locked and conventional free-running LDAs. b: Comparison of divergence values for VBG-locked and conventional free-running LDAs.

the data point shown in red. This was taken at an operating temperature of 15 °C, with a reduced pump power similar to the level available at 55 °C. When compared to that at 55 °C, both the near and far field values are very similar. As a result, the VBG-locked LDA performed similarly to that of the conventional LDA pumped configuration. At similar operating temperatures and pump powers, only a 2% reduction in the near and far field diameters was observed between the two configurations.

The properties of the laser cavity beam do not vary when compared to the conventional LDAs. This demonstrates that the use of VBG-locked LDAs can provide similar beam quality and near field properties to that provided by the conventional LDAs. Matching of the FWHM does appear to ensure the beam properties do not degrade. The far field divergence values are similar to within 1%, and near field diameters to within 2% when operating at similar pump powers. These are key parameters when considering the replacement of free-running LDAs with VBG-locked LDAs.

The performance of the VBG-locked LDAs pumping a Q-switched Nd:YAG laser has shown the issue highlighted in section 7.5. The reduction in the LDA output power over temperature does impact on the performance of the laser resonator. The result is

the reduction in output energy of the laser cavity over temperature. The reduction in output energy will ultimately limit the use of the devices in laser products. Operation over the required temperature range of 100 °C will be more complex as a result of the decrease in output power from the LDAs and subsequent laser energy. From their current performance, the VBG-locked LDAs were not considered as a complete solution to a drop-in replacement for current production lasers. The conclusion of this investigation was to look for other possible methods of meeting the temperature range requirements, whilst trying to optimise the VBG locking to improve performance.

7.7 Conclusion

In this chapter the design and operation of VBG-locked LDAs has been investigated. The design of an un-lensed, spectrally broadband VBG-locked device has been presented, with the motives and design parameters detailed. Modelling of the VBG locking has shown that the chirped MQW gain structure used in this configuration should be capable of a 70 °C locking range. Testing of the spectral performance shows locking was achieved over a 50 °C range, although spectral components outside of the locked region were observed. Up to 24% of the power leaked from the unlocked spectral regions over this range. Analysis of the locked laser diode performance has shown a reduction in power and efficiency of up to 25% when compared to a conventional laser diode. The devices were then used to pump an Nd:YAG zigzag slab within a cross-Porro resonator. The locked LDAs were found to provide comparable near and far field profiles to the conventional LDAs. However, the output energy was found to degrade with temperature. At a temperature of 45 °C the VBG-locked LDA-pumped resonator produced 18% less energy than the conventional LDAs. The output energy from the resonator degraded further as the temperature was increased. The degradation was shown to be due to the reduction in overall pump power and the locked power from the LDAs.

As a result, whilst the performance of the locked VBG LDAs has shown a much wider operating range than has previously been demonstrated for an un-lensed configuration, the temperature range is still smaller than that required for a military laser. VBG-locked LDAs were therefore not considered as a replacement for current temperature-controlled LDAs. The devices could still have a number of uses in industrial lasers, where the temperature range is often much smaller. The removal of thermal control from these lasers could have a number of advantages in terms of cost and usability.

Chapter 8

Temperature-Insensitive Pumping of Zigzag Slabs using Multi-Pass Pump Setup

Figure 8.1 – Selex Athermal Type 163 Targeting Laser

8.1 Introduction

In this chapter, a new multiple-bounce diode-pumping setup is explored, with the aim of achieving thermally insensitive operation by increasing the absorption depth. This chapter focuses on the development of a QCW laser-diode array with reflectors, pumping a thick zigzag slab. The chapter considers the performance of the design with respect to absorption efficiency, small signal gain, thermal lensing and laser resonator performance. Characterisation of different prototypes is then presented.

This work is part of the development of a new athermal laser designator at Selex. The technology outlined in this chapter is subject to patent application AU2011333947 (A1) and is used in the Type 163 laser, shown in Fig. 8.1. To date eight of these lasers, using the pumping scheme described in this chapter, have been produced and tested over an operating temperature of -40 °C to 85 °C. A further 50 units will be produced

in 2014.

8.1.1 Temperature Insensitive Operation Requirements

The aim of this chapter is to develop a laser diode pumping scheme that can operate in an environmental temperature range of -40 to +60 °C. Man-portable lasers, described in chapter 1 section 1.1.8, must also operate without any form of active cooling such as fans or water-cooling. As a result of the thermal response of the laser chassis, the LDA bases will actually reach a maximum temperature of 85 °C when firing. This maximum temperature was determined from thermal modelling completed at Selex. The LDA operating temperature requirement for man-portable lasers is therefore -40 to 85 °C.

As well as operation over the stated temperature range, the design must also be compatible with the current zigzag slab described in section 1.1.2 of chapter 1 and the cross-Porro and ring resonator cavity designs described in chapter 1 section 1.1.4 and 1.1.7. This requirement is to ensure compatibility with other laser products produced at Selex.

If locking of the wavelength cannot occur over the entire temperature range, the wavelength of the LDA will drift at a rate of 0.27 nm/°C. A pump configuration in which the absorption length is greatly increased would reduce the variation in absorbed power over temperature. In chapter 7 Fig, 7.1, the absorption of the pump light within a side-pumped 5 mm zigzag slab with a double-pass was shown. If the diode emission path length within the slab could be further increased, then the performance would be improved over the temperature range. Using Beer-Lambert's law and the absorption spectrum of Nd:YAG with a 1.1% doping, the variation in absorbed power over temperature and wavelength can be calculated. Taking an 808 nm diode at 35 °C, a path length of 3.5 cm would be required to achieve a minimum absorption efficiency of 70% over the full temperature range.

8.1.2 Increased Path Length Configurations

A change in the pumping geometry from that of the conventional design would be required to achieve the increased path length described in the previous section. The simplest method of increasing the absorption depth is to change from a side pumped geometry to an end or edge-pumped configuration. A number of different end / edge-pumped zigzag slab configurations have been demonstrated [151] [152] [153]. One

of the disadvantages of longitudinal pumping is the variation in the thermal gradient across the slab, which is not corrected by the zigzag path [154]. Increased temperature gradients close to the slab face will occur, as well as end-bulking effects which cause an increase in the strength of the thermal lens. As the wavelength varies, the absorption depth will also change, increasing or decreasing the strength of the thermal lens [155]. This will cause the beam quality to vary over the temperature range. Thermal lensing can be reduced by the use of undoped end-caps [60]. However, the use of these would significantly increase the cost of the slabs. The induced thermal lens from the variation in absorption depth would still cause variations in the beam quality.

For these reasons it is often preferred to use a side-pumped zigzag slab geometry for military lasers. To achieve an increased absorption depth within this configuration, multiple passes of the slab would be required.

Other pumping configurations also suffer from limited absorption depths. Side-pumped thin slabs used in high power CW configurations have limited absorption due to the thickness of the gain medium, typically $\leq 200\,\mu$m [156]. The low absorption allows for reduced thermal gradients in the slab and a homogeneous gain deposition. The efficiency of side-pumped configurations of this type suffer due to the limited absorption. A novel configuration for achieving an increased absorption depth has been described by Faulstich *et al.* [157]. In this configuration a reflective medium with small transmitting patches is placed between the emitting bars and the gain medium to reflect the incident light. An example of this is shown in Fig. 8.2.

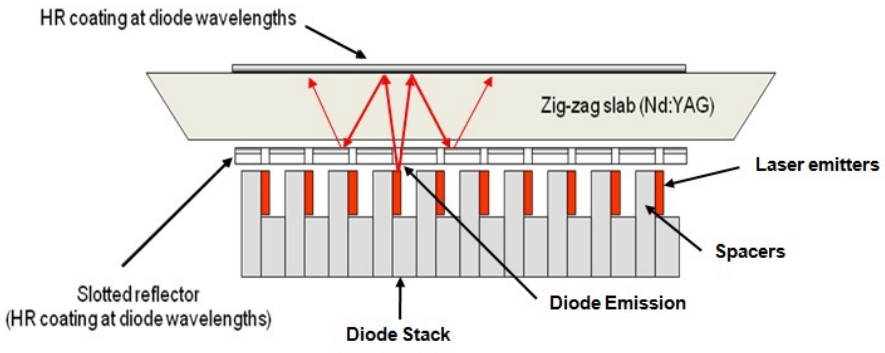

Figure 8.2 – Diagram of a side-pumped slab with a slotted reflective plate.

The reflector placed between the LDAs allows for light not absorbed in the first pass to undergo multiple passes of the gain medium. The absorption efficiency increases significantly due to the increased absorption length. The large divergence of the emission will limit the amount of light retro-reflected back into the emitters. By matching the size of the slots to the emitter size, losses from pump light re-incident on the semiconductor substrate are limited.

Another configuration, where individual reflectors have been placed onto the laser diode spacer material, has also been reported [157]. However, the cost of this configuration would limit its use for this design. Other pump configurations, in which the slab is placed within a reflective chamber, have been reported [23]. The inclusion of a chamber may complicate the laser-diode emitter configuration and would be difficult to implement in the current cavity designs. The simplest configuration for implementing a multi-bounce pump design is therefore the use of a single reflector, with transmitting patches, that is attached to the LDA. This configuration is compatible with the current cavity designs and does not require a change to the laser resonator configuration.

8.2 LDA with Reflector Design

To improve the efficiency of the multi-pass effect, a number of changes to the pump configuration were investigated. The changes are highlighted in the list below and the performance parameters are outlined in the subsequent sections. The following design parameters were investigated:

1. Rotating bars to swap the fast and slow axis.
2. Bar spacing optimisation to improve multi-bounce efficiency.
3. Use of multiple bars with different wavelengths to expand temperature range.
4. Reflector material placed on the LDA.

8.2.1 Rotating Bars to Swap the Fast and Slow Axis

A schematic of the conventional configuration is shown in Fig. 8.3a. In this configuration the fast axis divergence of 36 ° is in the y-plane, perpendicular to the zigzag path. The rays diverging in this axis at the angular extremes, and even those with modest angles, do not achieve any subsequent passes, as they are incident on the diffuse surfaces at the top and bottom of the slab. The limit to the number of bounces achieved is therefore the height of the slab.

An improved geometry is shown in Fig. 8.3b. By rotating the bars so that the fast axis diverges in the z-plane, the same as the zigzag path, the pump emission can now achieve multiple bounces along the slab length. The reflective plate ensures that the emission that is reflected after a double-pass of the slab, is reflected back into the slab again.

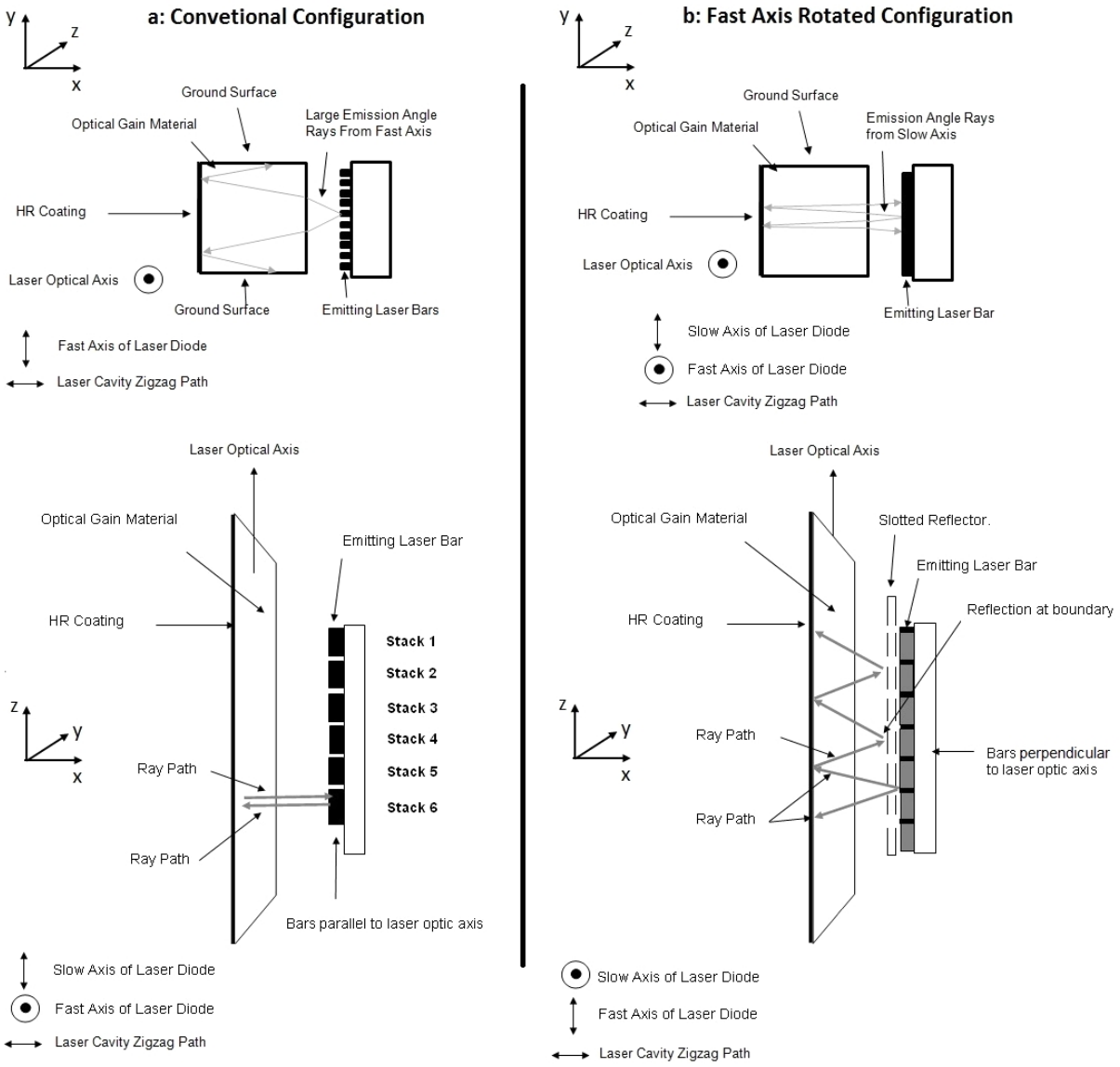

Figure 8.3 – a: Schematic diagram of single-pass configuration, top and side view. b: Schematic diagram of multi-pass configuration with slotted reflector top and side view.

As a result of the slow axis divergence, which is typically 16°, losses will still occur in a similar manner to those shown in the top view in Fig. 8.3a. The losses are reduced due to the reduced divergence angle.

The actual light reflected back into the emitting diodes is relatively small due to the large angular emission of the fast axis. By placing the reflector close to the emitters, and tailoring the hole size and location, the overall transmitting area of the reflector is small. The large reflecting region will also allow for the light to achieve as many bounces as possible.

The largest change to the actual construction of the laser-diode bars is the change in the fast axis direction from the y-plane to the z-plane. To match the height of the slab however, the length of the bars must be 5 mm. In the current design, 10 mm bars

are used, which is the industry standard length. A reduction in the overall bar length would reduce the output power from the bar. Currently, the 10 mm bars produce 100 W, a reduction in the bar size to 5 mm would typically see the power reduce to 50 W. The required power will be even higher than the conventional design, in order to counteract any reduction in the absorption efficiency. In section 8.1.1 the absorption efficiency was expected to decrease to 70%. To achieve a comparable amount of absorbed power, an increase in the overall available pump power is needed. The simple solution would therefore be to use a greater number of higher power bars. Whilst not the most cost effective method, when no other parameters within the program constraints can be further improved, it allows for the absorbed power levels to be maintained. After discussions with laser diode manufacturers Lasertel, the development of a 5 mm half bar was completed [158]. The bar also had a reduced emitter spacing and increased emitter cavity length to allow for power scaling up to 130 W from a single 5 mm bar. The drive current was increased from 96 A to 130 A as a result of this change.

In this chapter, the traditional 10 mm bars are still used due to the limited availability of the new 5 mm bars during the development stage. When pumping a 5 mm slab, over half the emission is lost as a result.

8.2.2 Bar Spacing Optimisation

To maximise the number of bounces achieved, the laser bar locations must be optimised for the 5 mm zigzag slab. In a simple single bar scenario, the coupling would be optimum, as only a small amount the emission is lost from the slot in the reflective plate. All other emission can receive multiple bounces along the slab length to the end of the reflective plate. The largest losses will therefore arise from the slow axis divergence, leading to rays leaking around the top and bottom of the slab or hitting the slabs diffuse surfaces.

If there are a number of bars, and therefore slots present, more losses will arise from light incident on the slots. Light incident on the slot regions will reflect off the AR-coated facet of the bar itself. The reflection coefficient of the coating on the output facet is 10%. Therefore, any emission that is incident on the actual laser bars would be strongly attenuated after only a few reflections.

An illustration of the different sources of losses in the same diagram as Fig. 8.3b is shown in Fig. 8.4.

To limit the overall losses, the reflector slots should be as small as possible. From

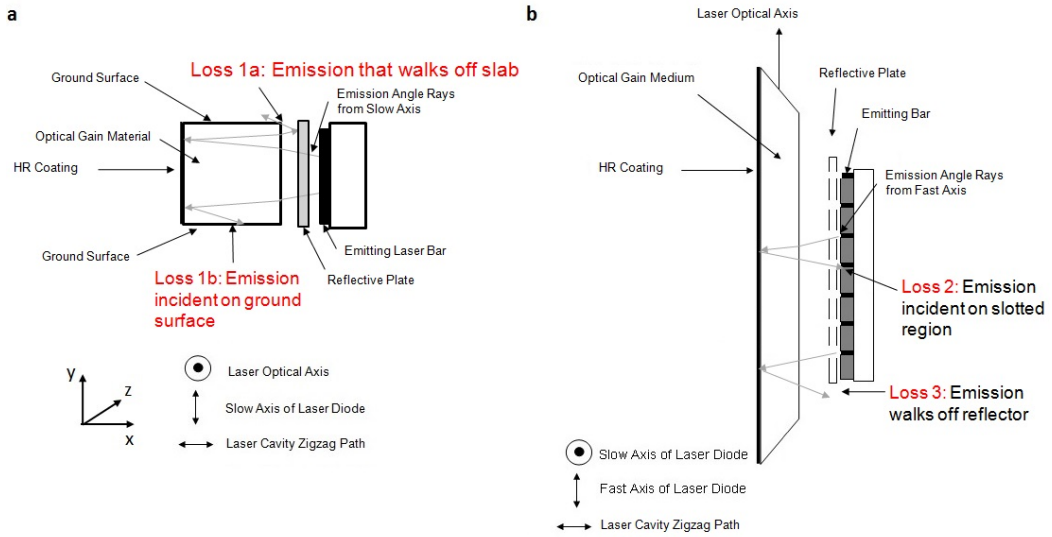

Figure 8.4 – a: Side view of ray paths. b: Top view of ray paths.

discussions with the diode manufacturer, the tolerances of both the reflective plate and the alignment of the bars themselves limited the slot size to $\geq$160 μm.

The spacing between the bars will also impact on the absorption efficiency of the arrays. If the bars are tightly spaced at the centre, more light would be incident on the slotted regions. As the spacing of the diodes is increased, the coupling of light into the high loss regions will vary.

A ray-tracing model was constructed in ASAP to analyse the optimum spacing of the diode bars and to limit the losses outlined in Fig. 8.4. The ray-trace analysed the absorbed intensity in the slab for a single wavelength with an absorption coefficient of 0.35 cm^{-1}, the smallest absorption coefficient expected at the temperature extremes. The initial analysis contained 20 emitting bars, 5 mm in length. The spacing between each bar was varied from 350 - 1300 μm. Separate reflectors with a reflection coefficient of 98% were included in the model. The slot sizes were set to 160 μm with a reflection efficiency of 10%. The spacing between the emitting bars and the slab face was set to 2 mm. Figs 8.5a and b show renderings from the ASAP model output. Fig. 8.5a shows the multiple bounces achieved by a single ray, Fig. 8.5b shows the absorbed power within the active gain region.

The ray-tracing calculation is then repeated with different slot spacings, recording the absorbed power in each scenario. From this calculation, the absorption efficiency and the effective average path length can be calculated. Fig. 8.6 shows the modelled path length and the efficiency as the diode spacing is increased. The path length is computed using Beer-Lambert's law, by calculating the length required to achieve

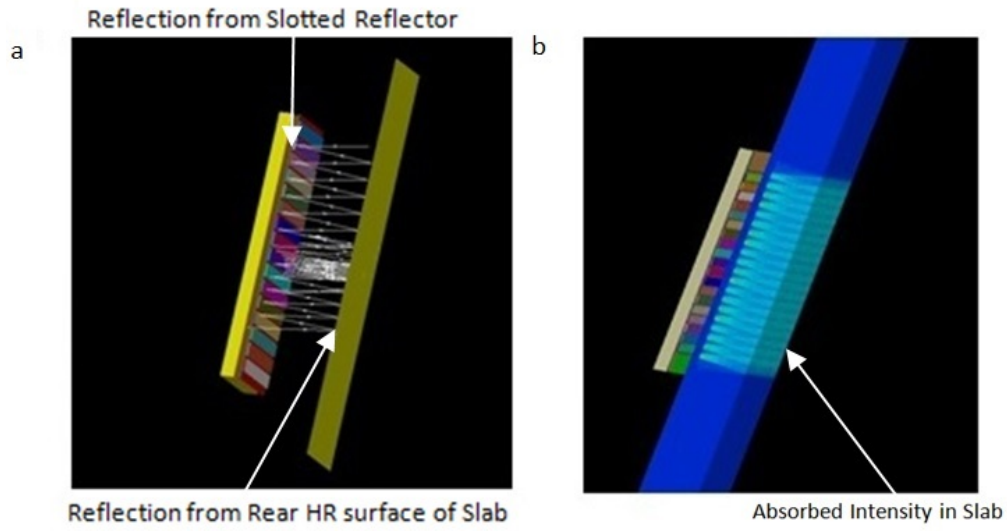

Figure 8.5 – a. Single ray trace from emitter in absorption model. b: Absorbed intensity within slab in absorption model.

the same absorption efficiency returned by the ray-tracing model, with a $0.35\,\mathrm{cm}^{-1}$ absorption coefficient.

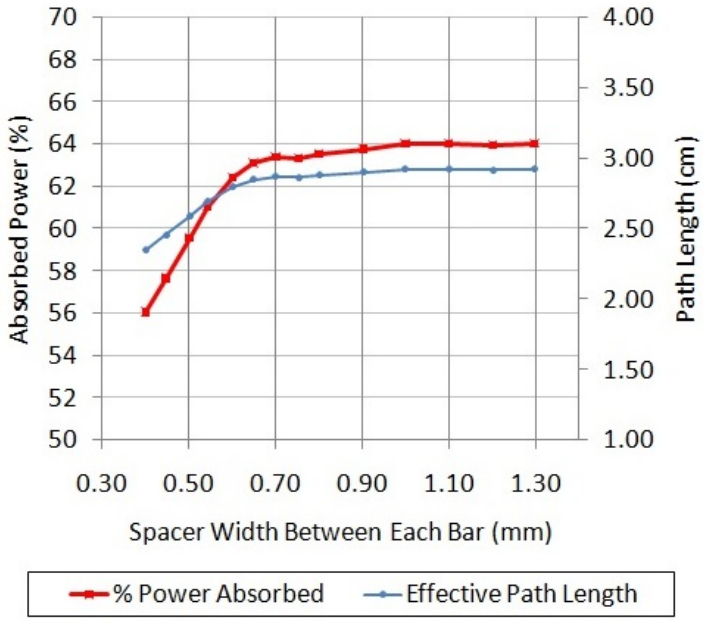

Figure 8.6 – Absorbed power with increasing diode spacing.

Fig. 8.6 shows that as the spacing of the bars is increased from 350μm, the absorption efficiency of the setup also increases, up to a spacing of 1 mm. Beyond this, the efficiency does not increase significantly, suggesting that the losses are predominantly due to another mechanism.

From the model, two improvements in efficiency from increasing the spacer and

reflector length are observed. Firstly, the amount of light incident on the low reflectivity slots is reduced. This is due to the larger reflective regions allowing for an increased number of bounces. This allows for increased absorption to occur before each ray is incident on a slot. The other improvement in efficiency occurs from the increased overall reflector length, which increases the number of bounces each ray can achieve before it walks off the end of the reflector.

However, at 800 μm and beyond, limited improvement from these effects occurs. The losses are now increasingly from the slow axis divergence, allowing rays to vertically walk off the slab or be incident on the diffuse regions. No improvement from increasing the reflector length further is achieved due to loss from slow axis divergence.

The modelling results in Fig. 8.6 also show the average path length, as the spacer width is increased beyond 800 μm, is 2.9 cm. To increase the absorption efficiency further, parameters such as the slab size, the slot losses, slot size or the reflectivity of the plate would have to be changed. These parameters are all limited by engineering issues. The slot size is limited due to alignment tolerances. The slot losses are set by the laser diode facet reflectivity and the plate already has a HR-coating of 98%. Changes to other parameters, such as slab thickness, are limited by requirements of the laser development programme.

Whilst the 2.9 cm absorption length is below the $\approx$3.5 cm outlined in section 8.1.1, the short fall in absorption length could be counteracted by improvements or enhancements in other parameters, such as a further increased diode power or the use of multi-wavelength devices discussed later in section 8.2.3.

The change in absorbed power density within the slab will also be affected by the bar spacing. As a result, other parameters that could be affected by increasing the diode spacing are the induced thermal lens and the small signal gain profile within the slab. These parameters are also investigated in subsequent sections.

Spatially Variant Small Signal Gain

The deposition of the absorbed intensity will determine the spatially variant small signal gain, as well as the thermal lens within the slab. Spacing the diode bars widely to achieve an increased absorption path, as discussed in the previous section, will also create a varying gain profile within the slab, as well as optical path length errors introduced by thermal gradients. The zigzag path of the resonator will act to homogenise the beam to an extent. The image rotation within the cavity designs discussed in chapter 1 section 1.1.4 will also further homogenise the gain profile. Depending on the

deposition of the gain however, the resultant gain profile may impact on the number of modes within the resonator when compared to other pump head geometries. A change in both the number and order of the modes within the resonator will change the divergence of the laser, impacting on the overall targeting system performance.

The spatially dependent small signal gain of the resonator beam is analysed to investigate this effect. The gain profile in the slab will contribute to the overall modal profile within the resonator. By varying the profile, either the lower or higher order modes can be selected, improving or degrading the beam quality. The conventional pump geometry is used as a baseline for the performance and modelling. In this configuration the pump profile will ultimately fill the slab aperture and to first order, the allowed modes will be dependent on the aperture of the slab. The effect of changing the size of the slab to increase or decrease the divergence has been discussed in chapter 1. If the new gain profile is better matched to the extraction of higher order modes, the beam quality of the laser could be reduced. A degradation in the mode profile would be expected if the gain is distributed towards the edges of the slab, where the higher order modes typically extract from.

Using the ray-tracing analysis completed in the previous section, the overall gain profile in the slab can be determined. Starting with the absorbed power density calculated in the ray-tracing model for each diode spacing, the effective population inversion throughout the slab is known. A second ray-trace method, performed in a script the author wrote in Matlab, sums the gain for rays traversing the zigzag path in the slab. This represents the single-pass gain of the beam. The spatial gain is calculated by completing a series of ray traces within the 5 mm aperture of the slab. To include the 90° cavity image rotation, the gain profile is also rotated by 90° and summed cumulatively four times to achieve the overall gain profile observed in the cavity. Fig. 8.7 shows the small signal gain for different bar spacings compared to the conventional LDA pump head.

Fig. 8.7 shows three cases of the normalised small signal gain for different diode bar spacings and the gain from the conventional LDA setup. For the conventional LDAs, the gain peaks in the centre and reduces towards the four corners. This is a result of lower absorption in the corner regions of the slab. The peak small signal gain coefficient of the conventional LDA design is larger than all the slotted reflector configurations.

For the reflector configuration, when the diode spacing is 600 μm, a more homogeneous profile with a peak in the centre of the beam is observed. The peak is lower than

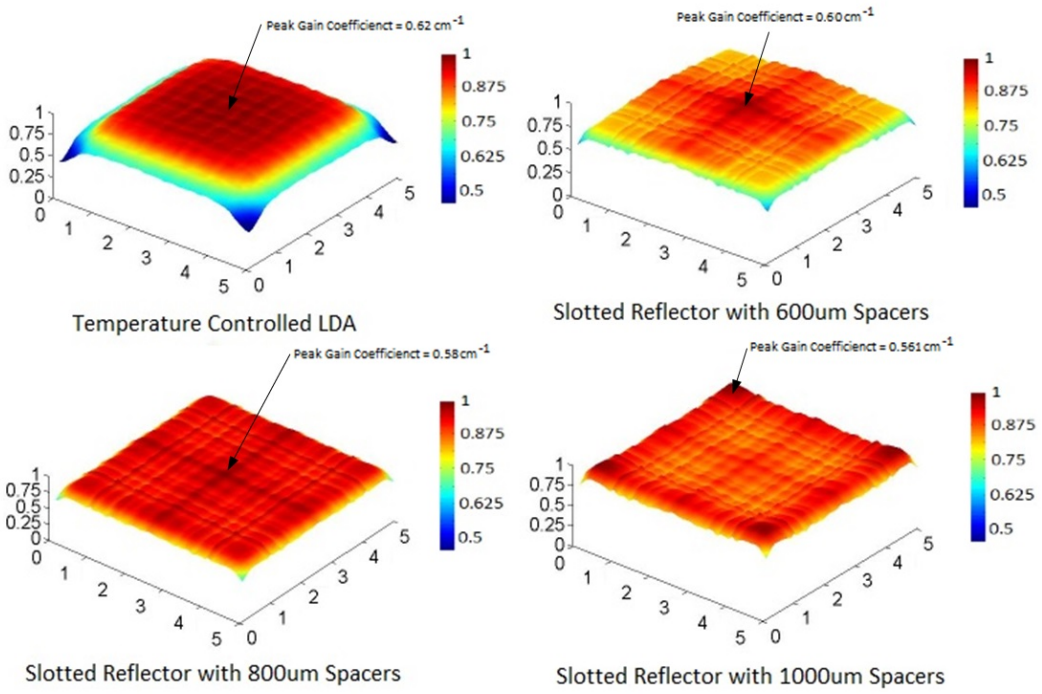

Figure 8.7 – Normalised spatial small signal gain for conventional LDA and reflector design with various spacer lengths.

the conventional LDA, as the gain is distributed further into the corners of the beam. As the spacing is increased to 800 μm, the profile starts to develop peaks towards the edges of the beam and the peak gain coefficient, whilst still at the centre, has reduced further. With the spacing at 1 mm, the profile has peaks in the four corners of the beam and the overall gain is again reduced. The profile has reduced gain in the centre regions and higher gain in the corners. The peaks towards the corners of the gain profile are a result of the slow axis divergence spreading the gain into the corners of the slab. As the reflector length is increased, the absorption of the divergent rays walk towards the edges of the slab and have the ability to be absorbed.

Compared to the standard pump head configuration, the slotted reflector has more gain towards the edges of the slab rather than in the centre. From chapter 1 section 1.1.3, the diameter of the higher order modes were shown for a square aperture. The gain profile shown in Fig. 8.7, for the 800 μm spacer case, could preferentially seed higher order modes, that extract gain from the edges of the slab, rather than the lower order modes which will typically extract from the centre. From this result it would be expected that the beam quality would reduce as a result of an 800 μm spacing between the bars.

It must be considered, however, that the visual impact of the small signal gain in Fig. 8.7 is not a definitive measurement of the degradation in the beam quality. To fully calculate the impact on the beam quality, a model of the modal build-up

during the pulse would be required. Fox-Li [40] computations have been reported that provide modal analysis of the cavity. Further work is proposed at Selex to complete this analysis.

8.2.3 LDA Wavelength Specification and Multi-Colour Analysis

The absorption profile of 1.1% doped Nd:YAG was introduced in section 7.2 of chapter 7. A wide absorption band is present from 790 nm to 820 nm. It is this absorption band width that defines the effective temperature range for efficient pumping. At a tuning rate of 0.27 nm/°C, the absorption band provides an operational temperature range of 111°C. This range is smaller than the 125°C required for -40°C to 85°C operation. To widen this temperature range techniques such as broad bandwidth diode pumping have been presented [159].

Laser-Diode Temperature-Dependent Slope Efficiency

A parameter that was not considered up until this point was the temperature dependence of the output power from the bars themselves. As discussed in chapter 7 section 7.4, the optical power from the emitters will reduce as the temperature is increased. Fig. 8.8a shows the normalised variation in output power. This data was taken from experimental results at Lasertel provided by McElhinney *et al.*. The power is normalised to 20 °C to allow for a comparison of bars with differing output powers from various manufacturers.

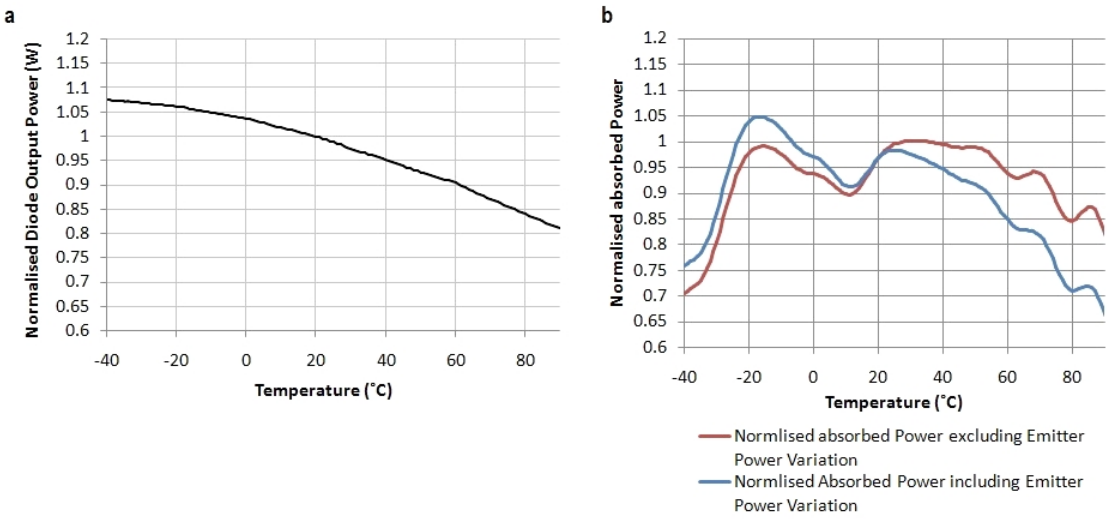

Figure 8.8 – a: Normalised diode output power over temperature. b: Absorption efficiency with and without diode slope efficiency included, with a 3.5 cm path length.

From Fig. 8.8a, the output power of a laser bar operating at 85 °C would be ≈20% less than the output power at 20 °C. Fig. 8.8b shows two normalised absorbed power

plots. The first plot, shown in red, demonstrates the absorption efficiency of an LDA with a path length of 3.5 cm and a centre wavelength of 808 nm at 35 °C. The second plot in blue shows the normalized absorbed power, taking into consideration the reduction in output power shown in Fig. 8.8a. The absorbed power at 85°C has now dropped from 86% to 71%.

Another aspect of the performance to consider is manufacturability of such arrays. The performance shown in Fig. 8.8 will be greatly affected by any variances in the centre wavelength. If an array was centred at 806 nm, for example, the 2 nm is the equivalent of a further 7.5 °C temperature drift, leading to an effective temperature of -47.5 °C. The performance of any solution must allow for a ±3.5 nm variance in order to achieve a low production cost. The ±3.5 nm variance allows for a full wafer to be used in the production of the laser bars, eliminating any wafer wastage. The cost reduction by reducing the tolerance specifications from a typical ± 1 nm to ± 3.5 nm is estimated to be 30%.

LDAs with Multiple Wavelengths

To widen the temperature range and limit the overall affect of the change in absorption depth, the use of arrays constructed from a series of bars, each with a significantly different wavelength, has been reported [159] [160] [158]. These are known within the industry as multi-colour-arrays (MCA). The spectrum of an array with four different wavelengths, at the temperature extreme of 85 °C, is shown later in section 8.4; where Fig. 8.14b shows the spectral intensity of the array. The presence of multiple spectral peaks, distributed across the absorption band, ensures that at any given temperature a section of the spectrum is strongly absorbed. In Fig. 8.14b at the temperature extreme, at least two spectral components will achieve strong absorption, thereby ensuring a minimum performance level.

The use of discrete wavelengths, spaced over the absorption band of Nd:YAG, also limits the changes in the absorption profile within the gain medium over temperature [159]. Furthermore, by optimising the spectral wavelengths to counteract the change in diode slope efficiency, a flatter absorption profile can be produced over the temperature range.

To achieve an optimum performance over temperature, a Monte-Carlo optimisation routine that determines the optimum wavelength specification was written. The model calculated the minimum absorbed power in a 2.9 cm path length over the required temperature range. This was completed for all possible combinations of an array with four different centre wavelengths. The path length has been reduced from 3.5 cm to

2.9 cm to represent the optical path length calculations in section 8.2.2. All possible combinations of wavelengths from 760-830 nm (at 25 °C) were considered, each with a FWHM of 3 nm. For each possible wavelength combination, a second calculation that included a ±3.5nm variation on each centre wavelength was performed. The minimum of this calculation was then stored as the true minimum of the original wavelength combination. The best performing spectral contribution was then chosen. For a four-wavelength array, the optimum wavelengths were calculated to be 794, 800, 804 and 810 nm, providing a spectral bandwidth of 17 nm. Fig. 8.9a shows the normalised absorbed power over temperature for an MCA with the optimum wavelengths and a single-colour array at 808 nm with a 3.5 nm FWHM. The calculations include the temperature dependent optical power efficiency from Fig. 8.8a.

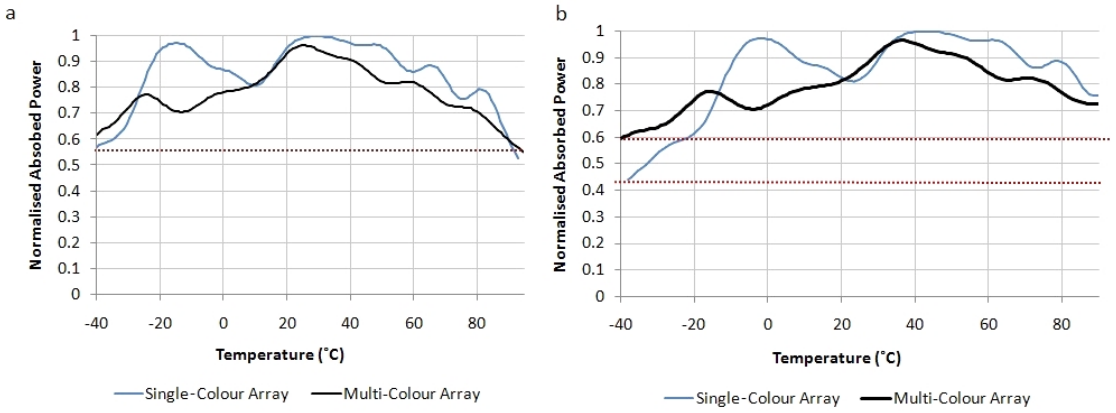

Figure 8.9 – Comparison of normalised absorbed power over temperature for a MCA array and a single-colour array with a: Optimum specification wavelengths. b: Worst case ±3.5nm manufacturing tolerance.

At -40 °C, the MCA normalised absorbed power is 0.63 compared with 0.57 for the single-colour array. The temperature performance is therefore improved by moving from a single-colour configuration to that of a multi-colour one.

As shown in Fig. 8.9a, the overall performance of the MCA compared to that of a single colour array, was not significantly increased. The wavelength specification must also allow for a ±3.5 nm variation in each wavelength, thereby providing the manufacturability required for a production laser. Fig. 8.9b shows a comparison of the absorbed power from an MCA with the four wavelengths described previously, shifted by 3.5 nm. The wavelengths are therefore centred at 791.5, 796.5, 800.5 and 806.5 nm, providing the worst case solution. This is compared to a single-colour array centred at 804.5 nm, again representing the worst case scenario for an optimum centre wavelength of 808 nm that has been shifted by 3.5 nm.

The worst performing MCA combination has increased the normalised absorbed

power to 0.60 compared to 0.41 for the single-colour array. For a centre wavelength tolerance of ±3.5 nm, the single-colour array performance at the temperature extremes is greatly reduced. In a single-colour configuration, a further 20% reduction in the absorbed power is observed compared to the MCA configuration. The use of MCAs therefore provides a significantly improved performance, whilst allowing for wide production tolerances to be used.

8.2.4 Reflector Material

One of the determinants in the efficiency of the multi-pass setup is the strength of the reflection from the reflective plate. Other reported configurations mentioned HR optical coatings [157] or gold reflectors to provide high reflection coefficients. Coupling losses due to the inclusion of reflectors are often present due to clipping of emitters and transmission losses from the optical surfaces. The actual alignment of the slots within the reflective plate can be difficult due to the narrow slots used to improve efficiency. The reflective plate is often custom-made for a given array design. One of the biggest disadvantages is the cost of the actual reflective plate and the fitting. Estimates from the suppliers Lasertel suggested up to 40% of the total cost of the package was due to the reflective plate.

A configuration that does not require a reflective plate would provide a cheaper solution. The simplest solution would be to use the copper tungsten (CuW) spacers themselves. This would remove the need for any further processing of the laser-diode bars or a separate optical component. The performance of the configuration would be limited due to the reduced reflectivity coefficient of the diode spacer. The material reflection coefficient was measured to be $\geq 70\%$, reducing the efficiency of the multi-pass setup. The material itself is also slightly diffuse, increasing the scattering of incident rays. The increased scattering would increase the number of rays clipped by the slab aperture.

A comparison of the two configurations was completed in the ray-tracing programme described earlier in section 8.2.2. The reflectivity of the spacers was reduced to 70%. The model was also updated to include the multi-colour aspect introduced in the previous section. An array with 20 bars consisting of three 794 nm bars, four 800 nm bars, four 804 nm bars and three 810 nm bars was modelled. A full temperature analysis of the two devices was completed to determine the variation in performance. This is shown in Fig. 8.10. The modelling looks only at the absorption efficiency and does not include the roll-off in diode power, as this will be present in both configurations.

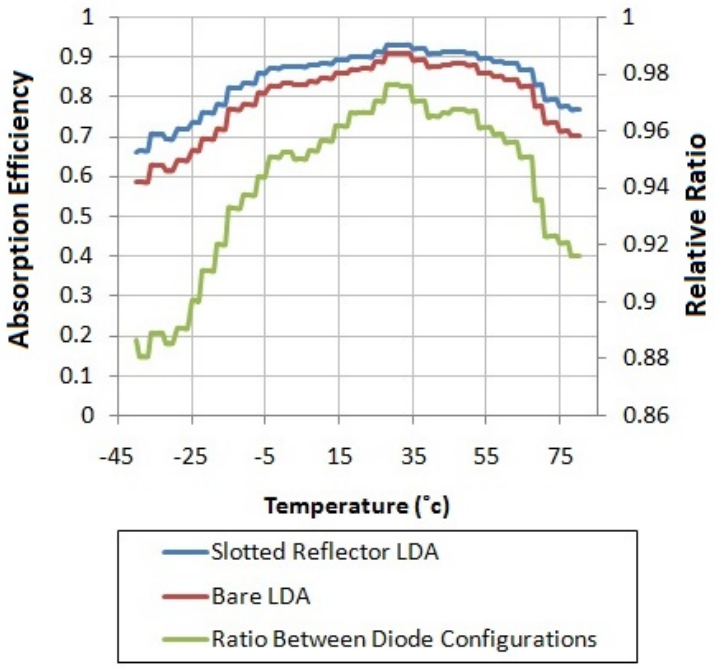

Figure 8.10 – Comparison of slotted reflector LDA and bare (CuW reflector) LDA absorption efficiency.

From Fig. 8.10, the LDA with the original copper tungsten diode, hereby referred to as the CuW reflector LDA, provides up to 88% of the absorbed intensity of the slotted reflector design. At the higher and lower temperatures, where the absorption coefficients of some of the colours are very low, the difference in performance is larger. At these operating points, the number of bounces required to achieve sufficient absorption is larger, and the reduction in the reflection coefficient of the spacers will have an increased effect. From this analysis, the bare diode reflector has reduced absorption performance compared to the slotted reflector, but it has a number of advantages in terms of cost and production.

In section 8.4 the performance of an LDA with reflective plates is experimentally investigated. Initially, the performance over temperature is investigated in terms of small signal gain. The performance characteristics of slotted reflector pumping a Nd:YAG zigzag slab is then characterised. A comparison of the LDA with and without a reflective plate is then completed in section 8.6, to determine the change in performance.

8.3 Thermal Lens Calculations

As highlighted in section 8.2.2, the thermal lens will also be dependent on the deposition of the gain. By calculating the temperature profile within the slab, a map of the optical path length error can be produced. Thermal lensing modelling capabilities

at Selex have been developed over a period of years. The models detailed here have been produced by the author, however, the process of generating a thermal lens from a temperature gradient has been followed from previous models based at Selex and has been reported in the literature [37].

Using the absorbed profile for the 800 μm spaced diodes with the four-colour MCA specification, the temperature gradient was modelled using the FEA program Comsol. The model is based on an average power assumption and therefore will not take into account the transient nature of the thermal lens. However, reasonable agreement with the measured and modelled results for the conventional LDA, modelled in this manner, is shown in this section.

The pump power used for the model was 2 kW or 100 W per bar. The 2 kW represents the minimum energy required to meet the man-portable energy specifications. A second model of the conventional five-LDA pump-head configuration, with 2 kW pump power was also completed to provide a comparison.

The comparison of the two different systems does not actually provide a definitive analysis of improved or degraded beam quality from a given pump configuration, due to the significant difference in the overall pump area, 5 cm for the conventional design and 2 cm for the LDA with a reflector. The aim of this analysis is to show that the resultant optical path length error produced by the reflector design will not significantly degrade the divergence further than that of the conventional LDA pump configuration. If the profile or magnitude of the thermal lens was significantly different, a large change in the divergence or far field profile could occur.

The temperature gradient within the slab is shown in Fig. 8.11a. For this calculation the heat fraction was taken to be 0.39 [25], with a dn/dt coefficient of 7.8×10^{-6}.

The optical path length variation plot is generated using the temperature plot of the slab and a ray-trace of the zigzag path through the slab. The optical path length variation of each ray is then stored in a matrix that represents the beam. This is shown in Fig. 8.11b and c for the slotted reflector and conventional LDA respectively. Using this method, a comparison of the double-pass thermally-induced optical path length variation of both the slotted reflector and temperature-controlled LDAs can be completed.

The overall path length variation in the horizontal and vertical directions for the slotted reflector LDA are similar to the conventional LDA. By fitting a curvature

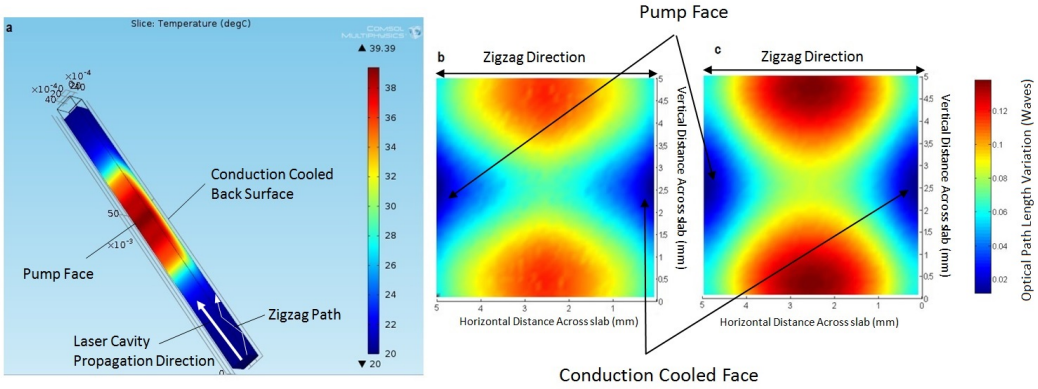

Figure 8.11 – a: Modelled temperature profile of zigzag slab pumped with slotted reflector. b: Optical path length variation for temperature gradient for LDA with reflective plate. c: Optical path length variation for conventional LDA.

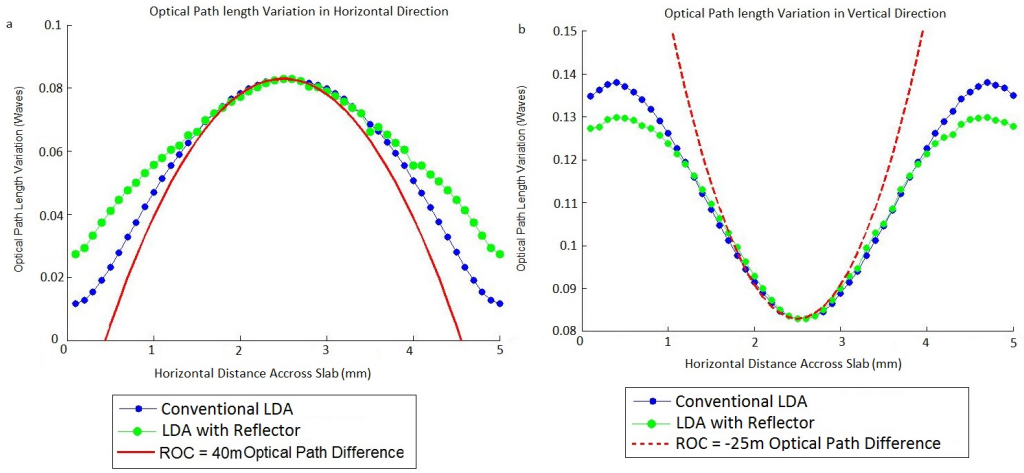

Figure 8.12 – a: Comparison of optical path length variation across the slab in the horizontal direction. b: Comparison of optical path length variation across the slab in the vertical direction.

to the path length variation, the thermal lens strength can be calculated. Fig. 8.12 shows a plot of the optical path-difference for both configurations in the horizontal and vertical directions, from the centre point of the slab. Over the central 2 mm, the thermal lens radius of curvature for both configurations is 40 m in the vertical direction and -25 m in the horizontal direction. As a result, the slotted reflector should not exhibit large changes in the beam parameters from the induced thermal lens strength, when compared to the temperature controlled LDA.

The calculation of the thermal lens does not take into account stress-induced refractive index changes or thermal expansion. It may be possible that the slotted reflector exhibits a different thermal lens strength due to these effects. The overall temperature profile, shown in Fig. 8.11a, does show large temperature gradients close to the surface of the slab. The actual temperature gradients in these regions will also be larger than those shown in the model. The average power assumption of the model

shows the steady state temperature of the slab. In a transient analysis, it would be expected that the gradient at the end of a 230 μs pulse would be much larger than in the CW case. The limitation of completing a transient analysis is due to the computing power and memory requirements of such a calculation.

8.3.1 Modelling Conclusions

In conclusion, the modelling has shown that the slotted reflector design can provide an increased absorption length as a result of the multi-pass effect. Changes to the laser diode construction to achieve the slotted reflector design have been disclosed. The improvement in absorption efficiency from multi-colour arrays compared to that of a standard single-colour array was also presented. It has also been shown however that the slotted reflector design may impact on the beam quality of the laser. The increased power towards the edges of the slab will impact on the performance of the laser and may ultimately degrade the beam quality as well as change the near field profile. Changes to the design of the resonator or the gain material that could correct for this effect is limited. This is primarily due to requirement for compatibility with current laser resonator designs and the cost of any changes required.

8.4 Slotted Reflector Experimental Prototypes

The modelling completed in the previous section has allowed for the definition of the key parameters for the optimum performance of the slotted reflector LDA. From these results, a prototype LDA with a slotted reflector was constructed by Lasertel. The spacing of the laser bars was set to 800 μm to achieve the maximum absorption length, whilst minimising the thermal lens strength and gain profile effects. A four-colour array was specified with the wavelengths 794, 800, 804 and 810 nm with the same bar composition as described in section 8.2.3. A slotted reflector, with a slot gap of 166 μm, was produced by metal deposition onto glass substrate. The substrate was then AR-coated in the slot regions to minimise the optical losses. The metal layer provides up to 98% reflectivity in the 808 nm region, allowing for efficient reflection. Fig. 8.13 shows the slotted reflector with the metalised plate. The initial LDA consisted of a 20 bar stack providing 2 kW within a 5 mm emission height. The actual bars were 10 mm wide, rather than the required 5 mm bars. The reason for this geometry was ease of construction and package availability. The number of bars was kept to 20 to reduce any yield issues.

The insertion loss of the slotted reflector was measured at Lasertel to be 2%. The losses are thought to be primarily due to the transmission through the glass substrate and a small amount of clipping from the metal reflectors. This efficiency could be

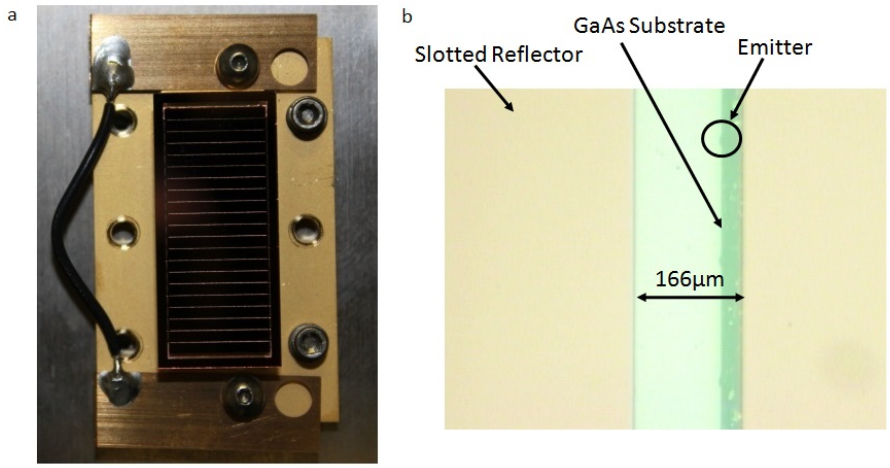

Figure 8.13 – a: Slotted reflector LDA b: High magnification image of laser bar and slotted reflector.

improved further by both increasing the spacing of the slots to minimise clipping and by improving the coating on the glass substrate.

The spectral performance of the device was characterised over the temperature range 10-85 °C. The LDA spectrum was measured using an Ocean Optics USB2000 spectrometer with a resolution of 0.15 nm. The measurement is shown in Fig. 8.14.

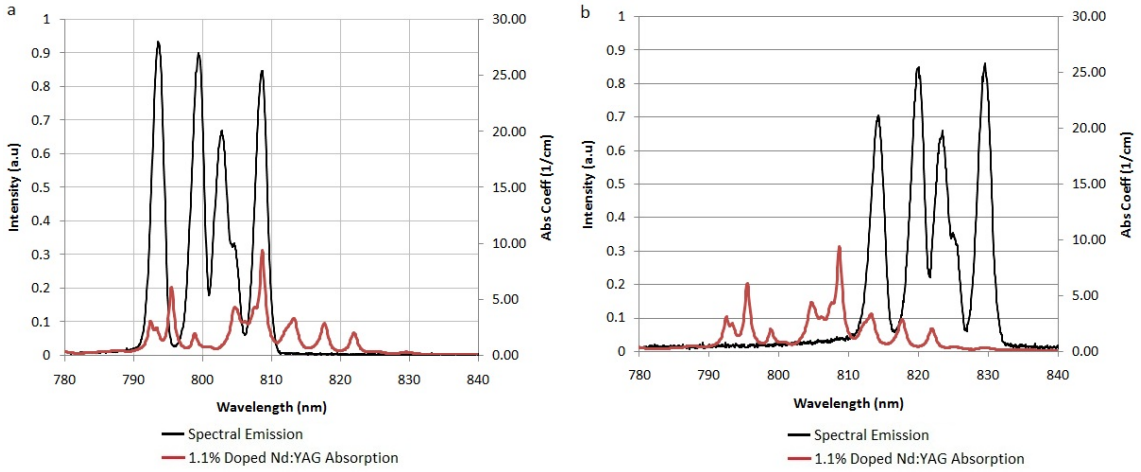

Figure 8.14 – a: Spectral output at 12 °C. b: Spectral Output at 85 °C.

The spectral peaks, shown in Figs 8.14a and b, shift at an average rate of 0.25 nm/°C, as expected. The spectrums are overlaid with the absorption coefficient for 1.1% doped Nd:YAG. The effect of the multi-colour absorption can be interpreted from these graphs. At 85 °C, one of the peaks in the LDA spectrum is outside the absorption band of Nd:YAG and will therefore contribute a smaller amount to the overall absorbed power. The three other peaks are aligned with peaks in the absorption spectra and will therefore be strongly absorbed. At the lower temperatures the situation will be reversed and the higher wavelengths will contribute to the overall absorbed power. The output power of the array was also measured and found to agree roughly with the

modelled results in Fig. 8.8a.

8.4.1 Small Signal Gain Experimental Measurements

Measurement of the small signal gain will allow for the variation in absorbed power to be observed as a function of LDA temperature. Any changes in the absorption will reduce the overall gain within the slab. The LDA was configured to pump the conventional 5 mm zigzag. A 1064 nm probe beam was used to measure the single-pass amplification. The probe beam diameter was 1.5 mm through the slab, allowing for the gain through the central zigzag path to be measured. Fig. 8.15 shows the experimental setup and the modelled and measured single-pass amplification. The modelled small signal amplification is calculated from the equation (1.5). The gain was calculated using the actual spectrum and output power roll-off measured previously. The LDA drive conditions were fixed over the temperature range at 200 A with a diode drive pulse width of 230 μs. The LDA was operated at 5 Hz to limit the overall rise in temperature during firing. This allows for a more accurate temperature measurement. The LDA was mounted onto a TEC to control the temperature whilst the slab was held at room temperature by a heat sink.

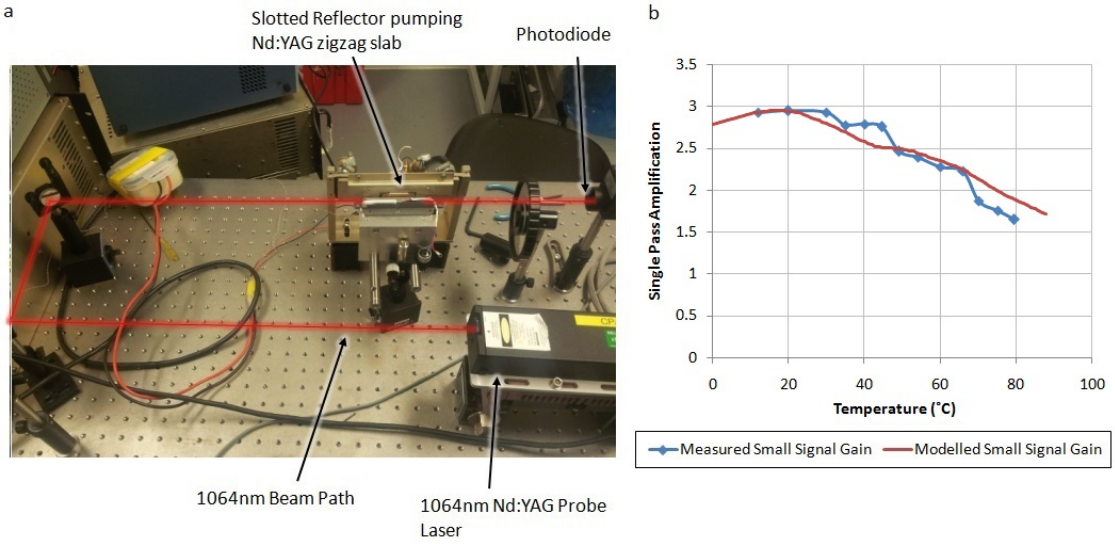

Figure 8.15 – a: Experimental setup of single-pass amplification measurement. b: Single-pass amplification measurements and modelled results using 2.9 cm path length.

Fig. 8.15b shows the results for the measured single-pass amplification and the modelled results using a 2.9 cm absorption depth. The single-pass amplification peaked at 20 °C with a value of 2.93, giving a small signal gain of 0.5 cm^{-1} for a path length of 2.3 cm within the active pumping region. The results show reasonable agreement between the measured and modelled performance. However, above 67°C, there is a slight drop in the measured values compared to the modelled results. Adjusting the

values of the absorption length to fit these data points gives a 0.5 cm path length. The slab itself, including reflection of the back surface, will provide a minimum path length of 1 cm. Coatings on the slabs are specified to provide a strong reflection at these operating wavelengths and should not attenuate the pump light significantly. It is possible that the coatings spectral response is different from the manufacturing specifications. The limitation may also be due to the test equipment, the maximum specified operating temperature of the TEC used is 70 °C. The TEC may be operating at a less than optimum condition, possibly creating a large gradient across the LDA leading to the reduction in output power and an increased emission wavelength.

Measurement of the single-pass gain has allowed for verification of the modelling up to a temperature of 66 °C, with good agreement between the two. The results show an increase in the path length to a value of around 2.9 cm. When operating at temperatures beyond 66 °C, the single-pass gain reduced below that of the calculated values. The cause of this behaviour may be related to test equipment.

8.4.2 Slotted Reflector Thermal Lens Measurements

The magnitude of the thermal lens will also affect the beam quality of the laser. In a similar manner to the small signal gain, the change in the absorption profile of the new pump configuration will result in a change in heat deposition and therefore in the temperature gradient within the slab. The strength of the thermal lens is therefore characterised and compared to the conventional array. To measure the thermal lens, the change in the wave front curvature as a result of a double pass through the zigzag slab whilst pumping was measured. The commercial wavefront measurement system Fibsa OPtik μPhase2 interferometer [161] was used to measure the wavefront distortion within the Nd:YAG Slab.

The strength of the thermal lens will be a function of both the absorbed pump energy and the distribution of the energy within the slab. To maintain a constant absorbed pump energy, the LDA power is varied as per the results in Fig. 8.9. The slab temperature was held at room temperature by conduction-cooling from a large heat sink. A small amount of slab heating may be present due to convective heating from the LDA.

The passive wave front of the zigzag slab, measured without any thermal load, was -72 m in the horizontal zigzag plane and -14.6 m in the vertical plane. A phase map of this taken from the FISBA optik is shown in Fig. 8.16a. Fig. 8.16b shows the pump induced phase profile of the slab. Qualitatively, we observe that the optical phase map is similar to the modelled profile shown in section 8.3.

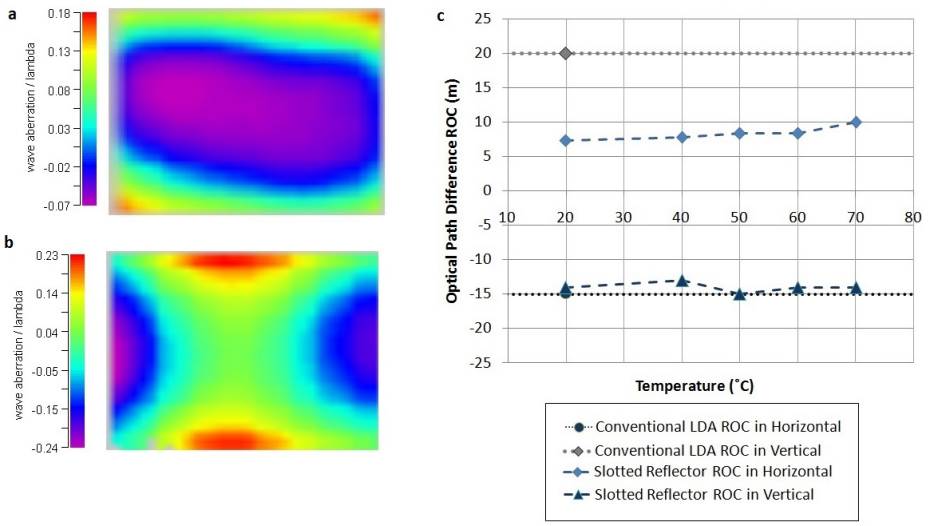

Figure 8.16 – a: Un-pumped wave front distortion of the zigzag slab b: Pumped wave-front distortion of the zigzag slab. c: Measured thermal lens strength over temperature.

Fig. 8.16c shows the measured thermal lens radius in the vertical and horizontal planes for the slotted LDA compared to the conventional LDA. The magnitude of the vertical curvature is typically dominated by the passive wave front error. Both the conventional LDA and the slotted reflector LDA have similar curvatures to the passive measurement in this dimension. However, in the horizontal zigzag plane, there is a significant difference between the slotted LDA, which has a measured radius of curvature of between 7-10 m, and the conventional LDA, which has a 20 m radius of curvature.

The conventional LDA measurements are consistent with those modelled in section 8.3. When combined with the static lens measurements of 72 m, a simple thin lens approximation would give a modelled radius of curvature (ROC) of 25 m for the conventional LDA, similar to the measured results of 20 m. The slotted reflector LDA thermal lens ROC is 7 m, much larger than the modelled results. A small variation in the slotted reflector thermal lens also occurs over temperature with the induced lens decreasing as the temperature is increased.

From these measurement, a large variation in the measured and modelled results of the slotted reflector is present, primarily in the zigzag plane. The limitations of the thermal lens modelling have been discussed previously, but this method does provide good agreement with the conventional LDA results. This suggests that a change in the absorbed power has led to a change in the validity of the assumptions within the model. The biggest limitation is the CW heat load assumption. If a transient analysis was completed, the temperature gradient across the slab would be much larger. The actual temperature profile across the slab does differ for the

two types of modelled LDAs. The temperature profile shown in Fig. 8.12a shows significant thermal hot spots at the pumping face of the slab. The hot spots in the slotted reflector profile would not be significantly averaged as a result of the zigzag path. If the gradient of the temperature profile of both configurations were to increase, the induced wavefront distortion from the slotted reflector would increase at a much larger rate than for the conventional design. By moving to a transient model, the modelled lens for the slotted reflector LDA would increase at a larger rate than that of the conventional LDA, possibly providing better agreement with the measured results. The limitations of completing this have been discussed in section 8.3.

As a result of the increased thermal lens strength for the slotted reflector LDA, a degradation in the divergence of a given laser would be expected, as discussed in chapter 1 section 1.1.3. The image rotation of the resonator will average the lens in both axes, creating a spherical lens. The average focal length for the slotted reflector thermal lens would be $\approx 26\,\mathrm{m}$. Using the approximation introduced in chapter 1 section 1.1.3, the divergence should be slightly less than the 1 mrad calculated for an array with the full 5 kW of pump power. This result shows that whilst the slotted reflector will degrade the divergence of a laser system compared to a pump configuration of a similar optical power, the overall divergence will not be significantly higher than the current higher energy targeting lasers developed at Selex. This allows for other components, such as expanding telescopes used to reduce the beam divergence to be used in the same manner.

For the conventional LDA, running at a reduced pump power, the average thermal lens strength is actually negative. The averaging of the thermal lens will occur due to the cavity image rotation. The cavity will be close to plane-plane, if not slightly unstable as a result. The limitation of the resonator becoming plane-plane is the wavefront error on all the optical components within the cavity. The cumulative wavefront errors can push the resonator into the stable region of the cavity stability criterion. A near plane-plane or slightly unstable resonator should provide a reduced divergence compared to the 1-1.3 mrads introduced in chapter 1 section 1.1.3.

8.5 Slotted Reflector Laser Resonator Testing

After the small signal gain and thermal lens testing, the LDA was then used to pump a slab in a laser resonator. The effects characterised previously will affect the resonator performance in terms of energy, divergence and near field profile. The laser resonator was a Q-switched cross-Porro resonator similar to that described in chapter 7 section 7.6. The experimental configuration is shown in Fig. 8.17. The resonator was initially

characterised using the conventional temperature-controlled LDAs at 806 nm, and then compared to that of the slotted reflector LDA. Both devices were fitted with a TEC to allow for temperature control. The conventional LDAs were kept at a constant temperature of 45 °C throughout the testing, whilst the slotted reflector LDA temperature was varied from 10 to 80 °C.

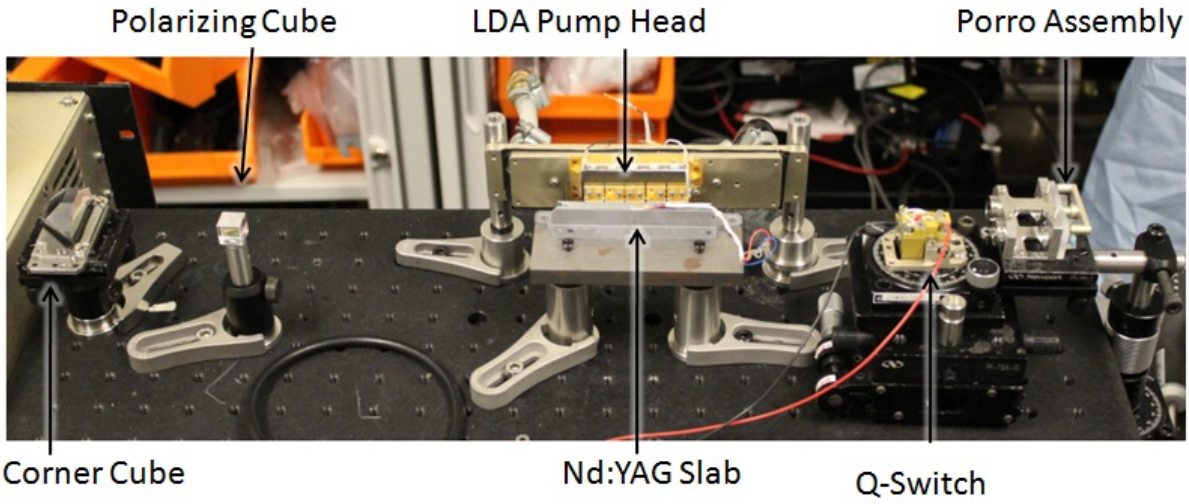

Figure 8.17 – Experimental setup of Nd:YAG cross-Porro resonator.

The initial investigation looked to compare the output energy of the slotted reflector LDA, at the optimum temperature of 25 °C, to that of the conventional LDAs operating at 45 °C, where the centre wavelength is at 806 nm. The current of the conventional LDAs was reduced to match the room temperature pump power of the slotted reflector. The nominal current of the conventional LDAs is 96 A providing 4.8 kW of pump power. Reducing the current to 65 A reduced the output power to 2 kW. The pump energy was then varied by reducing the drive current with a fixed pump pulse duration of 230 μs. Fig. 8.18 shows the slope efficiencies of the two configurations.

The comparison of the two different pump configurations shows that the slope efficiencies are different for each setup. The temperature-controlled LDAs have a slope efficiency of 0.35 compared with 0.31 for the slotted reflector. From Fig. 8.9, it was shown that the room temperature absorption of the slotted LDA is 94%. This compares to 98% for the conventional LDAs. A larger slope efficiency from the temperature controlled LDAs would be expected as a result.

A comparison of the near and far field properties for the two pump heads was then completed. The near field beam was measured using a Cohu 4812 6 mm CCD camera placed 30 cm from the polarising cube. The far field divergence was measured using a 1 m mirror with the same CCD camera placed at the focal plane. Fig. 8.19 shows

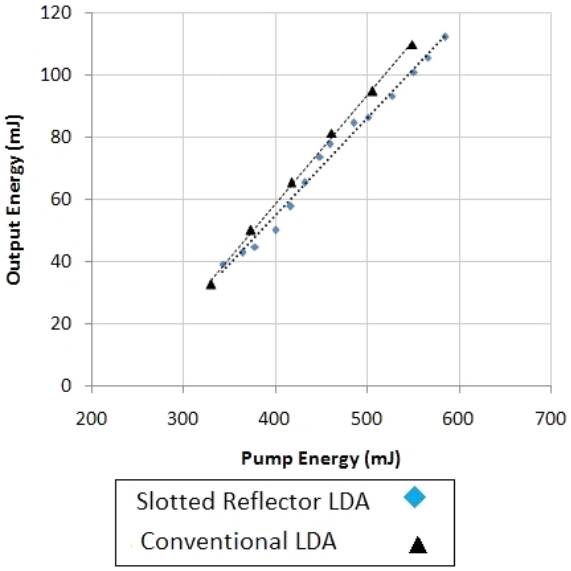

Figure 8.18 – Slope efficiency of conventional LDAs and slotted reflector LDA at room temperature.

both the near field profiles and the far field diameters for each configuration. For both pump configurations, the output energy of the laser was 100 mJ. The pump energy was 500 mJ for the conventional LDA and 550 mJ for the slotted reflector LDA. The pump pulse duration for both setups was 230 μs.

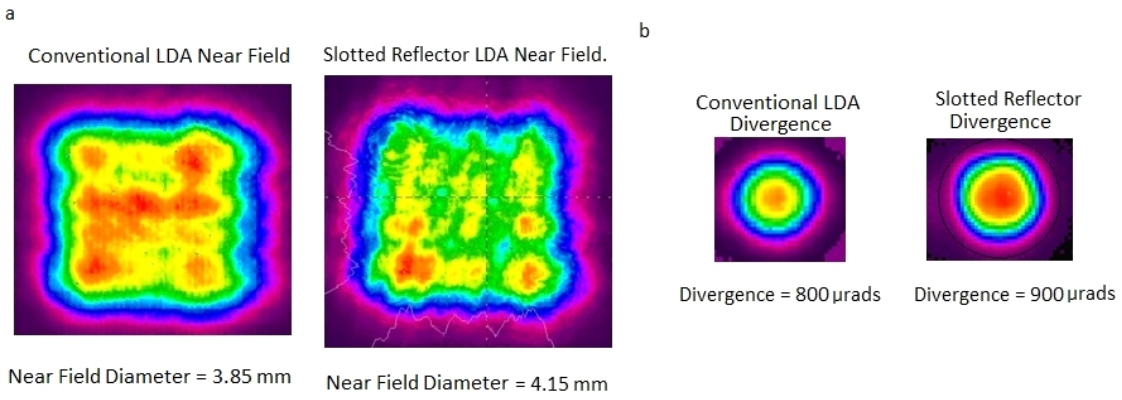

Figure 8.19 – Comparison of resonator beam characteristics. a: Near field profiles. b: Far field profiles.

The slotted reflector produced a $1/e^2$ near field diameter of 4.15 mm compared to 3.85 mm for the conventional LDA. The asymmetry of the near fields were 1.07 and 1.05 for the conventional and slotted reflector LDA respectively. The low asymmetry is a result of the image rotation in the cavity design. A change in the profile of the near field beam for the slotted reflector configuration can be observed. Fig. 8.19 shows that the profile is degraded, in particular, the edges of the beam look much more noisy than for the conventional LDA. The far field beam of the slotted reflector also increases. The $1/e^2$ full angle divergence was 900 μrads for the slotted reflector compared with 800 μrads for the conventional design. The beam parameter product (BPP)[8], which

is a similar measurement to the M^2 beam quality measurement, has therefore increased from 3 mm mrad to 3.7 mm mrad. Note that the BPP in this measurement uses the full beam diameter and full angle divergence, as is consistent with terminology used at Selex.

The change in beam quality will be due to a number of factors, the spatial small signal gain and the increase in the thermal lensing measured in the previous section will be the main contributors to this change. When modelling the small signal gain, an increased amount of absorbed power in the edges of the beam was predicted. In the near field measurement of the laser, the actual beam diameter of the resonator is larger. This may be a direct result of the increased gain in the edges of the slab. Modes which fill the full aperture of the slab, may also experience diffraction losses from the slab aperture, causing the noisy profile of the near field.

The increased lensing will also allow for higher order modes to oscillate in the cavity, as highlighted in chapter 1 section 1.1.3. With the gain distributed into the edges of the slab, these modes will also observe larger gain than in the conventional LDA configuration. The far field profile of the slotted reflector is also larger, highlighting that the number of modes within the laser has increased.

Despite an overall increase in the beam parameter product, the magnitude is still consistent with those currently produced at Selex. Such lasers will typically produce beam parameter products of ≈ 4 mm mrad. The performance characteristics of this laser in a targeting context, will therefore be similar to other production lasers.

The temperature performance of the slotted reflector was then characterised in the cross-Porro resonator. Two different methods of operation were investigated, the first looked to use a fixed diode drive pulse duration of 230 μs with the maximum output energy from the laser measured over temperature. The second method looked to maintain a constant energy across the temperature range by adjusting the diode drive pulse width. In this method of operation the diode drive pulse width was varied from 150 to 230 μs to maintain an energy of 60 mJ. Fig. 8.20 shows the performance in both methods of operation. Using the calculated results for the absorption efficiency, the expected performance is also modelled from the equations in chapter 1 section 1.1.5. The model used an intra-cavity loss of 10%, a cavity reflectivity of 43% and a pump power of 2 kW. The modelling also included a 7 °C offset from the base temperature of the LDA to the actual emitter temperature.

From Fig. 8.20a, a reduction in the output energy is observed when the resonator is pumped with a constant pump pulse duration. The output energy reduces from

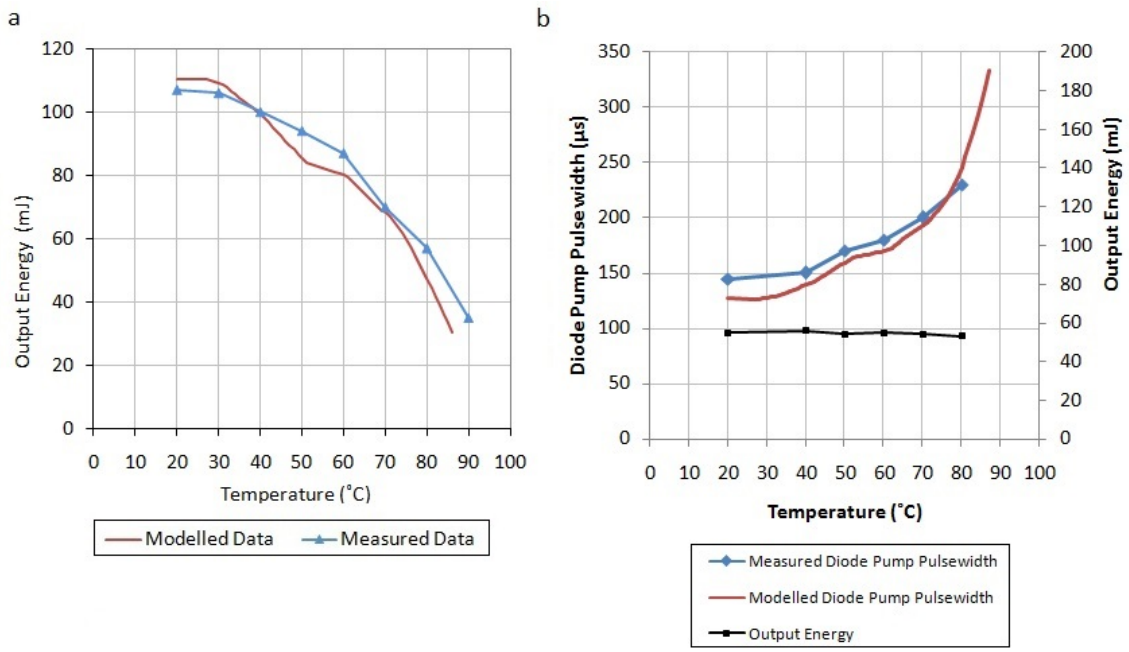

Figure 8.20 – a: Maximum output energy with fixed diode drive current. b: Required LDA pump pulse width for a constant energy of 60 mJ.

105 mJ at 20 °C to just 51 mJ at 80 °C. From Fig. 8.20b, the increase in the required diode pulse width to maintain a constant energy is shown. The modelled data, which uses the power measurements and absorption modelling completed previously, gives good agreement with the measured data in both methods of operation. This data shows that the changes in output energy are primarily due to the reduction in the diode output power and absorption efficiency.

The beam parameters were also measured over the temperature range. These parameters were measured whilst operating in the constant energy mode described previously. The near field diameter and the far field divergence as a function of temperature are shown in Fig. 8.21.

From Fig. 8.21a, a small reduction of 7% in the near field diameter is observed, as the temperature is increased beyond 40 °C. The spatial profiles, shown at the bottom in Fig, 8.21a, do not appear to vary significantly over the temperature range, other than the actual size of the beam. The beam profiles were all taken at similar output energies. The change in the near field diameter could be due to a change in the distribution of gain or change in the thermal lens strength. The overall affect on the beam size is fairly small.

Testing of the slotted reflector in a cross-Porro resonator has shown that an increased absorption path length in the pump configuration allows for operation up to 80 °C, whilst achieving an output energy of ≈60 mJ. The diode pulse duration was

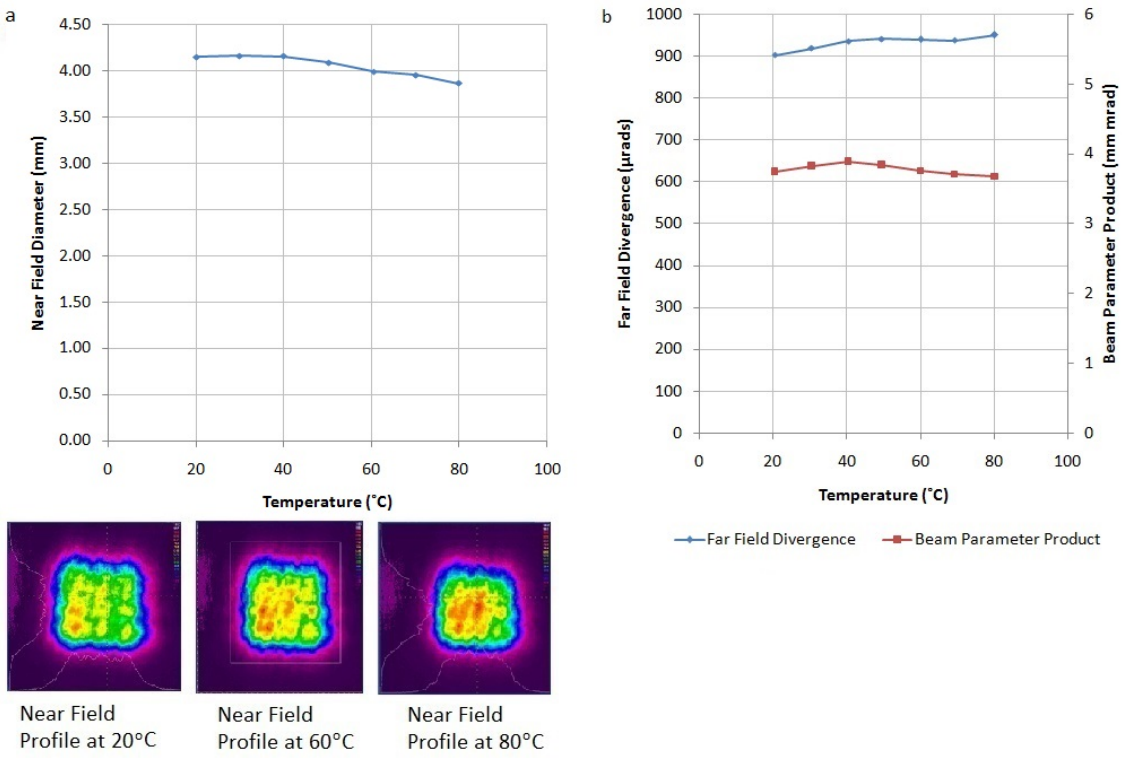

Figure 8.21 – a: Near field diameter over temperature. b: Far field divergence and beam parameter product over temperature.

varied from 150 μs to 230 μs, with variation in output energy agreeing with the modelled results, which included and absorption length of 2.9 cm. The far field divergence of the laser is fairly stable over the temperature range varying by only 5%. Overall, the beam parameter product varies by only 5% over the temperature range. As a result, the performance of the slotted reflector pump head does not significantly alter the beam characteristics, over temperature.

8.6 CuW Reflector LDA Prototype

As discussed in section 8.2.4, an LDA with the reflector removed should provide comparable performance. A second prototype was ordered without the slotted reflector plate on the LDA. This is shown in Fig. 8.22

One of the items not considered was the presence of solder on the spacers. The solder is used to allow current through the array. The overrun occurs as a result of the production process as the bars are pressed together. The solder will reduce the overall reflection of the spacers and may limit the overall performance.

To further reduce the cost, the number of colours within the array was reduced to three. Whilst the increased number of colours provides less variation in absorbed intensity over the temperature range, the number of differing colours does have an

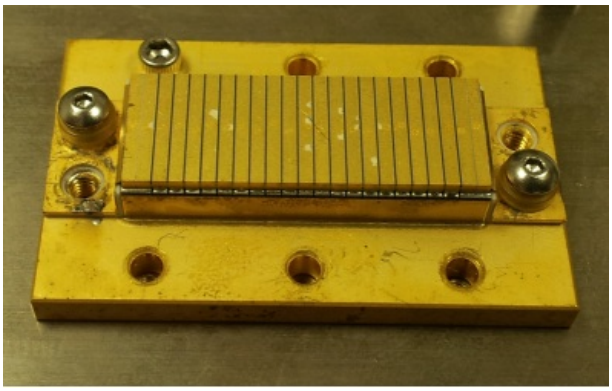

Figure 8.22 – Second CuW reflector LDA without slotted reflector fitted.

impact on the yield, as well as the manufacturing complexity. The three-colour array possessed a total bandwidth of 16 nm, compared with 17 nm for the four-colour array. The centre wavelengths were 795, 803 and 811 nm. An analysis showed that only a 2% reduction in absorbed power would be expected from the three-colour configuration, compared to the previous four-colour arrangement. The limitation of reducing the number of colours further is the increased variation in absorbed power. A two-colour device would significantly increase the variation in absorbed power, but will also not meet the ±3.5 nm centre wavelength tolerance requirement outlined previously.

To validate the performance of the bare diode compared to the slotted reflector, two tests were completed. Initially the single-pass amplification was measured in the same setup described in section 8.23. Secondly, the performance of the CuW Reflector LDA within a cross-Porro resonator was completed. Fig. 8.23 shows the measured single-pass amplification.

The measured results shows similar behaviour to the modelled comparison in Fig. 8.10, with the slotted reflector LDA providing slightly more gain than the bare LDA. The largest difference between the two measurements occurred at 80 °C, where the bare LDA provided only 92% of the amplification achieved in slotted reflector LDA configuration.

8.6.1 CuW Reflector LDA Resonator Testing

The bare LDA was then used to pump a cross-Porro resonator identical to the setup in Fig. 8.17. The components used for this experiment were the same design, but were not the same actual optics. Both configurations were re-tested in this configuration. The performance of the CuW Reflector LDA was compared to that of the slotted reflector LDA in terms of both output energy and the beam parameters. The results are shown in Fig. 8.24.

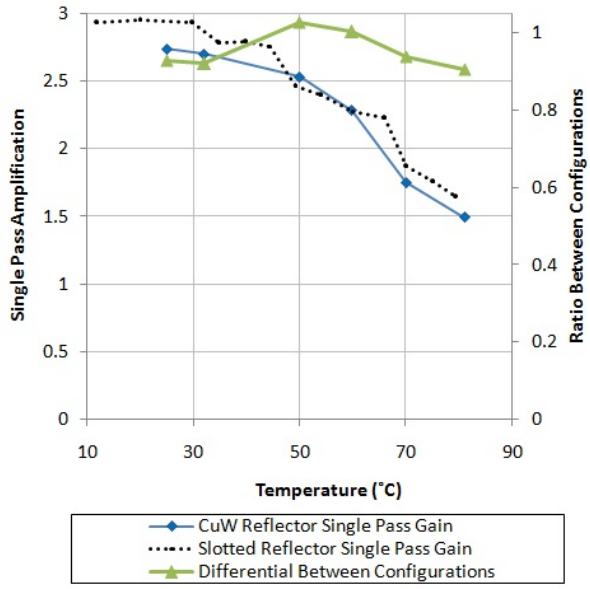

Figure 8.23 – Comparison of single-pass amplification for the slotted reflector LDA and the CuW reflector LDA.

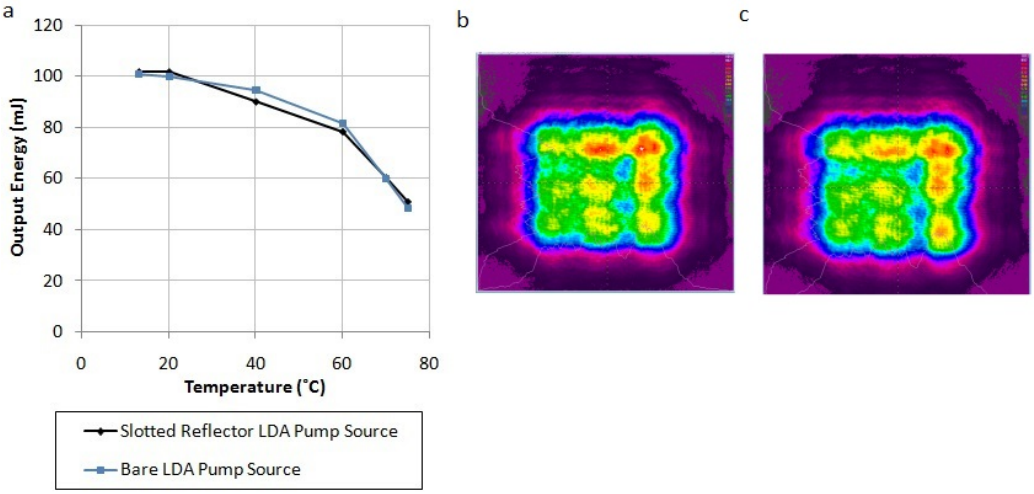

Figure 8.24 – a: Comparison of output energy of slotted reflector LDA and CuW reflector LDA. b: Near field beam from slotted reflector LDA. c Near field beam from CuW reflector LDA.

The overall performance of the two configurations is very similar. The maximum difference in output energy is 5 mJ at a temperature of 75 °C. This corresponds to a difference of 4%. The near and far field beams were also compared. Two captured near field profiles are shown in Fig. 8.24b and c for the slotted reflector and CuW Reflector LDA respectively. Very little difference between the two pump configurations was present. This shows that the thermal lensing and small signal gain profile does not vary significantly between each pump configuration.

The results show that the CuW diode performs very similar to the slotted reflector

LDA. Reduced energy from the CuW LDA at the higher temperatures is observed, but the actual difference is no more than 4%. The performance of the CuW diode is therefore close enough to the slotted reflector design to allow for athermal operation over the required temperature range. To improve the bare diode performance further, a number of modifications could be made. Firstly, the presence of solder on the diode bars could be reduced. The solder is used to provide thermal and electrical contact to each bar within the array. Its presence is therefore vital to the operation of LDAs. The run-off of the solder typically happens at the construction phase, where the solder leaks out from the bars as they are pressed. If the amount of solder used could be limited, this may reduce the amount of solder over-run.

The actual bar reflectivity could be improved by polishing to remove the rough finish. Due to the cost implications of this, a full analysis has not been completed.

8.7 Low Temperature Testing

In the previous sections, the ability of the slotted reflector and the bare LDA to provide efficient absorption over a wide temperature range has been demonstrated. However, the low temperature performance of the LDA has not been verified. The eventual incorporation of the LDA design will involve operation at temperatures as low as -40 °C. As such, the setup must be tested over this temperature range. An existing optical module assembly (OMA) was used to allow for testing in the low temperature range. The OMA contains a laser cavity, driven from commercial off-the-shelf equipment, which is external to the testing chamber. This configuration allows for the separation of the laser performance from any electrical issues that often occur at lower temperatures. The OMA is shown in Fig. 8.25.

Figure 8.25 – Optical module assembly for diode testing.

The OMA is a sealed unit, backfilled with nitrogen to prevent any condensation

within the optical cavity. The internal cavity is configured in a ring configuration. This differs from the previous testing which was completed with the cross-Porro resonator. The ring resonator has been discussed in chapter 1 section 1.1.7. The configuration is shown in Fig. 8.26a. The testing was completed with the different resonator design simply due to the requirement to have a sealed laser chassis to test over the full temperature range.

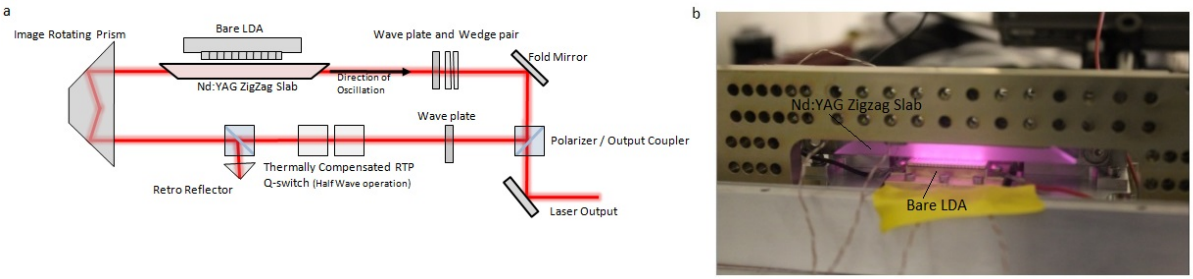

Figure 8.26 – a: Optical schematic of ring resonator. b CuW reflector LDA pumping Nd:YAG slab.

The ring resonator was configured to provide a 90 ° image rotation per round trip. The same type of zigzag slab used in all the previous chapters was again used in this configuration. Due to time constraints, testing could only be completed on the bare diode and therefore a comparison between the slotted reflector and bare LDA could not be completed. The test was primarily used to determine the absorption efficiency of the bare LDA. The beam parameters were not analysed in the results presented here. The testing completed in the previous section has shown that the slotted reflector has limited impact on the beam parameters over temperature.

The resonator performance in the ring resonator configurations was slightly different. The required diode pulse width for 55 mJ was only 130 μs for the OMA ring resonator, compared to 155 μs for the cross-Porro resonator tested previously. The difference in energy between the two cavities will be due to a variation in the round trip losses as a result of different components used in the cavity.

The performance of the cavity was then characterised over the temperature range from -40-60 °C. The cavity was configured to run in the constant energy mode discussed in the previous section. This is typically the method of operation the laser would be expected to be operated in. Fig. 8.27a shows the diode drive pulse width required to achieve an output energy of 60 mJ over temperature. Using the data from the ray-tracing model, the expected diode drive pulse width was also calculated. Within the model, the intra-cavity losses were estimated to be 7%. The output coupling value was estimated to be 73% and the absorption length 2.9 cm. The model uses the LDA

power roll-off measured in the previous section and the actual spectrum of the bare LDA.

The required pulse widths are measured over a 3 min firing period, with the energy measured at the end of the firing period.

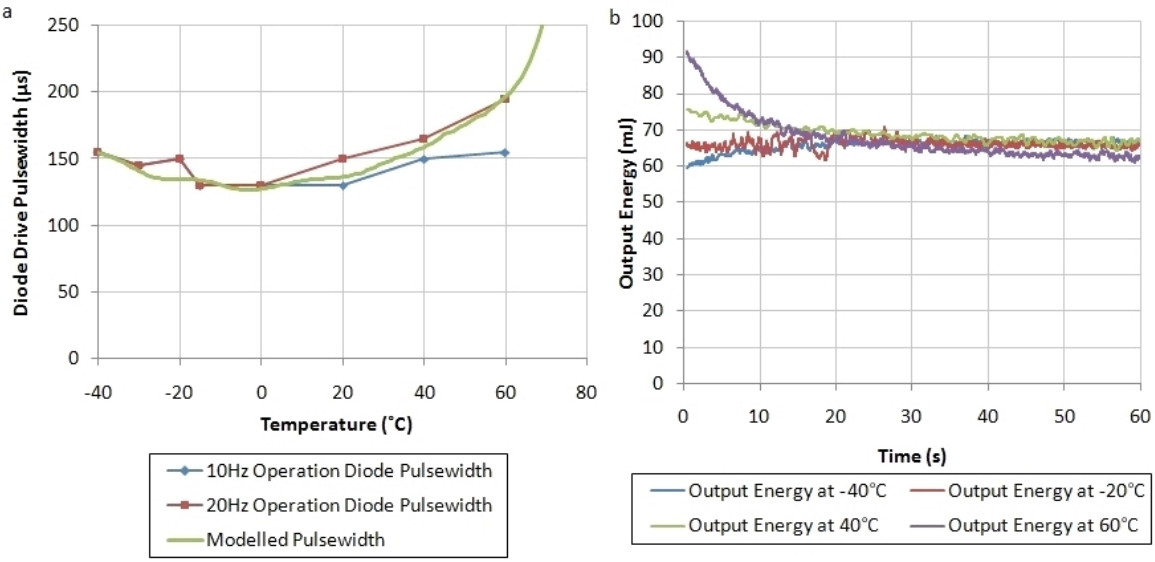

Figure 8.27 – a: Required diode drive pulse width over temperature. b: Transient output energy at various temperatures.

The maximum required diode pulse duration was 195 μs at 60 °C and 150 μs at -40 °C. The modelled pulse durations give good agreement with the measured values. A transient plot of the output energy is shown in Fig. 8.27b at various temperatures. Fig. 8.27b shows the large roll-off or roll-up in energy, as firing commences. The transient output energy is simply caused by the LDA heating up as it fires. A roll-up is observed at the cold temperatures, as the absorption becomes more efficient as the LDAs get hotter. Conversely, at the higher temperatures a large roll-off is observed, as the absorption and pump power drop as a function of temperature. The measured results give good agreement with the modelled results. The performance of the CuW Reflector LDA over the wide temperature range proves that multiple passes within the slab are present, and the CuW Reflector LDA's ability to provide the required energy level over the temperature range from -40 °C + 60 °C

8.8 Conclusion

In this chapter, the use of a new pump design, which incorporates multiple passes into a side-pumped thick zigzag slab was investigated. Two different pump designs were tested. The first used a metallic slotted reflector to allow for multiple passes through the slab. The second design has similar device characteristics, but uses the bare diode

spacers to achieve the multi-pass operation. The devices have been tested over the temperature range from 15-80 °C, confirming the presence of the multi-bounce effect. The multi-bounce effect was therefore shown to increase the absorption length to 2.9 cm. The slotted reflector was found to slightly degrade the beam quality compared to the conventional LDAs with the beam parameter product increasing from 3.1 to 3.7 mm mrads. A comparison of the performance of the bare spacer reflection LDA to the slotted reflector LDA shows that the devices perform very similarly over the temperature range. Testing over the full temperature range has shown the ability of the bare diode to operate down to temperatures as low as -40 °C, whilst still providing sufficient pump energy for the laser to operate.

The work completed in this chapter forms an integral part of a new Selex product. The slotted reflector design allows for a high-energy laser to be operated over the full temperature range, whilst maintaining the beam quality and minimising cost.

Chapter 9

Microchip-Locked Laser-Diode Arrays

9.1 Introduction

In the previous chapters we have shown the ability of the slotted reflector LDA and VBG-locked LDAs to achieve athermal operation. The two devices operate in the 808 nm $F_{5/2}$ absorption band of Nd:YAG. In this chapter we investigate the possibility of operating an athermal Nd:YAG laser pumped at 885 nm. By moving from the wide 808 nm $F_{5/2}$ band, to the 885 nm band, we can achieve increased efficiency and reduced thermal loading of the gain material. The absorption band in the 885 nm region is much smaller and has a number of features that limit efficient absorption. In this chapter, we develop a wavelength locked device that allows the wavelength of the LDA to drift and lock at different wavelengths. The work presented in this chapter is planned for publication in the future. The initial idea and technology was developed by the author, whilst working at laser diode manufacturer Lasertel Inc.

The quantum defect of 808 nm pumped Nd:YAG will create a thermal heat fraction of around 0.24 [25], as a result of the decaying ions from $F_{5/2}$ pump level to the laser transition levels R1 and R2. By pumping at 885 nm, the ions are promoted straight into the upper lasing manifold $F_{3/2}$. The resultant quantum defect is reduced from 0.76 to 0.83. The heat fraction is also reduced from 0.24 to 0.17 [162]. As a result of the reduced heat fraction, pumping at 885 nm reduces the thermal lensing within the Nd:YAG gain material [163]. The efficiency of the laser is also improved by the decreased phonon interactions that occur from the transfer of ions from the upper pump band to the laser transition level [164]. The efficiency has been shown to increase by up to 10% when pumping at 885 nm compared to 808 nm.

The performance improvements achieved by pumping at 885 nm compared to 808 nm has been shown in a number of different configurations [165] [166]. One of the disadvantages of pumping at 885 nm is the reduced absorption coefficient. Fig. 9.1 shows a comparison of the two different pump regions, for 1% doped Nd:YAG.

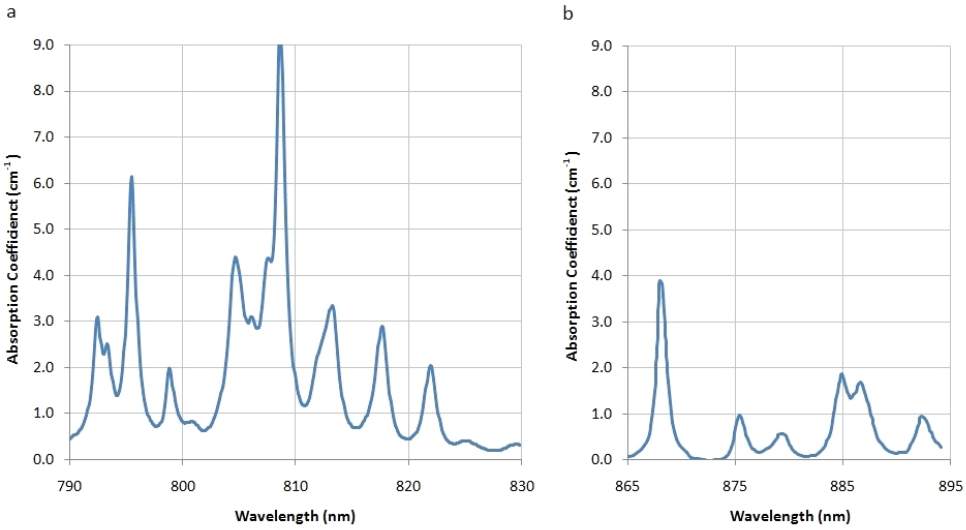

Figure 9.1 – a: Absorption profile of 1% doped Nd:YAG at 808 nm. b: Absorption profile of 1% doped Nd:YAG at 885nm.

For a 1% doped Nd:YAG laser crystal, the peak absorption coefficient is 1.9 cm^{-1} at 885 nm, compared with 9.5 cm^{-1} in the 808 nm region. We also observe a number of troughs in the 885 nm spectrum, where the absorption coefficient drops to very low levels. The actual peaks in the spectrum are also narrower when compared to the 808 nm spectrum. As a result, the average absorption coefficient over a 30 nm range is 2.1 cm^{-1} in the 808 nm region, compared with 0.27 cm^{-1} in the 885 nm region. To achieve efficient absorption in this region, VBG-locked LDAs are typically used. By narrowing the spectrum and locking the centre wavelength to the peak absorption coefficient, the absorption efficiency can be improved.

With a peak absorption coefficient of 1.9 cm^{-1} at 885 nm, the overall absorption efficiency of 0.5 nm bandwidth source at 885 nm, in the 5 mm Nd:YAG zigzag slab introduced in chapter 1 section 1.1.2, is 95%. This was calculated using the same ray tracing algorithm described in chapter 8 section 8.2.2. In this configuration we would expect the VBG-locked LDAs to provide improved performance when compared to 808 nm pumped configurations.

We have previously discussed the requirement for athermal operation in new laser products at Selex. It is therefore a defining requirement to achieve athermal operation at 885 nm. Whilst VBG locking can provide a locked wavelength over a wide temperature range, chapter 7 has shown the difficulty in efficiently locking over the full temperature range. The solution to achieving athermal operation in the 808 nm region was to increase the absorption length from 1 cm to 3 cm, by using a slotted reflector design. The performance of the same configuration operating at 885 nm is shown in

Fig. 9.2. The modelled pump configuration used a three-colour device, optimised using a Monte-Carlo method to determine the optimum wavelength. The centre wavelengths modelled were 873, 880 and 883 nm at 0 °C.

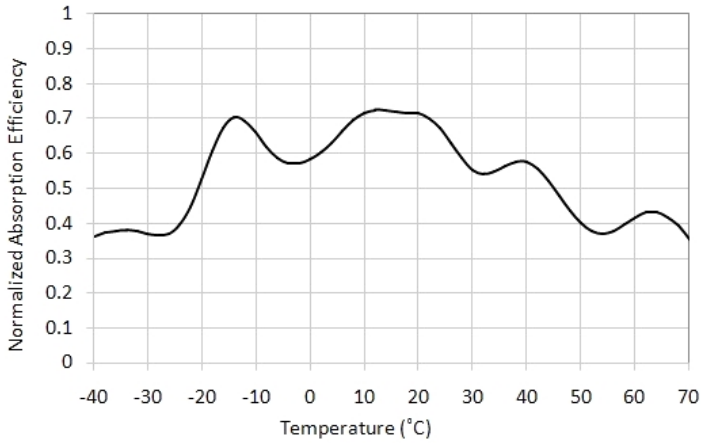

Figure 9.2 – Absorption efficiency of 1% doped Nd:YAG pumped at 885 nm over temperature using three-colour array.

The performance of the athermal operation at 885 nm shows significant troughs in the absorption efficiency. The presence of the peaks and troughs in the absorption spectrum cannot be flattened out by the multi-colour profile. The overall absorption is much lower than that of the 808 nm spectrum and therefore any improvements in efficiency would be lost due to the reduced absorption efficiency. As a result, the slotted reflector design is not capable of providing full athermal operation in this pump region.

To provide full athermal operation in the 885 nm pump region, a different method of operation is required. The challenge of locking the LDA to a single wavelength is the temperature-dependant gain curve of the emitters within the LDA. The absorption spectrum of Nd:YAG, shown in Fig.9.2, does possess a number of peaks at 885 nm that would provide efficient absorption. If a feedback spectrum with multiple peaks, aligned with the strongly absorbing regions in Nd:YAG, could be created, the LDA would lock to each peak as the gain curve shifts. The drop in power associated with locking the LDA emission away from the peak in the gain curve would be limited as the gain curve would always be close to a locking region.

9.1.1 Intra-Cavity Absorber Analysis

Equation (9.1), introduced in chapter 7 section 7.4, shows the threshold condition of an emitter. Until this point we have focused on locking the LDAs by increasing the reflectivity of α_m, which changes the threshold of a particular point in the gain

spectrum. The same effect could also be achieved by affecting the spectral losses of the cavity.

$$\Gamma g(\lambda) = \alpha_i + \alpha_m \tag{9.1}$$

The intrinsic loss factor α_i would become a function of λ instead of the mirror losses α_m. To create an intrinsic loss, we require a material that can preferentially absorb spectral sections of the pump light. Using the actual semiconductor material, it would be difficult to apply a wavelength dependent loss without the addition of other materials in the growth chamber. If we used an element external to the emitter, and created an external cavity, we have the ability to use any material.

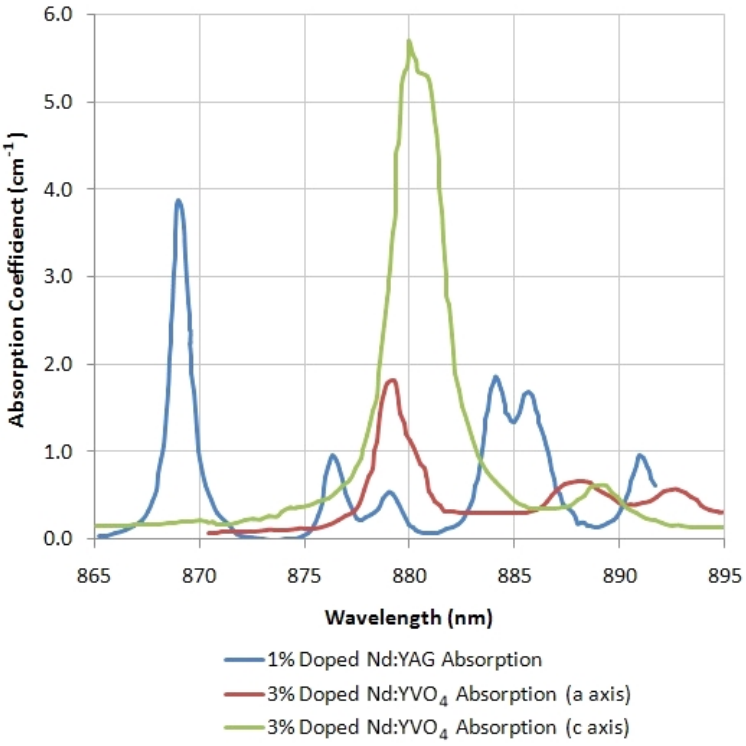

Figure 9.3 – Comparison of absorption spectra of Nd:YAG and Nd:YVO_4.

One of the challenges is availability of materials that possess narrow absorption bands at the desired wavelengths. Most filters provide broad-band spectral responses. We therefore require an absorptive material with absorption peaks similar to that of Nd:YAG, but shifted, to allow for operation in the required spectral regions.

The absorption bands in Nd:YAG are created by the insertion of the Nd^{3+} atoms into the host material Yttrium Aluminium Garnet. When using a different host material, the position of the pump bands, and the subsequent Stark splitting of the levels, modify the absorption spectrum. The result is a slightly different absorption

profile, with peaks in different locations. Fig. 9.3 shows the absorption profile of Nd:YAG and Nd:YVO_4.

The absorption profile shows that the peaks are different for the two host materials. Importantly, the peaks in the two different gain spectra do not overlap. As a result, the Nd:YVO_4 would provide losses at a number of points where troughs in the absorption spectrum of Nd:YAG are present. If the losses of the Nd:YVO_4 could be inserted into the laser-diode cavity, the spectral emission should shifted into to the Nd:YAG absorption peaks.

By incorporating a small piece of Nd:YVO_4 into the external laser-diode cavity, we may be able to tune the spectrum of the emitter onto the absorption peaks of Nd:YAG. The actual configuration of the external cavity would be similar to the VBG-locked devices shown in chapter 7 section 7.3.2. Fig. 9.4 shows the possible incorporation of the external-cavity laser-diode.

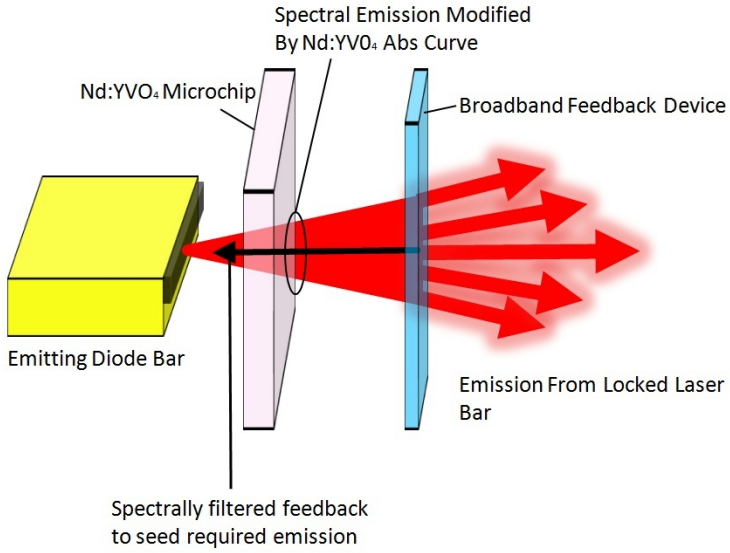

Figure 9.4 – Diagram of Nd:YVO_4 locked device.

A small piece of AR-coated Nd:YVO_4 is placed between the emitter and a broadband low reflectivity mirror. For an external cavity, the emitter end-face is AR-coated. A secondary component is therefore required to achieve feedback into the emitter. This could simply be achieved by coating the back surface of the Nd:YVO_4, allowing for a short cavity. The Nd:YVO_4 will then absorb strongly at the peak of the absorption curve. The strong absorption will affect the threshold of the laser over the spectral range, and the emitter will lase on the lowest threshold point.

9.2 Laser-Diode Threshold Modelling

In the same manner as completed in chapter 7 section 7.4, we can analyse the threshold of the emitter over the temperature range. At the peaks in the absorption curve of Nd:YVO_4, we would expect to observe a shift in the lowest threshold point. Fig. 9.5 shows a comparison of the threshold of a normal emitter to that of an external cavity with a Nd:YVO_4 absorber. In this case we have assumed the gain region is constructed from a SQW, with the same gain characteristics as that shown in Fig.7.2 in chapter 7. For this analysis the shape and magnitude of the gain was assumed to be constant over temperature. The reflectivity of the output coupler was assumed to be 10%. We did not account for any increased losses from the external mirror. The modelled thickness of the Nd:YVO_4 was 0.5 mm, with a doping density of 3%. The model also assumes the absorbers c-axis is aligned with that of the emitter. Only the c-axis absorption is considered in this calculation as a result.

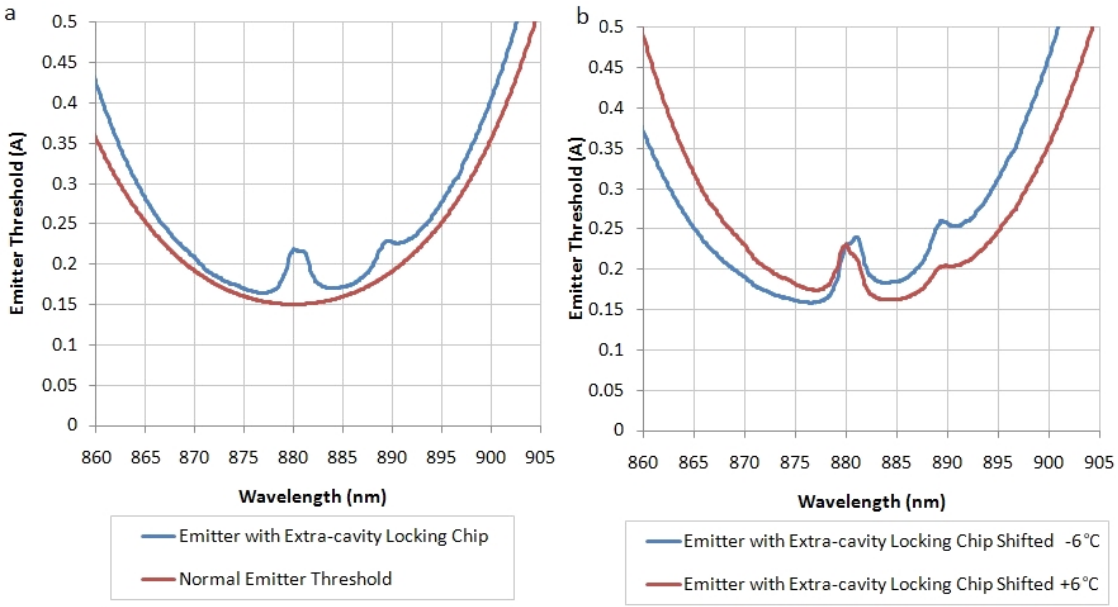

Figure 9.5 – a: Comparison of spectral threshold of normal emitter and external-cavity emitter. b: External-cavity emitter shifted by ±6 °C.

The effect of introducing the Nd:YVO_4 on the threshold can be observed at the central wavelength of 880 nm, in Fig. 9.5a. At this operating point, the lowest threshold will occur at 877 nm, rather than 880 nm. If we assume that the emitter will lase at the lowest threshold point, the insertion of the Nd:YVO_4 should shift the operating wavelength of the emitter to this point. As the temperature of the emitter increases, the Nd:YVO_4 absorber will increase the threshold in this region, ensuring that lasing cannot occur. This can be seen from the spectral threshold plots of the emitters shifted by 6 °C in Fig. 9.5b. The absorber will ensure the spectrum does not tune continuously across this region, but will instead jump from one side of the absorbing region to the

other. Two smaller peaks at 890 nm also exist in the Nd:YVO_4 spectrum, in this region we would also expect the lowest threshold point to be shifted by a smaller amount. The presence of the peaks in this region should ensure the emitter does not lase at 889 nm, where a trough in the Nd:YAG absorption spectrum exists, but instead shift to 891 nm, closer to the peak in the absorption.

We have shown how the threshold is affected by the insertion of the Nd:YVO_4 absorber in the cavity. By making the assumption that the laser will always lase at the lowest threshold, we can predict the centre wavelength for an emitter locked over temperature. Starting with a centre wavelength of 865 nm, we tune the emitter over a 100 °C temperature range, in 1 °C steps, and calculate the wavelength with the lowest threshold. Fig. 9.6 shows a plot of the Nd:YAG absorption curve, overlaid are red dots which show the calculated centre wavelength position of the locked emitter, for each temperature point. This plot allows us to view where we would expect the emitter to lase, as we vary the temperature.

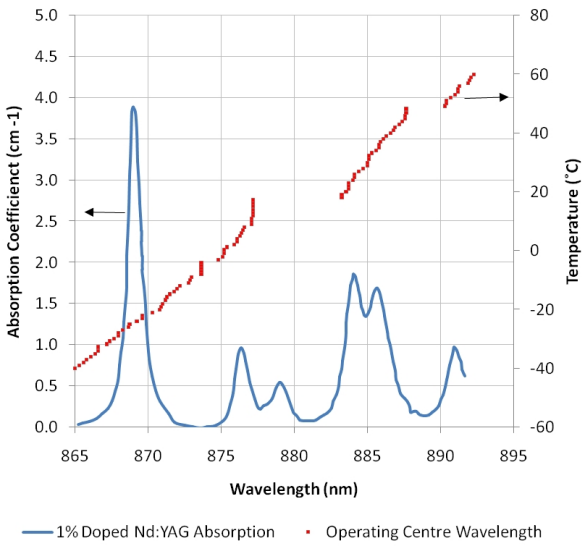

Figure 9.6 – Plot of Nd:YAG absorption, overlaid is expected centre wavelength of LDA over temperature range, shown in red.

Fig. 9.6 shows how the centre wavelength jumps large sections of the spectrum. In the region from 877-895 nm, we observe how the absorber helps tune the centre wavelength to better match that of the peaks in the absorption curve of Nd:YAG. The troughs at 880 and 889 nm in the Nd:YAG absorption align with the regions where the emitter cannot operate. In this 20 nm range, the Nd:YVO_4 locked LDA may provide improved absorption efficiency, when compared to a free-running device.

Fig.9.7 shows the absorbtion efficiency over the wavelength range compared to

a free-running laser. The absorption length for this calculation was 3 cm, similar to the absorption length of the slotted reflector configuration. No coupling losses were used in this calculation and therefore the absorption increases to 1 in the high absorption coefficient regions. In this calculation we have also assumed an infinitely narrow spectrum, the actual output spectrum of the emitter would typically possess a linewidth of around 1 nm. As a result, the actual spectral shape of the emission at any given temperature will differ slightly to the calculated result shown here. At operating points close to the large absorption peaks of the intra-cavity absorber we would expect to see the spectrum split between the two bands. The power would then drift from one emission peak to another as the temperature is increased.

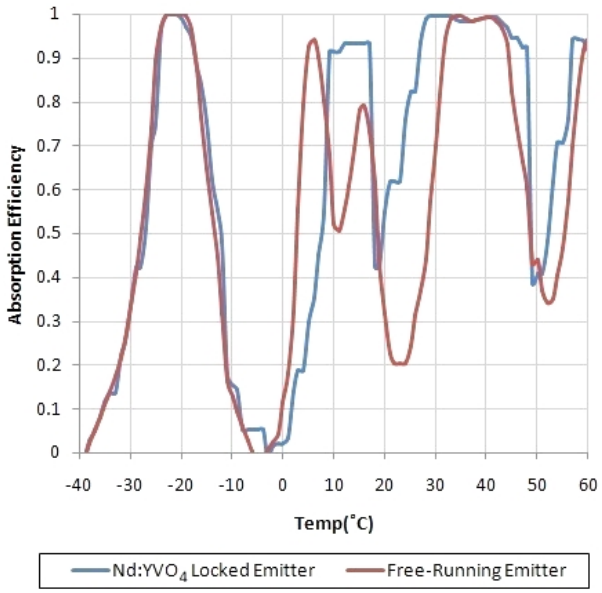

Figure 9.7 – Comparison of absorption efficiency over temperature of locked and free-running emitters.

From 5 °C to 50 °C, the locked emitter should provide improved performance, compared to the free-running one. In the region from 20-50 °C, the locked emitter absorption efficiency is improved compared to the free-running emitter. However, in the region from -40 °C to 5 °C, no improvement is observed from the free-running to the locked emitter. Operation in this temperature region represents a gain curve centre wavelength range of 865 - 874 nm. In this region, the absorption features of the Nd:YVO_4 are limited and as a result, no locking occurs. If the locking could be improved in this wavelength region, the locked emitter could provide significantly improved performance compared to a free-running emitter.

As the model assumes only a single wavelength, the broader spectrum expected from the LDA may also improve the performance, compared to the results shown here. For example, we would expect that at an operating wavelength of 877 nm, we would

not have the full spectrum in this wavelength region. Some of the actual linewidth of the laser will already be operating in the 885 nm region, thereby improving the performance compared to that shown in Fig. 9.7.

The thickness of the Nd:YVO_4 will also affect the locking region. By increasing the thickness of the gain material, we can increase the strength of the locking. However, if we increase the strength too much, the residual absorption will limit the performance. Fig. 9.8a shows the temperature performance of the LDA, as we increase the thickness of the Nd:YVO_4. The doping density remained at 3% for all the calculations. Fig. 9.8b shows the normalized threshold of the LDA over temperature.

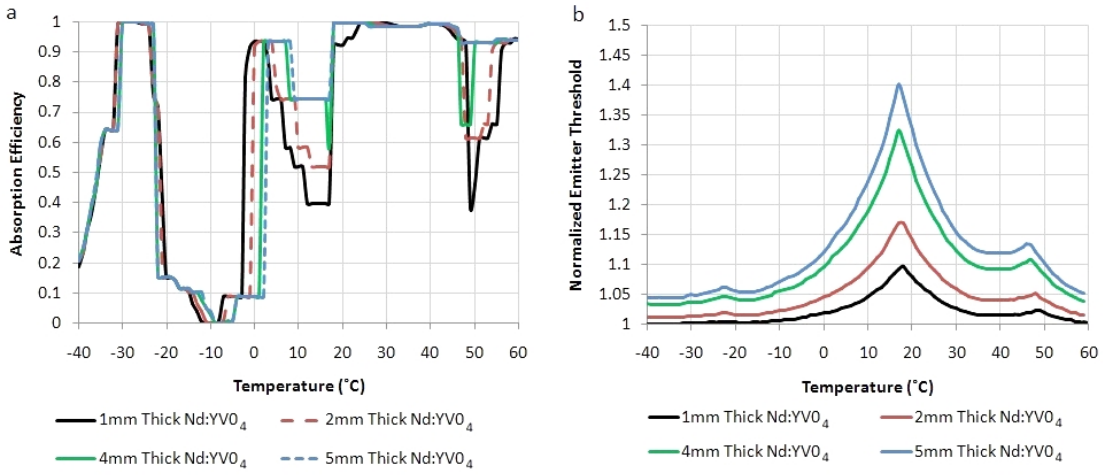

Figure 9.8 – a: Absorption efficiency of locked emitter over temperature at various absorber thicknesses. b: Locked emitter relative threshold over temperature.

From Fig. 9.8, we observe that increasing the thickness of the device will improve the locking range. With a 5 mm thick Nd:YVO_4 absorber, the dips in performance from 17-60 °C are no longer present. By increasing the overall strength of the absorption, the ability to control the spectrum increases. This effect could also be observed by increasing the doping density of the Nd:YVO_4, should commercial sources become available. There is a trade-off in performance, with the increase in thickness reducing the performance in the 10-20 °C range.

Fig. 9.8a shows that as the thickness of the absorber is increased, an increase in the threshold of the device is observed. The change in threshold arises from the locking of the LDA. To shift the operational wavelength, the emission is forced further up the emitter threshold curve, as previously shown in Fig. 9.5. The stronger the locking effect, the further up the curve the centre wavelength will be, and subsequently, the higher the emitter threshold. We would therefore expect the threshold to be largest when the locking leads to the biggest shift in the centre wavelength.

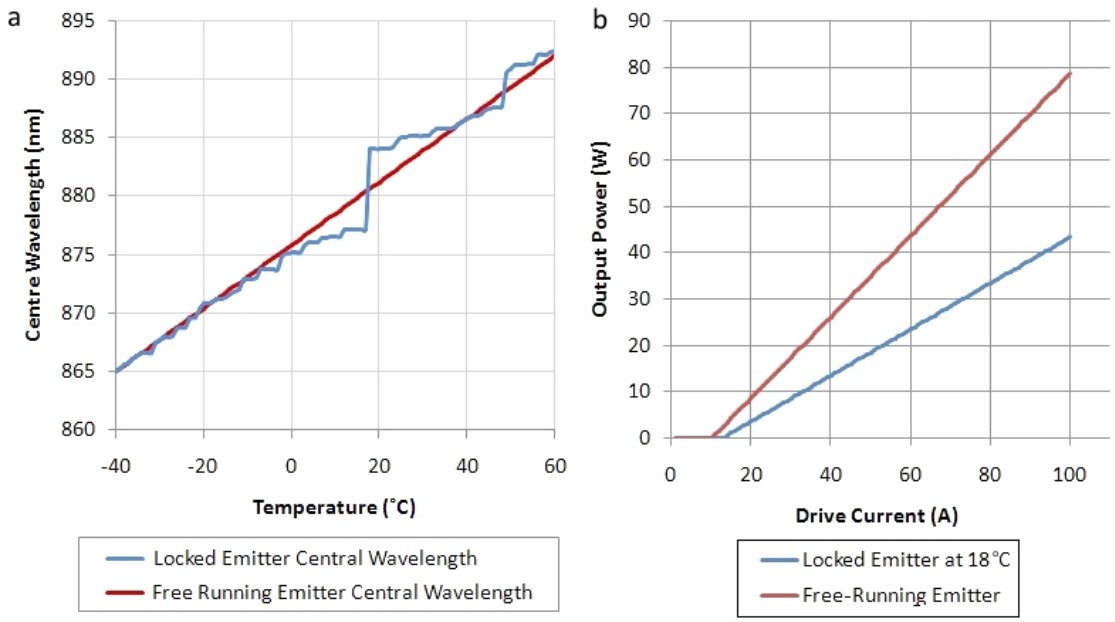

Figure 9.9 – a: Comparison of centre wavelength of locked and free-running emitter. b: Comparison of locked and free-running emitter slope efficiency.

Fig. 9.9a shows a comparison of the centre wavelength of the locked emitter, compared to a free-running emitter. The initial locking can be observed from 0 °C, where the wavelength of the two start to diverge. From this point, up to 19 °C, the locked emitter experiences a reduction in the wavelength temperature tuning rate. Beyond this temperature, a large shift from 876 nm to 884 nm occurs, as the spectrum jumps the absorption peak in Nd:YVO_4. In the region just before the large shift occurs, the emitter will be locked at the furthest distance away from the centre threshold point. This corresponds to the peak in the threshold in Fig. 9.8b.

The increased threshold is due to the reduction in gain in the emitter. As the emitter is forced to lase away from the peak gain point in the quantum-well structure, the gain coefficient reduces. The result will also be a reduction in the slope efficiency of the emitter. Fig. 9.9b shows the modelled slope efficiency of a free-running emitter and the locked emitter operating at 18 °C. This show that locking the emitter wavelength away from the peak in the gain curve has an impact on the slope efficiency of the device.

The modelling has shown the ability of the Nd:YVO_4 locked emitter to improve the absorption efficiency, compared to an unlocked emitter, when pumping an Nd:YAG gain material. The performance of the locked emitter is similar to that of the free-running emitter in the emission region 865-874 nm, where no features in the Nd:YVO_4 absorption spectrum are present. When operating in the centre wavelength range of 877-890 nm, the wavelength is locked by the absorption of the Nd:YVO_4, shifting the

centre wavelength to the peak of the absorption spectrum in Nd:YAG. The threshold of the emitters increases by up to 70% as a result of the locking. The ability to achieve efficient locking, whilst limiting the drop in output power, could allow for improved performance when pumping Nd:YAG over a wide temperature range, in the 885 nm region.

9.3 Nd:YVO_4 Locked Emitter Testing

The ability of the setup to provide locking over the temperature range was then investigated using a laser bar. The bar consisted of 60 emitters, operating at a centre wavelength of 875 nm at room temperature. An AR-coating was applied to the output facet, providing 2% reflectivity. In this investigation the device was operated in a QCW regime, at a repetition rate of 20 Hz and a pulse duration of 230 μs. The initial investigation used FAC on the LDA to improve the feedback of the device. Future work will look to operate the locked device without FAC. The setup in Fig. 9.10a shows the emitting bar placed in a c-mount. A 3% doped Nd:YVO_4 crystal, with a thickness of 0.5 mm, was ordered from OptoCity. The crystal is an off-the-shelf component, originally designed for a microchip laser configuration. The crystal width was 3 mm, compared with a laser bar width of 10 mm. The 3 mm chip was chosen simply due to availability of the components. All measurements taken in this setup used a 3 mm aperture placed behind the setup, to ensure only the locked section of the LDA was investigated. The output power measurements were taken using a Coherent Fieldmaster power meter and LM10 power head. The spectral traces were analysed using a fibre coupled Ocean Optics spectrometer with a 0.3 nm resolution.

A 1 cm thick sapphire plate was used as a feedback device, providing 18% reflectivity combined from the front and rear surfaces. The effect of the external feedback device without the Nd:YVO_4 absorber in the cavity was completed by characterizing the laser with and without the sapphire feedback element. This is shown in Fig. 9.11. Fig. 9.11a show a comparison of the slope efficiencies with and without the sapphire feedback element. Fig. 9.11b shows the output spectrum with and without the feedback element.

Fig. 9.11a shows the performance improvement, as a result of the increased feedback in the cavity. The slope efficiency of the emitter with the feedback was 0.42 W/A, compared with 0.35 W/A for the emitter without the feedback element. The spectrum itself is not significantly different for the two configurations, although the centre wavelength has shifted by 2.5 nm. It was found that by adjusting the angle of the feedback, the centre wavelength could be tuned continuously across a 5 nm range. The etalon effects in the sapphire feedback element should not effect the operating

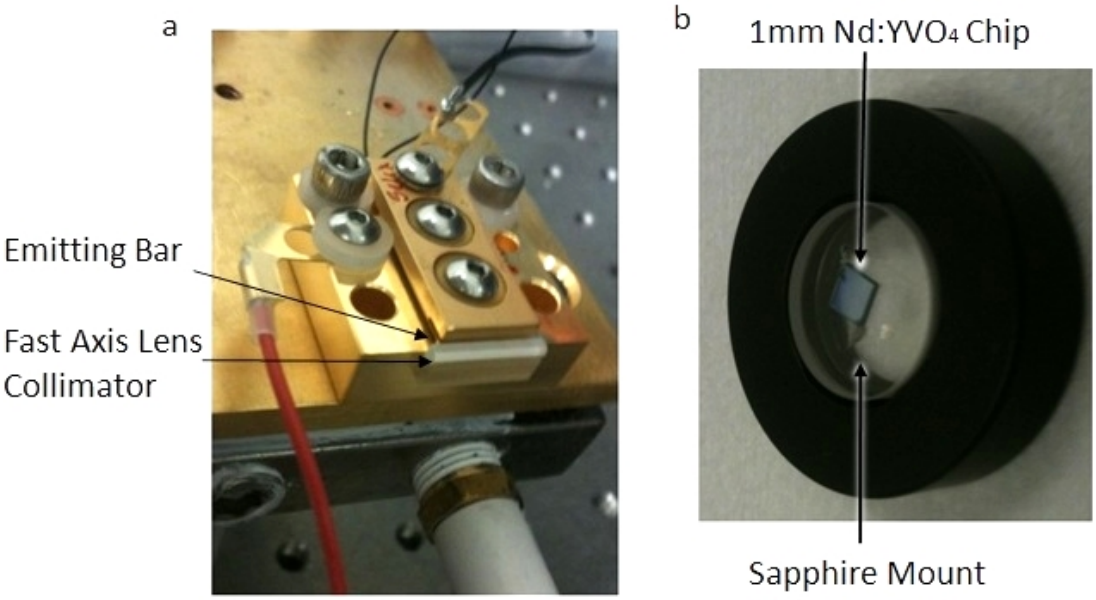

Figure 9.10 – a: Laser bar with FAC. b: Nd:YVO_4 chip bonded to sapphire mount.

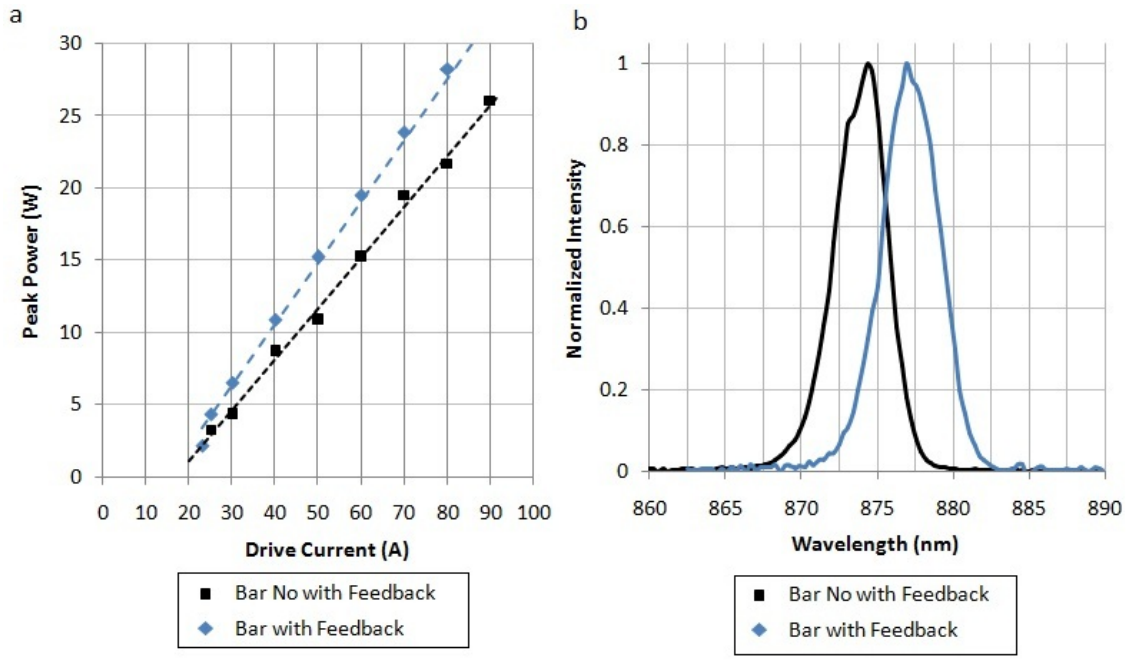

Figure 9.11 – a: Slope efficiency of laser bar configurations. b: Output spectrum of laser bar configurations.

wavelength, as the free spectral range is only 0.02 nm. The tuning effect from the angular adjustment of the mirror may arise due to the longitudinal spacing of the actual external cavity. By adjusting the angle of the mirror, the mode spacing changes. At the peak of the gain curve, only a small change in the overall cavity gain will lead to a change in the centre wavelength. The presence of spatial hole burning within cavity, as well as the spatial variation in the gain due to the carrier induced refractive index, is the main determination of the actual centre wavelength of the emitter over this region [167]. Over the peak gain region, small changes to either the angle or mode

spacing will have a large impact on the centre wavelength.

The Nd:YVO_4 was then pressed and bonded onto the sapphire feedback element, as shown in Fig. 9.10. The bonded Nd:YVO_4 is actually touching the sapphire plate, allowing for a small amount of heat conduction. The bonded device was then mounted 1.5 cm away from the emitters. This is shown in Fig. 9.12. The laser was aligned by adjusting the angle of the sapphire feedback in the same manner as the unlocked configuration. The slope efficiency and spectrum at room temperature is shown in Fig. 9.13.

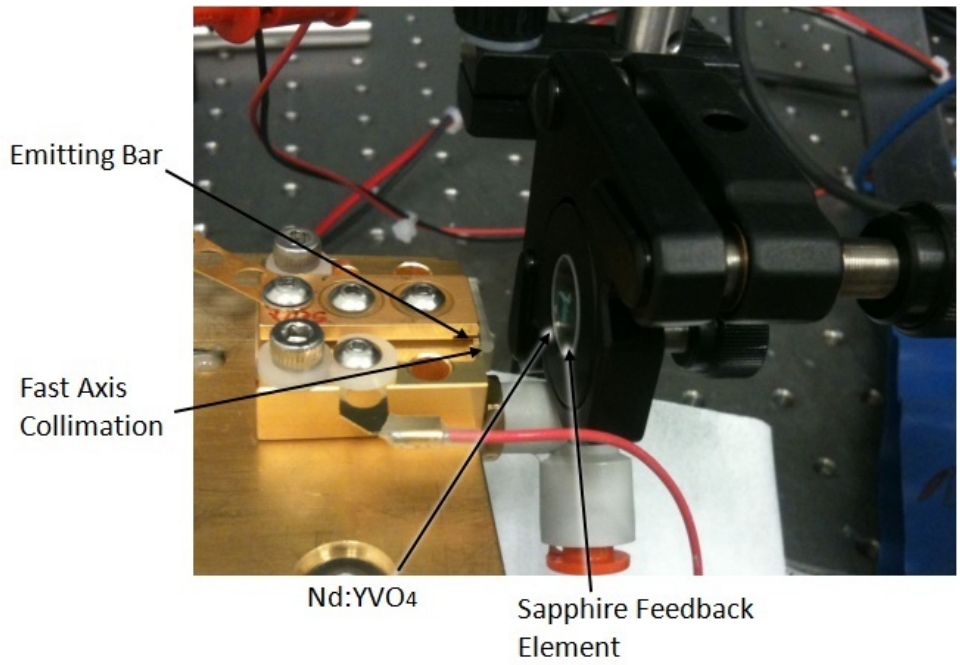

Figure 9.12 – Nd:YVO_4 locked LDA configuration.

The locked laser bar has a slope efficiency of 0.34 W/A, compared with 0.42 W/A for the unlocked laser bar. As expected from the modelling, the locking of the laser bar results in a reduction in the slope efficiency. Fig. 9.13b shows the output spectrum of the locked LDA. A significant change is observed compared to the unlocked laser bar shown in Fig. 9.11. The output now has two peaks, compared with one in the unlocked spectrum. Fig. 9.13 also shows the absorption spectrum of Nd:YVO_4. In this region there are no specific features that would cause the double peak to occur. However, we do have a different absorption values for the different polarisation states. The laser bar will typically emit TE polarisation. Each emitter is capable of emitting both polarisations at threshold; in this operating region we will have higher losses for one polarisation compared to the other. If the feedback of one polarisation is much stronger than the other, a particular polarisation state can be seeded.

The polarisation is typically determined by either heavy or light-hole recombination

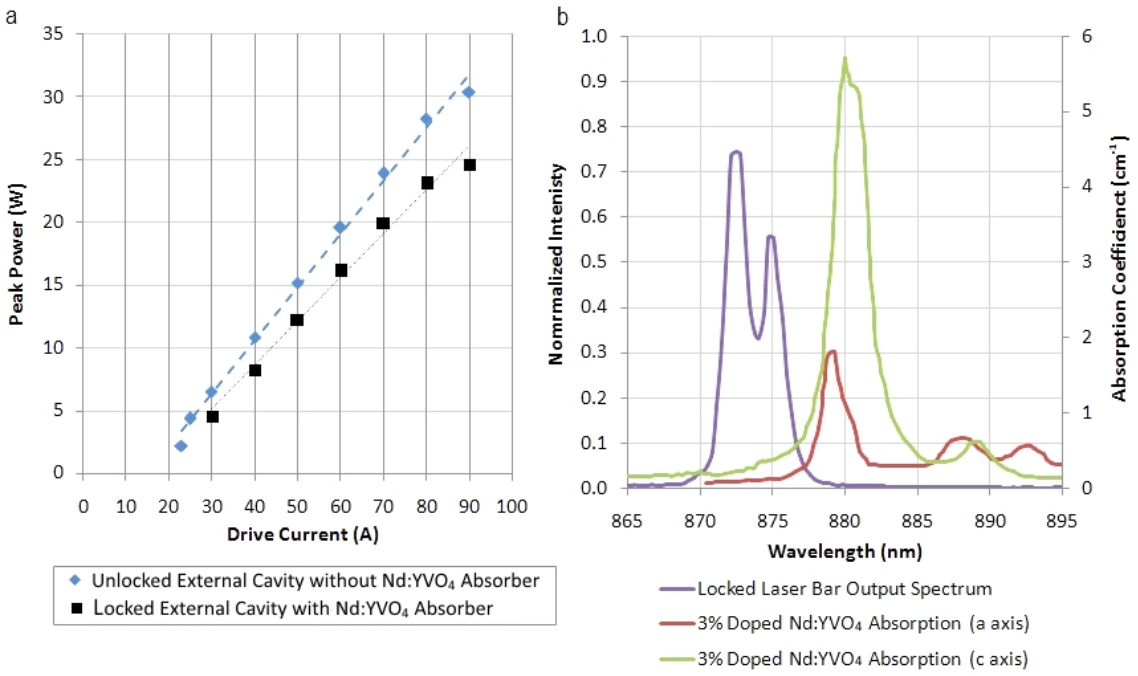

Figure 9.13 – a: Slope efficiency of Nd:YVO_4 locked and unlocked array. b: Spectrum of locked LDA at 30 °C

within each emitter gain region. Heavy holes will only allow for TE polarisation, whilst light holes are dominated by TM polarisation. Typically, heavy-hole recombination is dominant, due to the different shapes of the energy band for each hole type, with heavy bands possessing a much broader curve than the light holes. As a result, the emitters will favour lasing on TE polarisation. If, however, the overall gain including the cavity feedback is increased for the TM polarisation comparative to the TE polarisation, light-hole recombination can still occur. The emission of unlocked laser bar was TE polarisation. The locking has therefore caused a change in the polarisation output of the bar. This has been inferred from the spectrum results only. In future work the polarisation state of the laser will be analysed over temperature.

The temperature performance of the device was then analysed, with the temperature of the emitter varied from 15-65 °C. Fig. 9.14 shows the emission spectrum over the temperature range.

In the range from 20-25 °C in Fig. 9.14a, there are no features in the Nd:YVO_4 to allow for locking. As a result, the spectrum does not appear to be shifted. The emission will therefore operate in the low absorption region of Nd:YAG. We would expect the performance of an Nd:YAG laser, pumped with this spectrum, to be reduced due to the limited absorption. As the temperature is increased to 30 °C, the spectrum begins to lock to the absorption peak at 876 nm. As discussed earlier, the doubled peaked spectrum is due to emission from the two different polarisations.

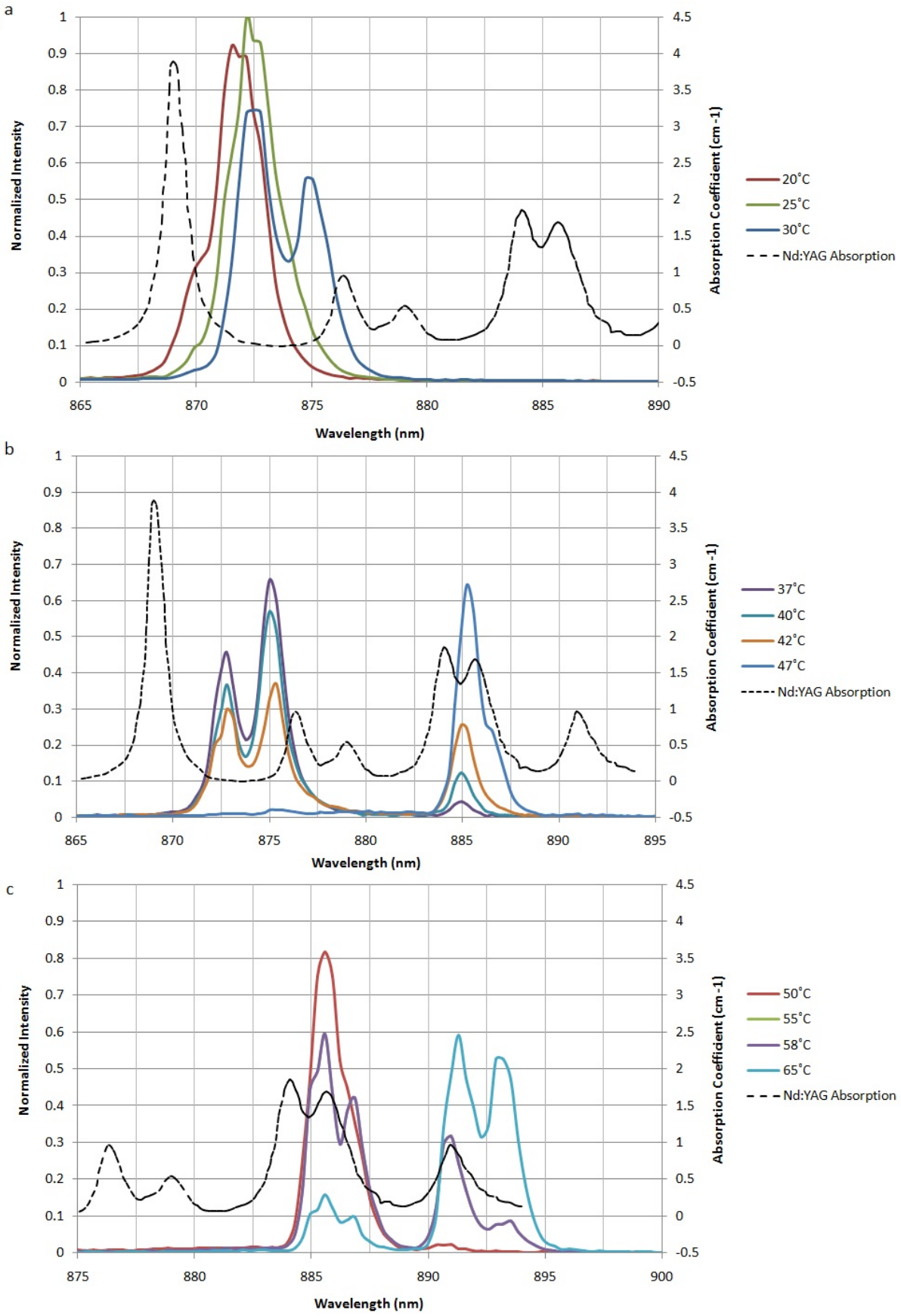

Figure 9.14 – a: Spectrum of locked LDA from 20-30 °C. b: Spectrum of locked LDA from 37-47 °C. c: Spectrum of locked LDA from 50-68 °C.

The peak due to the TM emission is actually better aligned with the absorption spectra of Nd:YAG than the TE polarisation emission. The strong absorption of the Nd:YVO_4 does still allow for the emission to stay locked in both polarisation states. Fig. 9.14b shows the spectral emission jump across the strong absorption peak in Nd:YVO_4 at 880 nm. The result is to shift the spectral emission from one peak in the Nd:YAG absorption to the other. The final shift occurs in Fig. 9.14c, where the peak of the emitting LDA tunes from to 885 to 887.5 nm . We again observe a double peak due to the polarisation state shift. The peak at 890 nm is due to the TM polarisation sitting in a trough in the absorption profile of the a-axis at 889 nm. The second peak is due to the TE polarisation peak in the absorption profile at 889 nm.

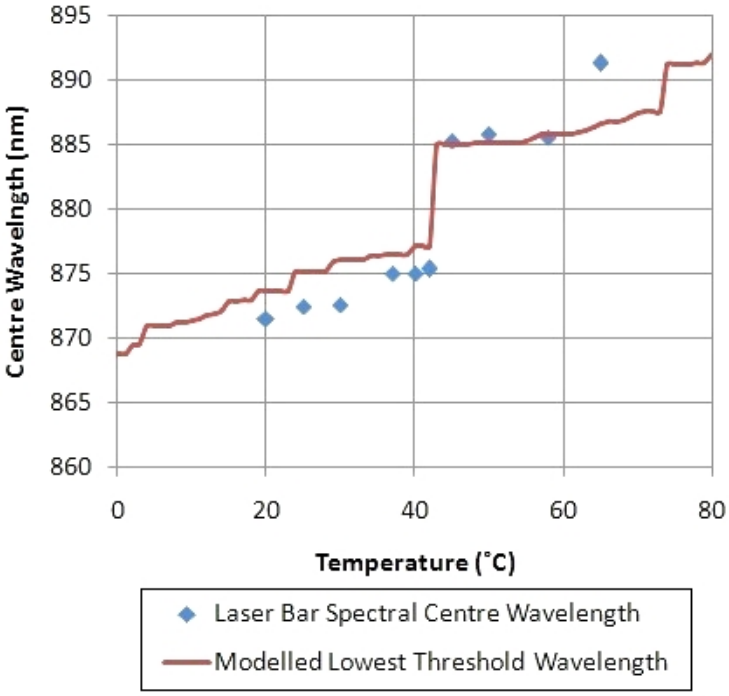

Figure 9.15 – Comparison of measured centre wavelength and modelled lowest threshold wavelength.

The Nd:YVO_4 locked laser bar has shown the ability to shift the laser emission into peaks in the Nd:YAG absorption curve. From the spectral performance, it is clear the centre wavelength threshold point has been shifted by the inclusion of the absorber. Fig. 9.15 shows a plot of the measured central wavelength and the predicted centre wavelength with the lowest threshold. The modelled gain spectrum has a centre wavelength of 872 nm at 20 °C.

The calculated centre wavelength gives good agreement with the actual operating centre wavelength, although a small offset of 1 nm at the low temperatures is present. There are some other inconsistencies between the modelled and measured data. The

first jump in the laser bar's emission occurs from 873-875 nm. This is due to the change in polarisation state, which is not included in the model. The large jump from 876 nm to 885 nm is predicted by the model correctly. The final jump from 885 - 892 nm occurs 7 °C earlier than predicted in the model. However, at this operating temperature we experience a change in the polarisation state. The double peak spectrum shown previously in Fig. 9.14c is a result of the TM polarisation shifting the wavelength to 891 nm, and the TE polarisation shifting the second peak to 893 nm. The second shift does not feature strongly until 68 °C, similar to the modelled value.

The calculation of the centre wavelength therefore agrees reasonably well with the measured values. To improve the accuracy of the model, the ability to determine when polarisation shifts will occur is necessary. To achieve this, the inclusion of the TM spectral gain curve is needed. The spectral bandwidth of the TM gain will be narrower than the TE gain, due to the differences in the energy curves. If we included this spectrum, a comparison of the lowest threshold point for both polarisation states could be included, and the lowest threshold polarisation state predicted.

The output power of the bar was also measured over the temperature range and is shown in Fig. 9.16. The same drive parameters described previously were used, with a repetition rate of 20 Hz and pulse duration of 230 μs.

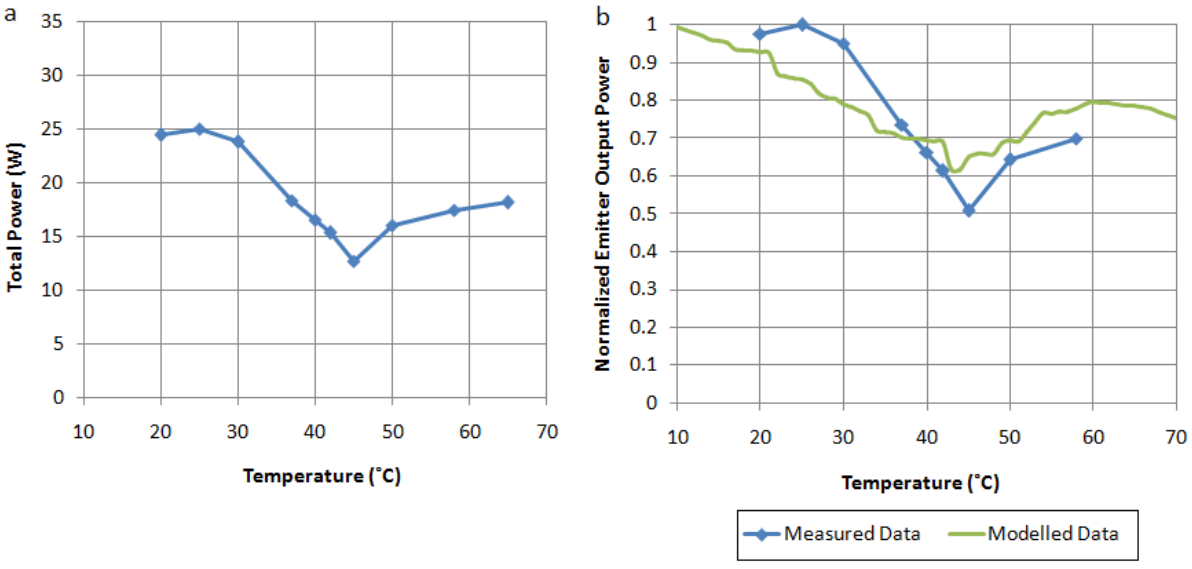

Figure 9.16 – a: Measured output power over temperature. b: Comparison of normalised output power of measured and modelled results.

Fig. 9.16a shows the drop in output power, as the temperature is increased. A distinct trough is also present at 45 °C. The drop in the output power is observed in the region which is strongly locked by the absorber. The previous analysis has

shown that the strong locking regions do cause an increase in the threshold value and a reduction in the output power. The modelled data shown in Fig. 9.16b does predict a slightly higher power than the actual measured value, with a normalised output of 0.61, compared to 0.5 for the measured value. The normalised values do show a similar variation over the temperature range, although the measured values appear to roll-off quicker than the modelled results. A number of factors could be contributing to this. The model only considers the a-axis absorption, the shift in the emitting polarisation prior to the 885 nm peak may cause the efficiency of the emitters to decrease. The actual coupling of the feedback may also be different to those modelled due to variations in the coating of the absorber. A variation in the doping density from the modelled data to that of the actual crystal used could also cause the difference observed.

Using the output spectrum and output power from the locked LDA, we can predict the absorbed power in the 5 mm thick zigzag slab described in chapter 1. The absorption length was 3 cm, which is consistent with the slotted reflector performance presented in chapter 8 section 8.2.2. Fig. 9.17 shows the absorption efficiency of the actual emission wavelength of the emitter and the absorption efficiency of the modelled centre wavelength calculated previously in Fig. 9.9. The normalised absorbed power of a free-running emitter is also shown.

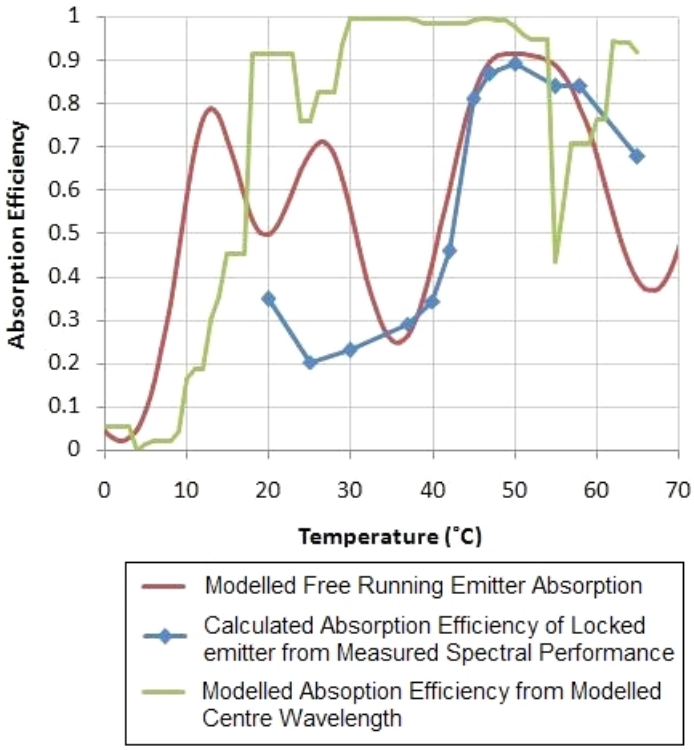

Figure 9.17 – Absorption efficiency of locked emitter calculated from experimental results compared to the modelled results of a free-running emitter and a locked emitter with the centre wavelength dependence presented in Fig. 9.9.

The red line in Fig. 9.17 shows the absorption efficiency of a free-running emitter. The green line shows the expected absorption performance had the diode performed exactly as modelled in Fig. 9.9. The blue line shows the absorption efficiency calculated for the measured spectral emission of the locked LDA, shown in Fig. 9.14. The results show that the overall absorption efficiency does not dramatically improve as a result of the locking. In the temperature range from 20-30 °C, we actually observe a decrease in the efficiency when compared to the unlocked emitters. The results also show there is a significant difference between the modelled efficiency from expected centre wavelength and the absorption efficiency of the actual centre wavelength.

An analysis of the difference in the measured and modelled absorption profiles is first considered. Whilst the modelled and measured results presented previously in Fig. 9.15 appeared to show good agreement, the small 1 nm offset does appear to significantly affect the overall absorption efficiency. The predicted centre wavelength and the actual spectrum measured are compared in Fig. 9.18, at 30 and 60 °C. At 30 °C, we can observe a maximum difference of 4 nm between the modelled and measured centre wavelengths. In Fig. 9.18, the threshold calculation suggests that the spectrum should be sitting at 876 nm. Instead, we have two peaks at the absolute minimum of the two absorption spectra for the a and c-axis. The behaviour suggests the locking of the wavelength is actually too strong, resulting in any small profile in the absorption spectrum locking the emission wavelength. The absorption profile of Nd:YVO_4 therefore appears to limit the emission wavelength to below 875 nm. By changing the thickness of the Nd:YVO_4, the strength of the locking will reduce, and the locked spectrum will shift to the right, improving the absorption efficiency.

The cause of the increased locking strength compared to the modelled values could be due to a number of parameters. One of the main assumptions of the model was the Lorentzian lineshape of the gain curve. If the profile has a broader gain spectrum, the intra-cavity losses required to shift the centre wavelength will be much smaller. Increased feedback could also increase the strength of the locking. The spectral performance of the coatings on the absorber may be larger than specified, increasing the locking strength. Whilst in this configuration, the locking does not provide optimum performance, by reducing the locking strength, we should be able to achieve the performance predicted in the model. As outlined earlier, the locking strength can be reduced either by reducing the crystal length or decreasing the doping density.

One of the main issues with the performance of the locked emitter was the change in polarisation over temperature. Initially, we had aligned the laser bar to emit parallel

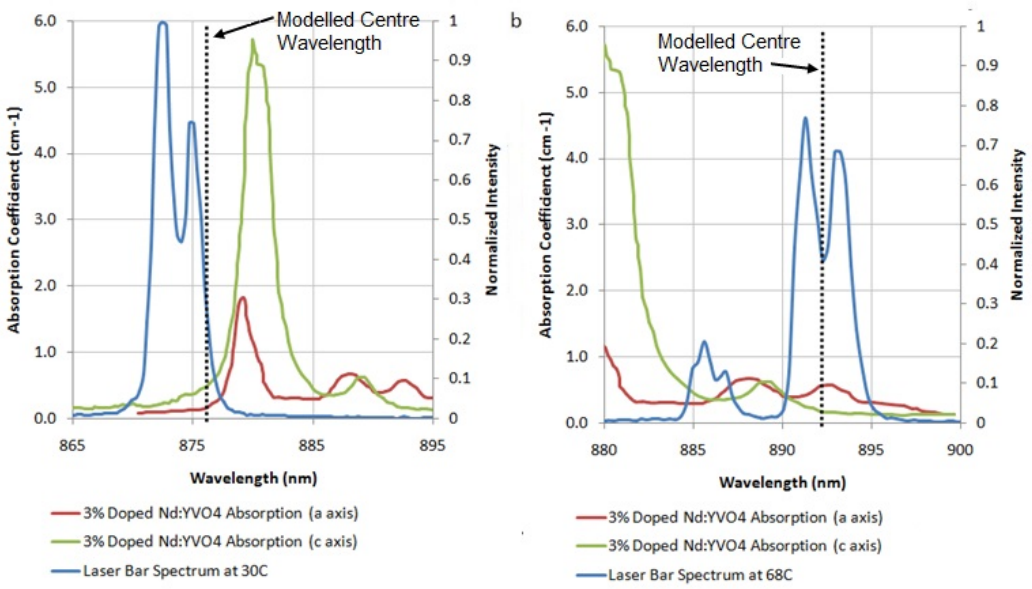

Figure 9.18 – a: Locked spectrum at 30 °C compared to Nd:YVO_4 absorption spectrum. b: Locked spectrum at 68 °C compared to Nd:YVO_4 absorption spectrum.

to the c-axis. However, as we have shown, depending on the losses of each polarisation, the spectrum will jump between the two. For the device to operate efficiently, we ideally require one polarisation. From analyzing the results, the optimum performance may be achieved by aligning the emission to the a-axis, rather than the c-axis. We can see from Fig. 9.18a, at 20-30 °C, the right-hand peak of the spectrum is better aligned to the absorption band at 876 nm, rather than the left-hand peak. In Fig. 9.18b, the spectrum at 68 °C is shown. The a-axis absorption has two small peaks, with the emission sitting in the trough between the two. The locking of the wavelength to this peak is ideally aligned to the peak in the Nd:YAG spectrum at 891 nm. The polarisation would still have to be locked to a given state.

Locking of the polarisation is typically achieved by introducing strain into the wafer. The inclusion of materials such as InGaAsP introduces strain into the lattice structure, which changes the shape of the energy curves for both the heavy and light holes. This allows for operation on the TM polarisation. By locking the emission to one polarisation, the performance of the locked emitter would improve. Threshold analysis would still have to be performed on the stressed gain structure. Whilst the change in the band structure allows for one polarisation to be favoured, it does not forbid the transition from occurring. As a result, even with a lattice with induced strain, operation on the undesired polarisation could occur if the differential in the round trip losses were large enough to overcome the transition selection strength.

The Nd:YVO_4 locking material has shown the ability to modify the spectral properties of the emitter to better match the absorption peak of Nd:YAG. The centre

wavelength of the emission was similar to the modelled data in the previous section. The change in polarisation of the emitters did cause a difference between the modelled and measured values. By adapting the model to include the TM gain curve and the Nd:YVO_4 a-axis absorption, the accuracy of the model would be improved. We also observed good agreement with the measured and modelled output power of the locked laser bar.

9.4 Further Development and Future Work

To improve the output power of the emitters over temperature, a change to the shape of the gain curve could be made. The decrease in output power in the strongly locked region will ultimately limit the performance. The cause of this is the absorber, forcing operation at the edges of the gain spectrum, where the threshold is at its highest. The modelled spectrum was 9 nm wide, which is typical of an SQW structure [133]. In this region we are attempting to shift the spectrum by almost 9 nm from 877 nm to 885 nm. As a result, the emission will be locked to the lowest gain points in the spectrum. By moving from a SQW to a MQW, in a similar manner to that completed for the VBG-locked array in chapter 7, the gain spectrum would be much wider, allowing the emitter to tune across this region, without a large reduction in power.

For temperatures below 20 °C, the calculated performance of the Nd:YVO_4 locked laser bar shows no improvement compared to free-running devices. To improve the performance, future work will look to add a second material into the cavity, further shifting the centre wavelength in the lower temperature region. The absorption peaks of Nd:YLF appear ideally suited to locking the wavelength to the peaks of the Nd:YAG absorption. Future work is intended to develop the possibility of a double microchip configuration, using a highly doped Nd:YLF chip, combined with a Nd:YVO_4 chip, to greatly improve the overall locking range.

9.5 Conclusion

In this chapter we have introduced a new method of locking a laser-diode, by using an active laser gain material. The material is chosen so that the peaks in the absorption spectrum align with troughs in the chosen gain material used in the diode-pumped solid-state laser configuration. Here, pumping of Nd:YAG using a 0.5 mm thick Nd:YVO_4 locking chip is considered, demonstrating the ability of an external configuration to modify the output spectrum. We have also shown the external locking configuration can allow for a change in the polarisation state of the laser due to the anisotropic

material properties of the gain medium. To achieve full athermal performance, a two-chip solution is presented as a possible solution.

Chapter 10

Conclusions

As is the nature of the Engineering Doctorate, the work completed in this thesis covers broad areas of different laser fields that were of interest to the industrial partner Selex. The collection of work has been successful in developing a new class of high-energy targeting lasers at Selex and investigating CW Nd:YVO_4 lasers for countermeasure applications.

In chapter 1, the requirements for the investigation of a visible source capable of generating a series of wavelengths for countermeasure purposes is outlined, and the development of a volume Bragg grating (VBG) as resonator components of solid-state lasers is discussed. Chapter 1 also introduces the military targeting laser technology, based on Q-switched Nd:YAG lasers.

In chapter 2, the theory of Bragg scattering is introduced and two different modelling methods are outlined to characterise the performance of a VBG. The chapter is successful in setting the scene for both the performance of the VBG and the grating parameters that affect this performance. The chapter is also successful in developing a thermal model of a distorted VBG, allowing for the performance implications to be highlighted.

In chapter 3, the development and construction of two end-pumped Nd:YVO_4 solid-state lasers, utilising VBGs as cavity end-mirrors, is presented. The aim of this chapter was to demonstrate the viability of a VBG cavity, at higher power than has previously been demonstrated. Operating at centre wavelengths of 1064 nm and 1342 nm, output powers of 6.2 W and 3.8 W respectively were generated, each with an M^2 of ≤ 1.3. This performance is, to the best of our knowledge, the highest power demonstrated in a low M^2 neodymium-based laser, using VBGs as end-mirrors. This chapter shows the ability of VBGs to function as end-mirrors in cavities of this type, with limited degradation in performance. This result highlights the capability of VBGs as drop-in replacements for HR mirrors. With the knowledge of the performance

of the VBG cavities from this work, in the future, VBG cavities could be used for countermeasure activities and also within industrial lasers. Work from this chapter has been reported in the following publication [55]. Building on from this work, the chapter discusses an optimised cavity design that would limit the power density on the VBG, to allow for scaling to higher output powers. This is planned for future work.

Chapter 4 builds on from the work completed in chapter 2, by experimentally demonstrating the thermal effects of VBGs. The aim of this chapter was to quantify the performance of VBG, under high thermal loads. The construction of a thermally limited VBG cavity is shown and the effects on the beam quality and reflectivity are presented. The results of this chapter shows that the thermal effects within VBGs, will ultimately limit performance for certain configurations. The knowledge gained should, in the future, drive the cavity design to minimise these effects, using the model presented in this chapter. As a result, the analysis completed in this chapter can be repeated for future cavity designs, allowing for optimization of parameters such as the cavity linewidth. The results of this chapter will therefore serve as input to the design parameters for future investigations. The results also provided input into the work completed in chapter 5. From the results of chapter 4, the requirement for the future development of a fully coupled model of the VBG thermal effects and intra-cavity intensity is clear. This would allow for the thermal-coupling of VBG reflectivity and intra-cavity power, shown in this chapter, to be fully understood.

In Chapter 5, a 1342 nm Nd:YVO_4 double-VBG laser is constructed to further enhance the linewidth narrowing performance and enable operation on a single longitudinal mode. The application of spatial hole burning modelling to that of a double VBG cavity is presented for the first time, allowing for the VBG tuning requirements to be calculated. The double VBG laser cavity operated on a single longitudinal mode up to an output power of 2.3 W. This represents higher power than has previously been demonstrated by Hemmer *et al.* [95] using a Ti:Sapphire gain material. The demonstration of a double VBG cavity shows not only the ability of this configuration to operate in SLM, but the possibility of power scaling SLM linear cavities, to higher powers than can be achieved by current technology. By further increasing the laser parameters and addressing the highlighted limitations of the VBGs spectral performance, much higher powers than those demonstrated here, and in the literature, should be possible.

In Chapter 6, the operation of a Q-switched Nd:YVO_4 VBG laser with average powers of up to 4 W at 1064 nm is presented. The improvements in second harmonic conversion efficiency, obtained by using a linewidth-narrowed VBG cavity, is success-

fully shown. An increase of 20% in the overall second harmonic output power is observed from the VBG cavity. This chapter highlights the significant improvements that arise from a switch from traditional dielectric mirror, to the VBG cavity. With limited degridation in the laser parameters, the chapter highlights the limited impact the inclusion of a VBG would have on current laser designs. The chapter shows that the simple change of replacing a HR mirror for a VBG, in a configuration that is used in a number of commercial and scientific lasers, could have a significant impact on the cost / performance ratio of the laser. The chapter also discusses the future possibility of a multi-spectral IR source, that allows for high conversion efficiency into the visible region. The potential for efficient second harmonic generation and sum frequency generation is discussed, with reference to the dual-wavelength work completed after this thesis and reported in [55].

A distinct shift in laser technology to those used in military targeting lasers for mass production, is presented from chapter 7 onwards. The subsequent chapters focus on the development of temperature-insensitive pumping configurations of zigzag slabs, within a low repetition rate high-energy Q-switched Nd:YAG laser. The section first presents the use of VBG-locked laser-diodes to achieve the required temperature insensitivity. The work was completed in collaboration with Lasertel, a major laser-diode manufacturer. The design of a custom-chirped, multiple-quantum-well gain structure within a single laser-diode emitter is presented, from work completed by M. McElhinney. Whilst the work was successful in terms of its performance in the scope of state-of-the-art technology, overall, it did not fully achieve its required temperature range. As a result of the highlighted performance limitations, the work did steer the development towards other methods such as those detailed in chapters 8 and 9. Further development of the gain structure and feedback may, in the future, allow for this technology to meet the desired range. The ability to lock the wavelength of a laser-diode over such a wide temperature range, as shown in this chapter, is definitely useful not only to military products, but also within industrial applications, for example in attaining rapid warm-up times, or to reduce the environmental impact of cooling equipment. Future work, to further optimize the gain structure and VBG feedback to extend the temperature to 120 °C, is currently underway.

In Chapter 8, the design of a pump configuration for a new hand-held targeting laser source is presented. A laser-diode pump configuration for a 5 mm zigzag slab laser is presented that enables operation over a 120 °C range. The improved temperature range allows lasers such as the Type 163 laser, produced by Selex, to operate without any form of active cooling. As a result of work completed in this chapter, the pump head design is now included in two different production products at Selex and is the

subject of a patent application [168]. At the time of writing, over 20 laser have been produced using this technology. The outcome of this chapter has allowed Selex to produce lasers that operate with increased energies and improved beam qualities over a wide temperature range, compared to competitor products. The design changes, compared to the conventional LDA, include a change in the bar construction, the bar orientation, and the spectral output of the arrays, which is widened by including laser bars with widely spaced centre wavelengths. The pump design increases the absorption path length of the pump light from 1 cm to 3 cm, as a result of improved pump light confinement. A pump design that provides multiple bounces of the pump light is experimentally shown, and testing of the LDA design within a military laser product has now demonstrated operation at the required 60 mJ output energy over the environmental temperature range of -40 °C to + 60 °C. Future work to further improve the pump light confinement and reduce the cost of the LDAs is currently underway at Selex.

Chapter 9 presents a new technology for temperature insensitive pumping of Nd:YAG. This original device is an alternative to the VBG-locking presented in chapter 7, developed specifically for pumping at Nd:YAG at 885 nm. Due to the fortuitous overlaps of the two absorption spectra, an Nd:YVO_4 absorber chip is used to lock the wavelength of an emitting bar into the peaks of the absorption spectrum of Nd:YAG. The ability of the configuration to lock the wavelength into multiple peaks over a 45 °C temperature range is shown. The locking range of the external absorber cavity is modelled and optimisation of the locking material used is presented. The use of this technology could provide an improved temperature performance over the configurations presented whilst also allowing for pumping in the narrow band 885 nm pump region. Optimisation of the absorber structure and testing other absorber materials to increase the operational temperature range are planned for future work.

Appendices

.1 Interferogram Measurement Technique

A method for measuring the linewidth of a source using a solid etalon has previously been demonstrated by Lavi *et al.* . The setup was developed to allow for linewidth measurements from a single shot source to be made. Fig. A1 shows the typical measurement technique, utilising a CCD camera.

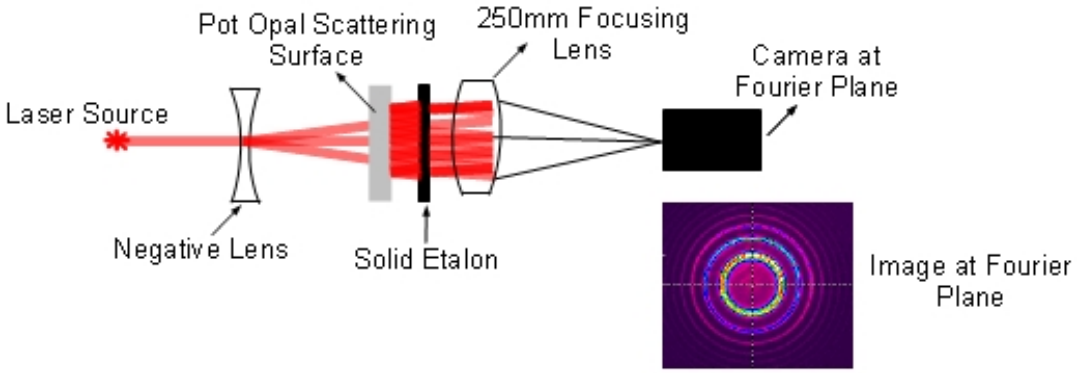

Figure A1 – Experimental setup of linewidth measurement test.

The setup uses the transmission through Fabry-Perot etalon to produce a series of rings. The transmission through the etalon will produce peaks in intensity, with a spacing of $_e$ where

$$\Delta L_e = \frac{c}{2n_e\, L_e} \tag{1}$$

Where L_e is the etalon length and n_e is the refractive index of the etalon. In order for the measurement to be accurate, we must know both the length and refractive index of the etalon extremely accurately. Any small errors in these values will lead to an erroneous measurement and limited accuracy. For the experiments used in this thesis, a solid etalon, with a width of 10 mm and a flatness of $\lambda/10$ was used. The spacing between subsequent sets of rings is also called the free spectral range (FSR). $_e$ is therefore equal to the FSR. By analysing the intensity profile from the CCD camera, the relative spacing of the fringes can be calibrated to the known values of the etalon. The intensity profile of a Helium-Neon laser (HeNe), which has a doppler-broadened gain bandwidth of 1.6 GHz was measured in the configuration shown in Fig. A1, using a 250 mm focusing lens used to image onto a silicon ccd camera. The laser was a Melles-Griot Helium-Neon 25LH-691, with a mode spacing of 822 MHz. The intensity profile is shown in Fig. A2.

To determine the linewidth from the intensity profile in Fig. A2, the following equation can be used

$$\Delta\nu(cm^{-1}) = \frac{\Delta r_1 R_1}{n_e L_e({R_2}^2 - {R_1}^2)} \tag{2}$$

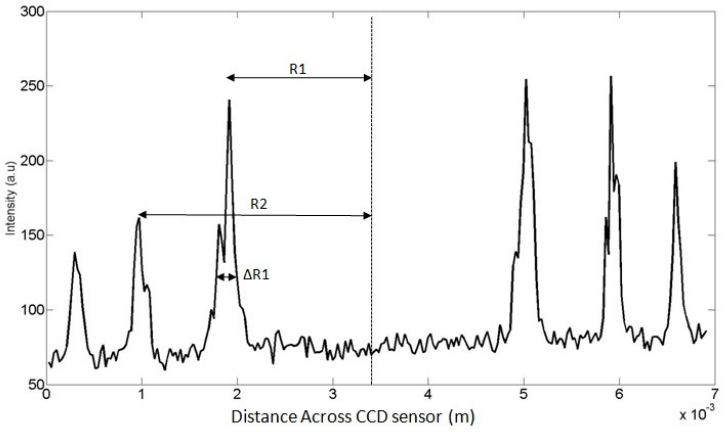

Figure A2 – Intensity profile of HeNe laser using interferogram configuration.

Using equation (2) the linewidth of the HeNe was calculated to be 1590 MHz, similar to the expected value. The mode spacing can also be calculated from the same equation by defining 1 as the mode spacing. The mode spacing was calculated to be 900 MHz, close to the 822 MHz quoted for the device.

The finesse of the etalon will inevitably limit the resolution of the measurement. The finesse of the etalon is determined by the equation

$$F = \frac{\pi\sqrt{R}}{1-R} \tag{3}$$

The minimum width of the fringe with a given finesse F is

$$\delta\lambda = \frac{\Delta\lambda}{F} \tag{4}$$

The reflectivity of the etalon was 60% at 1342 nm, giving a finesse 6. At 1064 nm, the reflectivity was 90%, giving a finese of 29. The etalon was made from fused silica, the refractive index of which is 1.44614 at 1342 nm. The FSR of the etalon at this wavelength is 10 GHz or 60 pm. The minimum FWHM from the etalon is therefore 1 GHz or 10 pm. Consquently, we must have a mode spacing larger than the minimum resolvable FWHM, otherwise, the mode structure will not be seen. The overall linewidth can still be caluculated, provided it is larger than the minimum FWHM.

References

[1] T.H.Maimen. Stimulated optical radiation in ruby masers. *Nature*, 187, 1960.

[2] A Sjian. Low cost laser targeting pod business proposal, July 1 2003.

[3] A Sjian. Selex internal document: Hand held targeting laser business proposal, July 1 2007.

[4] Jie Shan and Charles K Toth. *Topographic laser ranging and scanning: principles and processing*. CRC Press, 2008.

[5] Robert W. Seidel. From glow to flow: A history of military laser research and development. *Historical Studies in the Physical and Biological Sciences*, 18(1):pp. 111–147, 1987.

[6] Sahapong Kruapech and Joewono Widjaja. Laser range finder using gaussian beam range equation. *Optics Laser Technology*, 42(5):749 – 754, 2010.

[7] Ahmed H Elghandour and Chen D Ren. Modeling and comparative study of various detection techniques for fmcw lidar using optisystem. In *ISPDI 2013-Fifth International Symposium on Photoelectronic Detection and Imaging*, pages 890529–890529. International Society for Optics and Photonics, 2013.

[8] W. Koechner. *Solid-state Laser Engineering*. Springer series in optical sciences. Springer, 2006.

[9] Eunchong Kanchanavaleerat, Didier Cochet-Muchy, Milan Kokta, Jennifer Stone-Sundberg, Paul Sarkies, Julian Sarkies, and Jonathan Sarkies. Crystal growth of high doped nd:yag. *Optical Materials*, 26(4):337 – 341, 2004. Third International Symposium on Lasers and Nonlinear Optical Materials (ISLNOM-3).

[10] J Dong, P Deng, F Gan, Y Urata, R Hua, S Wada, and H Tashiro. Highly doped nd:yag crystal used for microchip lasers. *Optics Communications*, 197(46):413 – 418, 2001.

[11] H.G. Danielmeyer, M. Bltte, and P. Balmer. Fluorescence quenching in nd:yag. *Applied physics*, 1(5):269–274, 1973.

[12] David C Brown. Heat, fluorescence, and stimulated-emission power densities and fractions in nd: Yag. *Quantum Electronics, IEEE Journal of*, 34(3):560–572, 1998.

[13] Mark Dubinskii, Larry D Merkle, John R Goff, Gregory J Quarles, Vida K Castillo, Kenneth L Schepler, David Zelmon, Shekhar Guha, Leonel P Gonzalez, Matthew R Rickey, et al. Processing technology, laser, optical and thermal properties of ceramic laser gain materials. In *Defense and Security*, pages 1–9. International Society for Optics and Photonics, 2005.

[14] Larry D. Merkle, Mark Dubinskii, Kenneth L. Schepler, and S. M. Hegde. Concentration quenching in fine-grained ceramic nd:yag. *Opt. Express*, 14(9):3893–3905, May 2006.

[15] Akio Ikesue. Polycrystalline nd:yag ceramics lasers. *Optical Materials*, 19(1):183 – 187, 2002. Photonic Materials for the 21st Century. Proceedings of the 2nd International Symposium on Laser, Scintillator and Nonlinear Optical Materials.

[16] D. Sauder, A. Minassian, and M. Damzen. High efficiency laser operation of 2 at.% doped crystalline nd:yag in a bounce geometry. *Opt. Express*, 14(3):1079–1085, Feb 2006.

[17] L. Tong, Z. Zhao, L. Cui, C. Liu, J. Chen, Q. Gao, and C. Tang. 400-hz pulsed single-longitudinal-mode nd:yag laser with more than 100-mj pulse energy and good beam quality. *Laser Physics*, 21(1):52–56, 2011.

[18] David S. Sumida and T. Y. Fan. Room-temperature 50-mj/pulse side-diode-pumped yb:yag laser. *Opt. Lett.*, 20(23):2384–2386, Dec 1995.

[19] S. Matsubara, T. Ueda, T. Takamido, S. Kawato, and Takao Kobayashi. Nearly quantum-efficiency limited oscillation of yb:yag laser at room temperature. In *Lasers and Electro-Optics, 2005. (CLEO). Conference on*, volume 1, pages 325–327, May 2005.

[20] Christoph Wandt, Sandro Klingebiel, Mathias Siebold, Zsuzsanna Major, Joachim Hein, Ferenc Krausz, and Stefan Karsch. Generation of 220 mj nanosecond pulses at a 10 hz repetition rate with excellent beam quality in a diode-pumped yb:yag mopa system. *Opt. Lett.*, 33(10):1111–1113, May 2008.

[21] H. G. Danielmeyer. *Progress in Nd:YAG Lasers*, volume 4. Marcel Dekker, 1976.

[22] S. P. Chard and M. J. Damzen. Compact architecture for power scalingbounce geometry lasers. *Opt. Express*, 17(4):2218–2223, Feb 2009.

[23] C.M. Depriest, M.A. Decker, M.D. Hawk, S.J. Lindauer, L.S. Lingvay, G.D. Ross, and D.P. Stanley. Laser system with multiple wavelength diode pump head and associated method, July 8 2008. US Patent 7,397,828.

[24] B.F. Aull and H. Jenssen. Vibronic interactions in nd:yag resulting in nonreciprocity of absorption and stimulated emission cross sections. *Quantum Electronics, IEEE Journal of*, 18(5):925–930, May 1982.

[25] T.Y. Fan. Heat generation in nd:yag and yb:yag. *Quantum Electronics, IEEE Journal of*, 29(6):1457–1459, Jun 1993.

[26] Yannick Guyot and Richard Moncorge. Excited-state absorption in the infrared emission domain of nd3+-doped y3al5o12, ylif4, and lamgal11o19. *Journal of applied physics*, 73(12):8526–8530, 1993.

[27] J Eggleston, T Kane, K Kuhn, J Unternahrer, and R Byer. The slab geometry laser–part i: theory. *IEEE Journal of Quantum Electronics*, 20(3):289–301, 1984.

[28] TJ Kane, RC Eckardt, and RL Byer. Reduced thermal focusing and birefringence in zig-zag slab geometry crystalline lasers. *IEEE journal of quantum electronics*, 19(9):1351–1354, 1983.

[29] T.S. Rutherford, W.M. Tulloch, E.K. Gustafson, and R.L. Byer. A 100 w, edge-pumped, conduction-cooled nd:yag zig-zag slab laser with low thermal distortion. In *Lasers and Electro-Optics, 1999. CLEO '99. Summaries of Papers Presented at the Conference on*, pages 31–32, May 1999.

[30] Antonio Lapucci, Marco Ciofini, Maurizo Vannoni, and Andrea Sordini. High efficiency, diode pumped nd:yag ceramics slab laser with 230w continuous-wave output power. *Appl. Opt.*, 51(18):4224–4231, Jun 2012.

[31] Yong-Ho Cha, Sung-Man Lee, Gwon Lim, Sung-Hoon Baik, Sung-Ok Kwon, Byung-Heon Cha, Jung-Hwan Lee, and Eung-Cheol Kang. Development and characterization of a 400-w slab-type nd:yag gain module. *J. Opt. Soc. Korea*, 16(1):53–56, Mar 2012.

[32] Te yuan Chung and Michael Bass. General analysis of slab lasers using geometrical optics. *Appl. Opt.*, 46(4):581–590, Feb 2007.

[33] T. Kane, J.M. Eggleston, and R.L. Byer. The slab geometry laser - part ii: Thermal effects in a finite slab. *Quantum Electronics, IEEE Journal of*, 21(8):1195–1210, August 1985.

[34] A. D. Lyashedko, G. A. Bufetova, V. F. Seregin, V.B. Tsvetkov, and I.A. Shcherbakov. Thermooptical distortions in a nd:yag slab with a zigzag beam propagation. In *Lasers and Electro-Optics Europe (CLEO EUROPE/EQEC), 2011 Conference on and 12th European Quantum Electronics Conference*, pages 1–1, May 2011.

[35] Lasertel. Lasertel data sheet for 300w bars, July 8 2008.

[36] B. Chen, Y. Chen, J. Simmons, T.Y. Chung, and M. Bass. Thermal lensing of edge-pumped slab lasers-i. *Applied Physics B*, 82(3):413–418, 2006.

[37] Fu Xing, Liu Qiang, Yan Xing-Peng, and Gong Ma-Li. Dependence of curvature type of thermal lensing on number of bounces in a zigzag slab laser: numerical modeling. *Chinese Physics B*, 20(11):114210, 2011.

[38] Adelbert Owyoung and Peter Esherick. Stress-induced tuning of a diode-laser-excited monolithic nd: Yag laser. *Optics letters*, 12(12):999–1001, 1987.

[39] R. Paschotta. *Field Guide to Laser Pulse Generation*. Field Guide Series. Society of Photo Optical, 2008.

[40] T. Li A. G. Fox. Resonant modes in an optical maser. *Proc. IRE(Correspondence)*, 48:1904–1905, 1960.

[41] Jyh-Fa Lee and Chung Yee Leung. Method of calculating the alignment tolerance of a porro prism resonator. *Appl. Opt.*, 28(17):3691–3697, Sep 1989.

[42] M. Ishizu. Laser oscillator incorporating transverse mode rotation in the laser resonator, October 30 2007. US Patent 7,289,548.

[43] Arlee V. Smith and Mark S. Bowers. Image-rotating cavity designs for improved beam quality in nanosecond optical parametric oscillators. *J. Opt. Soc. Am. B*, 18(5):706–713, May 2001.

[44] Liesl Burger and Andrew Forbes. A model of the transverse modes of stable and unstable porro-prism resonators using symmetry considerations. In *Photonic Devices+ Applications*, pages 666305–666305. International Society for Optics and Photonics, 2007.

[45] O. Svelto. *Principles of Lasers*. Springer, 2010.

[46] A. E. Seigman. *Lasers*. University Science Books, Mill Valley.

[47] D. Legge. Timing of a q-switch to suppress pre-lasing of the laser, May 18 2007. WO Patent App. PCT/GB2006/050,336.

[48] Floyd E Hovis, Charles Culpepper, Tom Schum, and Greg Witt. Single-frequency 1 μm laser for field applications.

[49] John RM Barr. Laser manufacturing: strategies for dealing with the challenges. In *SPIE Security+ Defence*. International Society for Optics and Photonics, 2012.

[50] Cilas. Cilas dhy 307 data sheet, 2014.

[51] Military Intelligence Service. Militray intelligence bulletin, 1942.

[52] Laser Focus World. laser-energetics-launches-dazer-laser-non-lethal-laser-weapon, 2009.

[53] David C Shannon. Non-lethal laser dazzling as a personnel countermeasure. In *SPIE Security+ Defence*. International Society for Optics and Photonics, 2013.

[54] C.E.L. Mere. Laser countermeasure system and method, August 31 2004. US Patent 6,785,032.

[55] Andrew White, Ian Elder, and Gavin Hall. Single longitudinal mode and dual wavelength cw vbg lasers at 1342nm and 1064nm. In *SPIE Security+ Defence*. International Society for Optics and Photonics, 2012.

[56] Dhiraj K Sardar and Raylon M Yow. Stark components of 4f3/2, 4i9/2 and 4i11/2 manifold energy levels and effects of temperature on the laser transition of nd3+ in yvo4. *Optical Materials*, 14(1):5–11, 2000.

[57] AW Tucker, M Birnbaum, CL Fincher, and JW Erler. Stimulated-emission cross section at 1064 and 1342 nm in nd: Yvo4. *Journal of Applied Physics*, 48(12):4907–4911, 1977.

[58] Y.F. Chen. Design criteria for concentration optimization in scaling diode end-pumped lasers to high powers: influence of thermal fracture. *Quantum Electronics, IEEE Journal of*, 35(2):234–239, Feb 1999.

[59] K Mehdi S, Ebrahim. Simulation of thermal stress in a cw end-pumped a-cut nd:yvo4 crystal. *ournal of Physical Science and Application 3*, 3:171–174, Mar 2013.

[60] M.P. MacDonald, Th. Graf, J.E. Balmer, and H.P. Weber. Reducing thermal lensing in diode-pumped laser rods. *Optics Communications*, 178(46):383 – 393, 2000.

[61] Ian Elder, David Legge, and James Beedell. End-pumped q-switched nd: Yvo4 laser. In *Optics/Photonics in Security and Defence*. International Society for Optics and Photonics, 2006.

[62] Hengli Zhang, Peng Shi, Daijun Li, and Keming Du. Diode-end-pumped, electro-optically q-switched nd:yvo4 slab laser and its second-harmonic generation. *Appl. Opt.*, 42(9):1681–1684, Mar 2003.

[63] Hortz Statz and G DeMars. Transients and oscillation pulses in masers. In *Quantum electronics*, volume 1, page 530, 1960.

[64] J. Lee. *High power, diode-pumped, planar waveguide lasers with excellent beam quality*. PhD thesis, 2002.

[65] A. Alcock and J.E. Bernard. Diode-pumped grazing incidence slab lasers. *Selected Topics in Quantum Electronics, IEEE Journal of*, 3(1):3–8, Feb 1997.

[66] A. Minassian, B. Thompson, and M.J. Damzen. High-power {TEM00} grazing-incidence nd:yvo4 oscillators in single and multiple bounce configurations. *Optics Communications*, 245(16):295 – 300, 2005.

[67] Louis McDonagh, Richard Wallenstein, and Ralf Knappe. 47 w, 6 ns constant pulse duration, high-repetition-rate cavity-dumped q-switched tem00 nd:yvo4 oscillator. *Opt. Lett.*, 31(22):3303–3305, Nov 2006.

[68] Louis McDonagh and Richard Wallenstein. Low-noise 62 w cw intracavity-doubled tem00 nd:yvo4 green laser pumped at 888 nm. *Opt. Lett.*, 32(7):802–804, Apr 2007.

[69] T Chung, A Rapaport, Y Chen, V Smirnov, M Hemmer, LB Glebov, MC Richardson, and M Bass. Spectral narrowing of solid state lasers by narrow-band ptr bragg mirrors. In *Defense and Security Symposium*, pages 621603–621603. International Society for Optics and Photonics, 2006.

[70] Leonid B Glebov. High brightness laser design based on volume bragg gratings. In *Defense and Security Symposium*, pages 621601–621601. International Society for Optics and Photonics, 2006.

[71] N. Vorobiev, L. Glebov, and V. Smirnov. Single-frequency-mode q-switched nd:yag and er:glass lasers controlled by volume bragg gratings. *Opt. Express*, 16(12):9199–9204, Jun 2008.

[72] Herwig Kogelnik. Coupled wave theory for thick hologram gratings. *Bell System Technical Journal*, 48(9):2909–2947, 1969.

[73] J.E. Hellstrom, B. Jacobsson, V. Pasiskevicius, and F. Laurell. Finite beams in reflective volume bragg gratings: Theory and experiments. *Quantum Electronics, IEEE Journal of*, 44(1):81–89, Jan 2008.

[74] Igor V Ciapurin, Leonid B Glebov, and Vadim I Smirnov. Modeling of gaussian beam diffraction on volume bragg gratings in ptr glass. In *Proc. SPIE*, volume 5742, pages 183–194, 2005.

[75] Hong Shu and Michael Bass. Modeling the reflection of a laser beam by a deformed highly reflective volume bragg grating. *Appl. Opt.*, 46(15):2930–2938, May 2007.

[76] J. Hong, Weiping Huang, and T. Makino. On the transfer matrix method for distributed-feedback waveguide devices. *Lightwave Technology, Journal of*, 10(12):1860–1868, Dec 1992.

[77] Hong Shu. More on the iteration of the beam propagation method for analyzing bragg gratings. *J. Opt. Soc. Am. A*, 27(6):1424–1431, Jun 2010.

[78] T. Waritanant and Te-Yuan Chung. Influence of minute self-absorption of a volume bragg grating used as a laser mirror. *Quantum Electronics, IEEE Journal of*, 47(3):390–397, March 2011.

[79] Bjrn Jacobsson. *PHD Thesis: Spectral control of lasers and optical parametric oscillators with volume Bragg gratings*. PhD thesis, 2008.

[80] Alexei L Glebov, Oleksiy Mokhun, Alexandra Rapaport, Sébastien Vergnole, Vadim Smirnov, and Leonid B Glebov. Volume bragg gratings as ultra-narrow and multiband optical filters. In *SPIE Photonics Europe*, pages 84280C–84280C. International Society for Optics and Photonics, 2012.

[81] L. N. Glebova L. B. Glebov and V. I. Smirnov. Laser damage resistance of photo-thermo-refractive glass bragg gratings. *Solid State and Diode Laser Technology Review*, 2004,.

[82] O.M. Efimov, L.B. Glebov, V.I. Smirnov, and L. Glebova. Process for production of high efficiency volume diffractive elements in photo-thermo-refractive glass, July 1 2003. US Patent 6,586,141.

[83] Julien Lumeau, Larissa Glebova, and Leonid B. Glebov. Influence of uv-exposure on the crystallization and optical properties of photo-thermo-refractive glass. *Journal of Non-Crystalline Solids*, 354(29):425 – 430, 2008. Physics of Non-Crystalline Solids 11 11th International Conference on the Physics of Non-Crystalline Solids.

[84] Oleg M. Efimov, Leonid B. Glebov, Larissa N. Glebova, Kathleen C. Richardson, and Vadim I. Smirnov. High-efficiency bragg gratings in photothermorefractive glass. *Appl. Opt.*, 38(4):619–627, Feb 1999.

[85] Te-Yuan Chung, V. Smirnov, M. Hemmer, L.B. Glebov, M.C. Richardson, and M. Bass. Unexpected properties of a laser resonator with volumetric bragg grating end mirrors. In *Lasers and Electro-Optics, 2006 and 2006 Quantum Electronics and Laser Science Conference. CLEO/QELS 2006. Conference on*, pages 1–2, May 2006.

[86] Staffan Tjörnhammar, Björn Jacobsson, Valdas Pasiskevicius, and Fredrik Laurell. Thermal limitations of volume bragg gratings used in lasers for spectral control. *J. Opt. Soc. Am. B*, 30(6):1402–1409, Jun 2013.

[87] P. Jelger, P. Wang, J. K. Sahu, F. Laurell, and W. A. Clarkson. High-power linearly-polarized operation of a cladding-pumped yb fibre laser using a volume bragg grating for wavelength selection. *Opt. Express*, 16(13):9507–9512, Jun 2008.

[88] Sebastian Stark, John C. Travers, Nicolas Y. Joly, and Philip St. J. Russell. *Supercontinuum Sources Based on Photonic Crystal Fiber*, pages 63–96. Wiley-VCH Verlag GmbH Co. KGaA, 2012.

[89] Robert W Boyd. *Nonlinear optics*. Academic press, 2003.

[90] Juan LA Chilla, Stuart D Butterworth, Alexander Zeitschel, John P Charles, Andrea L Caprara, Murray K Reed, and Luis Spinelli. High-power optically pumped semiconductor lasers. In *Lasers and Applications in Science and Engineering*, pages 143–150. International Society for Optics and Photonics, 2004.

[91] Coherent Inc. Coherent optically pumped semiconductor laser range, 2015.

[92] AJ Lee, HM Pask, P Dekker, and JA Piper. High efficiency, multi-watt cw yellow emission from an intracavity-doubled self-raman laser using nd: Gdvo¡ sub¿ 4¡/sub¿. *Optics express*, 16(26):21958–21963, 2008.

[93] Y.R. Shen. *The principles of nonlinear optics*. Wiley classics library. Wiley-Interscience, 2003.

[94] Y. F. Chen, S. W. Tsai, S. C. Wang, Y. C. Huang, T. C. Lin, and B. C. Wong. Efficient generation of continuous-wave yellow light by single-pass sum-frequency mixing of a diode-pumped nd:yvo4 dual-wavelength laser with periodically poled lithium niobate. *Opt. Lett.*, 27(20):1809–1811, Oct 2002.

[95] Michael Hemmer, Yann Joly, Leonid Glebov, Michael Bass, and Martin Richardson. Volume bragg grating assisted broadband tunability and spectral narrowing of ti:sapphire oscillators. *Opt. Express*, 17(10):8212–8219, May 2009.

[96] H. J. Strauss, M. J. D. Esser, G. King, and L. Maweza. Tm:ylf slab wavelength-selected laser. *Opt. Mater. Express*, 2(8):1165–1170, Aug 2012.

[97] Björn Jacobsson, Jonas E. Hellström, Valdas Pasiskevicius, and Fredrik Laurell. Widely tunable yb:kyw laser with a volume bragg grating. *Opt. Express*, 15(3):1003–1010, Feb 2007.

[98] Michael Hemmer, Andreas Vaupel, Mark Ramme, Christina Willis, Joshua D. Bradford, Vadim Smirnov, Lawrence Shah, Leonid Glebov, and Martin Richardson. A vbg-stabilized narrow linewidth, spectrally tunable, yb:yag thin-disk laser. In *CLEO:2011 - Laser Applications to Photonic Applications*, page CWP3. Optical Society of America, 2011.

[99] D. Findlay and R. A. Clay. The measurement of internal losses in 4-level lasers. *Physics Letters*, 20:277–278, February 1966.

[100] V Lupei, N Pavel, and T Taira. Highly efficient laser emission in concentrated nd:yvo4 components under direct pumping into the emitting level. *Optics Communications*, 201(46):431 – 435, 2002.

[101] Te-Yuan Chung, S.S. Yang, Cheng-Wen Chen, Hung-Chih Yang, Chien-Ron Liao, and Yu-Hung Lien. Wavelength tunable single mode nd:gdvo4 laser using a volume bragg grating fold mirror. In *Lasers and Electro-Optics, 2007. CLEO 2007. Conference on*, pages 1–2, May 2007.

[102] Xavier Délen, François Balembois, and Patrick Georges. Temperature dependence of the emission cross section of nd:yvo4 around 1064nm and consequences on laser operation. *J. Opt. Soc. Am. B*, 28(5):972–976, May 2011.

[103] Julien Lumeau, Larissa Glebova, and Leonid B Glebov. Near-ir absorption in high-purity photothermorefractive glass and holographic optical elements: measurement and application for high-energy lasers. *Applied optics*, 50(30):5905–5911, 2011.

[104] Hideo Nagai, Masahiro Kume, Issey Ohta, Hirokazu Shimizu, and Masaru Kazumura. Low-noise operation of a diode-pumped intracavity-doubled nd: Yag laser using a brewster plate. *Quantum Electronics, IEEE Journal of*, 28(4):1164–1168, 1992.

[105] A.E. Siegman. *Lasers*. University Science Books, 1986.

[106] P. Hubner, M. Peterseim, I. Freitag, C. Fallnich, K. Danzmann, and H. Welling. Ultra-stable solid-state lasers for space applications. In *Lasers and Electro-Optics Europe, 2000. Conference Digest. 2000 Conference on*, pages 1 pp.–, Sept 2000.

[107] Björn Jacobsson, Valdas Pasiskevicius, and Fredrik Laurell. Single-longitudinal-mode nd-laser with a bragg-grating fabry-perot cavity. *Opt. Express*, 14(20):9284–9292, Oct 2006.

[108] J Y Long, D Y Shen, Y Sh Wang, J Zhang, and D Y Tang. Compact single-frequency tm:yag ceramic laser with a volume bragg grating. *Laser Physics Letters*, 10(7):075805, 2013.

[109] J. J. Zayhowski. Limits imposed by spatial hole burning on the single-mode operation of standing-wave laser cavities. *Opt. Lett.*, 15(8):431–433, Apr 1990.

[110] I. Dolev, A. Ganany-Padowicz, O. Gayer, A. Arie, J. Mangin, and G. Gadret. Linear and nonlinear optical properties of mgo:litao3. *Applied Physics B*, 96(2-3):423–432, 2009.

[111] I.-H. Bae, H.S. Moon, S. Zaske, C. Becher, S.K. Kim, S.-N. Park, and D.-H. Lee. Low-threshold singly-resonant continuous-wave optical parametric oscillator based on mgo-doped ppln. *Applied Physics B*, 103(2):311–319, 2011.

[112] T.J. Hall, R. Jaura, L.M. Connors, and P.D. Foote. The photorefractive effecta review. *Progress in Quantum Electronics*, 10(2):77 – 146, 1985.

[113] S. Sinha, D.S. Hum, K.E. Urbanek, Yin wen Lee, M. J F Digonnet, M.M. Fejer, and R.L. Byer. Room-temperature stable generation of 19 watts of single-frequency 532-nm radiation in a periodically poled lithium tantalate crystal. *Lightwave Technology, Journal of*, 26(24):3866–3871, 2008.

[114] X.P. Hu, G. Zhao, C. Zhang, Z.D. Xie, J.L. He, and S.N. Zhu. High-power, blue-light generation in a dual-structure, periodically poled, stoichiometric litao3 crystal. *Applied Physics B*, 87(1):91–94, 2007.

[115] Danail Chuchumishev, Alexander Gaydardzhiev, Torsten Fiebig, and Ivan Buchvarov. 0.7 mj, 0.5 khz mid-ir tunable ppslt based opo pumped at 1064 nm. In *Lasers, Sources, and Related Photonic Devices*, page AW4A.25. Optical Society of America, 2012.

[116] Kai Seger, Pär Jelger, Björn Jacobsson, Valdas Pasiskevicius, and Fredrik Laurell. Tunable and passively q-switched nd:yvo⁴laser using a chirped volume bragg grating. In *Conference on Lasers and Electro-Optics/International Quantum Electronics Conference*, page CTuP6. Optical Society of America, 2009.

[117] J. G. Sliney, K. M. Leung, Milton Birnbaum, and A. W. Tucker. Lifetimes of the 4f3/2 state in nd:yvo4. *Journal of Applied Physics*, 50(5), 1979.

[118] J.J. Zayhowski and P. L. Kelley. Optimization of q-switched lasers. *Quantum Electronics, IEEE Journal of*, 27(9):2220–2225, Sep 1991.

[119] W. R. Sooy. The natural selection of modes in a passive q-switched laser. *Applied Physics Letters*, 7(2):36–37, 1965.

[120] H. Weber and A.A. Grutter. The influence of spatial hole-burning in single mode q-switch operation. *Opto-electronics*, 2(2):63–67, 1970.

[121] Sten Helmfrid and Gunnar Arvidsson. Second-harmonic generation in quasi-phase-matching waveguides with a multimode pump. *J. Opt. Soc. Am. B*, 8(11):2326–2330, Nov 1991.

[122] F. J. Kontur, I. Dajani, Yalin Lu, and R. J. Knize. Frequency-doubling of a cw fiber laser using ppktp, ppmgslt, and ppmgln. *Opt. Express*, 15(20):12882–12889, Oct 2007.

[123] D. Eimerl. High average power harmonic generation. *Quantum Electronics, IEEE Journal of*, 23(5):575–592, May 1987.

[124] G. D. Boyd and D. A. Kleinman. Parametric Interaction of Focused Gaussian Light Beams. *Journal of Applied Physics*, 39:3597–3639, July 1968.

[125] J. A. Armstrong, N. Bloembergen, J. Ducuing, and P. S. Pershan. Interactions between light waves in a nonlinear dielectric. *Phys. Rev.*, 127:1918–1939, Sep 1962.

[126] Supriyo Sinha, David S. Hum, KarelE. Urbanek, Yin wen Lee, Michel J. F. Digonnet, Marty M. Fejer, and Robert L. Byer. Room-temperature stable generation of 19 watts of single-frequency 532-nm radiation in a periodically poled lithium tantalate crystal. *J. Lightwave Technol.*, 26(24):3866–3871, Dec 2008.

[127] Bhabana Pati, Kevin F. Wall, and Peter F. Moulton. High-efficiency 532-nm generation with ppslt. In *Lasers, Sources and Related Photonic Devices*, page ATuA17. Optical Society of America, 2010.

[128] Pinhas Blau, Shaul Pearl, Abraham Englander, Ariel Bruner, and David Eger. Average power effects in periodically poled crystals. *Proc. SPIE*, 4972:34–41, 2003.

[129] Sergey V. Tovstonog, Sunao Kurimura, Ikue Suzuki, Kohei Takeno, Shigenori Moriwaki, Noriaki Ohmae, Norikatsu Mio, and Toshio Katagai. Thermal effects in high-power cw second harmonic generation in mg-doped stoichiometric lithium tantalate. *Opt. Express*, 16(15):11294–11299, Jul 2008.

[130] Andrew White, Gavin Hall, John Barr, Mark McElhinney, Prabhu Thiagarajan, and Chuanshun Cao. Thermally insensitive laser diode arrays. In *SPIE Defense, Security, and Sensing*, pages 73250P–73250P. International Society for Optics and Photonics, 2009.

[131] Jens Buus, Markus-Christian Amann, and Daniel J Blumenthal. *Tunable laser diodes and related optical sources*. Wiley-Interscience New York, 2005.

[132] M McElhinney. Internal report: Thermallay insensitive laser diode arrays, 2008.

[133] G.P. Agrawal and N.K. Dutta. *Semiconductor Lasers*. Electrical Engineering. Van Nostrand Reinhold, 1993.

[134] G.P. Agrawal and C.M. Bowden. Concept of linewidth enhancement factor in semiconductor lasers: its usefulness and limitations. *Photonics Technology Letters, IEEE*, 5(6):640–642, June 1993.

[135] J.J. Coleman, A.C. Bryce, and C. Jagadish. *Advances in Semiconductor Lasers*. Semiconductors and semimetals. Elsevier Science, 2012.

[136] P.S. Zory, P.F. Liao, and P. Kelley. *Quantum Well Lasers*. Quantum Electronics–Principles and Applications. Elsevier Science, 1993.

[137] J.E. Carroll, J. Whiteaway, and D. Plumb. *Distributed Feedback Semiconductor Lasers*. IEE circuits and systems series: Institution of Electrical Engineers. Institution of Electrical Engineers, 1998.

[138] RM Lammert, SW Oh, ML Osowski, C Panja, D Qian, PT Rudy, T Stakelon, and JE Ungar. Advances in semiconductor laser bars and arrays. In *Optics & Photonics 2005*, pages 58870B–58870B. International Society for Optics and Photonics, 2005.

[139] P. Mills. Single mode operation of 1.55 m semi-conductor laser using a volume holographic grating,. *Electron. Lett.*, 21(15):648–649, 1985.

[140] BL Volodin, SV Dolgy, ED Melnik, E Downs, J Shaw, and VS Ban. Wavelength stabilization and spectrum narrowing of high-power multimode laser diodes and arrays by use of volume bragg gratings. *Optics letters*, 29(16):1891–1893, 2004.

[141] Gregory J. Steckman, Wenhai Liu, R. Platz, D. Schroeder, C. Moser, and F. Havermeyer. Volume holographic grating wavelength stabilized laser diodes. *Selected Topics in Quantum Electronics, IEEE Journal of*, 13(3):672–678, May 2007.

[142] A Gourevitch, G Venus, V Smirnov, and L Glebov. Efficient pumping of rb vapor by high-power volume bragg diode laser. *Optics letters*, 32(17):2611–2613, 2007.

[143] Bradley W. Schilling, Stephen R. Chinn, A. D. Hays, Lew Goldberg, and C. Ward Trussell. End-pumped 1.5 μm monoblock laser for broad temperature operation. *Appl. Opt.*, 45(25):6607–6615, Sep 2006.

[144] Leonid B Glebov, Sergiy V Mokhov, Vadim I Smirnov, and Boris Ya Zeldovich. Analytic theory of light reflection from a chirped volume bragg grating. In *Frontiers in Optics*, page FWX5. Optical Society of America, 2009.

[145] Breaul. Breault ray tracing program asap.

[146] David Pabœuf, Deepak Vijayakumar, Ole Bjarlin Jensen, Birgitte Thestrup, Jun Lim, Slawomir Sujecki, Eric Larkins, Gaëlle Lucas-Leclin, and Patrick Georges. Volume bragg grating external cavities for the passive phase locking of high-brightness diode laser arrays: theoretical and experimental study. *J. Opt. Soc. Am. B*, 28(5):1289–1299, May 2011.

[147] B. Tromborg, J. Osmundsen, and H. Olesen. Stability analysis for a semiconductor laser in an external cavity. *Quantum Electronics, IEEE Journal of*, 20(9):1023–1032, Sep 1984.

[148] F. Mogensen, H. Olesen, and G. Jacobsen. Locking conditions and stability properties for a semiconductor laser with external light injection. *Quantum Electronics, IEEE Journal of*, 21(7):784–793, Jul 1985.

[149] F. Schuda, American Association of Physicists in Medicine, and Society of Photo-optical Instrumentation Engineers. *Flashlamp pumped laser technology: 21-22 January 1986, Los Angeles, California*. Proceedings of SPIE–the International Society for Optical Engineering. SPIE–the International Society for Optical Engineering, 1986.

[150] R. Nagarajan, T. Kamiya, and A. Kurobe. Band filling in gaas/algaas multi-quantum well lasers and its effect on the threshold current. *Quantum Electronics, IEEE Journal of*, 25(6):1161–1170, Jun 1989.

[151] Gregory Goodno, Stephen Palese, Joseph Harkenrider, and Hagop Injeyan. High average power yb:yag end-pumped zig-zag slab laser. In *Advanced Solid-State Lasers*, page MA2. Optical Society of America, 2001.

[152] Arun Kumar Sridharan, Shailendhar Saraf, Supriyo Sinha, and Robert L. Byer. Zigzag slabs for solid-state laser amplifiers: batch fabrication and parasitic oscillation suppression. *Appl. Opt.*, 45(14):3340–3351, May 2006.

[153] H. Injeyan and C.S. Hoefer. End pumped zig-zag slab laser gain medium, July 3 2001. US Patent 6,256,142.

[154] T.S. Rutherford, W.M. Tulloch, E.K. Gustafson, and R.L. Byer. Edge-pumped quasi-three-level slab lasers: design and power scaling. *Quantum Electronics, IEEE Journal of*, 36(2):205–219, 2000.

[155] Sebastien Chenais, F. Balembois, F. Druon, G. Lucas-Leclin, and P. Georges. Thermal lensing in diode-pumped ytterbium lasers-part i: theoretical analysis and wavefront measurements. *Quantum Electronics, IEEE Journal of*, 40(9):1217–1234, Sept 2004.

[156] D P Shepherd, S J Hettrick, C Li, J I Mackenzie, R J Beach, S C Mitchell, and H E Meissner. High-power planar dielectric waveguide lasers. *Journal of Physics D: Applied Physics*, 34(16):2420, 2001.

[157] Andreas Faulstich, Howard J. Baker, and Denis R. Hall. Diode-pumped, thin slab solid-state lasers. In *Advanced Solid State Lasers*, page LA3. Optical Society of America, 1995.

[158] P. Thiagarajan and M. McElhinney. Laser-diode arrays: Multicolor uncooled diode array efficiently pumps nd:yag laser, May 17 2007. US Patent 7,944,955.

[159] J.C. McCarthy. Multi-pass laser amplifier with staged gain mediums of varied absorption length, November 12 2009. US Patent App. 12/151,384.

[160] J. Kraenert, H. Kuehn, S. Kufert, and H. Mueller. Diode-pumped high performance solid state laser, November 17 1998. US Patent 5,838,712.

[161] Fisba OPtik. Fisba optik uphase, November 17.

[162] Raphael Lavi and Steven Jackel. Thermally boosted pumping of neodymium lasers. *Appl. Opt.*, 39(18):3093–3098, Jun 2000.

[163] M Frede, D Freiburg, R Wilhelm, and D Kracht. High-power 885nm end-pumped nd: Yag laser. In *Lasers and Applications in Science and Engineering*, pages 64510G–64510G. International Society for Optics and Photonics, 2007.

[164] J. Levy, R. Feeler, and J. Junghans. VBG controlled narrow bandwidth diode laser arrays. In *Society of Photo-Optical Instrumentation Engineers (SPIE) Conference Series*, volume 8241 of *Society of Photo-Optical Instrumentation Engineers (SPIE) Conference Series*, February 2012.

[165] R. Lavi, S. Jackel, A. Tal, E. Lebiush, Y. Tzuk, and S. Goldring. 885 nm high-power diodes end-pumped Nd:YAG laser. *Optics Communications*, 195:427–430, August 2001.

[166] S. Bjurshagen, F. Laurell, R. Koch, and H.J. Hoffman. 946-nm nd:yag laser under direct diode-pumping at 869 nm. In *Lasers and Electro-Optics Europe, 2005. CLEO/Europe. 2005 Conference on*, pages 9–, June 2005.

[167] Masakatsu Okada, Mitsuo Hashimoto, and Takaaki Funakoshi. Wavelength switching of a fabry-perot semiconductor laser by optical input pulses. *Optical Review*, 3(5):356–360, 1996.

[168] J. Barr, A. White, and S. Moore. Laser system and method of operation, September 26 2013. US Patent App. 13/988,521.